



HAL
open science

Numerical simulation and physical analysis of the dispersion of charged inertial particles transported by stationary homogeneous isotropic turbulence

Athanasios Boutsikakis

► **To cite this version:**

Athanasios Boutsikakis. Numerical simulation and physical analysis of the dispersion of charged inertial particles transported by stationary homogeneous isotropic turbulence. Fluid Dynamics [physics.flu-dyn]. Institut National Polytechnique de Toulouse - INPT, 2020. English. NNT : 2020INPT0097. tel-04193612

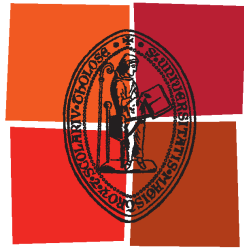
HAL Id: tel-04193612

<https://theses.hal.science/tel-04193612>

Submitted on 1 Sep 2023

HAL is a multi-disciplinary open access archive for the deposit and dissemination of scientific research documents, whether they are published or not. The documents may come from teaching and research institutions in France or abroad, or from public or private research centers.

L'archive ouverte pluridisciplinaire **HAL**, est destinée au dépôt et à la diffusion de documents scientifiques de niveau recherche, publiés ou non, émanant des établissements d'enseignement et de recherche français ou étrangers, des laboratoires publics ou privés.



Université
de Toulouse

THÈSE

En vue de l'obtention du

DOCTORAT DE L'UNIVERSITÉ DE TOULOUSE

Délivré par :

Institut National Polytechnique de Toulouse (Toulouse INP)

Discipline ou spécialité :

Dynamique des fluides

Présentée et soutenue par :

M. ATHANASIOS BOUTSIKAKIS

le jeudi 12 novembre 2020

Titre :

Numerical simulation and physical analysis of the dispersion of charged inertial particles transported by stationary homogeneous isotropic turbulence

Ecole doctorale :

Mécanique, Energétique, Génie civil, Procédés (MEGeP)

Unité de recherche :

Institut de Mécanique des Fluides de Toulouse (IMFT)

Directeur(s) de Thèse :

M. PASCAL FEDE

M. OLIVIER SIMONIN

Rapporteurs :

M. CRISTIAN MARCHIOLI, UNIVERSITE D'UDINE

MME IVANA VINKOVIC, UNIVERSITE LYON 1

Membre(s) du jury :

M. BEREND VAN WACHEM, IMPERIAL COLLEGE OF SCIENCE LONDRES, Président

M. MATHIEU GUNGO, EDF CHATOU, Membre

M. OLIVIER SIMONIN, INSA LYON, Membre

M. PASCAL FEDE, UNIVERSITE TOULOUSE 3, Membre

M. RAYMOND SHAW, UNIVERSITE DU MICHIGAN, Membre

Athanasios Boutsikakis

**Numerical simulation and physical analysis of the
dispersion of charged inertial particles transported
by stationary homogeneous isotropic turbulence**

IMFT, Toulouse, 2020

To my beloved Sofia

*who dared to join me
in this crazy journey*

Acknowledgments

The work presented in this thesis was carried out in the framework of PhD studies in Fluid Dynamics within both the Particle Spray and Combustion (PSC) group and the newly formed Fluids and Particles (F&P) group of the Institut de Mécanique des Fluides de Toulouse (IMFT) entirely funded by the French government via a scholarship of the French Ministry of Higher Education, Research and Innovation.

The writing of this section, marks the completion of this PhD thesis as well as the end of a very exciting journey in IMFT, a journey - though rough at times - that came out to be extremely fulfilling. After three years of working towards my goal to obtain a PhD in Fluid Dynamics, I find myself profoundly enriched in both a professional and personal level. I really enjoyed having worked on such a cool subject with so much to learn from: particles bearing electric charges transported by turbulence!

First and foremost, I would like to express my deep gratitude to both Dr. Pascal Fede and Prof. Olivier Simonin for their trust and support from the beginning till the end of this PhD, including the very challenging times of the outburst of the COVID-19 pandemic during the last crucial year. I really enjoyed working with them, as I learned a lot not only on the subject of turbulent particle-laden flows but also on how to conduct research in general. Firstly, this work would not be the same without the vigorous and passionate supervision of **Dr. Pascal Fede** who supported my endeavors and led me to the right direction when guidance was needed. I appreciate his constant availability and him listening and respecting my ideas and point of view, even when I was evidently wrong. He provided me with everything I needed and he always found the right way to respond to various issues that arose both scientifically, administratively and personally. I would also like to thank **Prof. Olivier Simonin** for his enthusiastic supervision. His insight in both the theoretical and the practical aspects of this subject along with his meticulous suggestions for improvement were crucial to the completion of this PhD. Furthermore, I would like to thank both of my advisors for their support in my Postdoc applications that enabled me to continue conducting research on multiphase flows, at the time of writing.

I would also like to thank all the members of the jury that honored me with their kind acceptance to review my work and their participation in my defense, especially in the difficult circumstances imposed by the COVID-19 global lockdown. Their constructive remarks before the defense helped me a lot to better understand several aspects of my work, and in addition to their interesting questions and comments during the defense, gave me ideas for future research on the topic. On a more personal note, I would like to mention **Prof. Cristian Marchioli** whom I had the chance to meet during the CISM-AIMETA Advanced School on "Anisotropic Particles in Viscous and Turbulent Flows" at Udine, Italy in the summer of 2019 and have since kept a mutual interest in each others' work. Thanks for the scanned annotated pages of the manuscript and for being the unofficial photographer of the PhD defense!

Moreover, it has been a real pleasure to work at **IMFT**, which apart being an extraordinary research facility, is also a welcoming friendly workplace with great people. I would like to thank all the the permanent and non-permanent personnel that made these three years so memorable as well as the **CoSiNus team** for their continuous IT support. At this point, I would like to extend my gratitude to **Ms. Annaïg Pedrono**¹, that has contributed a great

deal to the parallelization of the GASPART code, enabling us to perform massive parallel simulations. To run the latter, I would also like to thank the **CALMIP** center that allocated resources on its supercomputer OLYMPE. In addition, a big thanks to **Dr. Ainur Nigmatova**², **Dr. Azeddine Rachih**², **Dr. Mostafa Sulaiman**³ and **Dr. Thomas Ludwig Kaiser**⁴ for their warm welcome to PSC group upon my arrival at IMFT and for the *moments de convivialité* we shared together while working in the Nougaro building. A special mention to **Dr. Wenchao Yu**⁵ with whom not only I communicated a lot during these years, but also shared an office for several months. For our discussions about complicated algorithms for accurate rectangle slicing, for his interesting scientific input and our heated conversations about everything else. His eagerness to support me during this PhD is highly appreciated.

I also deeply appreciate **Dr. Yorgos Katsikis**⁶, **Dr. Ramzi Messahel**⁷ and **Dr. Georgios Theocharis**⁸ for their interest in my work, their friendship and their time during numerous talks over the years. Finally, I would like to thank my friends and NTUA alumni **Dr. Nikos Bempedelis**⁹ and **Dr. Nikos Simiriotis**⁹ who not only helped me substantially since my arrival at Toulouse, but also kept exchanging throughout all these years about anything imaginable. Our vivid discussions and arguments, proven to be a fruitful exchange of knowledge and experience. Last but not least, special thanks must be accorded to all my **family** and **friends** all the way from Greece to the US, that have supported me in undreamed of ways, I appreciate their love and support and I hope one day I can make them all proud.

¹CNES ²Eramet ³Princeton University ⁴TU Berlin ⁵Total ⁶MIT ⁷Dassault Systèmes
⁸LAUM UMR-CNRS ⁹Imperial College London

Résumé

Dans ce travail de thèse, nous étudions par simulation numérique l'effet des charges électriques sur la dispersion de particules transportées par un écoulement turbulent. Les équations de Navier-Stokes sont résolues par Simulations Numériques Directes (approche spectrale) couplées avec un solveur Lagrangien afin de calculer les trajectoires de chaque particule. Un forçage stochastique permet d'obtenir des écoulements turbulents statistiquement homogènes, isotropes et stationnaires. Dans la thèse, une méthode originale pour la prise en compte des forces électrostatiques a été développée et validée sur des configurations élémentaires. Dans cette méthode, les interactions à courte distance sont estimées via une somme des interactions inter-particules à une distance de coupure et celles à longue distance via une somme d'interactions de particules avec des paquets de particules qui, à une distance supérieure à la distance de coupure, sont considérés comme des pseudo-particules. La convergence, la précision et le coût de calcul de la méthode ont été étudiés en détail pour sa mise en œuvre pour des domaines tri-périodiques. L'ensemble de ces développements a été réalisé dans un code parallèle qui a permis d'effectuer des simulations sur un supercalculateur d'écoulements gaz-particules contenant jusqu'à 2×10^5 particules.

Dans un premier temps, l'analyse d'écoulements granulaires secs a permis de définir une échelle de temps caractéristique de l'effet des charges électriques et de la relier aux caractéristiques physiques des particules notamment le diamètre et leur agitation. Le mécanisme de transformation de l'énergie potentielle électrique en énergie cinétique des particules est analysé en fonction de cette échelle de temps. Dans un second temps, des simulations de turbulence homogène isotrope transportant des particules chargées de même signe ont été réalisées en faisant varier leur diamètre (nombre de Stokes dynamique) et leur charge (nombre de Stokes électrostatique). Les simulations montrent que, pour un Stokes dynamique donné, l'augmentation de la charge des particules conduit à une diminution de l'agitation de celles-ci alors que les forces électrostatiques (répulsives) sont conservatives. L'analyse détaillée montre qu'en fait, les forces électrostatiques conduisent à une destruction de la corrélation des vitesses fluide-particules qui, selon la théorie de Tchen-Hinze, pilote l'agitation des particules.

Outre l'agitation, la distribution spatiale des particules est aussi considérablement modifiée par les forces électrostatiques. En effet, les charges diminuent les valeurs de la fonction de distribution de paire à courte distance ce qui signifie que le phénomène de concentration préférentielle des particules est diminué. Dans le cas limite de fortes charges il est même complètement éliminé puisque que les forces électrostatiques tendent à uniformiser la distribution spatiale des particules. En effet, chaque particule a tendance à former une zone d'exclusion autour d'elle en raison de la forte répulsion à courte distance. Les fonctions de distribution de vitesse relative de paires de particules sont elles aussi affectées par la présence des charges. Enfin, l'effet de la fraction volumique des particules est examiné, où il est montré que son augmentation conduit à une densité d'énergie potentielle électrique du nuage des particules chargées plus élevée qui conduit à une augmentation de l'agitation des particules.

Mots clés: interaction électrostatique, interaction particule-turbulence, théorie de Tchen-Hinze, dispersion, concentration préférentielle

Abstract

In this work, we study by numerical simulation the effect of electric charges on the dispersion of particles transported by a turbulent flow. The Navier-Stokes equations are solved by Direct Numerical Simulations (spectral approach) coupled with a Lagrangian solver in order to calculate the trajectories of each particle. A stochastic forcing scheme allows to obtain statistically homogeneous, isotropic and stationary turbulent flows. In the thesis, an original method to take into account electrostatic forces has been developed and validated on elementary configurations. In this method, the short-range interactions are estimated via a sum of the inter-particle interactions inside a cut-off distance and the long-range ones via a sum of interactions of particles with groups of particles which, at a distance greater than the cut-off distance, are considered as pseudo-particles. The convergence, the precision and the computational cost of the method have been studied in detail for its implementation for tri-periodic domains. The ensemble of these developments has been carried out in a parallel code which allows to perform simulations on a supercomputer of gas-particle flows containing up to 2×10^5 particles.

Firstly, the analysis of dry granular flows allowed to define a characteristic time scale of the effect of electric charges and to link it to the physical properties of the particles, in particular their diameter and agitation. The mechanism of transformation of the electric potential energy into particle kinetic energy is analyzed according to this time scale. Secondly, simulations of homogeneous isotropic turbulence transporting like-charged particles were carried out by varying their diameter (dynamic Stokes number) and their charge (electrostatic Stokes number). The simulations show that, for a given dynamic Stokes, the increase in particle charge leads to a decrease in their agitation since the electrostatic (repulsive) forces are conservative. The detailed analysis shows that, in fact, the electrostatic forces lead to a destruction of the fluid-particle velocity correlation which, according to the Tchen-Hinze theory, drives particle agitation.

Besides agitation, the spatial distribution of particles is also considerably modified by electrostatic forces. In fact, the charges decrease the short-range values of the particle pair distribution function, which means that the phenomenon of preferential concentration of the particles is attenuated. In the limit of strong charges, it is even completely eliminated since electrostatic forces tend to uniformize the spatial distribution of the particles. This is because each particle tends to form an exclusion zone around it due to the strong repulsion at short distance. The relative velocity distribution functions of particle pairs are also affected by the presence of charges. Finally, the effect of the particle volume fraction is examined, where it is shown that its increase leads to a higher electric potential energy density stored the cloud of charged particles which leads to an increase of particle agitation.

Keywords: electrostatic interaction, particle-turbulence interaction, Tchen-Hinze theory, particle dispersion, preferential concentration

Contents

List of Tables	xiii
Nomenclature	xix
1 Introduction	1
1.1 Context and motivation	1
1.2 Background and state-of-the-art	7
1.3 Main objective	7
1.4 Outline of the thesis	8
Bibliography	9
2 Numerical simulation of turbulent particle-laden gas flows	15
2.1 Numerical simulation of particle-laden stationary HIT	15
2.1.1 Spectral method for the resolution of the Navier-Stokes equations	15
2.1.2 Particle tracking in a turbulent velocity field	19
2.1.3 Time-integration and numerical schemes	20
2.2 Configuration of non-settling charge-free reference case	21
2.2.1 Statistically steady homogeneous isotropic turbulence	21
2.2.2 Turbulence of reference	21
2.2.3 Stochastic models of fluid acceleration	27
2.2.4 Particle material properties	31
2.2.5 Fluid and particle characteristic time scales	33
2.3 Conclusion	36
Bibliography	36
3 Dispersion of charge-free inertial particles in stationary HIT	39
3.1 Tchen-Hinze theory for turbulent gas-particle flows	39
3.1.1 Single exponential model	40
3.1.2 Dispersion coefficient of a particle cloud	42
3.2 Statistical analysis of particle dispersion	45
3.2.1 Kinetic energy transfer from turbulence to particles	45
3.2.2 Stochastic models of fluid acceleration - particle velocity covariance	50
3.2.3 Particle dispersion coefficient	55
3.2.4 Spatial distribution of particles	58
3.2.5 Inter-particle relative motion	64
3.3 Conclusion	68
Bibliography	68
4 Numerical simulation of electrostatic forces in charged granular flows	71
4.1 Particle-particle electrostatic interactions	71
4.1.1 Definition of electrostatic forces for a particle dipole	71
4.1.2 N-body problem	71
4.2 Numerical calculation of particle-particle electrostatic forces	72

4.2.1	Electrostatic periodicity	73
4.2.2	Pseudo-particle method	80
4.2.3	Verification of the numerical methods	86
4.2.4	Comparison of the numerical methods and configurations	86
4.3	Numerical simulation of dry like-charged granular flows	88
4.3.1	Configuration of particle electrostatics	88
4.3.2	Coulomb collisions and electrostatic interactions	89
4.3.3	Time-step sensitivity analysis	92
4.3.4	Particle motion due to particle-induced electric field	94
4.3.5	Distribution and time scale of electrostatic forces	99
4.4	Conclusion	101
	Bibliography	101
5	Electrically charged particle-laden turbulent gas flows	103
5.1	Configuration of like-charged case studies	103
5.2	Effect of same-sign electric charges on particle dispersion	105
5.2.1	Energy transfer from turbulence to charged particles	107
5.2.2	Autocorrelation functions of fluid and particle velocity	116
5.2.3	Particle dispersion coefficient	120
5.2.4	Inter-particle electrostatic interactions in turbulent flows	123
5.3	Effect of repulsive electrostatic forces on spatial particle distribution	128
5.3.1	Preferential particle concentration	129
5.3.2	Relative inter-particle motion	136
5.4	Effect of particle number density	140
5.5	Conclusion	144
	Bibliography	145
6	Conclusion and prospects	149
6.1	Conclusions	149
6.2	Future work	151
	Appendices	155
A	Numerical schemes	157
A.1	2nd order Adams-Bashforth numerical schemes	157
A.1.1	Discretization of N-S momentum equation	157
A.1.2	Discretization of particle motion equation	158
A.2	Lagrange polynomial interpolation schemes	158
B	Pseudo-particle algorithm	161
B.1	Pseudo-particle rectangles	161
B.2	Optimal computational cost	161
C	Turbulent charged particle-laden gas flows	163
C.1	Nondimensionalization of the particle motion equation	163
C.2	Particle electric potential energy	164

List of Tables

2.1	Lagrange polynomials	20
2.2	Properties of the fluid and of the examined HIT	27
2.3	Fluid characteristic time scales for different models	31
2.4	Material properties of particles	32
2.5	Characteristic time scales $\tau_{f@p}^t$ and τ_p^t and particle Reynolds number Re_p	35
3.1	Characteristic time scales of the fluid "seen" at the particle position for various levels of particle inertia and two different models	54
3.2	Coefficients c_0 and c_1 for the model of Eq. (3.52) (Chun <i>et al.</i> , 2005)	64
4.1	Slow convergence of periodic anisotropy	74
4.2	Cut-off error of quasi-periodic BCs	80
4.3	Maximum number of short-range neighbourhood cells N_v^{\max}	87
4.4	Approximation error for different numerical algorithms/configurations	88
4.5	Properties of particle electrostatics	89
4.6	Characteristic scales of Coulomb interactions for $Q_p = 5Q_0$. Particles interact with each other having an effective Coulomb diameter $d_{pq}^C/d_p \simeq 34.36$	92
4.7	Time-step convergence	94
5.1	Stokes numbers and characteristic scales of Coulomb interactions of like-charged particles in turbulent gas flow for $Q_p = 5Q_0$	105
5.2	Equivalent particle electric charge for increasing N_p and given τ_{el}	140
C.1	Reference quantities for the particle motion problem	163

Nomenclature

Upper-case Roman

\mathcal{C}	algorithm computational cost in terms of summations (p. 76)
$C_f(\mathbf{x}, t)$	concentration of fluid elements at position \mathbf{x} and time t (p. 43)
C_p	particle concentration (p. 58)
\mathcal{D}	mean squared particle displacement (p. 55)
D_p^t	particle dispersion coefficient (p. 55)
$E(\kappa)$	tri-dimensional spectrum of turbulent energy (p. 25)
$\mathbf{E}(\mathbf{x}, t)$	particle-induced electric field at position \mathbf{x} and time t (p. 97)
$\mathbf{F}_p(\mathbf{x}_p, t)$	total force exerted on a particle at position \mathbf{x}_p and time t (p. 19)
$\mathbf{F}_d(\mathbf{x}_p, t)$	hydrodynamic drag force exerted on a particle at position \mathbf{x}_p at time t (p. 19)
$\mathbf{F}_e(\mathbf{x}_p, t)$	electrostatic force exerted on a particle at position \mathbf{x}_p at time t (p. 19)
$\mathbf{F}_g(t)$	gravity force exerted on a particle at time t (p. 19)
$\mathbf{F}_{k \rightarrow p}$	electrostatic force acting on particle p due to pseudo-particle Ω_k (p. 81)
$\mathbf{F}_{q \rightarrow p}$	electrostatic force acting on particle p due to particle q (p. 71)
L	length of computational domain (p. 18)
L_f	Eulerian longitudinal integral length scale (p. 25)
N	number of grid points per direction x, y, z (p. 21)
N_c	number of cells Ω_c that cover the computational domain (p. 58)
N_e	number of cells per direction for pseudo-particle algorithm (p. 80)
N_k	number of particles in cell Ω_k (p. 80)
N_p	number of particles in the computational domain (p. 31)
N_{per}	number of periodic layers around the computational domain (p. 74)
N_v	number of cells in particle neighbourhood per directions (p. 80)
\mathcal{P}	rate of turbulence production (p. 24)
Q_0	reference particle charge (p. 88)
Q_k^{eq}	equivalent electric charge of pseudo-particle Ω_k (p. 80)
Q_p	particle electric charge (p. 71)
$R_E(\tau)$	Eulerian time autocorrelation function of the fluid velocity (p. 25)
Re_λ	turbulent Reynolds number based on Taylor length scale λ (p. 26)
Re_{L_f}	turbulent Reynolds number based on L_f (p. 26)
Re_p	particle Reynolds number (p. 20)
$R_f(\tau)$	Lagrangian autocorrelation function of the fluid velocity (p. 25)
$R_{f@p}(\tau)$	Lagrangian autocorrelation function of the fluid velocity at particle position (p. 34)
$R_{f_e}(\tau)$	Lagrangian autocorrelation function of particle electrostatic forces (p. 100)
$R_p(\tau)$	Lagrangian autocorrelation function of the particle velocities (p. 34)
S_{pq}^C	Coulomb collision effective section (p. 90)
T_e	eddy turn-over time (p. 19)
T_F	characteristic time scale of turbulent forcing (p. 18)

T_{stat}	duration of calculation of statistical moments (p. 35)
V_p	particle neighborhood of direct dipole interactions (p. 80)
V_c	control volume occupied by cell Ω_c (p. 58)
$\mathbf{W}(t)$	vector-valued Wiener process at time t (p. 27)

Lower-case Roman

$\hat{\mathbf{a}}(\boldsymbol{\kappa}, t)$	stochastic force in Fourier space (p. 18)
$\mathbf{a}'_f(\mathbf{x}, t)$	fluid acceleration at position \mathbf{x} and time t (p. 27)
$\mathbf{a}'_{f@p}(\mathbf{x}_p, t)$	fluid acceleration at particle position \mathbf{x}_p and time t (p. 47)
$\hat{\mathbf{b}}(\boldsymbol{\kappa}, t)$	random complex vector in Fourier space (p. 17)
$\mathbf{b}_p(t)$	counter vector that tracks the times a particle crosses the periodic borders (p. 55)
d	number of physical (periodic) dimensions (p. 74)
d_p	particle diameter (p. 19)
d_{np}	nearest-neighbor particle distance (p. 60)
d_{pq}^C	effective Coulomb diameter (p. 89)
$f(q)$	probability density function of scalar variable q (p. 99)
g	gravitational constant (p. 19)
$g(r)$	radial distribution function (p. 62)
\hat{i}	imaginary unit (p. 16)
$\hat{\mathbf{i}}, \hat{\mathbf{j}}, \hat{\mathbf{k}}$	cartesian unit vectors (p. 75)
$\mathbf{l}_p(t)$	particle displacement vector (p. 44)
m_p	particle mass (p. 19)
m_{pq}	reduced mass of a pair of particles (p. 89)
n_p	particle number density (p. 31)
$p(\mathbf{x}, t)$	instantaneous fluid pressure at position \mathbf{x} and time t (p. 16)
q_f^2	fluid agitation (fluid kinetic energy per unit mass) (p. 23)
$q_{f@p}^2$	fluid agitation "seen" at the particle positions (p. 32)
q_{fp}	fluid-particle velocity covariance (p. 32)
q_p^2	particle agitation (particle kinetic energy per unit mass) (p. 32)
\mathbf{r}_{kp}	distance vector between particle p and pseudo-particle Ω_k pointing to p (p. 82)
\mathbf{r}_{pq}	distance vector between particles p and q pointing to p (p. 60)
\mathbf{r}_{pq}^\dagger	distance vector between particle p and periodic images of q pointing to p (p. 75)
$u_e(\mathbf{x}_p, t)$	electric potential energy stored in a particle at position \mathbf{x}_p and time t (p. 77)
u'_f	characteristic turbulent velocity (p. 25)
$\mathbf{u}_f(\mathbf{x}, t)$	instantaneous fluid velocity vector at position \mathbf{x} and time t (p. 16)
$\mathbf{u}_{f@p}(\mathbf{x}_p, t)$	undisturbed fluid velocity at particle position \mathbf{x}_p and time t (p. 19)
$\mathbf{u}_p(t)$	particle velocity at time t (p. 19)
$\mathbf{u}_r(\mathbf{x}_p, t)$	relative fluid-particle velocity at particle position \mathbf{x}_p and time t (p. 114)
\mathbf{w}_{pq}	relative velocity of two particles (p. 65)
w_r	radial projection of relative particle velocity (p. 65)
\mathbf{x}	Eulerian position vector (p. 16)

\mathbf{x}_c	intersection position of periodic cubic volume with periodic domain image (p. 83)
$\mathbf{x}_f(t)$	trajectories of fluid elements at time t (p. 25)
\mathbf{x}_k^c	center of pseudo-particle cell Ω_k (p. 80)
\mathbf{x}_k^{eq}	equivalent position vector of pseudo-particle electric charge Q_k^{eq} (p. 80)
$\mathbf{x}_p(t)$	particle position at time t (p. 19)

Upper-case Greek

Γ	Gamma function (p. 68)
Δt	time-step (p. 21)
Δx	cell size of Eulerian grid for the fluid phase (p. 21)
Δx_f	grid cell size for pseudo-particle algorithm (p. 80)
$\Delta \mathbf{x}_k$	dimensions of pseudo-particle rectangle X_k (p. 83)
Δx_v	size of particle neighbourhood V_p (p. 80)
Σ_p	global particle accumulation (p. 60)
X_k	pseudo-particle rectangle (p. 83)
Ω	computational domain (p. 74)
Ω_c	cell of Eulerian grid for particle concentration (p. 58)
Ω_k	cell of Eulerian grid for electrostatics (p. 80)

Lower-case Greek

α_c	edge of periodic cubic volume (p. 75)
α_p	solid volume fraction (p. 31)
$\delta(q - q_0)$	Dirac function of quantity q at q_0 (p. 43)
δ_{ij}	Kronecker delta (p. 16)
$\delta_k^{(n)}$	indicator function for particle n with regards to cell Ω_k (p. 80)
δl	particle mean free path (p. 93)
ϵ_f	rate of turbulent dissipation (p. 24)
ϵ_0	vacuum permittivity (p. 71)
$\epsilon_p^{N_e}(\mathbf{x}_p, t_0)$	relative pseudo-particle approximation error of electrostatic forces for N_e cells (p. 85)
$\epsilon_p^{N_{per}}(\mathbf{x}_p, t_0)$	relative quasi-periodic cut-off error of electrostatic forces for N_{per} layers (p. 78)
η_K	Kolmogorov length scale (p. 26)
θ_{pq}	angle of particle relative motion (p. 65)
$\kappa_{min}^F, \kappa_{max}^F$	smallest and largest simulated wavenumber (p. 17)
λ	Coulomb's constant (p. 71)
μ_f	fluid dynamic viscosity (p. 20)
ν_f	fluid kinematic viscosity (p. 16)
ν_{pq}^C	Coulomb collision frequency (p. 90)
ξ	random Gaussian variable (p. 18)
ρ_f	fluid density (p. 16)
ρ_p	particle density (p. 19)
ρ_Q	particle surface charge density (p. 88)

ρ_q	particle volume charge density (p. 97)
$\rho_{q,k}^{eq}$	equivalent (constant) charge density of pseudo-particle rectangle X_k (p. 83)
σ	Gaussian distribution variance of the turbulent radial relative velocity (p. 66)
σ_F^2	forcing variance (p. 18)
τ_a	characteristic time scale of turbulent fluid acceleration (p. 29)
$\tau_{a@p}$	characteristic time scale of fluid acceleration "seen" at the particle positions (p. 52)
τ_ϵ	characteristic time scale of turbulent energy dissipation (p. 29)
τ_E	Eulerian integral time scale of the fluid (p. 25)
τ_{el}	characteristic time scale of electrostatic interactions (p. 90)
τ_f^t	Lagrangian integral time scale of the fluid (p. 25)
$\tau_{f@p}^t$	Lagrangian integral time scale of the fluid "seen" at the particle positions (p. 34)
$\tau_{f_e}^t$	Lagrangian electrostatic integral time scale (p. 126)
τ_{fp}^a	characteristic time scale of turbulent dissipation of q_{fp} by $\langle \mathbf{a}'_{f@p} \mathbf{u}'_p \rangle_p$ (p. 48)
τ_{fp}^F	average particle relaxation time scale (p. 32)
τ_K	Kolmogorov time scale (p. 26)
τ_p	non-linear particle relaxation time (p. 20)
τ_{pq}^C	characteristic time scale of Coulomb collisions (p. 90)
τ_p^{St}	Stokes particle time scale (p. 32)
τ_p^t	Lagrangian particle integral time scale (p. 34)
v_k	Kolmogorov velocity scale (p. 26)
$\phi(\mathbf{x}, t)$	particle-induced electric potential field at position \mathbf{x} and time t (p. 97)
ω	angular frequency (p. 39)
$\omega_f(\mathbf{x}, t)$	turbulent vorticity vector at position \mathbf{x} and time t (p. 33)

Superscripts

$\tilde{q}(\boldsymbol{\kappa}, t)$	Fourier coefficient at wavenumber $\boldsymbol{\kappa}$ of function $q(\mathbf{x}, t)$ (p. 16)
\tilde{q}	nondimensional quantity q (p. 163)
q^*	complex conjugate of variable q (p. 18)
q'	fluctuating value of stochastic variable q (p. 23)
$\hat{\mathbf{r}}$	unit \mathbf{r} vector (p. 19)

Subscripts

$\langle q \rangle_e$	Eulerian average of stochastic variable q of projected particle electrostatics (p. 98)
$\langle q \rangle_f$	Eulerian average of stochastic variable q of the fluid phase (p. 24)
$\langle q \rangle_p$	Lagrangian average of stochastic variable q of the particle phase (p. 32)

Symbols

$\langle q \rangle$	arithmetic mean of stochastic variable q (p. 23)
\mathcal{H}	Heaviside function (p. 18)
$\mathcal{I}(z)$	imaginary part of complex number z (p. 18)
$\mathcal{R}(z)$	real part of complex number z (p. 18)

Acronyms

BCs	Boundary Conditions (p. 7)
CFL	Courant–Friedrichs–Lewy (p. 93)
DIR	Direct algorithm (p. 87)
DNS	Direct Numerical Simulation (p. 7)
FFT	Fast Fourier Transform (p. 20)
FMM	Fast Multipole Method (p. 73)
HIT	Homogeneous Isotropic Turbulence (p. 7)
LR	Linear Regression (p. 56)
MSD	Mean Squared Displacement (p. 55)
N-S	Navier-Stokes (p. 7)
PDF	Probability Density Function (p. 99)
PM	Particle-Mesh (p. 72)
P ³ M	Particle-Particle Particle-Mesh (p. 73)
PS	Pseudo-particle algorithm (p. 87)
RDF	Radial Distribution Function (p. 62)

1

Introduction

“ἀρχὴ γὰρ λέγεται μὲν ἡμισυ παντός
ἐν ταῖς παροιμίαις ἔργου¹”

- Plato, c. 427 – c. 347 BC

1.1 Context and motivation

The motivation for this work comes from numerous practical applications of turbulent particle-laden flows where particles are electrically charged and the inter-particle electrostatic interactions play an important role in the flow dynamics. The range of these applications is quite vast, including geophysical (pyroclastic flow, sediments transport, volcano ashes dispersion) and atmospheric flows (cloud formation, rain enhancement, fog elimination), industrial configurations (pneumatic conveying, olefin polymerization, Fluid Catalytic Cracking of oil, silo discharge), nano-material science, aerospace applications (space exploration, propulsion), biomolecular engineering (DNA charge clouds), chemical and pharmaceutical engineering (protein structure, coating techniques). Depending on the application, these interactions can be either an observed physical phenomenon or a choice of active/passive control of the flow.

Industrial applications

There are several industrial applications (pneumatic conveying, olefin polymerization, Fluid Catalytic Cracking of oil, silo discharge, ...) for which the inter-particle collisions or the particle-wall bouncing may lead the particles to accumulate electric charges which modify the dynamic behavior of the particles. As for example in fluidized beds (Kolehmainen *et al.*, 2016, Rokkam *et al.*, 2010), charges may lead the particles to form agglomerates Ciborowski & Wlodarski (1962) that can change the fluidization regime or to adhere on the walls (see Fig. 1.2). In case of pneumatic conveying Joseph & Klinzing (1983) or solid entrainment Baron

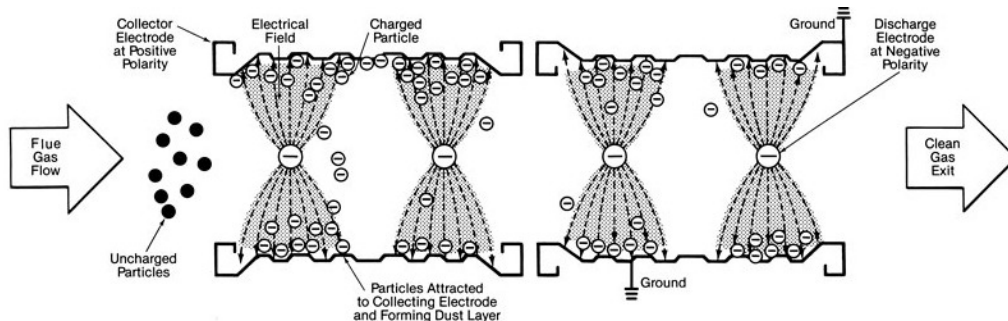


Figure 1.1: Working principle of a dry electrostatic precipitator (Sarkar, 2015).

¹For it is said in proverbs that the beginning is half of every work.

et al. (1987), charges may also alter granular flow dynamics. Electrostatic forces may also be important in colloids, particularly regarding deposition Li & Ahmadi (1993). In addition, as far as dilute turbulent gas-particle flows are concerned, which are the specific kind of flows examined in this PhD, there are several applications where electrostatic forces are actively used for particle separation or removal. Notably, one of these is the electrostatic separator (Matsusaka *et al.*, 2002, Peukert & Wadenpohl, 2001), used for example in the mining industry (Idres *et al.*, 2016) or for plastic/metal separation in the reprocessing industry (Iuga *et al.*, 2001, Kim & Park, 2018, Messal *et al.*, 2015) as well as in the recycling industry (Park *et al.*, 2008, Zeghloul *et al.*, 2017). Another application is that of electrostatic precipitator (see Fig. 1.1) used in coal power plants in order to remove the fine particles from the gases leaving the combustion chamber (Choi & Fletcher, 1998, Kallio & Stock, 1992, Yang *et al.*, 2019).

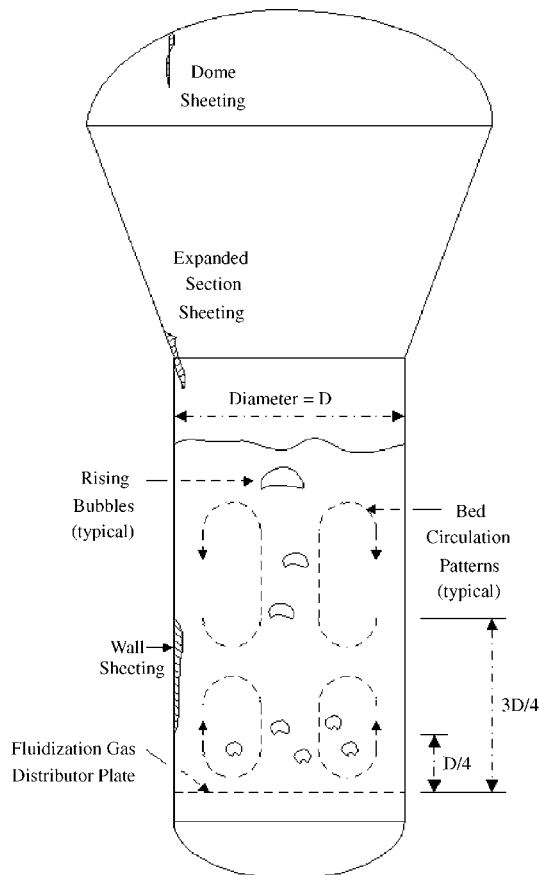


Figure 1.2: *Typical locations for fluidized bed sheeting due to electrostatic agglomeration (Hendrickson, 2006).*

Geophysical and atmospheric flows

Particulate flows have been studied extensively in the context of geophysical and atmospheric flows, as there is a number of occasions when we need to be able to simulate the dispersion of various particles in the atmosphere and accurately predict their flow characteristics so that we can take effective action to our interest. National Oceanic and Atmospheric Administration (2011) has looked into the Fukushima radioactive accident of 2011 in order to simulate in real time the dispersion of radioactive aerosols around the globe. In the same context, in

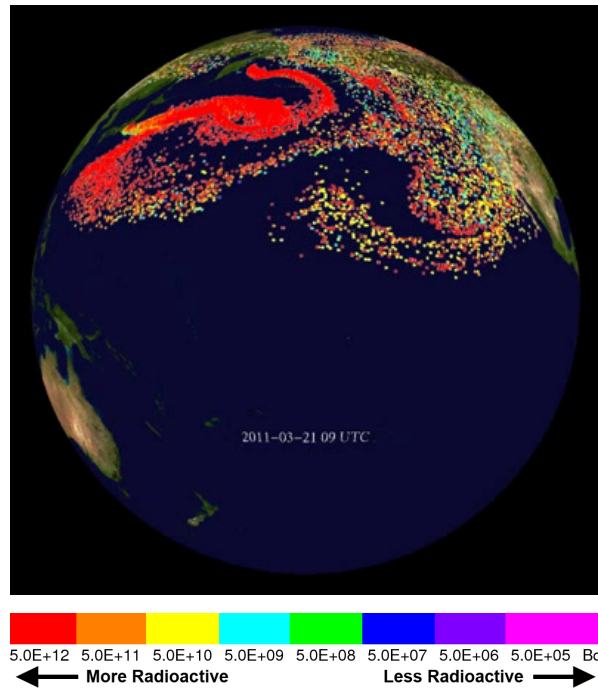


Figure 1.3: *Fukushima Radioactive Aerosol Dispersion (National Oceanic and Atmospheric Administration, 2011).*

Fig. 1.4 one can observe a visualization of a computer simulation of the spreading of ash and sulfur dioxide from a volcanic eruption conducted by NASA Goddard Space Flight Center (2016). A model that represents accurately the physics involved can provide a variety of useful information, such as the concentration of ash and SO_2 as well as the aerosol extinction rate for a given point in space and time.

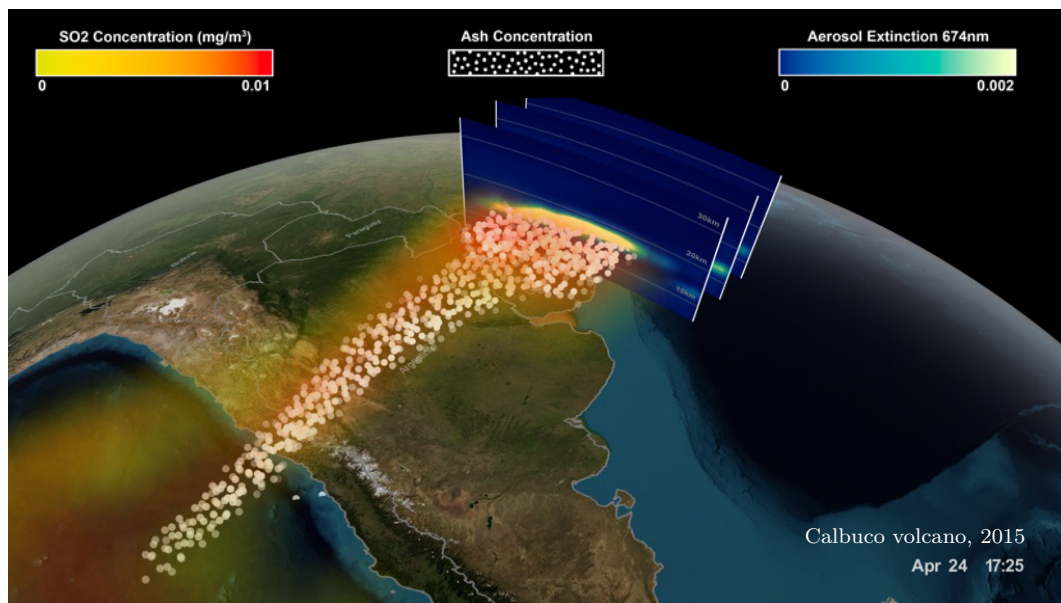


Figure 1.4: *Spreading model for ash and sulfur dioxide from a volcanic eruption (NASA Goddard Space Flight Center, 2016).*

More recently, another catastrophe whose monitoring required elaborate computational skills, is that of the California wildfires of 2020. In Fig. 1.5 one can observe the visualization of soot particle concentration using aerial images provided from the NASA Earth Observatory (2020). These types of flows are very complex, in the sense that they are driven by multi-physics mechanisms (particle-turbulence interaction, particle-particle interaction, heat/mass transfer, chemical/radioactive interactions, etc.). One particularly complex physical interaction that is

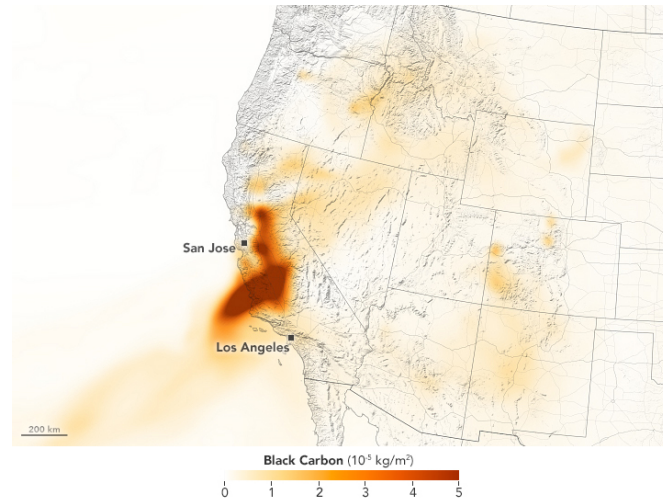


Figure 1.5: Concentration of black carbon particles (soot) (NASA Earth Observatory, 2020).

usually neglected but can play a significant role in a range of such atmospheric/geophysical flows is the presence of electric charges. Effects of charges on particle dynamics have been identified in geophysical flows especially for dust emission Esposito *et al.* (2016) and for the saltating motion of grains Schmidt *et al.* (1998), Zheng *et al.* (2006). A lot of research (James *et al.*, 2008, Lane *et al.*, 2011, Miura *et al.*, 1996) has also been conducted on the electrostatic phenomena in volcanic eruptions (see Fig. 1.6) as well as the effect of triboelectrification (Aplin *et al.*, 2014, Harper & Dufek, 2016) electrostatic interactions on the flow of volcanic ash (Genge, 2018, James *et al.*, 2003).



Figure 1.6: Sakurajima volcano, Japan, with lightning (10th February 2010). The ballistic trajectories represent hot magma clasts, with the electric discharge following an apparently more random path (Lane *et al.*, 2011).

Furthermore, Su (2006) has studied numerically the electrostatic interactions between two charged conducting droplets, aiming among other, to understand their role in cloud formation. Interestingly, electrostatic interactions between droplets have also been studied (Khain *et al.*, 2004) for rain enhancement and fog elimination by seeding them with charged droplets. A more recent computational study of the effect of charges on droplet-droplet collisions is that of Shardt *et al.* (2016) which is illustrated in Fig. 1.7. This work showed that once electric repulsion becomes comparable to the viscous shear force on the drops, the critical capillary numbers decrease suppressing coalescence as droplets now slide at lower shear rates.

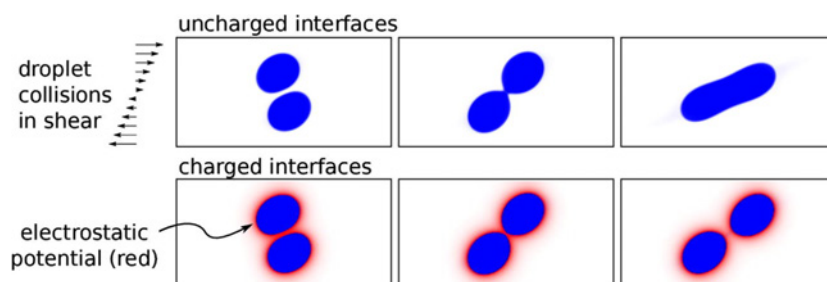
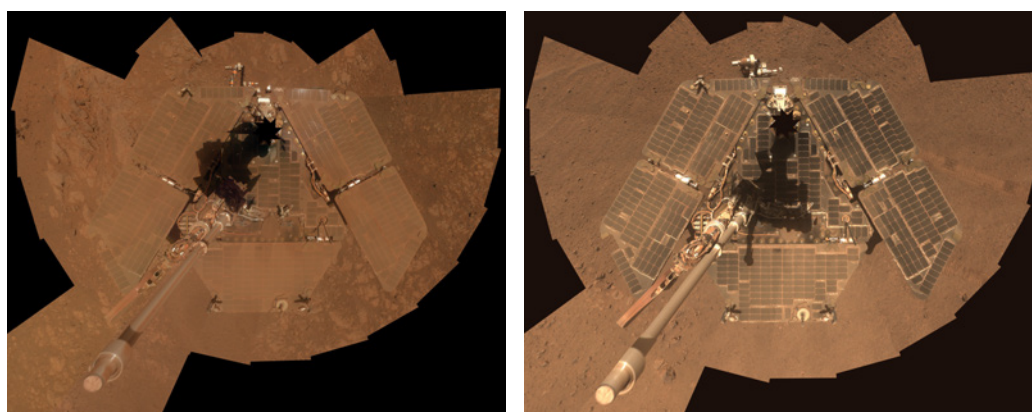


Figure 1.7: Simulations of charged and uncharged droplet collisions (Shardt *et al.*, 2016).

Space exploration

Furthermore, at the dawn of the 2020's decade, there is an augmented interest for further Mars exploration (NASA, 2020) that demands the design and execution of more unmanned missions to the red planet for the years to come. Most present and future missions to the surface of Mars entail the use of solar power as the primary source of energy, therefore the use of solar arrays. However, Mars atmosphere contains a significant load of suspended dust that carries a considerable amount of electric charge due to the dry, low-pressure environment that favors triboelectrification (Harrison *et al.*, 2016, Landis, 1997). This atmospheric dust has been shown to accumulate on the solar panel surface (see Fig. 1.8a) via various mechanisms (saltation, wind lifting), gradually degrading the performance of the photovoltaic power system due to both the decrease of the amount of sunlight hitting the surface and the shift of the spectrum of the available sunlight.



(a) Dust accumulation on rover solar panels.

(b) Dust removal due to wind events.

Figure 1.8: NASA's Mars Exploration Rover Opportunity before and after a cleaning event (JPL, 2014).

Dust is expected to adhere to the panel by Van der Waals adhesive forces, which are quite strong at the dust particle sizes expected. If the panel surface is insulating, it is possible that they may also be subject to electrostatic adhesion, which may also be extremely strong. Moreover, experimental studies on Viking landing sites by Gaier *et al.* (1994) have shown that wind gusts on the surface of Mars are not strong enough to remove adequate amounts of accumulated dust. Despite the observation of random cleaning events (see Fig. 1.8) due to uncommon high gusts ($\sim 35m/s$), they conclude that long-duration missions may require its periodic removal, especially unmanned ones. Consequently, it seems that dust deposition on solar panels of an autonomous solar powered system Mars exploration system can be detrimental for its lifetime, hence the longevity of the operation. Therefore, it is imperative that we be able not only to understand and predict the effect of inter-particle electrostatic interactions on such gas-particle flows on the surface of the red planet, but also to develop dust removal techniques that will be capable of clearing efficiently the solar panel surface. It has been proven (Landis, 2004) that the environment of Mars has been studied to be most suitable for the use of electrostatic mechanisms to do so.

Disease transmission

An honorable mention to the unending list of applications of (turbulent, not necessarily electrically charged) particle-laden flows, which is pertinent with the current global health crisis of the COVID-19 pandemic, is that of the dispersion of sneeze clouds (see Fig. 1.9).

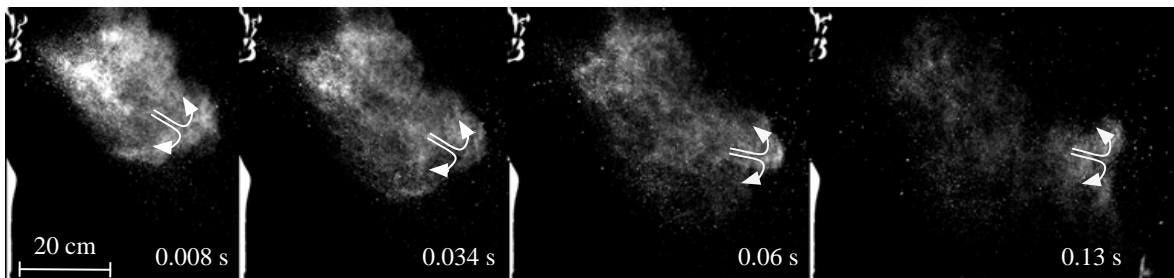


Figure 1.9: *Dispersion of a sneeze cloud (Bourouiba et al., 2014).*

In fact, at the time of writing researchers all around the world are trying to study, analyze and comprehend the underlying mechanisms of the generation and aerosolization of virus-laden respiratory droplets from a host (Mittal *et al.*, 2020). Part of this research is the study of the dispersion and deposition of such droplets that are emitted out of the nasal cavities when talking, shouting, singing and sneezing. The understanding of these mechanisms can lead to the prediction of the travel distance and lifetime of aerosols formed in spaces where humans interact with each other, as it is the main way of transmission of these type of corona-viruses. Consequently, this would lead not only to correct government decisions of suitable preventative measures such as the use of face masks, hand washing, ventilation of indoor environments and social distancing for mitigating and eventually eradicating this disease, but also prepare us for the reappearance of a similar one in the future.

1.2 Background and state-of-the-art

The present study is dedicated to the dispersion of inertial charged particles in turbulent flows. Several literature studies have been dedicated to charged particles transported by Homogeneous Isotropic Turbulence (HIT) Di Renzo & Urzay (2018), Di Renzo *et al.* (2019), Karnik & Shrimpton (2012), Lu & Shaw (2015), Lu *et al.* (2010), Yao & Capecelatro (2018) or by turbulent channel flow Rambaud *et al.* (2002). These studies essentially focus on the modification of preferential concentration in the case of charged particles.

Indeed, when solid non-charged particles are transported by a turbulent flow field, according to their inertia, they may accumulate in low-vorticity regions of the turbulence Fessler *et al.* (1994), Squires & Eaton (1991). Such a mechanism leads to large local concentrations of particles that may modify the collision rate Reade & Collins (2000), Sundaram & Collins (1997) or the coalescence rate if droplets are considered instead of solid particles Wunsch *et al.* (2010). Furthermore, external forces may modify preferential concentration, as for example, Fede & Simonin (2010) showed that inter-particle collisions enhance preferential concentration. In addition, Dejoan & Monchaux (2013) investigated experimentally the effect of gravity on preferential concentration. Karnik & Shrimpton (2012), Lu & Shaw (2015), Lu *et al.* (2010), Yao & Capecelatro (2018) have also showed that preferential concentration decreases when charges increase.

However, they do not investigate how particle dispersion, in terms of agitation, is modified by electrostatic interactions. Basically, particles transported by stationary homogeneous isotropic turbulence follow the Tchen-Hinze theory (Hinze, 1972, Tchen, 1947) that entails that the particle kinetic energy is directly linked to the fluid agitation (Fede & Simonin, 2006, Zaichik *et al.*, 2003) via fluid-particle velocity covariance. However, Laviéville (1997) and later Fede *et al.* (2015) showed that when inter-particle collisions occur, particle agitation decreases even for elastic collisions. The way that electrostatic forces act on the particles is similar to collisions via the mechanism of Coulomb collisions typically found in cold plasma (Callen, 2003).

1.3 Main objective

The main objective of this work is to study the effects of distance-dependent particle-particle interactions, such as the electrostatic forces, in turbulent gas flows laden with like-charged particles using an Euler-Lagrange simulation approach. The turbulent gas flow is accounted for via Direct Numerical Simulation (DNS) to the Kolmogorov scale using a spectral method to solve the Navier-Stokes (N-S) equations in a cubic computational domain with tri-periodic Boundary Conditions (BCs). This flow simulation is coupled (one-way) with a Lagrangian particle phase solver that performs particle trajectory tracking.

Electrostatic forces can be calculated using two different approaches. Firstly, the direct method consists of a sum of all inter-particle interactions for all the particles of the computational domain and their periodic images. However, this purely Lagrangian approach is computationally costly for a large number of particles, therefore another approximative approach is considered. According to it, one can estimate the short-range interactions via a sum of inter-particle interactions within a cut-off distance and the long-range ones via a sum of particle interactions with clusters of particles that, from a distance greater than the cut-off, are "seen" as one pseudo-particle.

This method is further adjusted in order to accommodate periodic boundary conditions, which are not trivial in the case of electrostatic interactions as periodicity entails an infinite

number of periodic domain images that has to be truncated to a finite one. In order to successfully represent these inter-particle electrostatic interactions, we give emphasis on the convergence and isotropy of the particle-induced electric field and we study its transient response which is different from the turbulent one. In addition, the mechanism of such interactions is investigated and it is shown that since electrostatic forces are conservative, they could be considered as elastic particle-particle collisions at a distance, namely Coulomb collisions. Moreover, since the magnitude of these forces is inversely proportional to the square of the inter-particle distance, a special effort has been made to secure their satisfactory time resolution which has been proven to be very important for an accurate representation of the described physics.

Simulations are then performed by varying the properties of the particles in terms of density (Stokes number) and charge (electrostatic Stokes number). In order to extract information from these simulations, a statistical analysis is performed in order to investigate how the dynamics of the turbulent gas-particle flow are affected by such distance-dependent particle-particle interactions, namely electrostatic forces. In order to obtain a full understanding of their effect, the statistical measures that have been deployed range from one-point statistics (average particle agitation, fluid-particle covariance, to fluid and particle autocorrelation functions, etc.) to two-point statistics such as relative particle velocity, inter-particle distance, etc.).

Explaining the observations made out of these statistics, via physical analysis, we aim to understand and interpret not only the effect of these interactions on the particle kinetic situation, namely particle agitation and dispersion, but also their very nature (probability density function, average and variance, etc.). A big emphasis is given on the characteristic time scales of the turbulent flow, so both of the fluid and particle phases, their (one-way coupled) interaction, but also of the particle-particle electrostatic interactions. Finally, a great focus has been placed on the spatial distribution of the particles inside the flow. The phenomenon of preferential concentration and its mitigation by the (repulsive) electrostatic forces is analyzed, as well as their effect on the relative particle motion.

1.4 Outline of the thesis

The PhD thesis is organized in six different Chapters. Although it has been written with a focus on coherence and continuity - hence the use of a global nomenclature and a throughout respect on definitions and notations - each chapter serves a clearly different purpose. Except for Chapters 1 and 6 which are the Introduction and the Conclusion, respectively, each of Chapters 2-5 is structured as a standalone article that has an abstract, a main body and a conclusion, as well as its own bibliography. This organization has been chosen in order to allow the reader to study separately any part of the thesis that is of interest to them, and facilitate the understanding of the presented physics.

To begin with, Chapter 1 provides the context for the subject of this PhD, as well as the motivation for the examined physics. It also presents a background and state-of-the-art for different aspects of the deployed numerical methodology and physical results. Finally, it presents the outline of the thesis in order for the reader to navigate through it more easily.

Furthermore, Chapter 2 details the numerical tools (schemes, techniques) used for the DNS of turbulent particle-laden gas flows. First, the fluid solver is presented along with a description of the forcing scheme as well as the one-way coupling with the solid particle phase. This is the chapter that deals with the configuration of the simulated turbulence, so its basic characteristics are also defined. At this point, we deduce a stochastic model of fluid acceleration based on a Langevin equation and we extend it for a double exponential form

of the fluid autocorrelation function. Then, we present the configuration of the non-settling charge-free reference case which inevitably makes use of several statistical quantities of the flow for both the fluid and particle phase. Thus, several fundamental elements of statistical analysis for turbulence are presented as well as characteristic length and time scales that define the physics that will be examined.

Following, Chapter 3 deals with the investigation of the dispersion of charge-free inertial particles transported by stationary homogeneous isotropic turbulence by means of statistical analysis of the performed DNS. The spectral analysis of turbulent gas-particle flows is presented that leads to the formulation of Tchen-Hinze theory. The latter is a theoretical framework that allows for a prediction of particle agitation based on fluid agitation and characteristic fluid/particle time scales, as well as a theoretical approach of particle dispersion. Following, the detailed analysis of the transport equations of particle agitation and fluid-particle covariance are used to explain the effect of particle inertia. The apparent term of fluid acceleration - particle velocity covariance creates the need to devise a stochastic model for fluid acceleration "seen" by the particles as an extension of the corresponding one for the fluid, presented in Chapter 2. Finally, follows a detailed statistical analysis (one- and two-point statistics) of all the aspects of particle dispersion that extends to the spatial distribution and relative motion of particles.

Chapter 4 presents the fundamental problem of calculation of electrostatic forces in a system of particles, the known N-body problem. Then it describes the intricate problem of applying periodic boundary conditions in such systems, where a truncation of the infinite periodic domain is proposed with a reasonable cut-off error. A scalable algorithm is presented that allows for a rather fast and precise calculation of electrostatic forces in a tri-periodic computational domain by separating them in long- and short-range parts, which are calculated exactly and approximately, respectively. The approximation error, computational cost and performance of the proposed algorithm are documented and thoroughly analyzed. The second part of the chapter deals with dry like-charged granular flows where the fundamentals physics of particle-particle electrostatic interactions are investigated via characteristic length and time scales. An attempt is made to provide analytical estimations for several statistical quantities which are compared to DNS measured values. Finally, the particle-induced electric field is presented and its characteristics are related to particle motion.

Last but not least, Chapter 5 presents the results obtained from DNS of like-charged particle-laden turbulent gas flows and their statistical analysis. At first the configuration for the simulations is presented where an electrostatic Stokes number is defined. Then, we examine the effect of electric charge on particle dispersion where the obtained results are verified via the transport equations of particle agitation and fluid-particle velocity covariance. The observed trends are interpreted physically using classical notions of particle-laden flows as well as the concept of Coulomb collisions presented in Chapter 4. To deepen our understanding of this effect, various statistics have been deployed such as autocorrelation functions of fluid and particle velocity, mean square particle displacement, probability density functions of particle velocities and electrostatic forces, etc. Following, we focus on the effect of (repulsive) electrostatic interactions on the spatial distribution of particles and their relative motion via the statistical measures of particle concentration and radial distribution functions as well as the nearest-neighbor distance characteristics. Lastly, we are interested in the effect of particle number density.

Finally, Chapter 6 various conclusions drawn from the analysis conducted within the scope of this PhD. In addition, it offers several perspectives which serve as pointers to the directions of a possible continuation of this work.

Bibliography

- Aplin, K., Houghton, I., Nicoll, K., Humphries, M., & Tong, A. 2014. *Proc . ESA Annual Meeting on Electrostatics 2014 1 Electrical charging of volcanic ash*.
- Baron, T., Briens, C.L., Bergougnou, M.A., & Hazlett, J.D. 1987. Electrostatic effects on entrainment from a fluidized bed. *Powder technology*, **53**(1), 55–67.
- Bourouiba, Lydia, Dehandschoewercker, Eline, & Bush, John W. M. 2014. Violent expiratory events: on coughing and sneezing. *Journal of fluid mechanics*, **745**, 537–563.
- Callen, J.D. 2003. *Fundamentals of plasma physics*. University of Wisconsin.
- Choi, B. S., & Fletcher, C. A. J. 1998. Turbulent particle dispersion in an electrostatic precipitator. *Applied mathematical modelling*, **22**(12), 1009–1021.
- Ciborowski, J., & Wlodarski, A. 1962. On electrostatic effects in fluidized beds. *Chemical engineering science*, **17**(1), 23–32.
- Dejoan, A., & Monchaux, R. 2013. Preferential concentration and settling of heavy particles in homogeneous turbulence. *Physics of fluids*, **25**(1).
- Di Renzo, M., & Urzay, J. 2018. Aerodynamic generation of electric fields in turbulence laden with charged inertial particles. *Nature communications*, **9**(1), 1676.
- Di Renzo, M., Johnson, P. L., Bassenne, M., Villafañe, L., & Urzay, J. 2019. Mitigation of turbophoresis in particle-laden turbulent channel flows by using incident electric fields. *Physical review fluids*, **4**(12), 124303.
- Eposito, F., Molinaro, R., Popa, C. I., Molfese, C., Cozzolino, F., Marty, L., Taj-Eddine, K., Achille, G. Di, Franzese, G., Silvestro, S., & Ori, G. G. 2016. The role of the atmospheric electric field in the dust-lifting process. *Geophysical research letters*, **43**(10), 5501–5508.
- Fede, P., & Simonin, O. 2006. Numerical study of the subgrid fluid turbulence effects on the statistics of heavy colliding particles. *Physics of fluids*, **18**(045103), 1–17.
- Fede, P., & Simonin, O. 2010. Effect of particle-particle collisions on the spatial distribution of inertial particles suspended in homogeneous isotropic turbulent flows. *Pages 119–125 of: Turbulence and interactions*. Notes on Numerical Fluid Mechanics and Multidisciplinary Design, vol. 110. Springer Berlin Heidelberg.
- Fede, P., Simonin, O., & Villedieu, P. 2015. Monte-carlo simulation of colliding particles or coalescing droplets transported by a turbulent flow in the framework of a joint fluid–particle pdf approach. *International journal of multiphase flow*, **74**(0), 165–183.
- Fessler, J.R., Kulick, J.D., & Eaton, J.K. 1994. Preferential concentration of heavy particles in a turbulent channel flow. *Physics of fluids*, **6**, 3742–3749.
- Gaier, J. R., Perez-Davis, M. E., Rutledge, S. K., & Hotes, D. 1994 (Sept.). *Aeolian removal of dust from radiator surfaces on Mars*. Tech. rept. NASA-TM-103205; CONF-900828-13. National Aeronautics and Space Administration, Cleveland, OH (United States). Lewis Research Center.

- Genge, Matthew J. 2018. Electrostatic levitation of volcanic ash into the ionosphere and its abrupt effect on climate. *Geology*, **46**(10), 835–838. Publisher: GeoScienceWorld.
- Harper, Joshua Méndez, & Dufek, Josef. 2016. The effects of dynamics on the triboelectrification of volcanic ash. *Journal of geophysical research: Atmospheres*, **121**(14), 8209–8228.
- Harrison, R. G., Barth, E., Esposito, F., Merrison, J., Montmessin, F., Aplin, K. L., Borlina, C., Berthelier, J. J., Déprez, G., Farrell, W. M., Houghton, I. M. P., Renno, N. O., Nicoll, K. A., Tripathi, S. N., & Zimmerman, M. 2016. Applications of Electrified Dust and Dust Devil Electrodynamics to Martian Atmospheric Electricity. *Space science reviews*, **203**(1), 299–345.
- Hendrickson, G. 2006. Electrostatics and gas phase fluidized bed polymerization reactor wall sheeting. *Chemical engineering science*, **61**(4), 1041–1064.
- Hinze, J.O. 1972. Turbulent fluid and particle interaction. *Prog. heat and mass transfer*, **6**, 433–452.
- Idres, Abdelaziz, Bouhedja, Ahcène, Bounouala, Mohamed, & Benselhoub, Aissa. 2016. New method of electrostatic separation of the oxidized iron ore. *Mining science*, **23**(Sept.), 33–41. Publisher: Politechnika Wroclawska.
- Iuga, A., Morar, R., Samuila, A., & Dascalescu, L. 2001. Electrostatic separation of metals and plastics from granular industrial wastes. *Iee proceedings - science, measurement and technology*, **148**(2), 47–54.
- James, M. R., Lane, S. J., & Gilbert, J. S. 2003. Density, construction, and drag coefficient of electrostatic volcanic ash aggregates. *Journal of geophysical research: Solid earth*, **108**(B9).
- James, M. R., Wilson, L., Lane, S. J., Gilbert, J. S., Mather, T. A., Harrison, R. G., & Martin, R. S. 2008. Electrical Charging of Volcanic Plumes. *Space science reviews*, **137**(1), 399–418.
- Joseph, S., & Klinzing, G.E. 1983. Vertical gas–solid transition flow with electrostatics. *Powder technology*, **36**(1), 79 – 87.
- JPL. 2014. *Self-portrait by freshly cleaned opportunity mars rover in march 2014*. Available online at: <https://www.jpl.nasa.gov/spaceimages/details.php?id=pia18079>.
- Kallio, G. A., & Stock, D. E. 1992. Interaction of electrostatic and fluid dynamic fields in wire–plate electrostatic precipitators. *Journal of fluid mechanics*, **240**(July), 133–166. Publisher: Cambridge University Press.
- Karnik, A.U., & Shrimpton, J.S. 2012. Mitigation of preferential concentration of small inertial particles in stationary isotropic turbulence using electrical and gravitational body forces. *Physics of fluids*, **24**(7), 073301.
- Khain, A., Arkhipov, V., Pinsky, M., Feldman, Y., & Ryabov, Ya. 2004. Rain Enhancement and Fog Elimination by Seeding with Charged Droplets. Part I: Theory and Numerical Simulations. *Journal of applied meteorology*, **43**(10), 1513–1529. Publisher: American Meteorological Society.
- Kim, Beom-Uk, & Park, Chul-Hyun. 2018. Electrostatic Separation of Copper and Glass Particles in Pretreated Automobile Shredder Residue. *Metals*, **8**(11), 879. Number: 11 Publisher: Multidisciplinary Digital Publishing Institute.

- Kolehmainen, J., Ozel, A., Boyce, C.M., & Sundaresan, S. 2016. A hybrid approach to computing electrostatic forces in fluidized beds of charged particles. *Aiche journal*, **62**(7), 2282–2295.
- Landis, G.A. 1997. Mars dust removal technology. *Pages 764–767 of: IECEC-97 Proceedings of the Thirty-Second Intersociety Energy Conversion Engineering Conference (Cat. No.97CH6203)*, vol. 1. Honolulu, HI, USA: IEEE.
- Landis, Geoffrey A. Baraona. 2004 (June). Exploring PV on the Red Planet: Mars Array Technology Experiment and Dust Accumulation and Removal Technology.
- Lane, S. J., James, M. R., & Gilbert, J. S. 2011. Electrostatic phenomena in volcanic eruptions. *Journal of physics: Conference series*, **301**(June), 012004. Publisher: IOP Publishing.
- Laviéville, J. 1997. *Simulations numériques et modélisation des interactions entre l'entraînement par la turbulence et les collisions interparticulaires en écoulement gaz-solides*. Ph.D. thesis, Université de Rouen.
- Li, A., & Ahmadi, G. 1993. Aerosol particle deposition with electrostatic attraction in a turbulent channel flow. *Journal of colloid and interface science*, **158**(2), 476–482.
- Lu, J., & Shaw, R.A. 2015. Charged particle dynamics in turbulence: Theory and direct numerical simulations. *Physics of fluids*, **27**(6), 065111.
- Lu, J., Nordsiek, H., Saw, E.W., & Shaw, R.A. 2010. Clustering of charged inertial particles in turbulence. *Physical review letters*, **104**(May), 184505.
- Matsusaka, Shuji, Umemoto, Hiroaki, Nishitani, Matami, & Masuda, Hiroaki. 2002. Electrostatic charge distribution of particles in gas–solids pipe flow. *Journal of electrostatics*, **55**(1), 81–96.
- Messal, Sara, Corondan, Razvan, Chetan, Ionut, Ouiddir, Rabah, Medles, Karim, & Dascalescu, Lucian. 2015. Electrostatic separator for micronized mixtures of metals and plastics originating from waste electric and electronic equipment. *Journal of physics: Conference series*, **646**(Oct.), 012030.
- Mittal, Rajat, Ni, Rui, & Seo, Jung-Hee. 2020. The flow physics of COVID-19. *Journal of fluid mechanics*, **894**(July). Publisher: Cambridge University Press.
- Miura, Toshiro, Koyaguchi, Takehiro, & Tanaka, Yoshikazu. 1996. Atmospheric electric potential gradient measurements of ash clouds generated by pyroclastic flows at Unzen Volcano, Japan. *Geophysical research letters*, **23**(14), 1789–1792.
- NASA. 2020. *Mars exploration future missions*. Available online at: https://www.nasa.gov/mission_pages/mars/main/index.html.
- NASA Earth Observatory. 2020. *Wildfire smoke shrouds the u.s. west (geos-fp model)*. Available online at: <https://earthobservatory.nasa.gov/images/147151/wildfire-smoke-shrouds-the-us-west>.
- NASA Goddard Space Flight Center. 2016. *Tracking volcanic ash with satellites*. Available online at: <https://svs.gsfc.nasa.gov/12221>.

- National Oceanic and Atmospheric Administration. 2011. *Fukushima radioactive aerosol dispersion model*. Available online at: <https://sos.noaa.gov/datasets/fukushima-radioactive-aerosol-dispersion-model>.
- Park, Chul-Hyun, Jeon, Ho-Seok, Yu, Hyo-Shin, Han, Oh-Hyung, & Park, Jai-Koo. 2008. Application of Electrostatic Separation to the Recycling of Plastic Wastes: Separation of PVC, PET, and ABS. *Environmental science & technology*, **42**(1), 249–255. Publisher: American Chemical Society.
- Peukert, W., & Wadenpohl, C. 2001. Industrial separation of fine particles with difficult dust properties. *Powder technology*, **118**(1), 136–148.
- Rambaud, P., Tanière, A., Oesterlé, B., & Buchlin, J.M. 2002. On the behavior of charged particles in the near wall region of a channel flow. *Powder technology*, **125**, 199–205.
- Reade, W.C., & Collins, L.R. 2000. Effect of preferential concentration on turbulent collisions rates. *Physics of fluids*, **12**, 2530–2540.
- Rokkam, Ram G., Fox, Rodney O., & Muhle, Michael E. 2010. Computational fluid dynamics and electrostatic modeling of polymerization fluidized-bed reactors. *Powder technology*, **203**(2), 109–124.
- Sarkar, Dipak K. 2015. Chapter 14 - air pollution control. *Pages 479 – 522 of: Sarkar, Dipak K. (ed), Thermal power plant*. Elsevier.
- Schmidt, D.S., Schmidt, R.A., & Dent, J.D. 1998. Electrostatic force on saltating sand. *Journal of geophysical research: Atmospheres*, **103**(D8), 8997–9001.
- Shardt, Orest, Mitra, Sushanta K., & Derksen, J. J. 2016. Simulations of charged droplet collisions in shear flow. *Chemical engineering journal*, **302**(Oct.), 314–322.
- Squires, K.D., & Eaton, J.K. 1991. Preferential concentration of particles by turbulence. *Physics of fluids a: Fluid dynamics*, **3**(5), 1169–1178.
- Su, Y. H. 2006. A numerical study of electrostatic interactions between two charged conducting droplets. *Physics of fluids*, **18**(4), 042108. Publisher: American Institute of Physics.
- Sundaram, Shivshankar, & Collins, Lance R. 1997. Collision statistics in an isotropic particle-laden turbulent suspension. Part 1. Direct numerical simulations. *Journal of fluid mechanics*, **335**(Mar.), 75–109. Publisher: Cambridge University Press.
- Tchen, C.M. 1947. *Mean value and correlation problems connected with the motion of small particles suspended in a turbulent fluid*. Ph.D. thesis, Delft, Martinus Nijhoff, The Hague.
- Wunsch, D., Fede, P., Simonin, O., & Villedieu, P. 2010. Numerical simulation and statistical modeling of inertial droplet coalescence in homogeneous isotropic turbulence. *Pages 401–407 of: Turbulence and interactions*. Notes on Numerical Fluid Mechanics and Multidisciplinary Design, vol. 110. Springer Berlin / Heidelberg.
- Yang, Ding, Guo, Baoyu, Ye, Xinglian, Yu, Aibing, & Guo, Jun. 2019. Numerical simulation of electrostatic precipitator considering the dust particle space charge. *Powder technology*, **354**(Sept.), 552–560.

- Yao, Yuan, & Capecelatro, Jesse. 2018. Competition between drag and Coulomb interactions in turbulent particle-laden flows using a coupled-fluid–Ewald-summation based approach. *Physical review fluids*, **3**(3), 034301.
- Zaichik, L.I., Simonin, O., & Alipchenkov, V.M. 2003. Two statistical models for predicting collision rates of inertial particles in homogeneous isotropic turbulence. *Physics of fluids*, **15**, 2995–3005.
- Zeghloul, Thami, Mekhalef Benhafssa, Abdelkader, Richard, Gontran, Medles, Karim, & Dascalescu, Lucian. 2017. Effect of particle size on the tribo-aero-electrostatic separation of plastics. *Journal of electrostatics*, **88**(Aug.), 24–28.
- Zheng, X.J., Huang, N., & Zhou, Y. 2006. The effect of electrostatic force on the evolution of sand saltation cloud. *The european physical journal e*, **19**(2), 129–138.

2

Numerical simulation of turbulent particle-laden gas flows

“πάντα χωρεῖ καὶ οὐδὲν μένει καὶ δις ἔς
τὸν αὐτὸν ποταμὸν οὐκ ἂν ἐμβαίῃς¹”

- Heraclitus of Ephesus, c. 540 – c. 480 BC

Abstract

This chapter details the numerical tool (schemes, techniques) used for the DNS of turbulent particle-laden gas flows. First, the fluid solver is presented along with a description of the forcing scheme as well as the one-way coupling with the solid particle phase. Then, we present the basic characteristics of the simulated stationary homogeneous isotropic turbulence, as well as a stochastic model for fluid acceleration. The configuration of the non-settling charge-free reference case inevitably makes use of several statistical quantities of the flow for both the fluid and particle phase. Thus, several fundamental elements of statistical analysis are presented as well as characteristic length and time scales that define the physics are under investigation.

2.1 Numerical simulation of particle-laden stationary HIT

The studied configuration is a stationary homogeneous isotropic turbulent gas flow carrying mono-disperse inertial particles. The incompressible Navier-Stokes equations are solved by using a pseudo-spectral method. Periodic BCs are applied on fluid and particle phase. Statistically steady flow is achieved by using the forcing scheme proposed by Eswaran & Pope (1988). The solid mass loading is sufficiently low for neglecting the turbulence modulation by the presence of particles. The DNS are performed using gas-particle solver **GASPART** developed in IMFT.

In literature there is a handful of works that have been deployed for similar studies. Notably, Deutsch *et al.* (1993) and Laviéville (1997) performed simulations of inertial particles transported by stationary HIT taking into account monodisperse inter-particle collisions. Furthermore, Février (2000) employed and validated a spectral method for gas-particle flows using Finite Volume Method neglecting collisions, while Vermorel *et al.* (2003) investigated the two-way coupling and Fedde & Simonin (2006) studied collisions of mono- and bi-disperse turbulent particle-laden flows.

2.1.1 Spectral method for the resolution of the Navier-Stokes equations

The governing equations for incompressible turbulent flow are

$$\frac{\partial u_{f,i}}{\partial x_i} = 0 \quad (2.1)$$

$$\frac{\partial u_{f,i}}{\partial t} + u_{f,j} \frac{\partial u_{f,i}}{\partial x_j} = -\frac{1}{\rho_f} \frac{\partial p}{\partial x_i} + \nu_f \frac{\partial^2 u_{f,i}}{\partial x_j \partial x_j} \quad (2.2)$$

¹All things flow and nothing remains still, and you cannot step twice into the same river.

where $\mathbf{u}_f = \mathbf{u}_f(\mathbf{x}, t)$ and $p = p(\mathbf{x}, t)$ are the instantaneous fluid velocity and the pressure at position \mathbf{x} , respectively. Furthermore, ρ_f is the fluid density, while ν_f is the fluid kinematic viscosity. Taking the divergence of the Navier-Stokes equations and Eq. (2.1) we obtain

$$-\frac{1}{\rho_f} \frac{\partial^2 p}{\partial x_i \partial x_i} = \frac{\partial^2 (u_{f,i} u_{f,j})}{\partial x_i \partial x_j}. \quad (2.3)$$

Following Canuto *et al.* (1988), Orszag (1969) and Vincent & Meneguzzi (1991), the fluid velocity can be expressed in term of Fourier series as

$$u_{f,i}(\mathbf{x}, t) = \int_{-\infty}^{\infty} \widehat{u}_{f,i}(\boldsymbol{\kappa}, t) \exp(\widehat{i}\boldsymbol{\kappa} \cdot \mathbf{x}) d\boldsymbol{\kappa} \quad (2.4)$$

where \widehat{i} is the imaginary unit and $\widehat{\mathbf{u}}_f(\boldsymbol{\kappa})$ denotes the Fourier transform of the fluid velocity \mathbf{u}_f at wavenumber $\boldsymbol{\kappa}$. Applying the Fourier transform on fluid velocity (spatial) derivatives of Eq. (2.2) gives

$$\widehat{u_{f,j} \frac{\partial u_{f,i}}{\partial x_j}} = \frac{\partial (\widehat{u_{f,i} u_{f,j}})}{\partial x_j} = \widehat{i}\kappa_j \widehat{u_{f,i} u_{f,j}} \quad (2.5)$$

$$\frac{\partial^2 \widehat{u_{f,i}}}{\partial x_j \partial x_j} = -\kappa^2 \widehat{u_{f,i}} \quad (2.6)$$

with $\kappa^2 = \kappa_j \kappa_j = \kappa_x^2 + \kappa_y^2 + \kappa_z^2$ and $\widehat{u_{f,i} u_{f,j}}$ the Fourier transform of the non-linear terms of the N-S equations. Using Eq. (2.5) & (2.6) the Navier-Stokes equations can be written in the spectral space as

$$\kappa_i \widehat{u_{f,i}} = 0 \quad (2.7)$$

$$\frac{\partial \widehat{u_{f,i}}}{\partial t} + \widehat{N}_i = -\frac{1}{\rho_f} \widehat{i}\kappa_i \widehat{p} - \nu_f \kappa^2 \widehat{u_{f,i}} \quad (2.8)$$

where $\widehat{N}_i = \widehat{i}\kappa_j \widehat{u_{f,i} u_{f,j}}$ is the Fourier coefficient of the non-linear terms. In order to eliminate pressure from Eq. (2.8) one can apply the Fourier transform on Eq. (2.3) that yields

$$-\frac{1}{\rho_f} \frac{\partial^2 \widehat{p}}{\partial x_i \partial x_i} = \frac{\partial^2 (\widehat{u_{f,i} u_{f,j}})}{\partial x_i \partial x_j} \quad (2.9)$$

$$\widehat{p} = -\rho_f \frac{\kappa_j \widehat{N}_j}{\kappa^2}$$

Finally, using Eq. (2.9), Eq. (2.8) can be written as

$$\frac{\partial \widehat{u_{f,i}}}{\partial t} + \widehat{i}\kappa_j \widehat{u_{f,i} u_{f,j}} = \widehat{i} \frac{\kappa_i^2 \kappa_j}{\kappa^2} \widehat{u_{f,i} u_{f,j}} - \nu_f \kappa^2 \widehat{u_{f,i}}$$

$$\frac{\partial \widehat{u_{f,i}}}{\partial t} + \left[\delta_{ij} - \frac{\kappa_i \kappa_j}{\kappa^2} \right] \widehat{i}\kappa_i \widehat{u_{f,i} u_{f,j}} = -\nu_f \kappa^2 \widehat{u_{f,i}} \quad (2.10)$$

$$\frac{\partial \widehat{u_{f,i}}}{\partial t} + \left[\delta_{ij} - \frac{\kappa_i \kappa_j}{\kappa^2} \right] \widehat{N}_j = -\nu_f \kappa^2 \widehat{u_{f,i}}$$

where δ_{ij} is the Kronecker delta. It is evident that the pressure acts like a projector onto a basis where the incompressibility condition is satisfied. Equation (2.10) is not solved in

numerical tool **GASPART**, as the divergence should always be satisfied during the computation. Instead, it is chosen to solve the following system

$$\frac{\partial \hat{u}_{f,i}^*}{\partial t} + \hat{N}_i^* = -\nu_f \kappa^2 \hat{u}_{f,i}^* \quad (2.11)$$

and the velocity field $\hat{\mathbf{u}}_f^*$ is corrected such as

$$\hat{u}_i = \hat{u}_{f,i}^* - \frac{\kappa_i \kappa_j \hat{u}_{f,j}^*}{\kappa^2}. \quad (2.12)$$

This approach ensures a free-divergence velocity field.

Turbulence forcing

In order to study particles carried by stationary homogeneous isotropic turbulence, one needs to address the natural tendency of turbulence to decay, so as to ensure the stationarity of the flow. Besides, equations that describe turbulence Eq. (2.1) & Eq. (2.2) are dissipative, therefore it is necessary to artificially inject energy into the fluid so as to keep its kinetic energy statistically steady. For this, there are two main methodologies from literature: the deterministic and the stochastic approach.

- i. The deterministic approach consists in resetting the spectrum of simulated turbulence for each wavenumber based on a reference spectrum by Deutsch (1992) and Overholt & Pope (1998). Generally, this reference spectrum is an analytical spectrum whose parameters are adjusted to match a grid turbulence experiment. The drawback of this type of turbulence forcing is that it cannot be used for simulations where the effect of the particles on the fluid is taken into account (two-way coupling) (Boivin, 1996).
- ii. The stochastic approach developed by Eswaran & Pope (1988) consists in applying a random force at the level of the small wavenumbers of the energy spectrum. This type of forcing was employed by Février (2000) because it makes it possible to control the properties of the generated turbulence as well as the study of two-way coupling.

In this work, it is chosen to use the stochastic approach (Eswaran & Pope, 1988). It consists in adding a random force $\hat{\mathbf{a}} = \hat{\mathbf{a}}(\boldsymbol{\kappa}, t)$ in the equation of momentum (2.10) in the Fourier space. This force is applied on all the nodes of the Fourier space that are found inside a spherical shell of internal radius κ_{min}^F and of external radius κ_{max}^F , where κ_{min}^F is the smallest simulated wavenumber which corresponds to the size of the domain κ_{min}^F . Taking into account turbulent forcing, the mass and momentum equation of the fluid are written in spectral space as

$$\kappa_i \hat{u}_{f,i} = 0 \quad (2.13)$$

$$\frac{\partial \hat{u}_{f,i}}{\partial t} + \left[\delta_{ij} - \frac{\kappa_i \kappa_j}{\kappa^2} \right] \hat{N}_j = -\nu_f \kappa^2 \hat{u}_{f,i} + \hat{a}_i \quad (2.14)$$

where \hat{a}_i corresponds to the Fourier transform of the stochastic force. To calculate the components of the stochastic force, Eswaran & Pope (1988) use the stochastic procedure Uhlenbeck-Ornstein that implies the construction of a random complex vector $\hat{\mathbf{b}}(\boldsymbol{\kappa}, t)$

$$\begin{aligned} \mathcal{R}(\hat{b}_i)(t + \Delta t) &= \left(1 + \frac{\Delta t}{T_F}\right) \mathcal{R}(\hat{b}_i) + \xi \sqrt{\frac{2\sigma_F^2 \Delta t}{T_F}} \\ \mathcal{I}(\hat{b}_i)(t + \Delta t) &= \left(1 + \frac{\Delta t}{T_F}\right) \mathcal{I}(\hat{b}_i) + \xi \sqrt{\frac{2\sigma_F^2 \Delta t}{T_F}} \end{aligned}$$

where \mathcal{R} is the real part, \mathcal{I} is the imaginary part, ξ is a random Gaussian variable, T_F is the time scale and σ_F^2 the variance of turbulent forcing. The stochastic procedure Uhlenbeck-Ornstein entails the following properties for the vector field $\hat{\mathbf{b}}$.

$$\langle \hat{\mathbf{b}}(\boldsymbol{\kappa}, t) \rangle = 0 \quad (2.15)$$

$$\frac{\langle \hat{b}_i(\boldsymbol{\kappa}, t) \cdot \hat{b}_j^*(\boldsymbol{\kappa}, t + \tau) \rangle}{2\sigma_F^2} = \exp\left(-\frac{\tau}{T_F}\right) \quad (2.16)$$

where the asterisk signifies the complex conjugate. Lastly, the stochastic force $\hat{\mathbf{a}}(\boldsymbol{\kappa}, t)$ is constructed via random complex vector $\hat{\mathbf{b}}(\boldsymbol{\kappa}, t)$ in order to satisfy the mass conservation in the spectral space Eq. (2.13)

$$\hat{\mathbf{a}}(\boldsymbol{\kappa}, t) = \hat{\mathbf{b}}(\boldsymbol{\kappa}, t) - \frac{\hat{\mathbf{b}}(\boldsymbol{\kappa}, t) \cdot \boldsymbol{\kappa}}{\boldsymbol{\kappa} \cdot \boldsymbol{\kappa}} \boldsymbol{\kappa} . \quad (2.17)$$

Finally, $\hat{\mathbf{a}}$ is applied on a given range of wavenumbers $[\kappa_{min}^F, \kappa_{max}^F]$ according to the following transfer function by Overholt & Pope (1998) in order to add a level of filtering on the Fourier space in order to obtain a more "regular" spectrum of turbulence.

$$f(\kappa, \kappa_{max}^F, \zeta) = \tanh\left(\frac{\kappa_{max}^F - \kappa}{\zeta \kappa_{max}^F}\right) \mathcal{H}(\kappa_{max} - \kappa)$$

where \mathcal{H} is the Heaviside function and $\zeta = 0.2$.

The aforementioned turbulence forcing scheme has three degrees of freedom: the range of forced wavenumbers $[\kappa_{min}^F, \kappa_{max}^F]$, the amplitude of the forcing σ_F^2 and the characteristic time of the forcing T_F . Therefore, the characteristics of the simulated turbulence depend on the calibration of these three degrees of freedom of the forcing. However it is not easy to give a physical criterion to evaluate the parametrization of turbulent forcing. Février (2000) proposes as a parameter the ratio of Eulerian integral time scale of the fluid on the eddy turn-over time, τ_E/T_e . The latter is defined as

$$T_e = \frac{L_f}{u'_f} \quad (2.18)$$

where L_f is the Eulerian longitudinal integral length scale (see Eq. (2.32)) and u'_f is the characteristic turbulent velocity, determined as a function of the kinetic energy of the fluid (see Eq. (2.29)). Since L_f depends on the range of forced wavenumbers $[\kappa_{min}^F, \kappa_{max}^F]$, u'_f on the forcing variance σ_F^2 and τ_E on the forcing time scale T_F , then it seems that ratio τ_E/T_e is significant for turbulent forcing. Février (2000) suggests $\tau_E/T_e = 1$ corresponding to a turbulence where large scales move at velocity u'_f (Taylor hypothesis). In the same work, an extensive study of the influence of each of these parameters was carried out, leading to the following conclusions:

- i. The forcing wavenumber range $[\kappa_{min}^F, \kappa_{max}^F]$ acts directly on the size of large vortices. The comparison of spectra from two DNS whose forced wavenumber ranges are $[0, 2\sqrt{2}\kappa_0]$ (where $\kappa_0 = 2\pi/L$ is the smallest resolved wavenumber for domain of length L) and $[2\kappa_0, 6\kappa_0]$, shows that small structures are not changed by this parameter. On the other hand, the large flow structures are greatly modified by the addition of energy due to forcing. Additionally, turbulence forcing carried out on $[0, 2\sqrt{2}\kappa_0]$ generates vortices of size comparable to the dimension of the domain, which is not desirable. According to the recommendations of Février (2000), for all of the conducted simulations, the range of forced wavenumbers is $[2\kappa_0, 6\kappa_0]$, which allows to have integral length scales about ten times smaller than the size of the domain.

- ii. The variance of the forcing scheme σ_F^2 makes it possible to control the quantity of energy injected and consequently the turbulent energy of the fluid.
- iii. On one hand, the characteristic time scale of forcing T_F acts directly on the Eulerian integral time scale of the fluid τ_E . On the other hand, it has no significant effect on the eddy turn-over time T_e , nor on the Lagrangian integral time scale of the fluid τ_f^t . Lastly, this study also shows that T_F must be equal to T_e .

All of the conducted numerical simulations have been configured to meet these criteria as seen in Subsect. 2.2.2. This type of stochastic turbulence forcing has been used for numerous studies (Boivin, 1996, Eswaran & Pope, 1988, Février, 2000, Sundaram & Collins, 1997, Yeung & Pope, 1989). It should be noted here, in particular, that Eswaran & Pope (1988) have shown that the small scales of turbulence are weakly "polluted" by forcing.

2.1.2 Particle tracking in a turbulent velocity field

The particles are considered as mono-disperse, spherical with diameter $d_p \ll \eta_K$ and inertial, with density $\rho_p \gg \rho_f$. From a numerical point of view, particles are considered, under the point-particle approximation, as dimensionless points of concentrated mass $m_p = \rho_p d_p^3 / 6$ that corresponds to the mass of a sphere of diameter d_p and density ρ_p .

The first studies on the hydrodynamic drag force exerted on a spherical solid particle that is transported by a fluid flow were realised by Basset (1888), Boussinesq (1885), Oseen (1927), Stokes (1851) for small values of particle Reynolds number. More recently, Maxey & Riley (1983) and Gatignol (1983) calculated the exact forces exerted on a particles suspended in a turbulent fluid flow whose diameter is less or equal to the Kolmogorov length scale and for low particle Reynolds numbers. Their analysis allows to write these forces as a function of the field of undisturbed fluid velocity at the particle position $\mathbf{u}_{f@p}^2 = \mathbf{u}_f(\mathbf{x}_p, t)$, where $\mathbf{x}_p = \mathbf{x}_p(t)$ is the particle position at time t .

In the case of solid particles, for a large particle-to-fluid density ratio ($\rho_p/\rho_f > 1000$) and for a particle diameter that is smaller than the Kolmogorov length scale η_K , the force acting on the particles is only the drag $\mathbf{F}_d(\mathbf{x}_p, t)$ and the gravitational force $\mathbf{F}_g(t)$, as demonstrated by Desjonqueres *et al.* (1986) and later by Elghobashi & Truesdell (1993). Lastly, if the particles are charged, then electrostatic force $\mathbf{F}_e(\mathbf{x}_p, t)$ is also considered, thus particle motion is governed by the following equations of motion

$$\frac{d\mathbf{x}_p}{dt} = \mathbf{u}_p \quad (2.19)$$

$$m_p \frac{d\mathbf{u}_p}{dt} = \mathbf{F}_p \quad (2.20)$$

where $\mathbf{F}_p(\mathbf{x}_p, t) = \mathbf{F}_d + \mathbf{F}_g + \mathbf{F}_e$ is the total force exerted on a particle at position \mathbf{x}_p and time t , while $\mathbf{u}_p = \mathbf{u}_p(t)$ is the particle velocity at time t . The gravitational force \mathbf{F}_g is defined as

$$\mathbf{F}_g = -m_p g \hat{\mathbf{k}}$$

where g is the gravitational constant and $\hat{\mathbf{k}}$ is the unitary vector of z -axis. In Eq. (2.20), the fluid-particle drag force is calculated by

$$\mathbf{F}_d = -\frac{\mathbf{u}_p - \mathbf{u}_{f@p}}{\tau_p} m_p \quad (2.21)$$

²Symbol @ reads "at", thus $\mathbf{u}_{f@p}$ signifies "fluid velocity at particle position"

where τ_p is the non-linear particle relaxation time given by Schiller & Naumann (1935)

$$\tau_p = \frac{\rho_p d_p^2}{18\mu_f} \frac{1}{1 + 0.15 Re_p^{0.687}} \quad (2.22)$$

where $\mu_f = \rho_f \nu_f$ is the fluid dynamic viscosity and Re_p the particle Reynolds number defined as

$$Re_p = d_p \frac{\|\mathbf{u}_p - \mathbf{u}_{f@p}\|}{\nu_f} \quad (2.23)$$

The definition of the total electrostatic force \mathbf{F}_e exerted on a particle is given in Subsect. 4.1.2.

Undisturbed fluid velocity at particle position

Since the fluid velocity \mathbf{u}_f is computed over an Eulerian grid and the particle trajectories are Lagrangian, one has to employ a Lagrange polynomial interpolation scheme to get the fluid velocity at the particle position $\mathbf{u}_{f@p}$.

The Lagrange polynomial interpolation is performed by calculating a polynomial $P(x)$ of degree $n \leq N - 1$ that passes through N points $(x_i, y_i = f(x_i))$, $i = 1, 2, \dots, N$.

$$P(x) = \sum_{i=1}^N f(x_i) p_i(x) \quad \text{with} \quad p_i(x) = \prod_{\substack{j=1 \\ j \neq i}}^{N-1} \frac{x - x_j}{x_i - x_j}. \quad (2.24)$$

In **GASPART** solver, the Eulerian grid is uniform so the interpolation scheme is based on the relative distance to the first node which is defined as

$$\alpha = \frac{x - x_1}{x_2 - x_1} = \frac{x - x_1}{\Delta x}.$$

The base polynomials for increasing order of accuracy n are presented in Table 2.1. Detailed calculations are found in Sect. A.2 of Appendices.

Table 2.1: *Lagrange polynomials*

p_i	1st-order	2nd-order	3rd-order	4th-order
p_1	$1 - \alpha$	$\frac{1}{2}(\alpha - 1)(\alpha - 2)$	$-\frac{1}{6}(\alpha - 1)(\alpha - 2)(\alpha - 3)$	$\frac{1}{24}(\alpha - 1)(\alpha - 2)(\alpha - 3)(\alpha - 4)$
p_2	α	$-\alpha(\alpha - 2)$	$\frac{1}{2}\alpha(\alpha - 2)(\alpha - 3)$	$-\frac{1}{6}\alpha(\alpha - 2)(\alpha - 3)(\alpha - 4)$
p_3		$\frac{1}{2}\alpha(\alpha - 1)$	$-\frac{1}{2}\alpha(\alpha - 1)(\alpha - 3)$	$\frac{1}{4}\alpha(\alpha - 1)(\alpha - 3)(\alpha - 4)$
p_4			$\frac{1}{6}\alpha(\alpha - 1)(\alpha - 2)$	$-\frac{1}{6}\alpha(\alpha - 1)(\alpha - 2)(\alpha - 4)$
p_5				$\frac{1}{24}\alpha(\alpha - 1)(\alpha - 2)(\alpha - 3)$

2.1.3 Time-integration and numerical schemes

Fluid and particle velocities are both time-advanced using an Adams-Bashforth 2nd order scheme Eq. (A.1) coupled with an integrating factor (as shown in Sect. A.1). Basically it means that for the fluid the viscous term is directly integrated before the discretization and for the particle it is the dissipative part of the drag force.

Numerical solver **GASPART** is fully parallelized for both the fluid and the particles. For the DNS, the Fast Fourier Transform (FFT) is performed by library **P3DFFT** (Pekurovsky, 2012). For the particle phase, with the help of Annaïg Pedrono from **COSINUS**, the particles are distributed over the processors and at the end of each time-step the latter exchange the particles crossing the CPU borders.

2.2 Configuration of non-settling charge-free reference case

In this section, the configuration of the reference case study is presented. It consists of a non-settling, charge-free particle-laden stationary HIT flow, where gravity and electrostatic forces are neglected, hence $\mathbf{F}_g = \mathbf{F}_e = 0$. Electrostatic forces are taken into account in Chapter 4 and 5.

2.2.1 Statistically steady homogeneous isotropic turbulence

In order to simulate stationary homogeneous isotropic turbulence, one needs not only to successfully calibrate turbulent forcing (3 degrees of freedom presented at Subsect. 2.1.1) but also to ensure that the simulated turbulence is adequately resolved. In Fig. 2.1 the algorithm for the successful calibration of forced turbulence is presented. At first, a preliminary grid resolution $N_x = N_y = N_z = N$ is chosen for a cubic computational domain of length $L_x = L_y = L_z = L$ that results in a space discretization $\Delta x = L/N$. A time-step Δt is also chosen based on empirical knowledge. Furthermore, two degrees of freedom of forcing: variance σ_F^2 and time scale T_F are arbitrarily initialized, while $[\kappa_{min}^F, \kappa_{max}^F] = [2\kappa_0, 6\kappa_0]$ as explained in Subsect. 2.1.1. Having set those, a first simulation of turbulence is performed and the Kolmogorov length scale η_K and turbulent Reynolds number Re_{L_f} are estimated from equations Eq. (2.33) and Eq. (2.34), respectively.

Then, the spatial resolution of the simulated turbulence is evaluated by checking if $\eta_K \geq \chi \Delta x$, where $\chi \in \mathbb{N}^*$ is the desired number of grid points within η_K . If the simulated turbulence is not well resolved, then σ_F^2 is decreased so as to lower turbulent intensity and the simulation is re-launched. Otherwise, the eddy turn-over time T_e is estimated from Eq. (2.18) and is compared to that of T_F and if $T_e \approx T_F$ then T_F is taken equal to T_e to ensure that $T_E \simeq e^{-\frac{\tau}{T_E}}$ according to F evrier (2000) and the simulation is re-launched. Otherwise τ_E is calculated and its value is compared to that of T_e in order to check if the Taylor hypothesis is satisfied. If not, the value of T_F is adjusted according to the following rule: if $\tau_E < T_e$ then T_F is increased and if $\tau_E > T_e$ then T_F is decreased, and the simulation is re-launched.

Lastly, if all the above criteria are met, the spatial resolution of the simulated turbulence is checked one last time via condition $\eta_K \kappa_{max}^F \geq \chi \pi$ where $\kappa_{max}^F = \pi/\Delta x$ is the largest simulated wavenumber. If it is not the case, the spatial resolution has to be increased and re-launch the simulation. Finally, the time-step is re-calibrated according to Pope's criterion

$$\Delta t \leq \frac{1}{20} \frac{\Delta x}{\sqrt{q_f^2}}. \quad (2.25)$$

2.2.2 Turbulence of reference

In the Direct Numerical Simulations of this work, the computational domain has length $L = 2\pi$ and is discretized in $N = 256$ grid points. The turbulent Reynolds number Re_{L_f} is about 100 and according to $\eta_K \kappa_{max}^F = 2.92$ the small turbulent scales are well resolved. To satisfy Pope's criterion (see Eq. (2.25)) for this turbulent Reynolds number, the time-step has to be $\Delta t \leq 6.9 \times 10^{-3} s$. Figure 2.2 shows the turbulent energy spectrum for the aforementioned configuration, where the achieved spatial resolution is observed. The random nature of the physical quantities and the extent of the characteristic scales representing turbulent flows, create the need for a statistical analysis of the data of the numerical experiments conducted in this work. This analysis includes one-point statistical moments (average, standard deviation, moment of order three, ...), two-point statistics (spatial and temporal velocity correlations). A

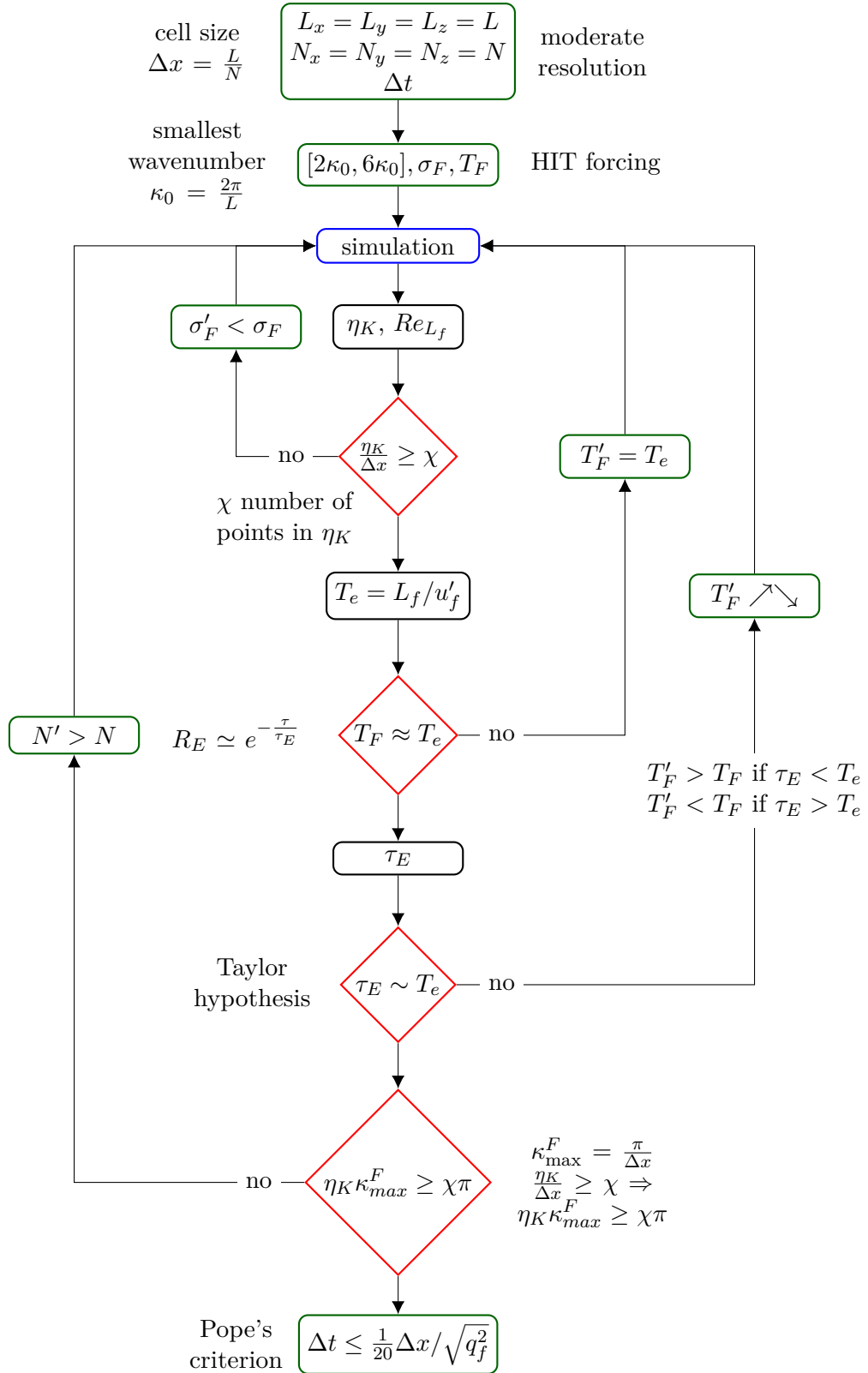


Figure 2.1: Flowchart for the calibration of resolved stationary HIT. Green color denotes a choice/modification for the value of the corresponding variable, red denotes checking the satisfaction of a criterion, black denotes the calculation of a statistic variable and blue the simulation of turbulence.

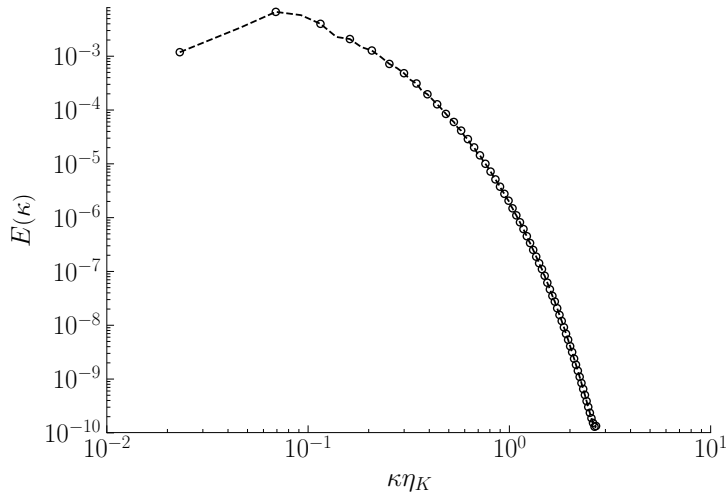


Figure 2.2: *Turbulent energy spectrum for $Re_{L_f} \simeq 100$.*

stochastic random variable $q = q(\mathbf{x}, t)$ can be decomposed into an average value $\langle q \rangle(\mathbf{x}, t)$ and a fluctuating value $q'(\mathbf{x}, t)$ as

$$q(\mathbf{x}, t) = \langle q \rangle(\mathbf{x}, t) + q'(\mathbf{x}, t) \quad \text{with} \quad \langle q' \rangle = 0 .$$

The average operator $\langle \cdot \rangle$ is defined as the arithmetic mean over a large number of independent realizations $\mathcal{N}_{f\&p}$ of the observed phenomenon, namely the two-phase flow as

$$\langle \cdot \rangle = \lim_{\mathcal{N}_{f\&p} \rightarrow \infty} \left[\frac{1}{\mathcal{N}_{f\&p}} \sum_{\mathcal{N}_{f\&p}} (\cdot) \right] \quad (2.26)$$

and it verifies the Reynolds axioms:

- linearity: $\langle \alpha q + \beta r \rangle = \alpha \langle q \rangle + \beta \langle r \rangle$
- idempotence: $\langle \langle r \rangle q \rangle = \langle q \rangle \langle r \rangle$
- commutativity with the derivation and integration operators

where q, r are stochastic variables and α, β are constants.

In this work, the statistical quantities are obtained by averaging in the directions of homogeneity of space and stationarity of time, which are equivalent to the ensemble average of Eq. (2.26) due to the ergodicity hypothesis of the stationary isotropic homogeneous turbulence. Considering time averages, the accuracy of the statistics is conditioned by the averaging duration with regard to the characteristic correlation time scales of the signal. In turbulence, the largest time scale of the turbulent velocity field is of the order of the Eulerian integral time scale τ_E . In principle, a statistical treatment over a duration of the order of $10\tau_E$ ensures a good precision of the statistic moments of order one. Similarly, convergence of the statistical moments of order one, averaged over space, is obtained when the dimension of the computational domain L is approximately of the order of $10L_f$.

Fluid agitation q_f^2 is defined as the average of kinetic energy per unit mass

$$q_f^2 = \frac{1}{2} \langle u'_{f,i} u'_{f,i} \rangle_f \quad (2.27)$$

where $\mathbf{u}_f = \mathbf{u}_f(\mathbf{x}, t)$ is the fluid velocity at position \mathbf{x} and time t , while $\langle \cdot \rangle_f$ denotes an Eulerian average on the grid of the fluid phase defined as

$$\langle \cdot \rangle_f = \frac{1}{V} \int_V (\cdot) dV .$$

Figure 2.3 shows the time evolution of fluid agitation, where two regimes can be observed: an initial transient phase where q_f^2 increases until it reaches a stationary state where it is statistically steady. When the fluid field reaches a stationary (statistically steady) state, the

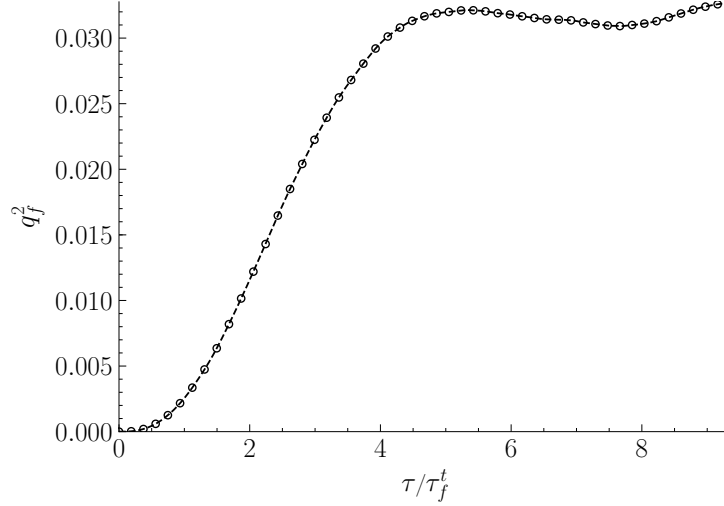


Figure 2.3: Fluid agitation with regard to normalized time. After an initial transient phase, fluid agitation reaches a stationary regime.

level of viscous dissipation adjusts to that of turbulent energy production from forcing. In stationary isotropic homogeneous turbulent, the equation for turbulent kinetic energy is written as follows

$$\frac{d}{dt} q_f^2 = \mathcal{P} - \epsilon_f \quad (2.28)$$

where ϵ_f is the rate of turbulent dissipation defined as

$$\epsilon_f = \frac{1}{2} \left\langle \left(\frac{\partial u_{f,i}}{\partial x_j} + \frac{\partial u_{f,j}}{\partial x_i} \right)^2 \right\rangle_f$$

and \mathcal{P} is the rate of turbulence production imposed from forcing and can be measured simply as $\mathcal{P} = dq_f^2/dt + \epsilon_f$. The evolution of the three terms of Eq. (2.28) are shown in Fig. 2.4 where the stationary regime is observed.

Stationary regime

For the stationary regime, $dq_f^2/dt \sim 0$, hence in addition to spatial averaging (allowed by homogeneity) one can perform time averaging (allowed by stationarity), therefore $\langle \cdot \rangle_f$ operator takes the form of a temporal average that due to the ergodicity property of HIT provides higher statistical convergence

$$\langle \cdot \rangle_f = \frac{1}{T} \int \frac{1}{V} \int_V (\cdot) dV dt .$$

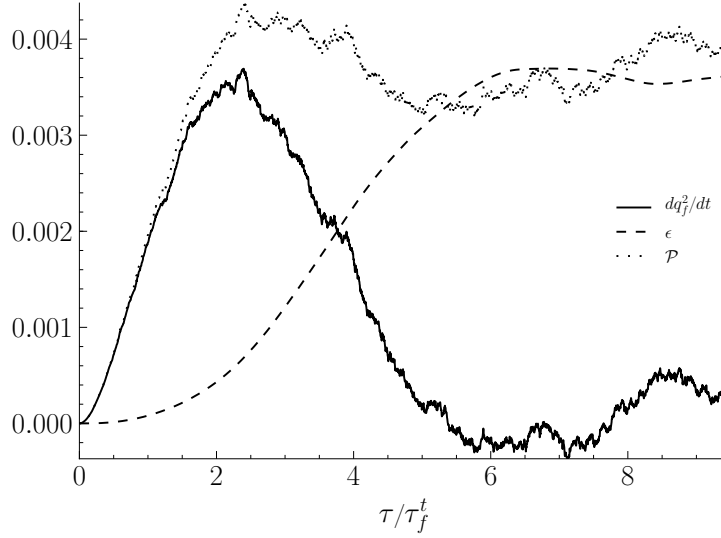


Figure 2.4: Terms of Eq. (2.28). In the stationary state $\mathcal{P} \sim \epsilon_f$ and $dq_f^2/dt \sim 0$.

The characteristic turbulent velocity u'_f , which is a measure of the mean velocity of eddy translation in the flow, can be estimated from fluid agitation q_f^2 as

$$u'_f = \sqrt{\frac{2}{3} q_f^2}. \quad (2.29)$$

The Eulerian time autocorrelation function of the fluid velocity, R_E is calculated in fixed points randomly distributed in the domain at positions \mathbf{x} as

$$R_E(\tau) = \frac{\langle u'_{f,i}(\mathbf{x}, t) u'_{f,i}(\mathbf{x}, t + \tau) \rangle}{2q_f^2(t)}$$

which allows to calculate the Eulerian integral time scale of the fluid, τ_E as

$$\tau_E = \int_0^\infty R_E(\tau) d\tau. \quad (2.30)$$

The autocorrelation time function R_E can be seen in Fig. 2.5. In addition, the Lagrangian autocorrelation function of the fluid velocity, $R_f(\tau)$ is calculated along the trajectories of fluid elements $\mathbf{x}_f(t)$ as

$$R_f(\tau) = \frac{\langle u'_{f,i}(\mathbf{x}_f(t), t) u'_{f,i}(\mathbf{x}_f(t + \tau), t + \tau) \rangle}{2q_f^2(t)}$$

which allows to calculate the Lagrangian fluid integral time scale, τ_f^t as

$$\tau_f^t = \int_0^\infty R_f(\tau) d\tau. \quad (2.31)$$

One of the ways to calculate the Eulerian longitudinal integral length scale L_f is from the tri-dimensional turbulent energy spectrum $E(\kappa)$ as

$$L_f = \frac{\pi}{2u'_f} \int_{\kappa_0}^{\kappa_{max}^F} \kappa^{-1} E(\kappa) d\kappa \quad (2.32)$$

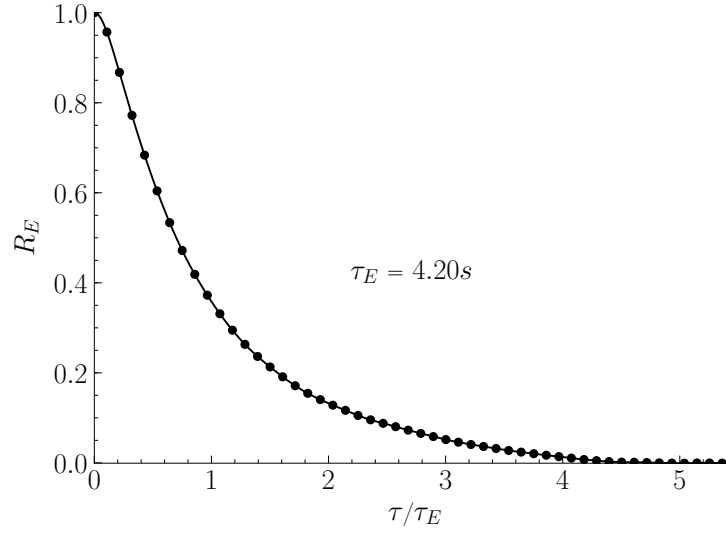


Figure 2.5: Autocorrelation functions of fluid velocity "seen" by motionless particles. Integration gives the Eulerian fluid integral time-scale τ_E .

where $E(\kappa)$ can be obtained by the Fourier transform of the instantaneous fluid velocity field defined as

$$E(\kappa) = \frac{1}{2} \sum_{|\kappa - \frac{\kappa_0}{2}| \leq |\tilde{\kappa}| \leq |\kappa + \frac{\kappa_0}{2}|} \hat{u}_{f,i}(\tilde{\kappa}) \hat{u}_{f,i}^*(\tilde{\kappa})$$

where $\hat{u}_{f,i}^*$ is the complex conjugate of $\hat{u}_{f,i}$. The advantage of using $E(\kappa)$ is that it is readily available due to the spectral method used for the resolution of the Navier-Stokes equations (presented in Subsect. 2.1.1). Based on the Eulerian longitudinal integral length scale L_f , Reynolds number Re_{L_f} can be defined as

$$Re_{L_f} = \frac{L_f u'_f}{\nu_f} . \quad (2.33)$$

and in analogy one can define Reynolds number Re_λ based on the turbulent Taylor length scale. It should be noted here, that turbulent energy dissipates to heat at the smallest turbulent structures that are found in the flow. These characteristic scales, namely the Kolmogorov length scale η_K , the Kolmogorov time scale τ_K and the Kolmogorov velocity scale v_K can be estimated via relations that can be deduced by dimensional analysis which leads to the following relations

$$\eta_K = \left(\frac{\nu_f^3}{\epsilon_f} \right)^{\frac{1}{4}} \quad (2.34)$$

$$\tau_K = \left(\frac{\nu_f}{\epsilon_f} \right)^{\frac{1}{2}} \quad (2.35)$$

$$v_K = (\nu_f \epsilon_f)^{\frac{1}{4}} . \quad (2.36)$$

The fluid material properties and main turbulence statistics presented in this subsection are gathered in Table 2.2.

Table 2.2: *Properties of the fluid and of the examined HIT*

Parameters	Symbol	Value	Units
Time-step	Δt	5×10^{-3}	s
Resolution	$\eta_K \kappa_{max}^F$	2.95	-
Fluid kinematic viscosity	ν_f	1×10^{-3}	m^2/s
Fluid density	ρ_f	1.0	kg/m^3
Fluid kinetic energy	q_f^2	3.29×10^{-2}	m^2/s^2
Characteristic turbulent velocity	u'_f	1.55×10^{-1}	m/s
Turbulent Reynolds number	Re_{L_f}	92.51	-
Taylor Reynolds number	Re_λ	42.86	-
Computational domain length	L	2π	m
Fluid longitudinal integral length scale	L_f/L	0.99×10^{-1}	-
Kolmogorov length scale	η_K/L	3.67×10^{-3}	-
Eddy turn-over time	T_e	4.21	s
Eulerian fluid integral time scale	τ_E/T_e	1.00	-
Lagrangian fluid integral time scale	τ_f^l/T_e	7.53×10^{-1}	-
Kolmogorov time scale	τ_K/T_e	1.26×10^{-1}	-

2.2.3 Stochastic models of fluid acceleration

Langevin (single exponential) model

The simplest stochastic Lagrangian equation on fluid acceleration in HIT is based on a Langevin equation and presented by Pope (2002b) is

$$\delta u'_{f,i} = -D u'_{f,i} \delta t + B \delta W_i \quad (2.37)$$

where $\delta \mathbf{u}'_f(t) = \mathbf{u}'_f(t + \delta t) - \mathbf{u}'_f(t)$ is the infinitesimal increment of the fluctuating component of fluid velocity which is given directly by

$$\delta u'_{f,i} = a'_{f,i} \delta t$$

and $\delta \mathbf{W}(t)$ is the infinitesimal increment of a vector-valued Wiener process which has the properties $\langle \delta \mathbf{W} \rangle = 0$ and $\langle \delta W_i \delta W_j \rangle = \delta t \delta_{ij}$. We can directly deduce the equations both on the variance of fluid velocity $\langle \mathbf{u}'_f{}^2 \rangle_f = \langle u'_{f,i} u'_{f,i} \rangle_f / 3$ and of fluid acceleration $\langle \mathbf{a}'_f{}^2 \rangle_f = \langle a'_{f,i} a'_{f,i} \rangle_f / 3$, but also of the velocity-acceleration correlation $\langle \mathbf{u}'_f \mathbf{a}'_f \rangle_f = \langle u'_{f,i} a'_{f,i} \rangle_f / 3$. More specifically, one can write the transport equations of these three terms as

$$\begin{aligned} \frac{\partial \langle \mathbf{u}'_f{}^2 \rangle_f}{\partial t} &= 2 \langle \mathbf{u}'_f \mathbf{a}'_f \rangle_f \\ \frac{\partial \langle \mathbf{a}'_f{}^2 \rangle_f}{\partial t} &= -2D \langle \mathbf{u}'_f{}^2 \rangle_f + B^2 \\ \frac{\partial \langle \mathbf{u}'_f \mathbf{a}'_f \rangle_f}{\partial t} &= \langle \mathbf{a}'_f{}^2 \rangle_f - D \langle \mathbf{u}'_f{}^2 \rangle_f . \end{aligned}$$

To better understand term $\langle \mathbf{u}'_f \mathbf{a}'_f \rangle_f$, one can develop it using Eq. (2.2) for $a_{f,i}$ as

$$a_{f,i} = -u_{f,j} \frac{\partial u_{f,i}}{\partial x_j} - \frac{1}{\rho_f} \frac{\partial p}{\partial x_i} + \nu_f \frac{\partial^2 u_{f,i}}{\partial x_j \partial x_j} . \quad (2.38)$$

Then under the homogeneity and incompressibility hypothesis, this is written as

$$\langle \mathbf{u}'_f \mathbf{a}'_f \rangle_f = -\nu_f \left\langle \frac{\partial u_{f,i}}{\partial x_j} \frac{\partial u_{f,i}}{\partial x_j} \right\rangle_f \quad (2.39)$$

so it is clear that, in homogeneous and incompressible flow, term $\langle \mathbf{u}'_f \mathbf{a}'_f \rangle_f$ represents turbulence dissipation. In stationary homogeneous isotropic turbulence, we can show from the above equations of the moments that the variance of velocity $\langle \mathbf{u}'_f{}^2 \rangle_f$ and of acceleration $\langle \mathbf{a}'_f{}^2 \rangle_f$ are written according to the coefficients of the model in the form

$$\begin{aligned} \langle \mathbf{u}'_f \mathbf{a}'_f \rangle_f &= 0 \\ \langle \mathbf{u}'_f{}^2 \rangle_f &= \frac{B^2}{2D} \\ \frac{\langle \mathbf{a}'_f{}^2 \rangle_f}{\langle \mathbf{u}'_f{}^2 \rangle_f} &= D. \end{aligned}$$

We can also show (Pope, 2002b) that the Lagrangian integral scale is given by the relation

$$\tau_f^t = \frac{1}{D}.$$

So, we can draw from these relations the following equations for the model coefficients D and B :

$$\begin{aligned} D &= \frac{\langle \mathbf{a}'_f{}^2 \rangle_f}{\langle \mathbf{u}'_f{}^2 \rangle_f} \\ B^2 &= 2 \frac{\langle \mathbf{u}'_f{}^2 \rangle_f}{\tau_f^t}. \end{aligned}$$

The Lagrangian autocorrelation function can be deduced from Eq. (2.37) as an exponential function,

$$R_f(\tau) = \exp\left(-\frac{\tau}{\tau_f^t}\right)$$

where the Lagrangian integral time scale τ_f^t can be written as

$$\tau_f^t = \frac{\langle \mathbf{u}'_f{}^2 \rangle_f}{\langle \mathbf{a}'_f{}^2 \rangle_f}.$$

Double exponential model

First Sawford (1991) and later Pope (1994, 2002a) expanded the stochastic Langevin model on fluid acceleration in HIT to the following form

$$\delta u'_{f,i} = -C a'_{f,i} \delta t - D u'_{f,i} \delta t + B \delta W_i \quad (2.40)$$

Using Eq. (2.40) one can write the transport equations of the three terms $\langle \mathbf{u}'_f{}^2 \rangle_f$, $\langle \mathbf{a}'_f{}^2 \rangle_f$ and $\langle \mathbf{u}'_f \mathbf{a}'_f \rangle_f$ as

$$\begin{aligned} \frac{\partial \langle \mathbf{u}'_f{}^2 \rangle_f}{\partial t} &= 2 \langle \mathbf{u}'_f \mathbf{a}'_f \rangle_f \\ \frac{\partial \langle \mathbf{a}'_f{}^2 \rangle_f}{\partial t} &= -2C \langle \mathbf{a}'_f{}^2 \rangle_f - 2D \langle \mathbf{u}'_f \mathbf{a}'_f \rangle_f + B^2 \\ \frac{\partial \langle \mathbf{u}'_f \mathbf{a}'_f \rangle_f}{\partial t} &= \langle \mathbf{a}'_f{}^2 \rangle_f - C \langle \mathbf{u}'_f \mathbf{a}'_f \rangle_f - D \langle \mathbf{u}'_f{}^2 \rangle_f. \end{aligned}$$

In stationary homogeneous isotropic turbulence, we can show from the above equations that the variance of velocity $\langle \mathbf{u}'^2 \rangle_f$, of acceleration $\langle \mathbf{a}'^2 \rangle_f$ are written according to the coefficients of the model in the form

$$\begin{aligned}\langle \mathbf{u}' \mathbf{a}' \rangle_f &= 0 \\ \langle \mathbf{a}'^2 \rangle_f &= \frac{B^2}{2C} \\ \langle \mathbf{u}'^2 \rangle_f &= \frac{B^2}{2CD} .\end{aligned}$$

We can also show (Pope, 2002b) that the Lagrangian integral scale is given by the relation

$$\tau_f^t = \frac{C}{D} .$$

So we can draw from these relations the following equations for the model coefficients D, C and B

$$\begin{aligned}D &= \frac{\langle \mathbf{a}'^2 \rangle_f}{\langle \mathbf{u}'^2 \rangle_f} \\ C &= \tau_f^t \frac{\langle \mathbf{a}'^2 \rangle_f}{\langle \mathbf{u}'^2 \rangle_f} \\ B^2 &= 2\tau_f^t \frac{[\langle \mathbf{a}'^2 \rangle_f]^2}{\langle \mathbf{u}'^2 \rangle_f} .\end{aligned}$$

The Lagrangian autocorrelation function can be written using a double exponential function as

$$R_f(\tau) = \frac{\exp\left(-\frac{\tau}{\tau_\infty}\right) - \frac{\tau_0}{\tau_\infty} \exp\left(-\frac{\tau}{\tau_\infty}\right)}{1 - \frac{\tau_0}{\tau_\infty}}$$

with

$$\begin{aligned}\tau_\infty &= \frac{1}{2} \tau_f^t \left[1 + \left(1 - 4 \frac{\tau_a \tau_\epsilon}{\tau_f^{t2}} \right)^{1/2} \right] \\ \tau_0 &= \frac{1}{2} \tau_f^t \left[1 - \left(1 - 4 \frac{\tau_a \tau_\epsilon}{\tau_f^{t2}} \right)^{1/2} \right]\end{aligned}$$

where τ_ϵ is the characteristic time scale of turbulent energy dissipation defined as

$$\tau_\epsilon = \frac{3 \langle \mathbf{u}'^2 \rangle_f}{2 \epsilon_f} \quad (2.41)$$

and τ_a the characteristic time scale of turbulent fluid acceleration time scale which is determined as

$$\tau_a = \frac{1 \langle \mathbf{u}'^2 \rangle_f}{\tau_\epsilon \langle \mathbf{a}'^2 \rangle_f} .$$

The characteristic times which appear in the integrals can be written as

$$\tau_f^t = \tau_\infty + \tau_0$$

and

$$\tau_a = \frac{\tau_\infty \tau_0}{\tau_\epsilon}.$$

By definition of characteristic times, the coefficients of the stochastic model can be written under the following form

$$\begin{aligned} D &= \frac{1}{\tau_\epsilon \tau_a} = \frac{1}{\tau_\infty \tau_0} \\ C &= \frac{\tau_f^t}{\tau_\epsilon \tau_a} = \frac{\tau_\infty + \tau_0}{\tau_\infty \tau_0} = \frac{1}{\tau_\infty} + \frac{1}{\tau_0} \\ B^2 &= 2 \langle \mathbf{u}'^2 \rangle_f \frac{\tau_f^t}{[\tau_a \tau_\epsilon]^2} = \frac{2 \langle \mathbf{u}'^2 \rangle_f}{\tau_\infty \tau_0} \left[\frac{1}{\tau_\infty} + \frac{1}{\tau_0} \right]. \end{aligned}$$

In practice, it is evident that we need to determine a characteristic time scale of the fluid, τ_f^t and the product of two characteristic time scales $\tau_a \tau_\epsilon$. These two coefficients of the model can be estimated directly from the autocorrelation function of the fluid measured along fluid element trajectories. To calculate τ_f^t , we can use Eq.(2.31), while for $\tau_a \tau_\epsilon$ the following relation can be used:

$$\tau_a \tau_\epsilon = - \left[\lim_{\tau \rightarrow 0} \left(\frac{d^2}{d\tau^2} R_f(\tau) \right) \right]^{-1}$$

supposing that the short-term response of the autocorrelation function can be represented by the oscillator function

$$\lim_{\tau \rightarrow 0} R_f = \lim_{\tau \rightarrow 0} \left(1 - \frac{1}{2} \frac{\tau^2}{\tau_a \tau_\epsilon} \right).$$

Figure 2.6 shows the Eulerian and Lagrangian autocorrelation functions of fluid velocity and the respective fluid time scales.

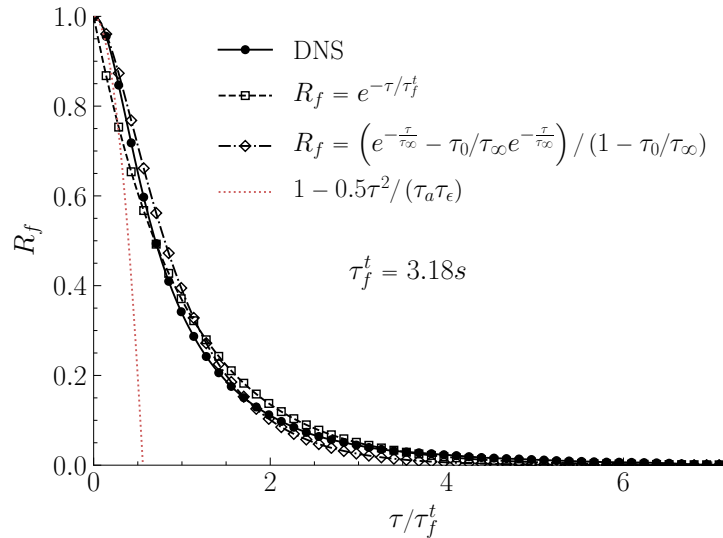


Figure 2.6: Autocorrelation functions of fluid velocity "seen" by fluid elements. Integration gives the Lagrangian fluid integral time-scale τ_f^t . A good agreement with the exponential models is observed. The red dotted line denotes the oscillator function.

Table 2.3 shows that the two models give estimations for $\tau_a\tau_\epsilon$, τ_0 and τ_∞ of the same order of magnitude

Table 2.3: *Fluid characteristic time scales for different models*

model	$\tau_a\tau_\epsilon$	τ_0	τ_∞	τ_f^t
DNS	-	-	-	-
$f(\langle \mathbf{u}'^2 \rangle_f, \langle \mathbf{a}'^2 \rangle_f)$	2.05	0.899	2.28	3.18
$\lim_{\tau \rightarrow 0} R_f(\tau)$	1.57	-	-	-

Subsequently, the Lagrangian stochastic equation of fluid acceleration can be put in the explicit form

$$\delta a'_{f,i} = - \left[\frac{1}{\tau_\infty} + \frac{1}{\tau_0} \right] a'_{f,i} \delta t - \frac{1}{\tau_\infty \tau_0} u'_{f,i} \delta t + \sqrt{\frac{2\langle \mathbf{u}'^2 \rangle_f}{\tau_\infty \tau_0} \left[\frac{1}{\tau_\infty} + \frac{1}{\tau_0} \right]} \delta W_i.$$

We can notice that when $\tau_f^t/\tau_a \gg 1$ we have in the first order approximation that $\tau_0 \rightarrow \tau_\epsilon \tau_a / \tau_f^t$, which corresponds to the form of the model initially proposed by Sawford (1991). To close the model, we find in the literature empirical forms of the variance of acceleration normalized by the Kolmogorov scales as a function of the turbulent Reynolds number based on the Taylor scale (see for example Zaichik *et al.* (2003)),

$$a_0 = \frac{\langle \mathbf{a}'^2 \rangle_f \tau_K}{\epsilon_f} = \frac{a_1 + a_{0,\infty} Re_\lambda}{a_2 + Re_\lambda}, \quad Re_\lambda = \sqrt{\frac{15\langle \mathbf{u}'^2 \rangle_f}{\nu_f \epsilon_f}}$$

with $a_1 = 11$, $a_2 = 205$ and $a_{0,\infty} = 7$ where τ_K is the Kolmogorov time scale defined in Eq. (2.35). Indeed, for any case of any stationary THI, if we know $q_f^2 = 3\langle \mathbf{u}'^2 \rangle_f/2$, ϵ_f , ν_f and τ_f^t , by using a correlation for the acceleration of the turbulence, the coefficients of the model can be calculated.

2.2.4 Particle material properties

Numerical simulations have been performed with $N_p = 10,000$ particles in the computational domain. The convergence of statistical moments is discussed at the end of Subsec. 2.2.5. In order to characterize the particle density in such a flow, one can define the particle number density n_p as the number of particles per unit volume

$$n_p = \frac{N_p}{L^3}.$$

However, information on the volume occupied by the particles would be more insightful, thus the solid volume fraction α_p is defined as the total particle volume to the domain volume

$$\alpha_p = \frac{n_p d_p^3}{6}.$$

For the simulations presented here, $\alpha_p = 2.64 \times 10^{-6}$ which is a level of solid volume fraction that corresponds to a dilute particle phase, allowing for particle collisions and two-way coupling to be neglected. Thus, the fluid velocity seen by the particles, $\mathbf{u}_{f@p}$, is computed by 3rd order polynomial interpolation (see Subsect. 2.1.2) of the fluid velocity field. In addition, all

particles have been considered of the same diameter so that $\eta_K/d_p = 4.56$ but they differ by density. Gravity and electrostatic forces are neglected for the case study presented in this chapter, since we are interested on the effects of turbulence on particle motion.

In Table 2.4, particle density and two Stokes numbers are presented: a Stokes number based on the Stokes drag and the Kolmogorov time scale, τ_p^{St}/τ_K and a Stokes number based on the particle relaxation time and the Lagrangian fluid integral time scale, τ_{fp}^F/τ_f^t . The Stokes particle time scale τ_p^{St} is defined as

$$\tau_p^{St} = \frac{\rho_p d_p^2}{18\mu_f}.$$

In addition, as we consider non-linear drag force (see Eq. (2.21)), the particle relaxation time scale τ_{fp}^F is introduced as

$$\tau_{fp}^F = \left[\left\langle \frac{1}{\tau_p} \right\rangle_p \right]^{-1} \quad (2.42)$$

where $\langle \cdot \rangle_p$ denotes a Lagrangian average on the particle phase defined as the arithmetic mean on all the particles in the computational domain

$$\langle \cdot \rangle_p = \frac{1}{N_p} \sum_{n=1}^{N_p} (\cdot)^{(n)}.$$

Table 2.4: *Material properties of particles*

class	ρ_p/ρ_f	τ_p^{St}/τ_K	τ_{fp}^F/τ_f^t
1	20,000	53.8	7.57
2	10,000	26.9	3.81
3	5,000	13.4	1.92
4	2,750	7.39	1.07
5	1,500	4.03	0.594
6	750	2.02	0.303
7	400	1.08	0.165
8	200	0.538	0.0839

An essential quantity for the statistical description of turbulent particle-laden gas flows, is the particle agitation q_p^2 defined as

$$q_p^2 = \frac{1}{2} \langle u'_{p,i} u'_{p,i} \rangle_p \quad (2.43)$$

which is a measure of the kinetic energy of the system of particles. Another important statistical quantity is the fluid agitation "seen" at the positions of the particles $q_{f@p}^2$ defined as

$$q_{f@p}^2 = \frac{1}{2} \langle u'_{f@p,i} u'_{f@p,i} \rangle_p \quad (2.44)$$

which is a measure of the kinetic energy of the fluid seen by the particles. Lastly, to quantify fluid-particle velocity correlation, one can calculate fluid-particle velocity covariance q_{fp} as

$$q_{fp} = \langle u'_{f@p,i} u'_{p,i} \rangle_p. \quad (2.45)$$

Figure 2.7 illustrates the evolution of particle agitation with regard to time normalized by the particle relaxation time τ_{fp}^F (see Eq. (2.42)). It is evident that the gas-particle flow achieves a stationary regime after several multiples of the particle relaxation time. Lighter particles achieve this stationary regime later in terms of τ_{fp}^F .

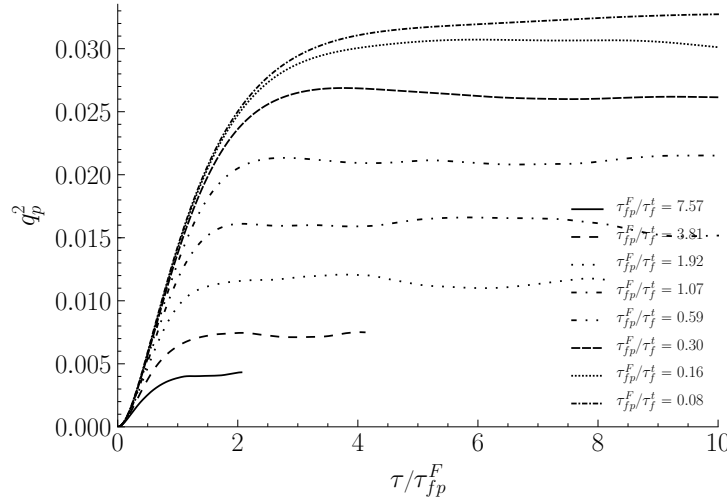


Figure 2.7: Evolution of particle agitation for various Stokes numbers in the transient regime. Stationarity is reached for every Stokes number after several multiples of τ_{fp}^F .

Stationary regime

For the stationary regime, $dq_p^2/dt \sim 0$, hence in addition to spatial averaging (allowed by homogeneity) one can perform time averaging (allowed by stationarity), therefore $\langle \cdot \rangle_p$ operator takes the following form

$$\langle \cdot \rangle_p = \frac{1}{T} \int \frac{1}{N_p} \sum_{n=1}^{N_p} (\cdot)^{(n)} dt. \quad (2.46)$$

In Fig. 2.8, it is shown particles with moderate inertia "see" a fluid agitation $q_{f@p}^2$ slightly smaller than the actual value of fluid agitation q_f^2 . This is due to the phenomenon of preferential concentration Fessler *et al.* (1994), Squires & Eaton (1991) as particles of moderate inertia get trapped in regions of low vorticity and therefore "see" in average slightly lower levels of fluid agitation. However, heavy particles tend to present the behavior of motionless observers, while lighter particles "see" a fluid agitation slightly larger than the actual value. This happens because lighter particles stay longer in certain zones of the turbulent flow that are more energetic in average. In fact it would be very surprising to have this equality $q_{f@p}^2 = q_f^2$ whereas the distribution of the particles is correlated with turbulent vorticity $\omega'_f = \nabla \times \mathbf{u}'_f$. This is possible because \mathbf{u}'_f and ω'_f are not very correlated in turbulence (especially at large Reynolds).

2.2.5 Fluid and particle characteristic time scales

One statistic quantity that allows to acquire a better understanding of the turbulent gas-particle flow, is the autocorrelation function of fluid and particle velocities. These functions enable a qualitative analysis of the decorrelation of the aforementioned velocities in the turbulent

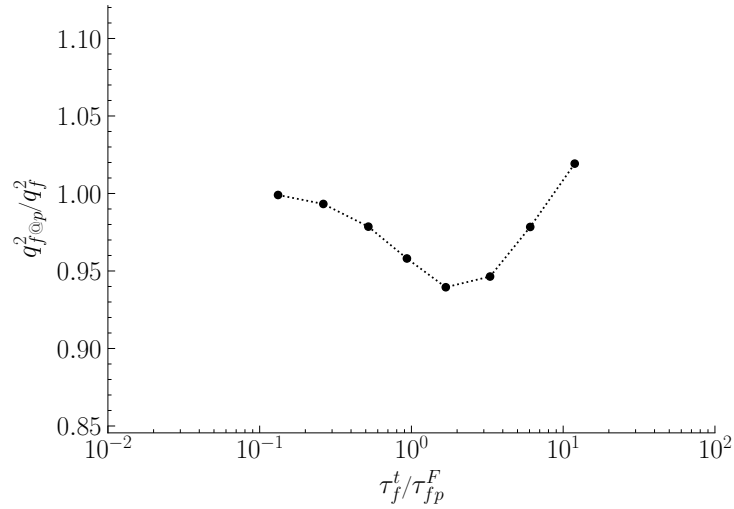


Figure 2.8: Fluid agitation seen by the particles $q_{f@p}^2$ with regard to particle inertia.

flow (via their shapes), as well as a quantification of the rate of such a decorrelation (via their integrals). The autocorrelation function of the fluid velocity measured at the position of the particles, $R_{f@p}(\tau)$ is defined as

$$R_{f@p}(\tau) = \frac{\langle u'_{f@p,i}(\mathbf{x}_p(t), t) u'_{f@p,i}(\mathbf{x}_p(t + \tau), t + \tau) \rangle_p}{2q_{f@p}^2(t)}. \quad (2.47)$$

The Lagrangian integral time scale of the fluid "seen" by the inertial particles, $\tau_{f@p}^t$ is defined by

$$\tau_{f@p}^t = \int_0^\infty R_{f@p}(\tau) d\tau. \quad (2.48)$$

When motionless particles are considered, Eq. (2.47) & (2.48) allow to compute the Eulerian time scale, τ_E and for fluid elements the Lagrangian fluid integral time scale, τ_f^t (see Fig. 2.6). Using $\tau_{f@p}^t$, one can define another particle Stokes number as $\tau_{fp}^F/\tau_{f@p}^t$. In correspondence with Eq. (2.47), one can define the Lagrangian autocorrelation function of particle velocity, $R_p(\tau)$ as

$$R_p(\tau) = \frac{\langle u'_{p,i}(t) u'_{p,i}(t + \tau) \rangle_p}{2q_p^2(t)}.$$

The Lagrangian particle integral time scale, τ_p^t is defined by

$$\tau_p^t = \int_0^\infty R_p(\tau) d\tau. \quad (2.49)$$

The values of these characteristic time scales, for the particle classes used in the numerical simulations of this work, are found in Table 2.5.

Table 2.5: Characteristic time scales $\tau_{f@p}^t$ and τ_p^t and particle Reynolds number Re_p

class	$\tau_{fp}^F/\tau_{f@p}^t$	τ_p^t/τ_f^t	Re_p
1	6.39	8.36	1.09
2	3.49	4.64	1.02
3	1.82	2.82	0.909
4	0.969	2.09	0.777
5	0.502	1.71	0.616
6	0.245	1.46	0.429
7	0.134	1.31	0.282
8	0.0733	1.17	0.163

To achieve statistical convergence, statistical moments have been calculated over a sufficiently long duration which is calculated as a multiple of the maximum characteristic time scales of all the physical mechanisms involved, $T_{stat} \geq 5 \times \max\{\tau_{f@p}^t, \tau_{fp}^F\}$. Also all time-dependent statistics presented in this chapter (autocorrelation functions, etc...) have been calculated as the average of 10 realizations that have been launched consecutively after a sufficient time offset. Figure 2.9 shows autocorrelation functions $R_{f@p}$ and R_p for various Stokes numbers. It seems that inertia does not change considerably the shape of the autocorrelation functions. However, that is not true for their integral which represents the Lagrangian integral time scale of the fluid from the point of view of the particles, $\tau_{f@p}^t$.

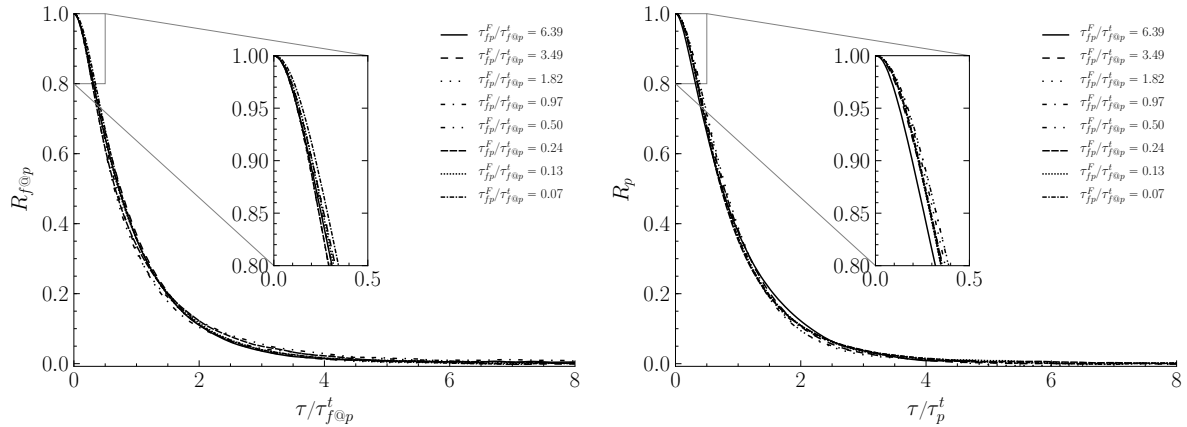
**Figure 2.9:** Autocorrelation function $R_{f@p}$ of fluid velocity "seen" at the particle positions (left) and R_p of particle velocity (right) with regard to time normalized by corresponding integral time scale for various Stokes numbers in the charge-free case.

Figure 2.10 illustrates the effect of particle inertia on $\tau_{f@p}^t$. In fact, at the limit of very heavy particles $\tau_{fp}^F \rightarrow \infty$, particles tend to behave as randomly distributed observers completely decorrelated from the turbulent fluid flow, hence $\tau_{f@p}^t \rightarrow \tau_E$. Inversely, at the limit of very light particles $\tau_{fp}^F \rightarrow 0$, particles tend to behave as fluid elements, hence $\tau_{f@p}^t \rightarrow \tau_f^t$. This behavior is captured by the semi-empirical model of Wang & Stock (1993) presented in Eq. (2.50), which is plotted in Fig. 2.10 for comparison.

$$\frac{\tau_{f@p}^t}{\tau_E} = 1 - \left(1 - \frac{\tau_f^t}{\tau_E}\right) \times \left(1 + \frac{\tau_{fp}^F}{\tau_E}\right)^{-0.4 \left(1 + 0.01 \frac{\tau_{fp}^F}{\tau_E}\right)}. \quad (2.50)$$

For the range of Stokes numbers examined in this work, decreasing particle inertia leads to a decrease of $\tau_{f@p}^t$ for heavy particles, a trend that follows the cited model. Then, particles of moderate inertia exhibit a considerable increase that is followed by a decrease for lighter ones towards the model's curve. This can be explained if we consider the phenomenon of particle preferential concentration. According to this phenomenon, particles of moderate inertia tend to stay more in average in certain turbulent structures with longer lifetimes, thus they exhibit this increase in the measured fluid integral time scale, $\tau_{f@p}^t$. However, heavier particles do not exhibit preferential concentration, hence they "see" a time scale close to the fluid Eulerian integral time scale, τ_E , which is calculated via randomly distributed motionless observers (see Eq. (2.30)). Finally, lighter particles do not also exhibit preferential concentration, hence they "see" a time scale close to the fluid Lagrangian integral time scale, τ_f^t , which is calculated along the trajectories of fluid elements (see Eq. (2.31)).

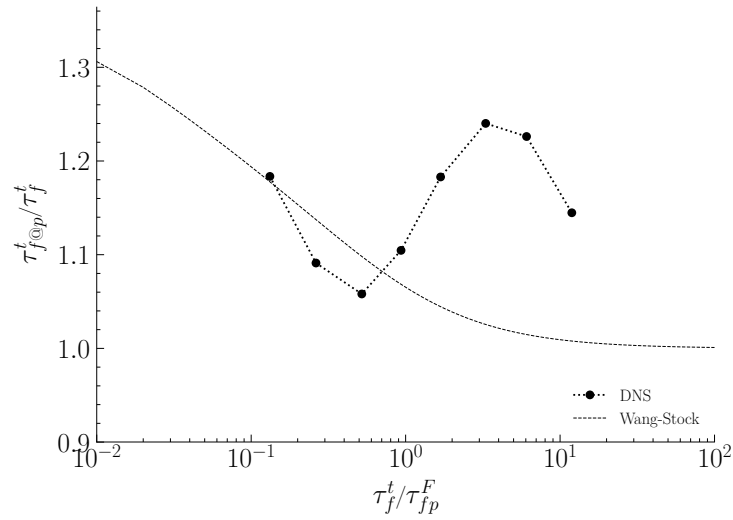


Figure 2.10: *Sensitivity of Lagrangian integral time scale of the fluid from the point of view of the particles with regard to particle response time. Semi-empirical model of Wang & Stock (1993) (see Eq. (2.50)) is also plotted for comparison.*

2.3 Conclusion

To simulate a stationary homogeneous isotropic turbulence, which is the aim of this work, one has to sustain the same level of turbulent kinetic energy of the fluid. In order to do that, a turbulence forcing scheme needs to be deployed to counter balance turbulent dissipation. Furthermore, when particles are transported by a turbulent fluid flow, one needs to carefully consider the involved length scales. If the charged inertial particles are smaller than the Kolmogorov length scale, they interact with rather large turbulent structures and the point-particle approximation can be used. This along with the fact that the particles are considered considerably more dense than the fluid, allows for a simplification of the forces exerted on them: the hydrodynamic drag, the gravity force and the electrostatic forces. Finally, several statistics have to be deployed that allow for the calculation of characteristic scales that are of paramount importance in the understanding of the dynamics of such gas-particle flows.

Bibliography

- Basset, A.B. 1888. *Treatise on hydrodynamics*. Vol. 2. Deighton Bell, London.
- Boivin, M. 1996. *Etude de l'influence des particules sur la turbulence à partir de simulations des grandes échelles d'écoulements diphasiques gaz-solides homogène isotropes stationnaires*. Ph.D. thesis, EDF-DRD.
- Boussinesq, J. 1885. *Sur la résistance qu'oppose un liquide indéfini en repos...* Comptes Rendus, Acad. Sci., Paris.
- Canuto, C., Hussaini, M.Y., Quarteroni, A., & Zang, T.A. 1988. *Spectral methods in fluids dynamics*. Springer-Verlag, New York.
- Desjonqueres, P., Gouesbet, G., Berlemont, A., & Picart, A. 1986. Dispersion of discrete particles by continuous turbulent motions : new results and discussions. *Physics of fluids*, **29**, 2147–2151.
- Deutsch, E. 1992. *Dispersion de particules dans une turbulence homogène isotrope calculée par simulation numérique directe des grandes échelles*. Ph.D. thesis, Ecole Centrale de Lyon.
- Deutsch, E., Adin, F., & Simonin, O. 1993. *Traitement des collisions entre particules dans le calcul des trajectoires en écoulement turbulent*. Tech. rept. EDF-HE44/93.12B. LNH Chatou.
- Elghobashi, S., & Truesdell, G.C. 1993. On the two-way interaction between homogeneous turbulence and dispersed solid particles. i : Turbulence modification. *Physics of fluids*, **5(7)**, 1790–1801.
- Eswaran, V., & Pope, S.B. 1988. An examination of forcing in direct numerical simulations of turbulence. *Computers & fluids*, **16**, 257–278.
- Fede, P., & Simonin, O. 2006. Numerical study of the subgrid fluid turbulence effects on the statistics of heavy colliding particles. *Physics of fluids*, **18(045103)**, 1–17.
- Fessler, J.R., Kulick, J.D., & Eaton, J.K. 1994. Preferential concentration of heavy particles in a turbulent channel flow. *Physics of fluids*, **6**, 3742–3749.
- Février, Pierre. 2000. *Etude numérique des effets de concentration préférentielle et de corrélation spatiale entre vitesses de particules solides en turbulence homogène isotrope stationnaire*. Ph.D. thesis, Institut National Polytechnique de Toulouse.
- Gatignol, R. 1983. The Faxén formulas for a rigid particle in an unsteady non)uniform stokes flow. *Journal de mécanique théorique et appliquée*, **9**, 143–160.
- Laviéville, J. 1997. *Simulations numériques et modélisation des interactions entre l'entraînement par la turbulence et les collisions interparticulaires en écoulement gaz-solides*. Ph.D. thesis, Université de Rouen.
- Maxey, M.R., & Riley, J.J. 1983. Equation of motion for a small rigid sphere in a non uniform flow. *Physics of fluids*, **26(4)**, 2883–2889.
- Orszag, S.A. 1969. Numerical methods for the simulation of turbulence. *The physics of fluids supplement*, **II**, 250–257.

- Oseen, C. W. 1927. *Neue methoden und ergebnisse in der hydrodynamik*. Akademische Verlag, Leipzig.
- Overholt, M.R., & Pope, S.B. 1998. A deterministic forcing scheme for Direct Numerical Simulations of turbulence. *Computers & fluids*, **27**, 11–28.
- Pekurovsky, D. 2012. P3dfft: A framework for parallel computations of fourier transforms in three dimensions. *Siam journal on scientific computing*, **34**(4), C192–C209.
- Pope, S. B. 1994. Lagrangian PDF Methods for Turbulent Flows. *Annual review of fluid mechanics*, **26**(1), 23–63.
- Pope, S.B. 2002a. A stochastic Lagrangian model for acceleration in turbulent flows. *Physics of fluids*, **14**(7), 2360–2375.
- Pope, S.B. 2002b. Stochastic Lagrangian models of velocity in homogeneous turbulent shear flow. *Physics of fluids*, **14**(5), 1696–1702.
- Sawford, B.L. 1991. Reynolds number effects in Lagrangian stochastic models of turbulent dispersion. *Physics of fluids*, **3**(6), 1577–1586.
- Schiller, L., & Naumann, A. 1935. A drag coefficient correlation. *V.d.i. zeitung*, **77**, 318–320.
- Squires, K.D., & Eaton, J.K. 1991. Preferential concentration of particles by turbulence. *Physics of fluids a: Fluid dynamics*, **3**(5), 1169–1178.
- Stokes, G.G. 1851. *On the effect of the inertial friction of fluids on the motion of pendulums*. Trans. Cambridge Phil. Soc.
- Sundaram, Shivshankar, & Collins, Lance R. 1997. Collision statistics in an isotropic particle-laden turbulent suspension. Part 1. Direct numerical simulations. *Journal of fluid mechanics*, **335**(Mar.), 75–109. Publisher: Cambridge University Press.
- Vermorel, O., Bédard, B., Simonin, O., & Poinso, T. 2003. Numerical study and modelling of turbulence modulation in particle laden slab flow. *Journal of turbulence*, **335**, 75–109.
- Vincent, A., & Meneguzzi, M. 1991. The spatial structure and statistical properties of homogeneous turbulence. *Journal of fluid mechanics*, **225**, 1 – 20.
- Wang, Lian-Ping, & Stock, David. 1993. Dispersion of heavy particles by turbulent motion. *Journal of the atmospheric sciences*, **50**(Jan.), 1897–1913.
- Yeung, P.K., & Pope, S.B. 1989. Lagrangian statistics from Direct Numerical Simulations of isotropic turbulence. *Journal of fluid mechanics*, **207**, 531–586.
- Zaichik, L.I., Simonin, O., & Alipchenkov, V.M. 2003. Two statistical models for predicting collision rates of inertial particles in homogeneous isotropic turbulence. *Physics of fluids*, **15**, 2995–3005.

3

Dispersion of charge-free inertial particles in stationary HIT

“πάντοτε ζητεῖν τὴν ἀλήθειαν¹”

- Diogenes the Cynic, c. 404 – c. 323 BC

Abstract

This chapter deals with the investigation of the dispersion of non-settling charge-free particles in stationary homogeneous isotropic turbulence by means of statistical analysis of the performed DNS. First, the spectral analysis of turbulent gas-particle flows is presented that leads to the formulation of Tchen-Hinze theory, a theoretical framework that allows for a prediction of particle agitation based on fluid agitation and characteristic fluid/particle time scales, as well as a theoretical approach of particle dispersion. Following, the detailed analysis of the transport equations of particle agitation and fluid-particle covariance are used to explain the effect of particle inertia. The apparent term of fluid acceleration - particle velocity covariance creates the need to devise a stochastic model for fluid acceleration "seen" by the particles as an extension of the corresponding one for the fluid, presented in Chapter 2. Finally, follows a detailed statistical analysis (one- and two-point statistics) of all the aspects of particle dispersion that extends to the spatial distribution and relative motion of particles.

3.1 Tchen-Hinze theory for turbulent gas-particle flows

Tchen (1947) and later Hinze (1972) devised a theory to link the fluid and particle turbulent spectra. In order to provide the fundamental elements of their theory, first one has to consider the particle motion Eq. (2.20), which in case of non-settling charge-free particles, is written as

$$\frac{\partial u'_{p,i}}{\partial t} = -\frac{u'_{p,i} - u'_{f@p,i}}{\tau_p} \quad (3.1)$$

The particle velocity can be expressed in term of Fourier series as

$$u'_{p,i}(t) = \int_0^{+\infty} \hat{u}'_{p,i}(\omega) \exp(i\omega t) d\omega$$

where $\hat{u}'_{p,i}$ is the Fourier transform of the particle velocity and $\omega = 2\pi f$ is the angular frequency. That implies that the time-derivative of the particle velocity is given by

$$\frac{\partial u'_{p,i}}{\partial t} = \int_0^{+\infty} i\omega \hat{u}'_{p,i}(\omega) \exp(i\omega t) d\omega .$$

Then particle equation (3.1) becomes:

$$i\omega \hat{u}'_{p,i}(\omega) = -\frac{\hat{u}'_{p,i}(\omega) - \hat{u}'_{f@p,i}(\omega)}{\tau_p}$$

¹Always seek the truth.

that eventually gives

$$\widehat{u}'_{p,i}(\omega) = \frac{1}{1 + \widehat{i\omega\tau_p}} \widehat{u}'_{f@p,i}(\omega) . \quad (3.2)$$

On the other hand, the Lagrangian turbulent particle spectrum $E_p(\omega)$ can be defined as

$$E_p(\omega) = \frac{1}{2} \widehat{u}'_{p,i}(\widehat{\omega}) \widehat{u}'_{p,i}^*(\widehat{\omega})$$

where $\widehat{u}'_{p,i}^*(\widehat{\omega})$ is the complex conjugate of Fourier particle velocity. Following, one can write

$$E_p(\omega) = \frac{1}{2} \frac{1}{[1 + \widehat{i\omega\tau_p}][1 + \widehat{i\omega\tau_p}]} \widehat{u}'_{f@p,i}(\widehat{\omega}) \widehat{u}'_{f@p,i}^*(\widehat{\omega}) .$$

So finally $E_p(\omega)$ is a function of $E_{f@p}(\omega)$ such that

$$E_p(\omega) = \frac{1}{1 + \omega^2 \tau_p^2} E_{f@p}(\omega) . \quad (3.3)$$

3.1.1 Single exponential model

To begin with, the average value of the square of particle velocity is defined as

$$\langle \mathbf{u}'_p{}^2 \rangle_p = \int_0^{+\infty} E_p(\omega) d\omega . \quad (3.4)$$

Here $\langle \rangle_p$ is rather the time average along the trajectory of a unique particle, however for a stationary homogeneous isotropic turbulence the property of ergodicity entails that it is equivalent with definition of Eq.(2.46). Assuming that the autocorrelation function of fluid velocity "seen" at the positions of the particles can be modeled by the following exponential function

$$R_{f@p}(\tau) = \exp \left[-\frac{\tau}{\tau_{f@p}^t} \right] \quad (3.5)$$

and the Lagrangian fluid turbulent spectrum is defined by

$$E_p(\omega) = \frac{\langle \mathbf{u}'_{f@p}{}^2 \rangle_p}{2\pi} \int_0^{+\infty} R_{f@p}(\tau) (-\widehat{i\omega\tau}) d\tau . \quad (3.6)$$

The integration² leads to

$$E_{f@p}(\omega) = \frac{1}{\pi} \frac{\tau_{f@p}^t}{1 + \omega^2 \tau_{f@p}^t} \langle \mathbf{u}'_{f@p}{}^2 \rangle_p .$$

Now the particle velocity spectrum takes the following form

$$E_p(\omega) = \frac{1}{\pi} \frac{1}{1 + \omega^2 \tau_{fp}^F} \frac{\tau_{f@p}^t}{1 + \tau_{f@p}^t} \frac{\langle \mathbf{u}'_{f@p}{}^2 \rangle_p}{\omega^2}$$

and the integration of this equation leads to

$$\int_0^{+\infty} E_p(\omega) d\omega = \frac{\tau_{f@p}^t}{\tau_{f@p}^t + \tau_{fp}^F} \langle \mathbf{u}'_{f@p}{}^2 \rangle_p .$$

Combining this result with Eq. (3.4) leads to the following relation:

$$\langle \mathbf{u}'_p{}^2 \rangle_p = \frac{\tau_{f@p}^t}{\tau_{f@p}^t + \tau_{fp}^F} \langle \mathbf{u}'_{f@p}{}^2 \rangle_p . \quad (3.7)$$

Fluid-particle velocity covariance

It is possible to perform the same analysis for the fluid-particle covariance. Indeed, the fluid-particle energy spectrum reads

$$E_{fp}(\omega) = \frac{1}{2} \left[\widehat{u}'_{p,i}(\tilde{\omega}) \widehat{u}'_{f@p,i}^*(\tilde{\omega}) + \widehat{u}'_{p,i}^*(\tilde{\omega}) \widehat{u}'_{f@p,i}(\tilde{\omega}) \right] .$$

Then via Eq. (3.2) one can rewrite it as

$$E_{fp}(\omega) = \frac{1}{1 + \omega^2 \tau_p^2} \widehat{u}'_{f@p,i}(\omega) \widehat{u}'_{f@p,i}^*(\omega) .$$

Finally, the fluid-particle covariance spectrum has the same form as Eq. (3.3). So by performing all integrations as shown previously and knowing that

$$\langle \mathbf{u}'_{f@p} \mathbf{u}'_p \rangle_p = \int_0^{+\infty} E_{fp}(\omega) d\omega$$

the following relation can be deduced

$$\langle \mathbf{u}'_{f@p} \mathbf{u}'_p \rangle_p = \frac{\tau_{f@p}^t}{\tau_{f@p}^t + \tau_{fp}^F} \langle \mathbf{u}'_{f@p}{}^2 \rangle_p . \quad (3.8)$$

Combining Eqs. (3.7) and (3.8) and using the definitions of Eqs. (2.43)-(2.45) allow for an a priori prediction of particle agitation that gives

$$2q_p^2 = q_{fp} = 2q_{f@p}^2 \frac{\tau_{f@p}^t}{\tau_{f@p}^t + \tau_{fp}^F} . \quad (3.9)$$

If we apply the Tchen hypothesis for small Stokes numbers $q_f^2 \simeq q_{f@p}^2$, then we can obtain the following equation as well

$$2q_p^2 = q_{fp} = 2q_f^2 \frac{\tau_f^t}{\tau_f^t + \tau_{fp}^F} . \quad (3.10)$$

Equations (3.9) and (3.10) constitute a theoretical framework hereafter called Tchen-Hinze theory (Hinze, 1972) and they are quite insightful in that they provide a prediction of particle agitation based on fluid agitation (actual or "seen" by the particles) and characteristic fluid/particle time scales. Figure 3.1 shows the comparison between particle agitation measured by DNS data and theoretical particle agitation provided by Eqs. (3.10) and (3.9). Numerical simulations are in agreement with theoretical predictions, while small discrepancies are observed for particles with small relaxation time scale. This is due to the assumption of an exponential autocorrelation function for the fluid velocity measured along the particle trajectory, $R_{f@p}$ that is too crude (see Fig. 3.8).

²The analytical integration of (3.6) with (3.5) is done using $\int_0^{+\infty} \exp(-\alpha|t|) \exp(-i\omega t) d\tau = \frac{2\alpha}{\alpha^2 + \omega^2}$

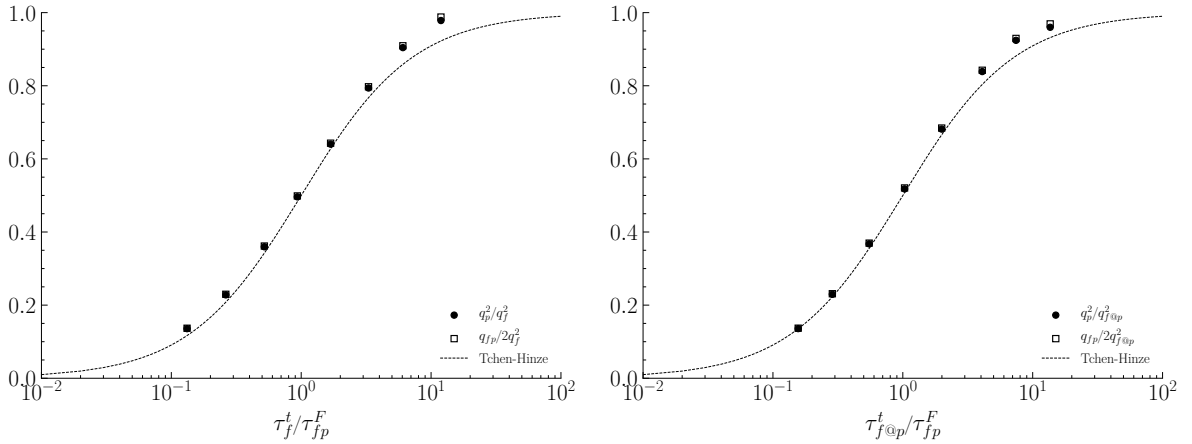


Figure 3.1: Particle agitation with regard to the inverse of the Stokes number. The dashed line corresponds to the Tchen-Hinze theory given by Eq. (3.10) (left) and its extension given by Eq. (3.9) (right). A good agreement of the DNS data with the two equations is observed.

It is evident that particle agitation as well as fluid-particle velocity covariance increases for light particles up to a saturation level which is effectively fluid agitation. That means that as particle inertia decreases, particles behave asymptotically as fluid elements, while as particle inertia increases, particles tend not to be affected by fluid agitation.

3.1.2 Dispersion coefficient of a particle cloud

Here, we try to describe the characteristics of the expansion of a particle cloud that is agitated by a homogeneous isotropic turbulent flow. The first studies of turbulent dispersion date back to 100 years and focused on the problem of turbulent diffusion of fluid elements. Taylor (1921) used a one-dimensional Lagrangian approach to describe the expansion of fluid elements emitted from a point source, while later Batchelor (1960) expanded this theory to the tri-dimensional case. Laviéville (1997) has provided a detailed theoretical analysis that describes how the theory of molecular diffusion gave birth to turbulent diffusion and then particle dispersion.

Turbulent diffusion

Before we proceed with the Tchen-Hinze theory of particle dispersion, it is important and helpful to set the fundamental elements of the theory of turbulent diffusion based on molecular diffusion. The displacement of a fluid element $\mathbf{l}_f(t)$ is defined as the integral of its velocity over time t .

$$\mathbf{l}_f(t) = \int_{t_0}^t \mathbf{u}_f(\mathbf{x}_f(t), t) d\tau \quad (3.11)$$

The variance of the displacement of fluid elements is directly linked to the Lagrangian autocorrelation function of the velocities of fluid elements as

$$\langle \mathbf{l}_f^2(t) \rangle = \int_{t_0}^t (t - \tau) \langle \mathbf{u}_f(\mathbf{x}_f(t), t) \mathbf{u}_f(\mathbf{x}_f(t - \tau), t - \tau) \rangle d\tau . \quad (3.12)$$

where $\langle . \rangle$ is here the ensemble average operator along the trajectories of fluid elements. Batchelor (1960) observes two asymptotic behaviors based on Eq. (3.12) which constitute the basis of the theory of turbulent diffusion:

i. If $t \rightarrow t_0$ then

$$\langle \mathbf{u}_f(\mathbf{x}_f(t), t) \mathbf{u}_f(\mathbf{x}_f(t - \tau), t - \tau) \rangle \simeq \langle \mathbf{u}_f^2 \rangle \Rightarrow \langle \mathbf{l}_f^2(t) \rangle \simeq \langle \mathbf{u}_f^2 \rangle t^2 \quad (3.13)$$

ii. If $t \rightarrow \infty$ then

$$\int_{t_0}^{\infty} \langle \mathbf{u}_f(\mathbf{x}_f(t), t) \mathbf{u}_f(\mathbf{x}_f(t - \tau), t - \tau) \rangle d\tau \simeq \langle \mathbf{u}_f^2 \rangle \tau_f^t \Rightarrow \langle \mathbf{l}_f^2(t) \rangle \simeq 2 \langle \mathbf{u}_f^2 \rangle \tau_f^t t \quad (3.14)$$

Following the analysis of molecular diffusion, Batchelor (1960) assumes that the correlation of the concentration of fluid elements $C_f(\mathbf{x}, t)$ and the velocity fluctuation follows a Fick-type law in the form

$$\langle C_f u'_{f,i} \rangle = -D_f^t \frac{\partial C_f}{\partial x_i} \quad (3.15)$$

where D_f^t is the turbulent diffusion coefficient. Considering the contribution of molecular diffusion negligible, one can write an Eulerian transport equation of the average concentration as

$$\frac{\partial}{\partial t} \langle C_f(\mathbf{x}, t) \rangle = \frac{\partial}{\partial x_i} \left[D_f^t \frac{\partial}{\partial x_i} \langle C_f(\mathbf{x}, t) \rangle \right]$$

which has the form of the transport equation of molecular diffusion. However, the transitional probability $p(\mathbf{x}, t | \mathbf{x}_0, t_0)$ defined as the probability of a fluid element \mathbf{x}_f in position \mathbf{x}_0 at time t_0 to be displaced in position \mathbf{x} at time instant t , satisfies the same equation as $\langle C_f(\mathbf{x}, t) \rangle$ since $\langle C_f(\mathbf{x}, t) \rangle = \int p(\mathbf{x}, t | \mathbf{x}_0, t_0) \langle C_f(\mathbf{x}_0, t_0) \rangle d\mathbf{x}_0$, thus

$$\begin{aligned} \frac{\partial}{\partial t} p &= \frac{\partial}{\partial x_i} \left(D_f^t \frac{\partial}{\partial x_i} p \right) \\ p(\mathbf{x}, t_0 | \mathbf{x}_0, t_0) &= \delta(\mathbf{x} - \mathbf{x}_0) \end{aligned} \quad (3.16)$$

where $\delta(\mathbf{x} - \mathbf{x}_0)$ is a Dirac function defined as

$$\delta(\mathbf{x} - \mathbf{x}_0) = \begin{cases} 1, & \text{if } \mathbf{x} = \mathbf{x}_0 \\ 0, & \text{otherwise.} \end{cases} \quad (3.17)$$

If D_f^t is considered to be constant, the solution of Eq. (3.16) follows a normal probability law since it can be written as

$$p(\mathbf{x}, t | \mathbf{x}_0, t_0) = [4\pi(t - t_0)]^{-3/2} \exp \left[-\frac{(\mathbf{x} - \mathbf{x}_0)^2}{4D_f^t(t - t_0)} \right] \quad (3.18)$$

that allows to rewrite the displacement variance as

$$\langle \mathbf{l}_f^2(t) \rangle = \int (\mathbf{x} - \mathbf{x}_0)^2 p(\mathbf{x}, t | \mathbf{x}_0, t_0) d\mathbf{x} = 6D_f^t(t - t_0) \quad (3.19)$$

Equations (3.19) and (3.14) allow to deduced the turbulent diffusion coefficient as

$$D_f^t = \frac{1}{6} \frac{d}{dt} \langle \mathbf{l}_f^2(t) \rangle = \frac{2}{3} q_f^2 \tau_f^t \quad (3.20)$$

Particle dispersion coefficient

Gouesbet *et al.* (1984), Hinze (1972), Tchen (1947) provided a general framework for the study of dispersion of particles transported by stationary homogeneous isotropic turbulence by generalizing the theoretical results of Batchelor (1960) for turbulent diffusion. The particle displacement vector $\mathbf{l}_p(t)$ is defined similarly to Eq. (3.11) as

$$\mathbf{l}_p(t) = \int_0^t \mathbf{u}_p(\tau) d\tau . \quad (3.21)$$

If we suppose that the components of $\mathbf{l}_p(t)$ exhibit a normal probability density, which is the hypothesis made for fluid elements by Batchelor (1960), we can finally derive particle dispersion coefficient D_p^t in analogy with D_f^t as

$$D_p^t = \frac{1}{6} \frac{d}{dt} \langle \mathbf{l}_p^2(t) \rangle = \frac{2}{3} q_p^2 \tau_p^t \quad (3.22)$$

where the Lagrangian particle integral time scale τ_p^t appears, which is defined by Eq. (2.49). However, there is a link between turbulent diffusion/particle dispersion and the fluid/particle turbulent spectrum, respectively as the former can be obtained from the Fourier transforms of the derivative of the variance of the respective displacements, so for both D_f^t and D_p^t we have

$$D_{f,p}^t(t) = \int_0^t E_{f,p}(\omega) \frac{\sin(\omega t)}{\omega} d\omega$$

which means that for $t \rightarrow \infty$ particles and fluid elements exhibit the same dispersion and diffusion, respectively. Hence

$$\lim_{\tau \rightarrow \infty} D_p^t = \lim_{\tau \rightarrow \infty} D_f^t = \frac{\pi}{2} E_p(0) = \frac{\pi}{2} E_f(0)$$

Moreover, combining Eqs. (3.20) and (3.22), one can deduce the following relation for the Lagrangian characteristic time scales of fluid and particles

$$\tau_p^t = \frac{q_f^2}{q_p^2} \tau_f^t .$$

This is a very meaningful result, as it states that for increasing particle inertia, the decrease of particle agitation entails an equivalent increase of the Lagrangian integral particle time scale, which is a measure of particle "memory" via inertia. Therefore, heavy particles exhibit low levels of agitation but high memory and conversely, lighter particles high levels of agitation and low memory effect. Now if we consider an exponential form for the Lagrangian autocorrelation function of the fluid (see Sect. 3.1), then using Eq. (3.10) we obtain

$$\tau_p^t = \tau_f^t + \tau_{fp}^F . \quad (3.23)$$

Based on Eq. (3.1), Deutsch (1992) deduces an equivalent relation for the particle dispersion coefficient based on the Lagrangian time scale of the fluid "seen" at the particle positions as

$$D_p^t = \frac{2}{3} q_{f@p}^2 \tau_{f@p}^t \quad (3.24)$$

that he extended to study the anisotropy of the particle dispersion coefficient in the parallel and perpendicular directions of crossing particle trajectories, however this is beyond the scope of the work conducted in this PhD thesis. In analogy with Eq. (3.23), using Eq. (3.9) one can obtain

$$\tau_p^t = \tau_{f@p}^t + \tau_{fp}^F . \quad (3.25)$$

3.2 Statistical analysis of particle dispersion

In this section, we focus on analyzing by means of suitable statistics the dispersion of inertial charge-free particles transported by a stationary homogeneous isotropic turbulent flow. Although this type of flows have been already studied thoroughly in the past, such an analysis is deemed useful not only to get familiar with the different notions presented but also to establish the charge-free case study as a reference when electrostatic forces come into play in Chapter 5.

3.2.1 Kinetic energy transfer from turbulence to particles

In turbulent particle-laden gas flows, particles move due to the hydrodynamic drag forces that are exerted on them from the fluid turbulent velocity field. More specifically, there are two mechanisms that dictate the particle motion: a particle accelerates due to the drag force while at the same time its kinetic energy is dissipated due to viscosity via the same force.

Particle agitation

In the pdf framework for gas-particle flows presented by Simonin (2000) one can obtain the following transport equation for the particle agitation

$$\frac{\partial}{\partial t} q_p^2 = \frac{1}{m_p} \langle \mathbf{F}'_p \mathbf{u}'_p \rangle_p \quad (3.26)$$

while for $\mathbf{F}_g = \mathbf{F}_e = 0$ the total force exerted on a particle is

$$\mathbf{F}'_p = -m_p \frac{\mathbf{u}'_p - \mathbf{u}'_{f@p}}{\tau_p} . \quad (3.27)$$

Thus, under a linear approximation for the drag force, which implies τ_p defined in Eq. (2.22) is constant, one can write

$$\frac{\partial}{\partial t} q_p^2 = \frac{q_{fp}}{\tau_{fp}^F} - \frac{2q_p^2}{\tau_{fp}^F} . \quad (3.28)$$

The left hand side of Eq.(3.28) represents the rate of specific kinetic energy of the particles and the right hand side the specific power associated with the drag force. Essentially, the specific drag force power can be decomposed in two parts: the first term corresponds to the viscous dissipation of kinetic energy due to drag force (hence negative), and the second term to the production of particle kinetic energy (hence positive). The evolution of all three terms of Eq. (3.28) is shown by Fig. 3.2 and the balance of the equation is verified in the transient regime for the charge free case corresponding to a Stokes number of $\tau_{fp}^F/\tau_{f@p}^t = 1.82$.

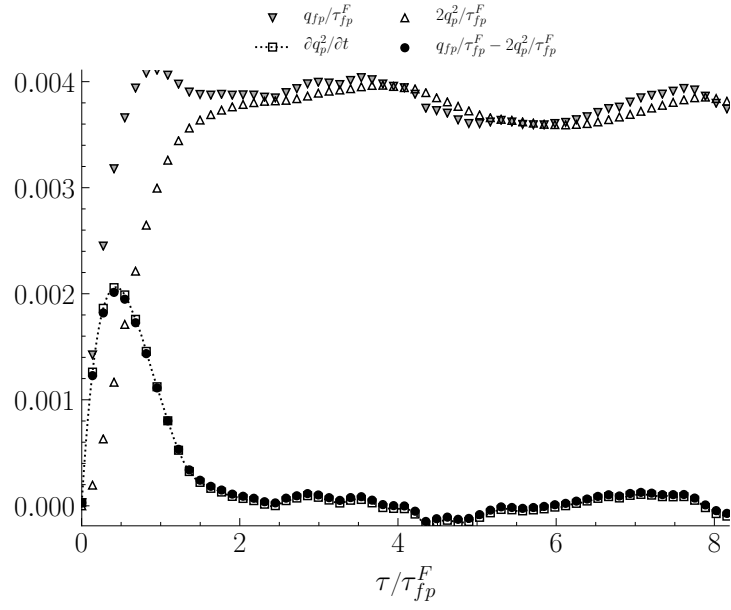


Figure 3.2: Terms of Eq. (3.28) in transient regime for $\tau_{fp}^F/\tau_{fp}^t = 1.82$ in the charge-free case. A very good agreement with the theoretical equation is observed.

In case of stationary flow, $\partial q_p^2/\partial t = 0$ therefore Eq. (3.28) becomes

$$q_p^2 = \frac{1}{2}q_{fp} \quad (3.29)$$

which shows the direct link of particle agitation q_p^2 to the fluid-particle velocity covariance q_{fp} as verified by Fig. 3.3.

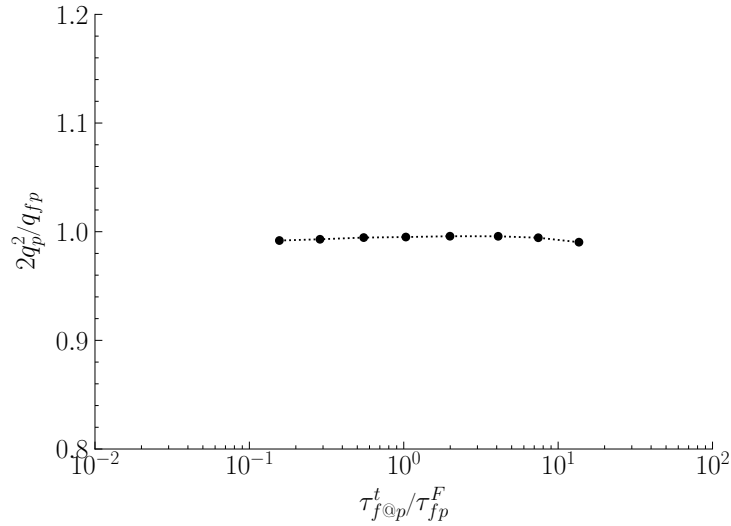


Figure 3.3: Verification of Eq. (3.29) with regard to particle Stokes number in the charge-free case. A very good agreement with the theoretical equation is observed.

Fluid-particle velocity covariance

Since it has been established that fluid-particle velocity covariance drives particle agitation, in order to better understand the latter, it would be useful to have an equation that defines the time evolution of the former. The transport equation of the fluid-particle velocity covariance can be derived from the joint-fluid-particle pdf equation in the kinetic theory framework (Simonin, 2000) that gives

$$\frac{\partial}{\partial t} q_p^2 = \langle \mathbf{a}'_{f@p} \mathbf{u}'_p \rangle_p + \frac{1}{m_p} \langle \mathbf{F}'_p \mathbf{u}'_{f@p} \rangle_p . \quad (3.30)$$

Using (3.27) under a linear approximation for the drag force, which implies $\tau_p = \text{const.}$, one can write

$$\frac{\partial}{\partial t} q_{fp} = \langle \mathbf{a}'_{f@p} \mathbf{u}'_p \rangle_p + \frac{2q_{f@p}^2}{\tau_{fp}^F} - \frac{q_{fp}}{\tau_{fp}^F} \quad (3.31)$$

The first term of the right hand side is the fluid acceleration - particle velocity covariance $\langle \mathbf{a}'_{f@p} \mathbf{u}'_p \rangle_p$ which in homogeneous incompressible flow, in analogy with term of turbulence dissipation $\langle \mathbf{a}'_f \mathbf{u}'_f \rangle_f$ seen in Subsect. 2.2.3, acts as a dissipative term, in the sense that it is a destruction term for fluid-particle correlation. It is written in terms of the fluid acceleration measured at the particle positions $\mathbf{a}'_{f@p}(\mathbf{x}_p, t) = \partial \mathbf{u}'_{f@p} / \partial t$. The second and third term are related to the specific power associated with the drag force which can be decomposed in two parts: the second term corresponds to the fluid kinetic energy "seen" by the particles (hence positive), and the third term to the decorrelation of fluid-particle velocity (hence negative). The evolution of all four terms of Eq. (3.31) is shown by Fig. 3.4 and the validity of the equation is verified in the transient regime for the charge-free case corresponding to a Stokes number of $\tau_{fp}^F / \tau_{f@p}^t = 1.82$.

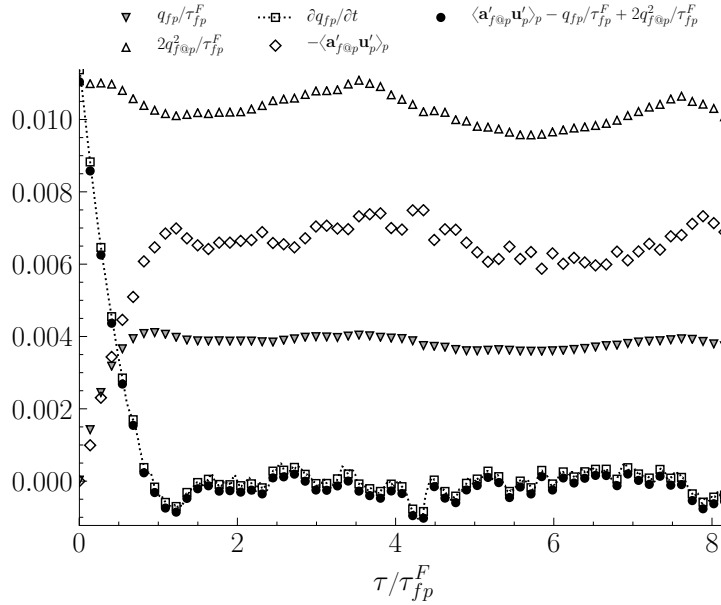
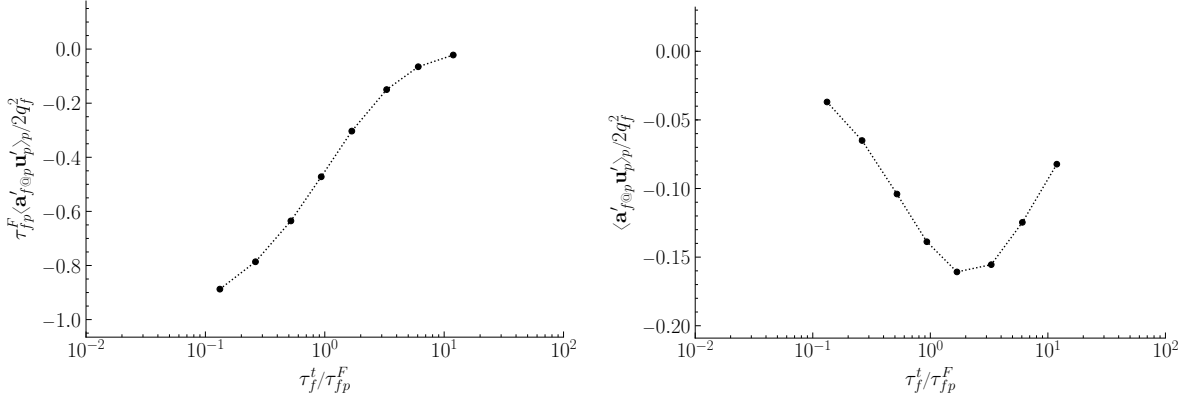


Figure 3.4: Terms of Eq. (3.28) in transient regime for $\tau_{fp}^F / \tau_{f@p}^t = 1.82$. A very good agreement with the theoretical equation is observed.

In case of stationary flow $\partial q_{fp} / \partial t = 0$, therefore Eq. (3.28) becomes

$$q_{fp} = \tau_{fp}^F \langle \mathbf{a}'_{f@p} \mathbf{u}'_p \rangle_p + 2q_{f@p}^2 . \quad (3.32)$$

The second term of the right hand side of Eq. (3.32) is the fluid agitation measured at particle positions (see Fig. 2.8). To acquire a better understanding of the physical meaning of the first term $\tau_{fp}^F \langle \mathbf{a}'_{f@p} \mathbf{u}'_p \rangle_p$, one has to examine how it behaves with regard to particle inertia. Figure 3.5a shows that it decreases to zero (in terms of absolute value) as particle inertia decreases $\tau_f^t / \tau_{fp}^F \rightarrow \infty$. However, this term contains both the effect of turbulent dissipation via $\langle \mathbf{a}'_{f@p} \mathbf{u}'_p \rangle_p$ and of particle inertia via the drag term τ_{fp}^F , so it is difficult to understand the underlying mechanism. Indeed, Fig. 3.5b shows that the effect of particle inertia on q_{fp} is predominant.



(a) First term of left-hand side of Eq. (3.32). (b) Fluid acceleration - particle velocity covariance.

Figure 3.5: Effect of particle inertia on fluid acceleration - particle velocity covariance $\langle \mathbf{a}'_{f@p} \mathbf{u}'_p \rangle_p$ for two different normalizations in the charge-free case.

In fact, term $\langle \mathbf{a}'_{f@p} \mathbf{u}'_p \rangle_p$ in homogeneous incompressible turbulent flow, acts as a destruction term on the correlation of fluid-particle velocity that eventually results in a decrease of particle agitation (hence negative). Heavier particles are subject to lower levels of fluid turbulent dissipation, so the effect of this term on q_{fp} is negligible as they do not react promptly to the local modifications of the turbulent velocity field due to inertia. The term becomes important for particles of moderate Stokes numbers and then again becomes weak for very light particles. To better understand this effect of turbulent dissipation, one could introduce a new characteristic time scale τ_{fp}^a as

$$\tau_{fp}^a = -\frac{q_{fp}}{\langle \mathbf{a}'_{f@p} \mathbf{u}'_p \rangle_p}$$

that denotes the destruction rate of fluid-particle covariance q_{fp} by the fluid acceleration - particle velocity covariance $\langle \mathbf{a}'_{f@p} \mathbf{u}'_p \rangle_p$. This time scale is identical to $\tau_{f@p}^t$ for the Langevin model of fluid acceleration that is presented in Subsect. 3.2.2. In Fig. 3.6, it is evident that this time scale increases for decreasing particle inertia, which essentially means that q_{fp} dissipates in lower rates, resulting to its increase.

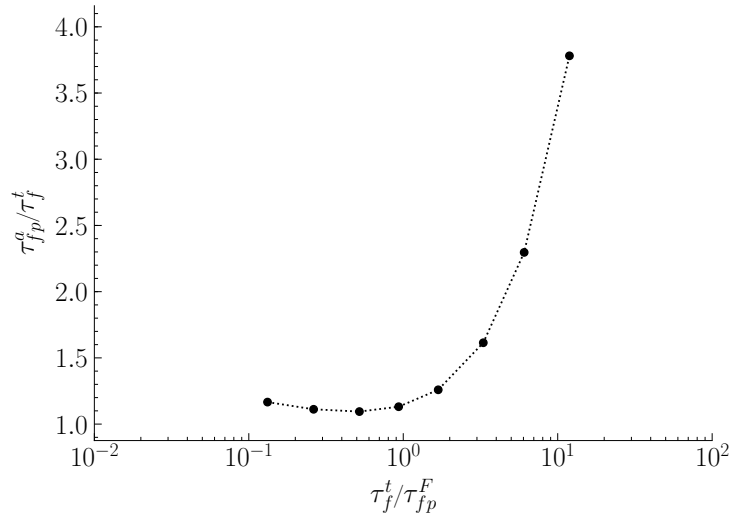


Figure 3.6: Time scale of turbulent destruction of fluid-particle correlation with regard to particle inertia in the charge-free case.

At this point, it would be interesting to examine the effect of inertia on the variance of fluid acceleration "seen" at the particle positions $\langle \mathbf{a}'_{f@p}{}^2 \rangle_p$. Figure 3.7 shows that for decreasing inertia there is a slight increase of $\langle \mathbf{a}'_{f@p}{}^2 \rangle_p$ up to moderate particle inertia $\tau_f^t/\tau_{fp}^F \sim 1$ and then a significant decrease for lighter particles $\tau_f^t/\tau_{fp}^F \rightarrow 0$. This essentially means that smaller particles "see" a fluid acceleration that is smaller than the average fluid acceleration $\langle \mathbf{a}'_f{}^2 \rangle_f = \langle a'_{f,i} a'_{f,i} \rangle_f / 3$ due to the fact that they interact more in average with less energetic turbulent structures of the flow due to preferential concentration (low-vorticity zones). This explains why it takes more time for turbulent dissipation to decorrelate fluid-particle velocities for lighter particles.

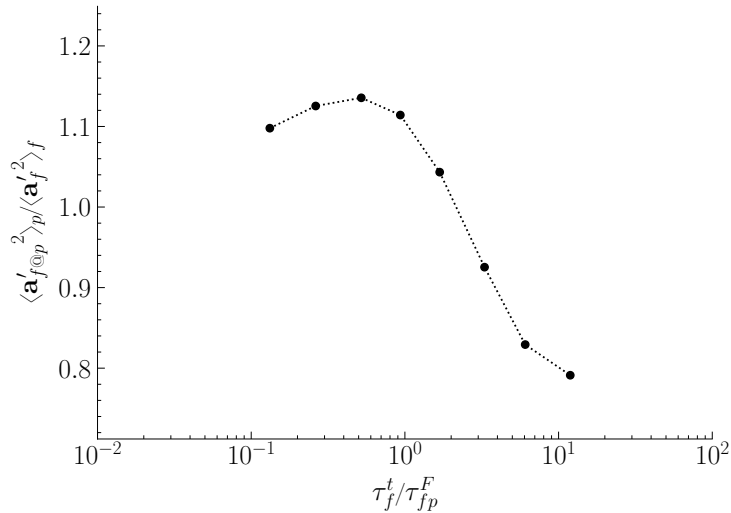


Figure 3.7: Fluid acceleration at particle position $\langle \mathbf{a}'_{f@p}{}^2 \rangle_p$ with regard to particle inertia.

3.2.2 Stochastic models of fluid acceleration - particle velocity covariance

Stochastic Lagrangian models for the fluid acceleration have been addressed in Chapter 2 and at this point we are interested in such models for the particle motion.

Langevin (single exponential) model

In analogy to the stochastic Lagrangian model for the fluid acceleration presented in Subsect. 2.2.3, one can extend it for the fluid acceleration measured along the particle trajectories. At a first order approximation, Simonin *et al.* (1993) adjusted the Langevin model of Eq. (2.37) to the following

$$\delta u'_{f@p,i} = -D u'_{f@p,i} \delta t + B \delta W_i . \quad (3.33)$$

where $\delta \mathbf{u}'_{f@p} = \mathbf{u}'_{f@p}(t + \delta t) - \mathbf{u}'_{f@p}(t)$ is the infinitesimal increment of the fluctuating component of the fluid velocity "seen" at the particle positions, which is given directly by

$$\delta u'_{f@p,i} = a'_{f@p,i} \delta t$$

Of course, these equations are coupled with the equation of particle trajectory Eq. (3.1). The equations of the variance of particle velocity $\langle \mathbf{u}'_p{}^2 \rangle_p = \langle u'_{p,i} u'_{p,i} \rangle_p / 3$, the fluid-particle velocity covariance $\langle \mathbf{u}'_p \mathbf{u}'_{f@p} \rangle_p = \langle u'_{p,i} u'_{f@p,i} \rangle_p / 3$ and the velocity-acceleration correlation $\langle \mathbf{u}'_p \mathbf{a}'_{f@p} \rangle_p = \langle u'_{p,i} a'_{f@p,i} \rangle_p / 3$ take the following forms

$$\begin{aligned} \frac{\partial \langle \mathbf{u}'_p{}^2 \rangle_p}{\partial t} &= \frac{2}{\tau_{fp}^F} \left[\langle \mathbf{u}'_p \mathbf{u}'_{f@p} \rangle_p - \langle \mathbf{u}'_p{}^2 \rangle_p \right] \\ \frac{\partial \langle \mathbf{u}'_p \mathbf{u}'_{f@p} \rangle_p}{\partial t} &= \langle \mathbf{u}'_p \mathbf{a}'_{f@p} \rangle_p - \frac{1}{\tau_{fp}^F} \left[\langle \mathbf{u}'_p \mathbf{u}'_{f@p} \rangle_p - \langle \mathbf{u}'_{f@p}{}^2 \rangle_p \right] \\ \frac{\partial \langle \mathbf{u}'_p \mathbf{a}'_{f@p} \rangle_p}{\partial t} &= -\frac{1}{\tau_{fp}^F} \left[\langle \mathbf{u}'_p \mathbf{a}'_{f@p} \rangle_p - \langle \mathbf{u}'_{f@p} \mathbf{a}'_{f@p} \rangle_p \right] - D \langle \mathbf{u}'_p \mathbf{u}'_{f@p} \rangle_p \end{aligned}$$

where $\langle \mathbf{u}'_{f@p} \mathbf{a}'_{f@p} \rangle_p = 0$. For stationary flows, these equations give the relations of Tchen equilibrium in the form

$$\begin{aligned} \langle \mathbf{u}'_p{}^2 \rangle_p &= \langle \mathbf{u}'_p \mathbf{u}'_{f@p} \rangle_p \\ \langle \mathbf{u}'_p \mathbf{u}'_{f@p} \rangle_p &= \langle \mathbf{u}'_{f@p}{}^2 \rangle_p + \tau_{fp}^F \langle \mathbf{u}'_p \mathbf{a}'_{f@p} \rangle_p \\ \langle \mathbf{u}'_p \mathbf{a}'_{f@p} \rangle_p &= -\tau_{fp}^F D \langle \mathbf{u}'_p \mathbf{u}'_{f@p} \rangle_p . \end{aligned}$$

Combining the last two equations, let the new form for the fluid-particle velocity covariance be

$$\langle \mathbf{u}'_p \mathbf{u}'_{f@p} \rangle_p = \langle \mathbf{u}'_{f@p}{}^2 \rangle_p \left[1 + \tau_{fp}^F D \right]^{-1} .$$

Therefore, inspired from the Langevin stochastic model of the fluid velocity (see Subsect. 2.2.3), using the expression

$$D = \frac{\langle \mathbf{a}'_{f@p}{}^2 \rangle_p}{\langle \mathbf{u}'_{f@p}{}^2 \rangle_p} \quad (3.34)$$

the Lagrangian autocorrelation function of the fluid velocity "seen" at the particle positions can be deduced from Eq. (3.33) as an exponential function,

$$R_{f@p}(\tau) = \exp\left(-\frac{\tau}{\tau_{f@p}^t}\right)$$

where the Lagrangian integral time scale $\tau_{f@p}^t$ can be written as

$$\tau_{f@p}^t = \frac{1}{\tau_{fp}^F} \frac{\langle \mathbf{u}'_{f@p}{}^2 \rangle_p}{\langle \mathbf{a}'_{f@p}{}^2 \rangle_p} .$$

Thus, we can write the fluid acceleration - particle velocity covariance in the form

$$\langle \mathbf{u}'_p \mathbf{a}'_{f@p} \rangle_p = -\frac{q_{fp}}{\tau_{f@p}^t} \quad (3.35)$$

and the fluid-particle velocity covariance in the form

$$\langle \mathbf{u}'_p \mathbf{u}'_{f@p} \rangle_p = \langle \mathbf{u}'_{f@p}{}^2 \rangle_p \frac{\tau_{f@p}^t}{\tau_{f@p}^t + \tau_{fp}^F} . \quad (3.36)$$

Hence, we find the classic theoretical relation of Tchen-Hinze theory Eq. (3.9) for an exponential function of the fluid turbulence "seen" at the particle positions. This is a result that has been also found in literature, such as the work of Zaichik *et al.* (2003), which essentially means that the time scale of turbulent dissipation of q_{fp} by $\langle \mathbf{a}'_{f@p} \mathbf{u}'_p \rangle_p$ is chosen to be equal to the Lagrangian integral time scale of the fluid "seen" at the particle positions, hence $\tau_{fp}^a \simeq \tau_{f@p}^t$.

Double exponential model

In analogy with Subsect. 2.2.3, we simply assume that we can apply the stochastic Lagrangian model for the fluid velocity derivative measured along the trajectory of the particles as it is.

$$\delta u'_{f@p,i} = -C a'_{f@p,i} \delta t - D u'_{f@p,i} \delta t + B \delta W_i .$$

Of course, these equations are coupled with the equation of particle trajectory Eq. (3.1). The equations of the variance of particle velocity $\langle \mathbf{u}'_p{}^2 \rangle_p$, the fluid-particle velocity covariance $\langle \mathbf{u}'_p \mathbf{u}'_{f@p} \rangle_p$ and the velocity-acceleration correlation $\langle \mathbf{u}'_p \mathbf{a}'_{f@p} \rangle_p$ take the following forms

$$\begin{aligned} \frac{\partial \langle \mathbf{u}'_p{}^2 \rangle_p}{\partial t} &= \frac{2}{\tau_{fp}^F} \left[\langle \mathbf{u}'_p \mathbf{u}'_{f@p} \rangle_p - \langle \mathbf{u}'_p{}^2 \rangle_p \right] \\ \frac{\partial \langle \mathbf{u}'_p \mathbf{u}'_{f@p} \rangle_p}{\partial t} &= \langle \mathbf{u}'_p \mathbf{a}'_{f@p} \rangle_p - \frac{1}{\tau_{fp}^F} \left[\langle \mathbf{u}'_p \mathbf{u}'_{f@p} \rangle_p - \langle \mathbf{u}'_{f@p}{}^2 \rangle_p \right] \\ \frac{\partial \langle \mathbf{u}'_p \mathbf{a}'_{f@p} \rangle_p}{\partial t} &= -\frac{1}{\tau_{fp}^F} \left[\langle \mathbf{u}'_p \mathbf{a}'_{f@p} \rangle_p - \langle \mathbf{u}'_{f@p} \mathbf{a}'_{f@p} \rangle_p \right] - C \langle \mathbf{u}'_p \mathbf{a}'_{f@p} \rangle_p - D \langle \mathbf{u}'_p \mathbf{u}'_{f@p} \rangle_p . \end{aligned}$$

For stationary flows, these equations give the relations of Tchen equilibrium in the form

$$\begin{aligned} \langle \mathbf{u}'_p{}^2 \rangle_p &= \langle \mathbf{u}'_p \mathbf{u}'_{f@p} \rangle_p \\ \langle \mathbf{u}'_p \mathbf{u}'_{f@p} \rangle_p &= \langle \mathbf{u}'_{f@p}{}^2 \rangle_p + \tau_{fp}^F \langle \mathbf{u}'_p \mathbf{a}'_{f@p} \rangle_p \\ \langle \mathbf{u}'_p \mathbf{a}'_{f@p} \rangle_p &= -\langle \mathbf{u}'_p \mathbf{u}'_{f@p} \rangle_p D \tau_{fp}^F \left(1 + C \tau_{fp}^F \right)^{-1} . \end{aligned}$$

The Lagrangian autocorrelation function of the fluid "seen" at the particle positions can be written using a double exponential function (see Fig. 3.8) as

$$R_{f@p}(\tau) = \frac{\exp\left(-\frac{\tau}{\tau_\infty}\right) - \frac{\tau_0}{\tau_\infty} \exp\left(-\frac{\tau}{\tau_\infty}\right)}{1 - \frac{\tau_0}{\tau_\infty}} \quad (3.37)$$

with

$$\begin{aligned}\tau_\infty &= \frac{1}{2}\tau_{f@p}^t \left[1 + \left(1 - 4\frac{\tau_{a@p}\tau_\epsilon}{\tau_{f@p}^t} \right)^{1/2} \right] \\ \tau_0 &= \frac{1}{2}\tau_{f@p}^t \left[1 - \left(1 - 4\frac{\tau_{a@p}\tau_\epsilon}{\tau_{f@p}^t} \right)^{1/2} \right]\end{aligned}$$

where and τ_ϵ is the characteristic time scale of turbulent energy dissipation defined in Eq. (2.41) and $\tau_{a@p}$ is the characteristic time scale of fluid turbulent acceleration "seen" at the particle positions defined as

$$\tau_{a@p}\tau_\epsilon = \frac{\langle \mathbf{u}'_{f@p}{}^2 \rangle_p}{\langle \mathbf{a}'_{f@p}{}^2 \rangle_p}. \quad (3.38)$$

The characteristic times which appear in Eq. (3.37) can be written as

$$\tau_{f@p}^t = \tau_\infty + \tau_0$$

and

$$\tau_{a@p} = \frac{\tau_\infty\tau_0}{\tau_\epsilon}.$$

By definition of characteristic times, the coefficients of the stochastic model can be written under the following form

$$\begin{aligned}D &= \frac{1}{\tau_{a@p}\tau_\epsilon} = \frac{1}{\tau_\infty\tau_0} \\ C &= \frac{\tau_{f@p}^t}{\tau_{a@p}\tau_\epsilon} = \frac{\tau_\infty + \tau_0}{\tau_\infty\tau_0} = \frac{1}{\tau_\infty} + \frac{1}{\tau_0}.\end{aligned}$$

Let the new form for the fluid-particle velocity covariance be

$$\langle \mathbf{u}'_p \mathbf{u}'_{f@p} \rangle_p = \langle \mathbf{u}'_{f@p}{}^2 \rangle_p \left[1 + \tau_{fp}^F{}^2 D \left(1 + C\tau_{fp}^F \right)^{-1} \right]^{-1}.$$

Therefore, using the expressions

$$D = \frac{\langle \mathbf{a}'_{f@p}{}^2 \rangle_p}{\langle \mathbf{u}'_{f@p}{}^2 \rangle_p} = \frac{1}{\tau_{a@p}\tau_\epsilon} \quad (3.39a)$$

$$C = \tau_{f@p}^t D \quad (3.39b)$$

we can write the fluid acceleration - particle velocity covariance in the form

$$\langle \mathbf{u}'_p \mathbf{a}'_{f@p} \rangle_p = -q_{fp} \frac{\tau_{fp}^F}{\tau_{a@p}\tau_\epsilon + \tau_{f@p}^t \tau_{fp}^F} \quad (3.40)$$

and the fluid-particle velocity covariance in the form

$$\langle \mathbf{u}'_p \mathbf{u}'_{f@p} \rangle_p = \langle \mathbf{u}'_{f@p}{}^2 \rangle_p \left[1 + \frac{\tau_{fp}^F{}^2}{\tau_{a@p}\tau_\epsilon + \tau_{f@p}^t \tau_{fp}^F} \right]. \quad (3.41)$$

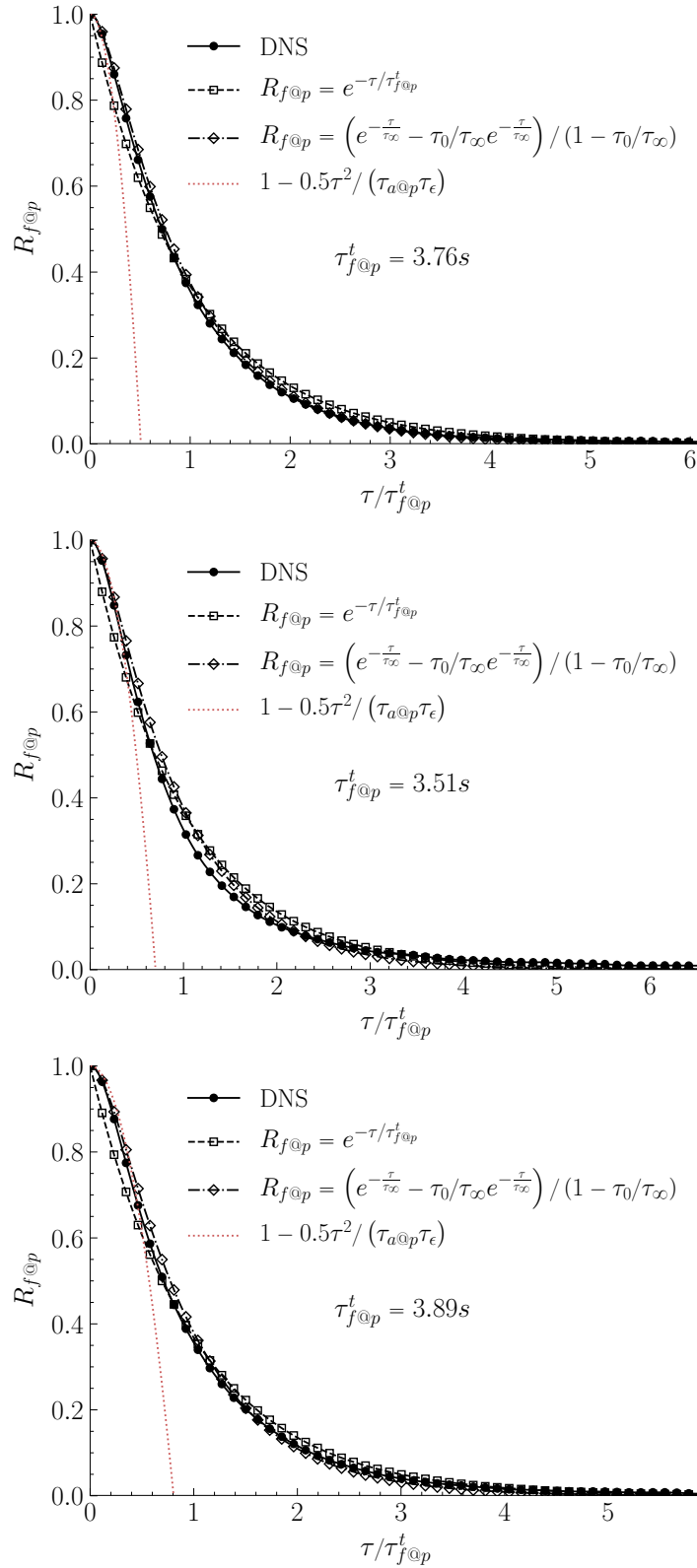


Figure 3.8: Autocorrelation functions of fluid velocity "seen" at the particle positions. Integration gives the Lagrangian fluid integral time-scale $\tau_{f@p}^t$. A good agreement with the exponential models is observed. The red dotted line represents the oscillator function.

By definition, $\tau_{f@p}^t$ and τ_ϵ are of the same order of magnitude and bigger than $\tau_{a@p}$ for high Reynolds turbulent flows, $\tau_{a@p} \ll \tau_\epsilon$. For high Stokes numbers we have $\tau_{fp}^F \gg \tau_{f@p}^t > \tau_{a@p}$, thus Eq. (3.41) can be written in the following form

$$\langle \mathbf{u}'_p \mathbf{u}'_{f@p} \rangle_p = \langle \mathbf{u}'_{f@p}{}^2 \rangle_p \left(1 + \frac{\tau_{fp}^F}{\tau_{f@p}^t} \right)^{-1}.$$

Hence, we find the classic theoretical relation of Tchen-Hinze theory Eq. (3.9) for an exponential function of the fluid turbulence "seen" at the particle positions. In analogy with what has been discussed in Subsect. 2.2.3, we need to determine a characteristic time scale of the fluid "seen" $\tau_{f@p}^t$, and the product of two time scales, $\tau_{a@p}\tau_\epsilon$. These two parameters of the model can be estimated directly from the autocorrelation function of the fluid measured along particle trajectories (see Fig. 3.8). Equation (2.48) gives $\tau_{f@p}^t$, while for $\tau_{a@p}\tau_\epsilon$, except for Eq. (3.39a) we can also use:

$$\tau_{a@p}\tau_\epsilon = - \left[\lim_{\tau \rightarrow 0} \frac{d^2}{d\tau^2} R_{f@p}(\tau) \right]^{-1} \quad (3.42)$$

supposing that the short-term response of $R_{f@p}$ can be represented by the oscillator function

$$\lim_{\tau \rightarrow 0} R_{f@p} = \lim_{\tau \rightarrow 0} \left(1 - \frac{1}{2} \frac{\tau^2}{\tau_{a@p}\tau_\epsilon} \right).$$

Table 3.1 shows the estimations for $\tau_{a@p}\tau_\epsilon$ of the two aforementioned models and their relation with τ_{fp}^F and $\tau_{f@p}^t$. Once these characteristic time scales have been calculated, one can compare the aforementioned models of the fluid acceleration - particle velocity covariance with DNS data.

Table 3.1: Characteristic time scales of the fluid "seen" at the particle position for various levels of particle inertia and two different models

class	$\tau_{a@p}\tau_\epsilon$	$\tau_{a@p}\tau_\epsilon$	τ_{fp}^F	$\tau_{f@p}^t$
	$- \left[\lim_{\tau \rightarrow 0} \frac{d^2}{d\tau^2} R_{f@p}(\tau) \right]^{-1}$	$\langle \mathbf{u}'_{f@p}{}^2 \rangle_p / \langle \mathbf{a}'_{f@p}{}^2 \rangle_p$		
1	1.82	1.86	24.03	3.76
2	1.75	1.81	12.09	3.47
3	1.21	1.76	6.11	3.36
4	3.02	1.76	3.40	3.51
5	2.16	1.84	1.89	3.76
6	1.19	2.09	0.96	3.94
7	4.92	2.42	0.52	3.89
8	2.94	2.64	0.27	3.64

Figure 3.9 shows the predictions of Eq. (3.35) and of Eq. (3.40) (for both models of $\tau_{f@p}\tau_\epsilon$). It seems that the former is not accurate for light particles which confirms the observation made in Fig. 3.1 that the classic Tchen-Hinze Eq. (3.9) slightly underestimates the fluid-particle agitation for light particles. However, the model of Eq. (3.40) seems to predict the DNS measurements rather accurately, especially using Eq. (3.39a) instead of Eq. (3.42) for $\tau_{a@p}\tau_\epsilon$. The discrepancies for the latter, may also come from the numerical calculation of this limit which is sensitive to the selection of the short-term part of the $R_{f@p}(\tau)$ time series, to which we fit a quadratic equation.

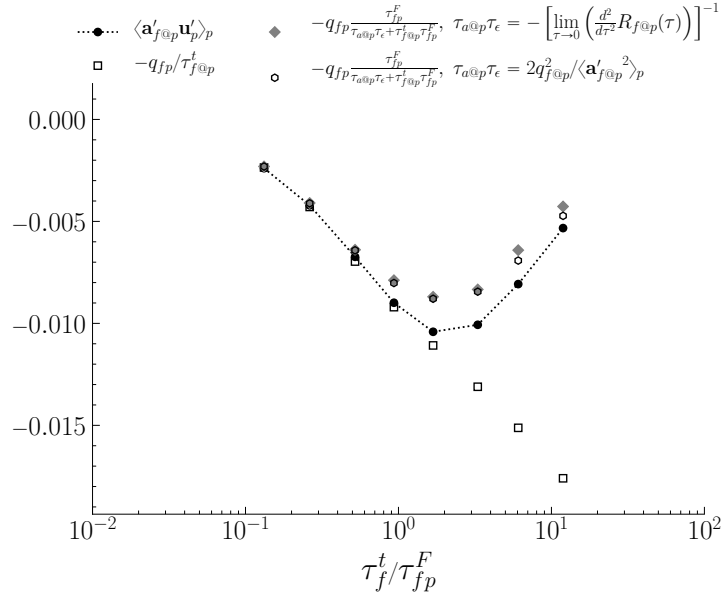


Figure 3.9: Comparison between DNS results (\bullet) and the predictions of the Langevin model (\square) as well as of the introduced stochastic model (\blacklozenge, \circ) of $\langle \mathbf{a}'_{f@p} \mathbf{u}'_p \rangle_p$ with regard to particle Stokes number.

3.2.3 Particle dispersion coefficient

To quantify particle dispersion, one can calculate the Mean Squared Displacement (MSD) for particle positions, here denoted as \mathcal{D} as

$$\mathcal{D}(\tau) = \frac{1}{3} \left\langle [\mathbf{l}_p(t + \tau) - \mathbf{l}_p(t)]^2 \right\rangle_p$$

where $\mathbf{l}_p(t)$ is the particle displacement defined in Eq. (3.21) which is calculated as

$$\mathbf{l}_p = \mathbf{x}_p + L \mathbf{b}_p$$

where $\mathbf{b}_p = \mathbf{b}_p(t) \in \mathbb{Z}^3$ is a counter vector, $\mathbf{b}_p(0) = 0$ that tracks the times a particle passes the periodic borders defined as

$$b_{p,i} = \begin{cases} b_{p,i} + 1 & \text{if } x_{p,i} \geq L \\ b_{p,i} - 1 & \text{if } x_{p,i} \leq 0. \end{cases}$$

In Fig. 3.10, one can observe the evolution of $\mathcal{D}(\tau)$ and how it is modified by inertia. In fact, inertial particles transported by HIT tend to disperse further away from their initial positions, however it takes less time in terms of their relaxation time τ_{fp}^F for heavier particles to reach the same value. Furthermore, at first evolution of $\mathcal{D}(\tau)$ is non-linear, but it seems to become rather linear after several multiples of τ_{fp}^F , which physically means that the growth rate of particle MSD becomes constant in the stationary regime.

The coefficient of particle dispersion D_p^t is directly associated to the particle MSD growth rate as

$$D_p^t = \lim_{\tau \rightarrow \infty} \frac{1}{2} \frac{d}{d\tau} \mathcal{D}(\tau). \quad (3.43)$$

Figure 3.10 shows the time evolution of particle dispersion for various particle Stokes numbers. Time evolution of $d\mathcal{D}/d\tau$ has been calculated by numerical differentiation of particle MSD

time-series using Savitzky-Golay filtering to remove numerical noise. Lighter particles need more time in terms of τ_{fp}^F in order to reach a stationary growth rate of particle MSD. It is evident that time derivative $d\mathcal{D}/d\tau$ is needed to calculate particle dispersion coefficient D_p^t .

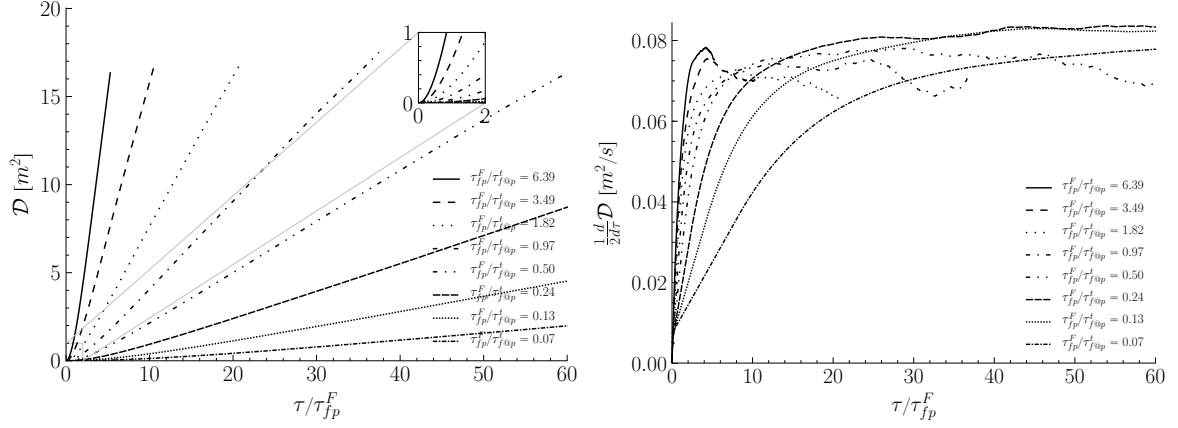


Figure 3.10: Mean squared particle displacement (left) and particle dispersion (right) with regard to time normalized by particle relaxation time scale for various Stokes numbers.

This is best estimated by performing a Linear Regression (LR) to the stationary part of the $\mathcal{D} - \tau/\tau_{fp}^F$ curve that seems to be rather linear, an assumption that is verified by the negligible LR residual R^2 as shown by Figure 3.11.

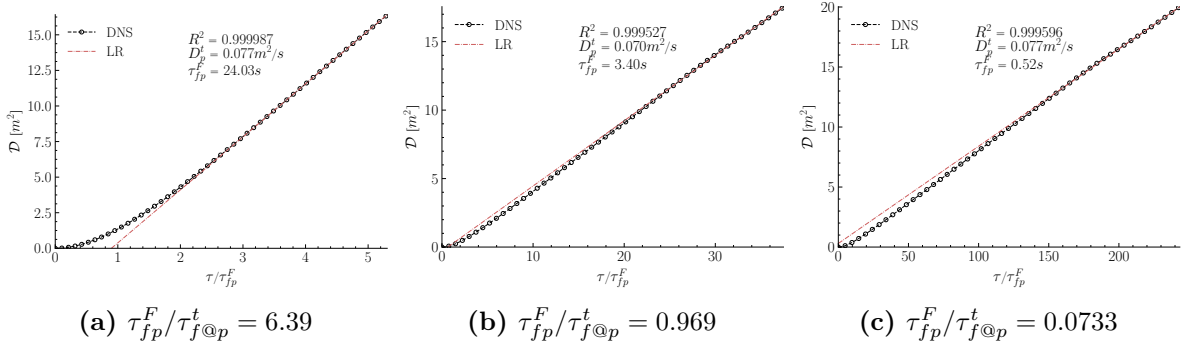


Figure 3.11: Mean squared particle displacement $\mathcal{D}(\tau)$ with regard to τ/τ_{fp}^F for two Stokes numbers. A non-linear short-term and a linear long-term evolution is observed.

In Fig. 3.12 one can examine the particle dispersion coefficient, defined in Eq. (3.43), for various Stokes numbers calculated using data from DNS following the aforementioned procedure. We observe that in the limit of very heavy particles and very light particles particles exhibit a dispersion coefficient close to that of fluid elements, D_f^t defined by Eq. (3.20). The increase for intermediate Stokes numbers, $\tau_f^t/\tau_{fp}^F \in [0.5, 5]$ has been also observed experimentally and numerically in shear flows in the work of Chung & Troutt (1988), Crowe *et al.* (1985), Longmire & Eaton (1992), Lázaro & Lasheras (1992) with the appearance of strong particle concentration zones. However, as noted by Février (2000), these flows are far from a HIT case like the one used here, so there is an argument that this increase could be an artifact of the turbulence forcing scheme as particle dispersion is driven by the large turbulent scales that are sensitive to the effects of the stochastic forcing scheme. However, D_p^t seems to follow closely the behavior

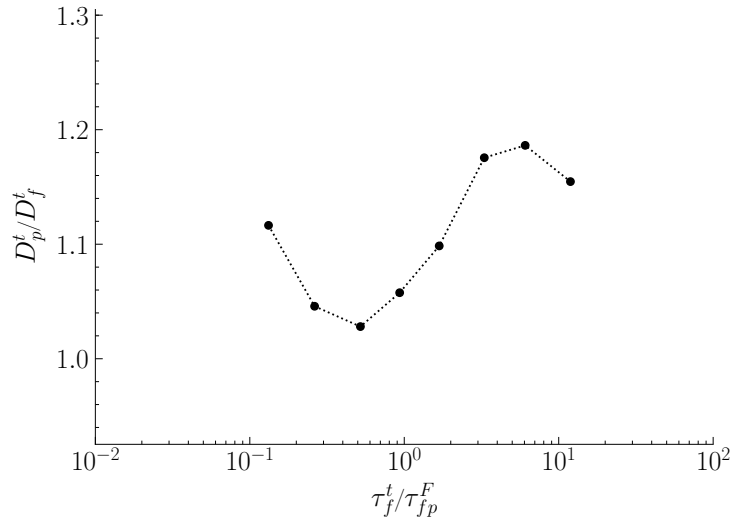


Figure 3.12: Particle dispersion coefficient with regard to particles Stokes number.

of the Lagrangian integral time scale of the fluid measured at the particle position, $\tau_{f@p}^t$ shown by Fig. 2.10. This can be explained by examining the theoretical prediction for the particle dispersion coefficient demonstrated in Subsect. 3.1.2 that gives for the charge-free case

$$D_p^t = \frac{2}{3}q_p^2\tau_p^t \simeq \frac{2}{3}q_{f@p}^2\tau_{f@p}^t. \quad (3.44)$$

Figure 3.13 draws a comparison between the values of particle dispersion coefficient measured by DNS calculations and Eqs. (3.44) derived from the Tchen-Hinze theory. In fact, it seems that the theoretical relations of the particle dispersion coefficient and the values measured from the DNS calculations, present a very good agreement. The last equality of Eq. (3.44) links D_p^t

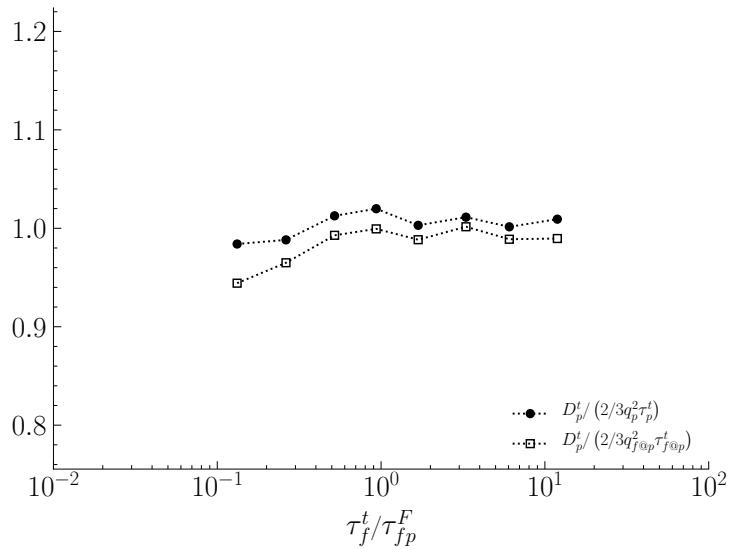


Figure 3.13: Models for particle dispersion coefficient with regard to particle Stokes numbers.

with the fluid agitation measured at particle position, $q_{f@p}^2$ and the Lagrangian integral time scale of the fluid measured at the particle position, $\tau_{f@p}^t$. Since $q_{f@p}^2$ does not vary greatly

(< 5%) for increasing particle inertia as seen in Fig. 2.8, we can conclude that $D_p^t \sim \tau_{f@p}^t$. Now, if we examine the behavior of $\tau_{f@p}^t$ in Fig. 2.10, we observe that it peaks for particles of moderate-to-low inertia. This happens exactly because these particles concentrate preferentially in low-vorticity zones, so they tend to correlate with turbulent structures of greater lifetimes, hence greater values of $\tau_{f@p}^t$. This means that particles that exhibit preferential concentration also exhibit higher values of dispersion coefficient.

3.2.4 Spatial distribution of particles

Figure 3.14 shows instantaneous snapshots of the turbulent vorticity field and the particle distribution for various levels of inertia, where one can observe the phenomenon of preferential concentration. This phenomenon occurs when solid non-charged particles are transported by a turbulent flow field. According to their inertia, they tend to accumulate in low-vorticity regions of the turbulence Fessler *et al.* (1994), Squires & Eaton (1991).

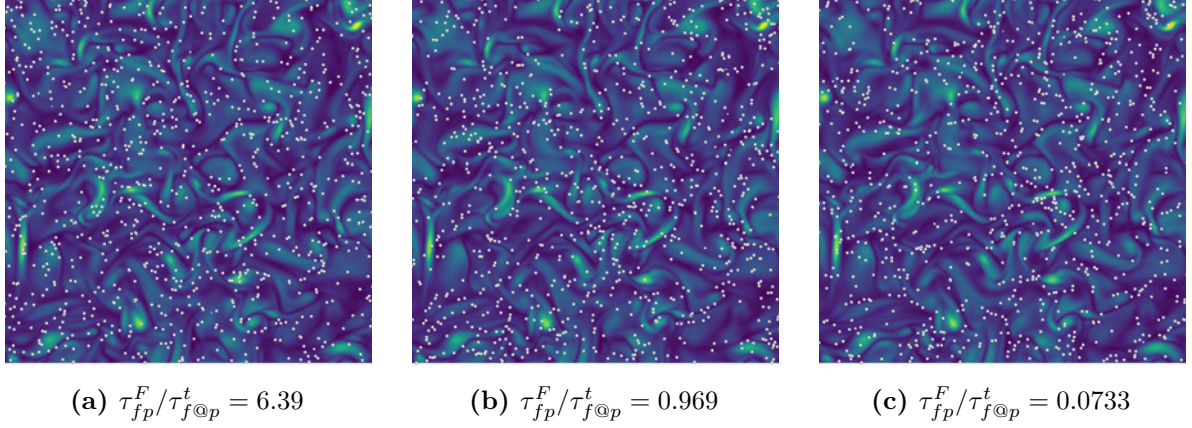


Figure 3.14: Instantaneous snapshots of the turbulent vorticity field and the particle distribution for various levels of inertia for $\Delta x = L_f$.

Preferential concentration of particles by turbulence

To quantify preferential concentration, a first simple statistic would be the PDF of particle concentration $f(C_p)$, as it constitutes a very intuitive and straightforward to calculate quantity that is usually found in similar studies of the relevant literature (Fede, 2004, Fessler *et al.*, 1994, Février, 2000). In order to calculate such a statistical measure, first the computational domain Ω of volume L^3 is partitioned in N_c cells Ω_c that occupy volume $V_c = L^3/N_c$. In this way, the particle concentration C_p inside cell Ω_c is calculated as

$$C_p = \frac{N_p^c}{V_c} \quad (3.45)$$

where N_p^c is the number of particles inside cell Ω_c at a given time. From these N_c values of C_p we can evaluate the PDF $f(C_p)$. When the particles are distributed randomly (uniformly) inside the flow (i.e. fluid elements), $f(C_p)$ should follow the Poisson distribution given by:

$$f(C_p) = \frac{n^{C_p} \exp(-n)}{C_p!} \quad (3.46)$$

where n is the average particle number in a cell Ω_c , given by $n = N_p/N_c$. Figure 3.15 shows that indeed fluid elements follow the Poisson distribution, which is expected as they follow turbulent trajectories which are inherently random (uniform) and independent.

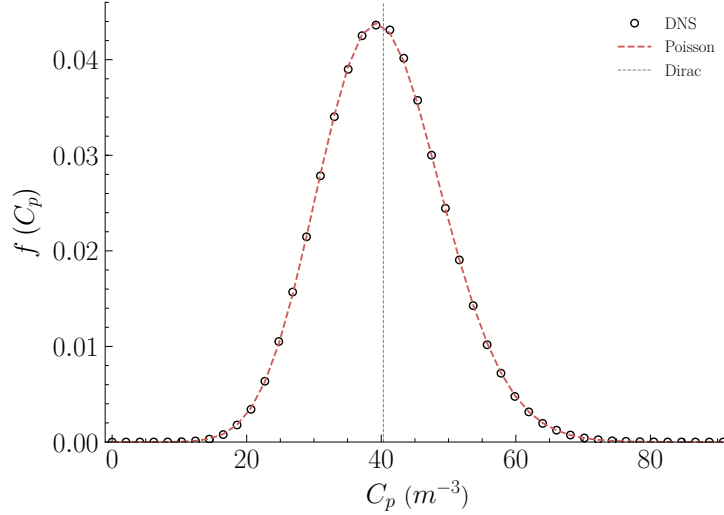


Figure 3.15: PDF of particle concentration for fluid elements. There is a perfect agreement with the Poisson distribution of Eq.(3.46) as their distribution is uniform.

If all cells have n particles, then the probability density function collapses to a Dirac distribution at the particle number density, n_p defined as

$$f(C_p) = \delta(C_p - n_p) . \quad (3.47)$$

For the following analysis we use $N_c = 8^3 = 512$. In Fig. 3.16 we observe that inertial particles exhibit particle concentration distributions very different from the Poisson distribution, which imply the presence of preferential concentration.

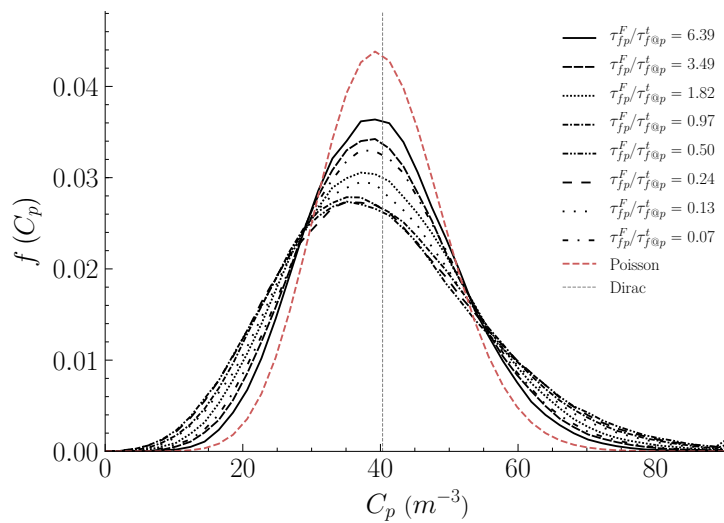


Figure 3.16: PDF of particle concentration for inertial particles of different levels of inertia in the charge-free case. Particles of moderate inertia do not follow the Poisson distribution.

Global particle accumulation

To further quantify particle distribution, one can define a measure of global particle accumulation, Σ_p as the relative difference of the standard deviation, $\sigma_{C_p} = \sqrt{\sum_{C_p} (C_p - n)^2 f(C_p)}$ of the particle distribution $f(C_p)$ with that of the Poisson distribution $\sigma_P = \sqrt{n}$ as

$$\Sigma_p = \frac{\sigma_{C_p} - \sigma_P}{n} . \quad (3.48)$$

Figure 3.17 shows the evolution of global particle accumulation for different levels of particle inertia, where it is clear that preferential particle concentration is more pronounced for particles of moderate-to-high inertia. However, it should be noted here that evidently, Σ_p depends on the size of cells Ω_c (Fessler *et al.*, 1994). This means that there is a cell size for which

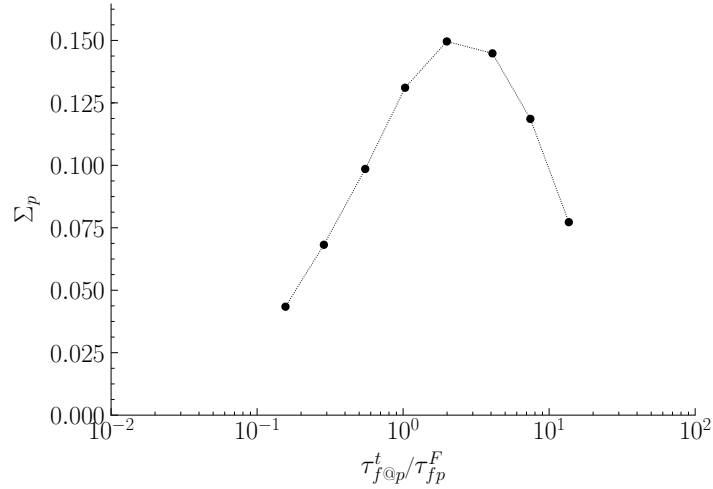


Figure 3.17: Global particle accumulation for various levels of particle inertia. Particles of moderate inertia present higher levels of accumulation as they concentrate preferentially.

Σ_p is maximum and Février (2000) proposes that this be the representative value for global accumulation of particles in the flow. Therefore, it would be very useful to examine another statistical quantifier of particle accumulation.

PDF of nearest-neighbor particle distance

Therefore, one can examine the PDF of the nearest-neighbor particle distance d_{np} . This is the minimum distance between a particle and all of its neighboring particles defined as

$$d_{np} = \min_{p,q \in \Omega} \{ \|\mathbf{r}_{pq}\| \} \quad (3.49)$$

where $\mathbf{r}_{pq} = \mathbf{x}_p - \mathbf{x}_q$ is the distance vector between particles p and q . The PDF of the nearest-neighbor particle distance for a uniform distribution has been derived theoretically, initially by Hertz (1909) and then by Chandrasekhar (1943) as

$$f(d_{np}) = 4\pi n_p d_{np}^2 \exp \left[-\frac{4\pi n_p d_{np}^3}{3} \right] . \quad (3.50)$$

In addition, the average value of such a distribution has been derived analytically by Chandrasekhar (1943) for a uniform particle distribution as $\langle d_{np} \rangle_p = \int_0^\infty d_{np} f(d_{np}) dd_{np} \approx$

$0.5539n_p^{-1/3}$, while the variance $\langle d'_{np}{}^2 \rangle_p \approx 0.040535n_p^{-2/3}$. Figure 3.18 shows that the PDF of this statistical measure for fluid elements is a perfect Hertz-Chandrasekhar distribution as they are distributed randomly (uniformly) in the computational domain.

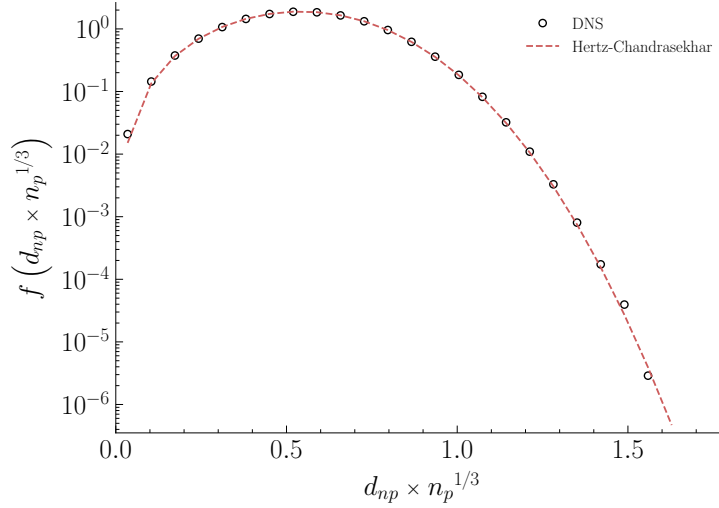


Figure 3.18: Nearest-neighbor particle distance normalized by the equidistant distribution distance $n_p^{-1/3}$ for fluid elements. There is a perfect agreement with the Hertz-Chandrasekhar distribution of Eq.(3.50) as their distribution is uniform in HIT.

However, in Fig. 3.19 we observe that inertial particles tend to have more neighbors at very short distances, but also at distances that are greater than the corresponding values of the Hertz-Chandrasekhar distribution due to the phenomenon of preferential concentration. This technique appears to yield results that are very similar to those of Voronoi tessellation, which can then be used to extract information about the length scale of particle clusters and voids (Manish & Sahu, 2018, Monchaux *et al.*, 2010). Furthermore, Fig. 3.20 shows that the average

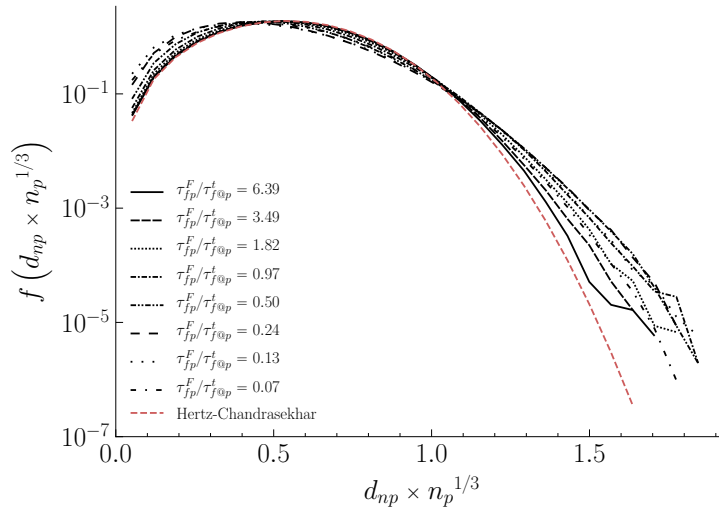


Figure 3.19: Nearest-neighbor particle distance normalized by the equidistant distribution distance $n_p^{-1/3}$ for various levels of particle inertia in the charge-free case.

nearest-neighbor particle distance, $\langle d_{np} \rangle_p$ slightly decreases for decreasing particle inertia while

its variance, $\langle d_{np}^{\prime 2} \rangle_p$ increases. Both statistics approach asymptotically the corresponding theoretical values for uniform particle distribution in the case of very heavy particles. This is because the latter do not exhibit any preferential concentration as they are decorrelated from the turbulent velocity field. The same asymptotical behavior is also to be expected for very light particles, as in their case, they would follow perfectly the independent trajectories of fluid elements, which are distributed uniformly in a HIT flow. The peak is found for a

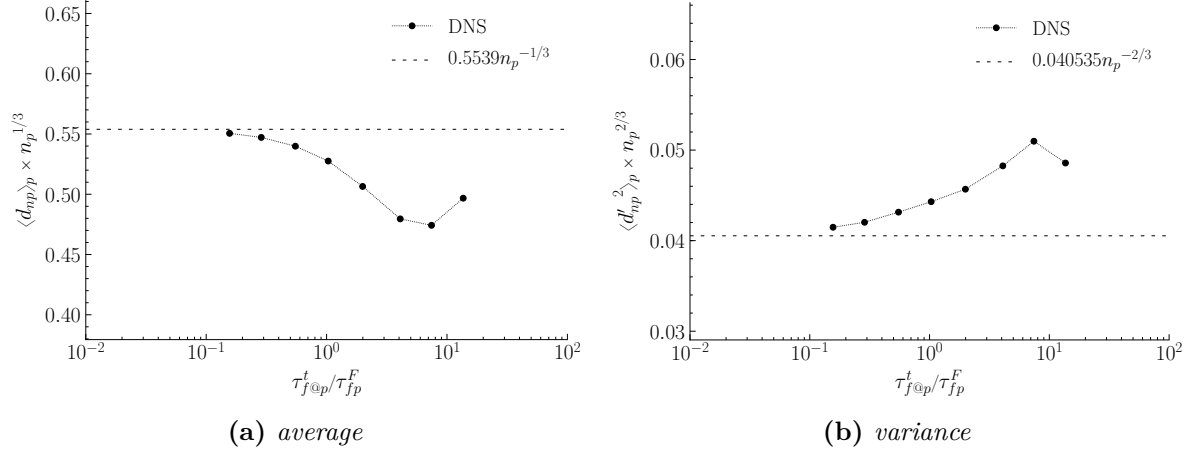


Figure 3.20: Average (left), and variance (right) of the nearest-neighbor particle distance normalized by the equidistant distribution distance $n_p^{-1/3}$ in the charge-free case. The dashed line denotes the theoretical values derived by Chandrasekhar (1943) for a random distribution.

bigger Stokes number than Fig. 3.17 as Σ_p depends on the size of the selected control volumes, making this statistical measure more reliable. One can observe that the particle class for which particle accumulation is maximum ($\tau_{f@p}^t / \tau_{fp}^F \simeq 7.46$) coincides with the one for which particle dispersion coefficient is maximum (see 3.12). This can be explained using the observation made in Subsect. 3.2.3, where it is argued that $D_p^t \sim \tau_{f@p}^t$, therefore particles that exhibit preferential concentration present higher values of D_p^t .

Radial distribution function

To further deepen our understanding of the spatial distribution of particles we deploy another important statistical measure: the radial distribution function (RDF). This is defined as the number of particle pairs found at a given separation normalized by the expected number of pairs found in a homogeneous distribution and is denoted as $g(r)$. For a test particle p , the RDF $g(r)$ is calculated by finding the separation distance $\|\mathbf{r}_{pq}\|$ between it and each other particles q around it. Each particle pair, according to their separation distance, is located in an annular shell of thickness Δr , centered on the test particle p . Hence, if N_r is the number of particle pairs separated by distance $r \pm \Delta r/2$, ΔV_r is the volume of the shell with thickness Δr located at separation distance r and $N_{pq} = N_p(N_p - 1)/2$ is the total number of pairs in the computational volume L^3 . Then, the radial distribution function, $g(r)$ is defined as

$$g(r) = \frac{N_r / \Delta V_r}{N_{pq} / L^3} . \quad (3.51)$$

This is a very meaningful statistical measure as $g(r) = 1$ represents a homogeneous distribution of particles, while $g(r) > 1$ denotes particle clustering. In Fig. 3.21 we observe the evolution

of the RDF of inertial particles which exhibit clustering at small separation distances $r < L_f$, which is expected in case of inertial particles transported by HIT. This RDF is obtained

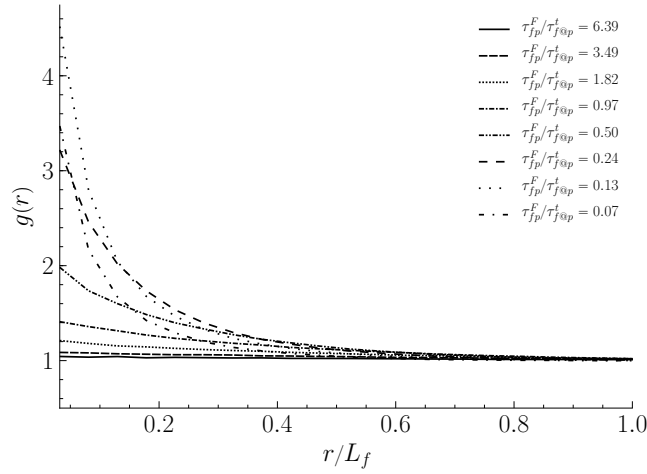


Figure 3.21: *RDF of inertial particles for different levels of inertia in the charge-free case.*

by averaging the RDFs of 64 test particles for 15,000 time-steps each. For each of the test particles, its RDF has been calculated using $r_{\min} = d_p$ and $r_{\max} = L/2$ so that $\Delta r = (r_{\max} - r_{\min})/100 \simeq 3.137 \times 10^{-2}m$. As the separation distance increases, the distribution around the particles becomes gradually homogeneous and at $r = L_f$ the particle number density found in the annular shell reaches the homogeneous value. This is an interesting result that shows that particles are not clustering in distances greater than the size of biggest turbulent eddies in the flow, which is the Eulerian longitudinal integral length scale, L_f .

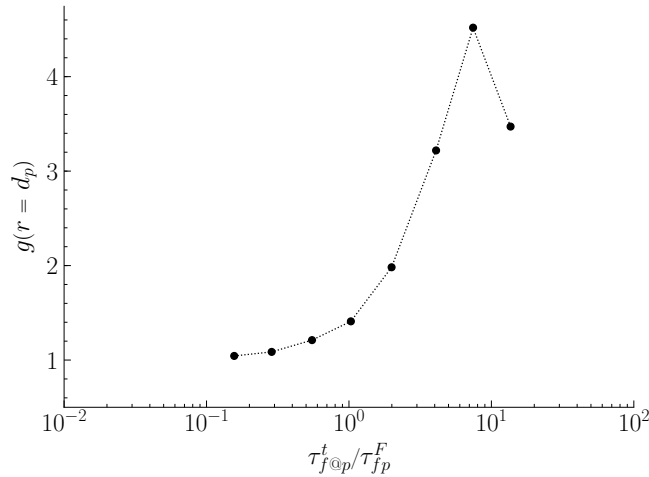


Figure 3.22: *RDF at separation distance $r = d_p$ in the charge-free case.*

Furthermore, in Fig. 3.22 we observe more clearly the evolution of particle clustering at separation distance $r = d_p$ for increasing Stokes number. This clustering seems to peak for particles of low-to-moderate inertia $\tau_{fp}^t / \tau_{fp}^F \in [5, 10]$, as they concentrate preferentially. Then, it decreases for heavier particles as they are less affected by hydrodynamic forces, hence do not exhibit clustering. It should be noted here, that the Stokes of the peak of accumulation agrees with the results presented in Fig. 3.20. Chun *et al.* (2005) has showed that particles

having small Stokes number τ_{fp}^F/τ_K appear to be clustering at distances smaller than the size of the smallest eddy, thus smaller than the Kolmogorov length scale $r < \eta_K$. For those, a theoretical relation for their RDF in the dissipative turbulent length range is derived as

$$g(r) = c_0 \left(\frac{\eta_K}{r} \right)^{c_1} \quad (3.52)$$

where c_0 and c_1 can be obtained from the theory of inertial particle clustering provided in Chun *et al.* (2005), where it is shown that c_1 scales as the square of the particle Stokes number in the small Stokes number limit. In this work, we calculate the coefficients by fitting this power law to the obtained DNS data for $r \leq 25\eta_K$, due to lack of sufficient data points in the $r \in [d_p, \eta_K]$ interval (see Table 3.2). We are aware that this is an approximation beyond the

Table 3.2: Coefficients c_0 and c_1 for the model of Eq. (3.52) (Chun *et al.*, 2005)

class	τ_{fp}^F/τ_K	c_0	c_1
1	46.50	1.049	0.009996
2	23.40	1.098	0.02024
3	11.82	1.229	0.05139
4	6.582	1.457	0.1003
5	3.650	2.018	0.2105
6	1.864	3.172	0.3803
7	1.013	4.126	0.5147
8	0.5160	3.169	0.4235

limits of the aforementioned model, albeit close. Figure 3.23 shows the RDFs for the particles with the three lowest Stokes numbers examined in this work. We can see that the model fits better the RDFs of particles of the lowest inertia.

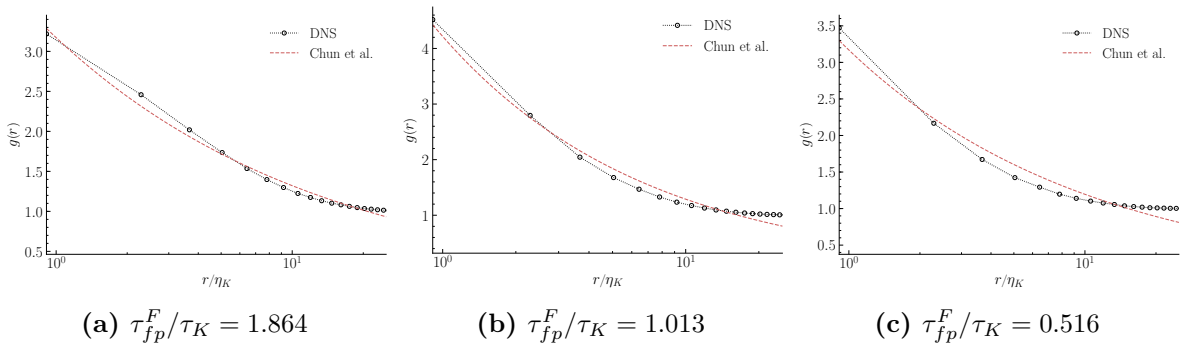


Figure 3.23: RDFs of inertial particles having low Stokes numbers, τ_{fp}^F/τ_K . The red dashed line corresponds to Eq. (3.52) that has been fitted via non-linear least squares optimization.

3.2.5 Inter-particle relative motion

Radial relative particle velocity

To further analyze the dynamic structure of the particle distribution in the domain, we are interested in the relative motion of neighboring particles. In Fig. 3.24, the various notations used to describe inter-particle relative motion are presented. For two particles p and q , one

can define the relative particle velocity $\mathbf{w}_{pq} = \mathbf{u}_p - \mathbf{u}_q$ and its radial projection w_r as

$$w_r = \frac{\mathbf{w}_{pq} \cdot \mathbf{r}_{pq}}{\|\mathbf{r}_{pq}\|}$$

If $w_r > 0$, then particles are approaching, while if $w_r < 0$, particles are departing from each other. The angle of particle relative motion θ_{pq} as the absolute angle between relative velocity \mathbf{w}_{pq} and distance vector \mathbf{r}_{pq} , that is given by

$$\theta_{pq} = \frac{\mathbf{w}_{pq} \cdot \mathbf{r}_{pq}}{\|\mathbf{w}_{pq}\| \|\mathbf{r}_{pq}\|} = \frac{w_r}{\|\mathbf{w}_{pq}\|}.$$

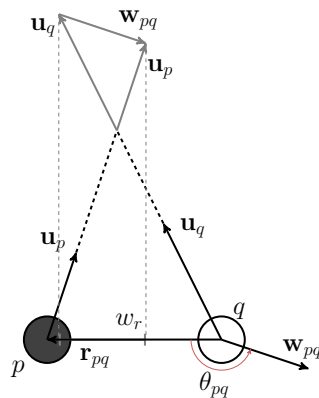


Figure 3.24: Notations for inter-particle relative motion.

The resulting effect of particle motion due to turbulence is the phenomenon of preferential concentration, that can be ascribed to two very different mechanisms that bring particles close:

- i. independent particle trajectories intersect in privileged zones, while they are simply deviated by the turbulence
- ii. particles stay together longer (in average) in low-vorticity zones, they are "captured" in those turbulent clusters and stay a certain time within them.

The second effect could be characterized by the relative velocity between the particles. More specifically, it is a consequence of the divergence of the correlated velocity field and, conversely, the decorrelated velocity tends to reduce the mechanism. Figure 3.25 shows the radial distribution function of the average radial relative velocity in the charge-free case.

One can observe that for high Stokes numbers, $|w_r|$ does not vary as particle velocities are decorrelated, while for low Stokes, it varies greatly as particle velocities are strongly correlated. Moreover, it seems that the general trend is that as particle separation distance increases, radial relative velocity increases. Particles close to each other see the same flow field and they stay together for longer time intervals, while particles away from each other have rather independent velocities and they stay at this distance for shorter time intervals. This explains why for short inter-particle distances $r < L_f$, light particles exhibit zero relative particle velocity (as they follow promptly fluid velocity modifications), while heavier particles present non-zero relative particle velocity, as their velocity is decorrelated from fluid velocity due to inertia.

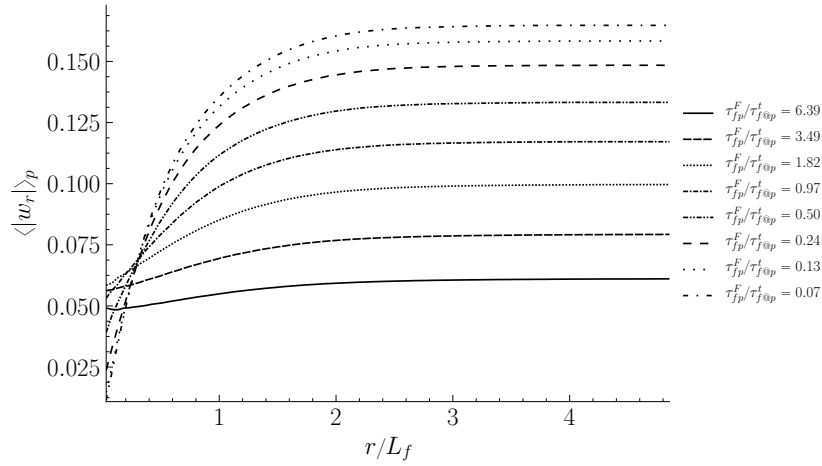


Figure 3.25: *RDF of average radial relative particle velocity in the charge-free case.*

For fluid elements and at the limit of very low Stokes numbers, Saffman & Turner (1956) have provided a model for the radial relative velocity as a Gaussian random variable with variance σ^2 equal to

$$\langle w_r'^2 \rangle_p = \frac{\epsilon f}{15\nu_f} r^2 = \sigma^2 \quad (3.53)$$

that is valid in the dissipative turbulent length range $r < \eta_K$. For isotropic Gaussian turbulence, the average value of the radial relative velocity can be deduced as

$$\langle |w_r| \rangle_p = \sqrt{\frac{2}{\pi}} \sigma. \quad (3.54)$$

Indeed, in Fig. 3.26 it seems that this model predicts rather accurately the radial relative velocity of fluid elements at the limit of the dissipative turbulent length range $\eta_K < r < 10\eta_K$.

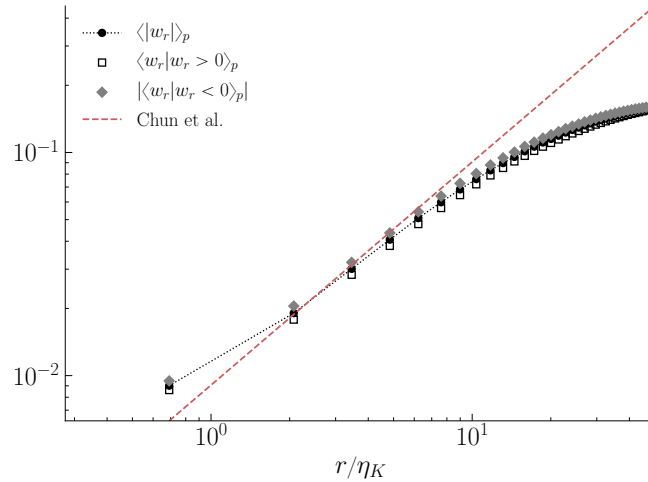


Figure 3.26: *RDFs of the average radial relative velocity for fluid elements compared with Saffman & Turner (1956) model of Eq. (3.54).*

If we try to extend this model to predict the average value of the radial relative velocity for inertial particles of relatively small Stokes numbers, we see in Fig. 3.27 that at the limit

of the dissipative turbulent length range $\eta_K < r < 10\eta_K$ and only for small particle Stokes numbers it can give a surprisingly good prediction, since the model was designed for distances smaller than that of the Kolmogorov length scale.

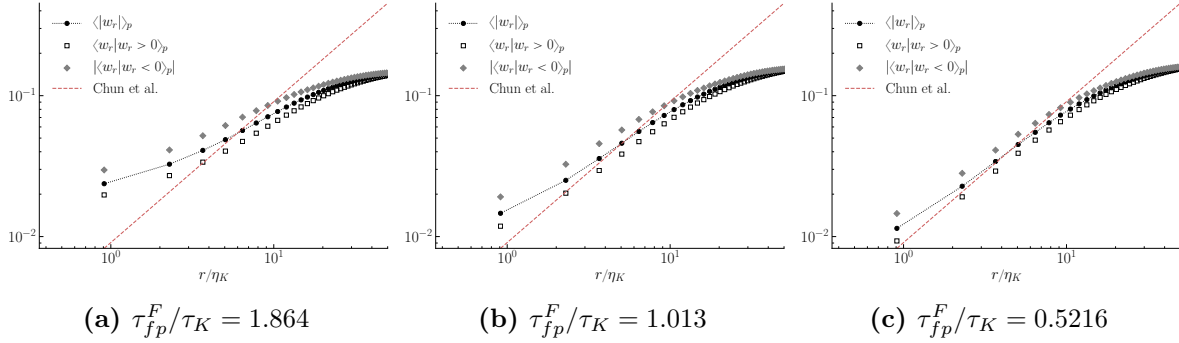


Figure 3.27: *RDFs of the average radial relative particle velocity for particles with the smallest Stokes number compared with Saffman & Turner (1956) model of Eq. (3.54).*

Finally, Fig. 3.28 shows the effect of particle inertia on the average and variance of the radial relative particle velocity. Interestingly, its average value seems to be rather constant at $\langle |w_r| \rangle_p \sim \sqrt{2q_{f@p}^2}/3$, unaffected by particle inertia, while its variance exhibits a slight increase for heavier particles.

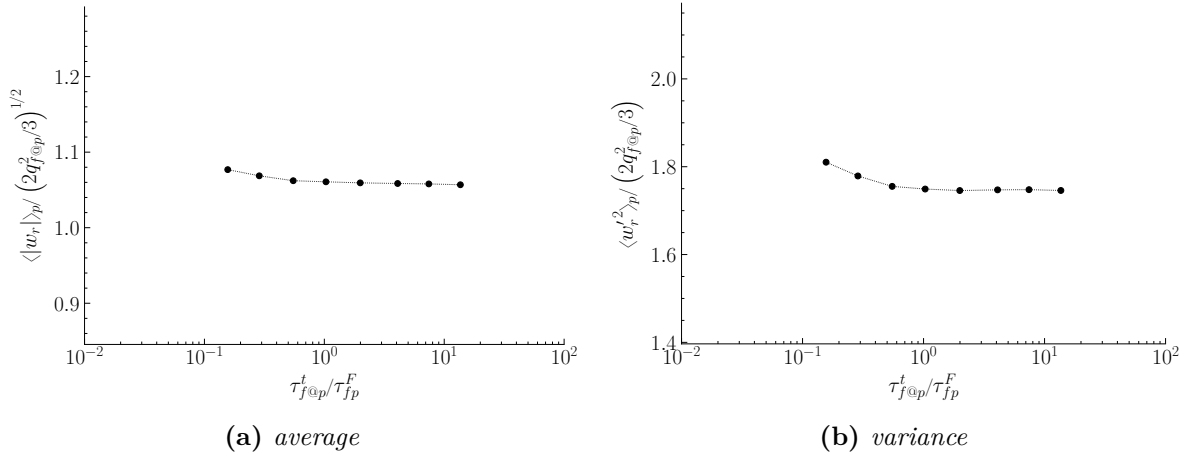


Figure 3.28: *Average (left), and variance (right) of radial relative velocity normalized by $2/3q_{f@p}^2$ in the charge-free case.*

PDF of particle velocities

Figure 3.29 shows the PDFs of the three components of particle velocities, for various levels of inertia. It can be deduced that, since the PDFs overlap, both the distribution of actual and relative particle velocities is isotropic as orientation does not modify the shape of the PDFs. This is in agreement with the isotropic properties of the simulated turbulence. In order to obtain a more precise idea of the form of the PDF of $u_{p,i}$, exponential and Gaussian functions are also plotted that are obtained by the following relation (Wang *et al.*, 2000)

$$f(x) = \frac{n}{2p^3\Gamma(3/n)} \exp\left[-\left(\frac{|x|}{p}\right)^n\right], \quad p = \sqrt{\frac{\Gamma(1/n)}{\Gamma(3/n)}}. \quad (3.55)$$

where Γ is the gamma function. This PDF has a unit standard deviation and $\int_{-\infty}^{\infty} f(x)dx = 1$. For $n = 1$, $f(x)$ gives an exponential distribution, while for $n = 2$ a Gaussian one. One can make two observations based on Fig. 3.29. It seems that for the charge-free case, the PDFs of particle velocities are almost perfect Gaussian distributions for all the presented levels of particle inertia, which is to be expected for particles transported by HIT.

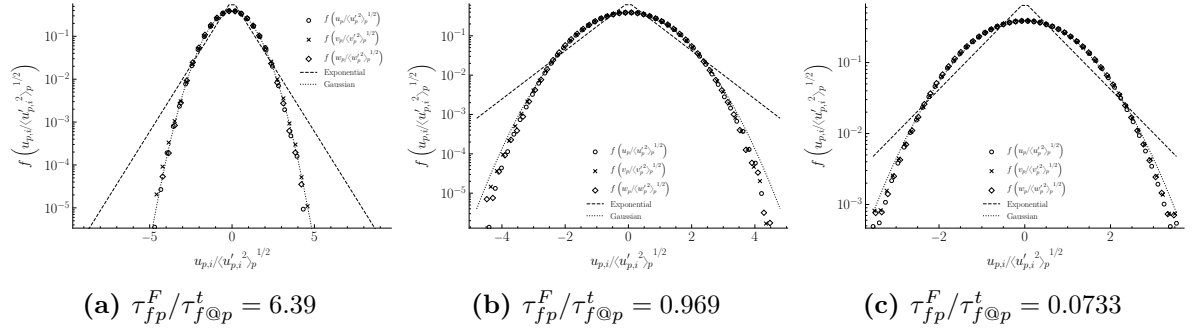


Figure 3.29: PDF of the three components of particle velocities for various levels of particle inertia in the charge-free case. The distributions are compared with the corresponding exponential and Gaussian distributions from Eq. (3.55).

3.3 Conclusion

A first step in understanding the dynamics of electrically charged particle-laden turbulent flows, is to acquire a concrete appreciation of the corresponding charge-free case. Such flows have been studied for many decades now, and there is a number of theoretical frameworks that facilitate their study, such as the Tchen-Hinze theory. This is the reason why such a detailed analysis of the charge-free case and settling-free case has been carried out in this chapter. The key property that characterizes particle dynamics in turbulent gas-particle flows is particle inertia.

In a first order approximation, particle agitation, hence particle dispersion is more pronounced for lighter particles as for decreasing inertia - to the limit of fluid elements - particles tend to be more susceptible to local fluid fluctuations. However, it is shown that particle agitation depends on fluid-particle covariance which is a measure of fluid-particle correlation. An attempt to describe the turbulent dissipation of the latter via the fluid acceleration - particle velocity covariance has been made. For the latter it is shown that a model based on a stochastic equation for fluid acceleration measured at particle positions, predicts it with better accuracy if the supposed form of the fluid autocorrelation function is a double exponential. Furthermore, while the latter dissipation mechanism is not greatly affected by the decrease of particle inertia, its effect via the hydrodynamic force becomes predominant and leads to fluid-particle decorrelation.

An even deeper analysis of such flows involves the structure of the particle distribution in the turbulent flow, and by observing the appropriate statistics (PDF of particle concentration and nearest-neighbor particle distance, radial distribution functions) a well studied behavior emerges: preferential concentration. According to this phenomenon, particles of moderate inertia tend to gather in low-vorticity regions of the flow and as a result, accumulation is observed in the spatial particle distribution.

Bibliography

- Batchelor, G.K. 1960. *Theory of homogeneous turbulence*. Cambridge University Press.
- Chandrasekhar, S. 1943. Stochastic Problems in Physics and Astronomy. *Reviews of modern physics*, **15**(1), 1–89. Publisher: American Physical Society.
- Chun, Jaehun, Koch, Donald L., Rani, Sarma L., Ahluwalia, Aruj, & Collins, Lance R. 2005. Clustering of aerosol particles in isotropic turbulence. *Journal of fluid mechanics*, **536**(Aug.), 219–251. Publisher: Cambridge University Press.
- Chung, J. N., & Troutt, T. R. 1988. Simulation of particle dispersion in an axisymmetric jet. *Journal of fluid mechanics*, **186**(Jan.), 199–222. Publisher: Cambridge University Press.
- Crowe, C. T., Gore, R. A., & Troutt, T. R. 1985. Particle Dispersion by Coherent Structures in Free Shear Flows. *Particulate science and technology*, **3**(3-4), 149–158.
- Deutsch, E. 1992. *Dispersion de particules dans une turbulence homogène isotrope calculée par simulation numérique directe des grandes échelles*. Ph.D. thesis, Ecole Centrale de Lyon.
- Fede, P. 2004. *Modélisation et simulation numérique de l'influence de la turbulence sur les collisions dans les écoulements mono- et bi-solides*. Ph.D. thesis, Institut National Polytechnique de Toulouse.
- Fessler, J.R., Kulick, J.D., & Eaton, J.K. 1994. Preferential concentration of heavy particles in a turbulent channel flow. *Physics of fluids*, **6**, 3742–3749.
- Février, Pierre. 2000. *Etude numérique des effets de concentration préférentielle et de corrélation spatiale entre vitesses de particules solides en turbulence homogène isotrope stationnaire*. Ph.D. thesis, Institut National Polytechnique de Toulouse.
- Gouesbet, G., Berlemont, A., & Picart, A. 1984. Dispersion of discrete particles by continuous turbulent motions. Extensive discussion of the Tchen's theory, using a two-parameter family of Lagrangian correlation functions. *The physics of fluids*, **27**(4), 827–837. Publisher: American Institute of Physics.
- Hertz, P. 1909. Über den gegenseitigen durchschnittlichen Abstand von Punkten, die mit bekannter mittlerer Dichte im Raume angeordnet sind | SpringerLink. *Mathematische annalen*, **67**(3), 387–398.
- Hinze, J.O. 1972. Turbulent fluid and particle interaction. *Prog. heat and mass transfer*, **6**, 433–452.
- Laviéville, J. 1997. *Simulations numériques et modélisation des interactions entre l'entraînement par la turbulence et les collisions interparticulaires en écoulement gaz-solides*. Ph.D. thesis, Université de Rouen.
- Longmire, Ellen K., & Eaton, John K. 1992. Structure of a particle-laden round jet. *Journal of fluid mechanics*, **236**(Mar.), 217–257. Publisher: Cambridge University Press.
- Lázaro, B. J., & Lasheras, J. C. 1992. Particle dispersion in the developing free shear layer. Part 2. Forced flow. *Journal of fluid mechanics*, **235**(Feb.), 179–221. Publisher: Cambridge University Press.

- Manish, M., & Sahu, Srikrishna. 2018. Analysis of droplet clustering in air-assist sprays using Voronoi tessellations. *Physics of fluids*, **30**(12), 123305. Publisher: AIP Publishing LLC/AIP Publishing.
- Monchaux, R., Bourgoïn, M., & Cartellier, A. 2010. Preferential concentration of heavy particles: A Voronoi analysis. *Physics of fluids*, **22**(10), 103304. Publisher: American Institute of Physics/AIP.
- Saffman, P. G., & Turner, J. S. 1956. On the collision of drops in turbulent clouds. *Journal of fluid mechanics*, **1**(1), 16–30. Publisher: Cambridge University Press.
- Simonin, O. 2000. Statistical and continuum modelling of turbulent reactive particulate flows. part 1 : Theoretical derivation of dispersed eulerian modelling from probability density function kinetic equation. *Pages – of: Lecture series 2000-06, von karman institute for fluid dynamics, rhodes saint genèse (belgium)*. Von Karman Institute for Fluid Dynamics.
- Simonin, O., Deutsch, E., & Minier, J. P. 1993. Eulerian prediction of the fluid/particle correlated motion in turbulent two-phase flows. *Applied scientific research*, **51**(1), 275–283.
- Squires, K.D., & Eaton, J.K. 1991. Preferential concentration of particles by turbulence. *Physics of fluids a: Fluid dynamics*, **3**(5), 1169–1178.
- Taylor, G. I. 1921. Diffusion by Continuous Movements. *Proceedings of the london mathematical society*, **s2-20**(1), 196–212.
- Tchen, C.M. 1947. *Mean value and correlation problems connected with the motion of small particles suspended in a turbulent fluid*. Ph.D. thesis, Delft, Martinus Nijhoff, The Hague.
- Wang, L.P., Wexler, A.S., & Zhou, Y. 2000. Statistical mechanical description and modelling of turbulent collision of inertial particles. *Journal of fluid mechanics*, **415**, 117–153.
- Zaichik, L.I., Simonin, O., & Alipchenkov, V.M. 2003. Two statistical models for predicting collision rates of inertial particles in homogeneous isotropic turbulence. *Physics of fluids*, **15**, 2995–3005.

4

Numerical simulation of electrostatic forces in charged granular flows

“ἡ δὲ φύσις φεύγει τὸ ἄπειρον.
τὸ μὲν γὰρ ἄπειρον ἀτελές,
ἡ δὲ φύσις ἀεὶ ζητεῖ τέλος¹”
- Aristotle, c. 384 – c. 322 BC

Abstract

This chapter deals with the heart of the scientific problem of this PhD thesis, particle-particle electrostatic interactions. It serves two purposes. To begin with, it presents the fundamental problem of calculation of electrostatic forces in a system of particles, the known N-body problem. Then it describes the intricate problem of applying periodic BCs in such systems, where a truncation of the infinite periodic domain is proposed with a reasonable cut-off error. A scalable algorithm is presented that allows for a rather fast and precise calculation of electrostatic forces in a tri-periodic computational domain by separating them in long- and short-range parts, which are calculated exactly and approximately, respectively. The approximation error, computational cost and performance of the proposed algorithm are documented and thoroughly analyzed. The second part of the chapter deals with dry like-charged granular flows where the fundamentals physics of particle-particle electrostatic interactions are investigated via characteristic length and time scales. An attempt is made to provide analytical estimations for several statistical quantities which are compared to DNS measured values. Finally, the particle-induced electric field is presented and its characteristics are related to particle motion.

4.1 Particle-particle electrostatic interactions

4.1.1 Definition of electrostatic forces for a particle dipole

Coulomb’s law allows to calculate the electrostatic force $\mathbf{F}_{q \rightarrow p}$ acting on p due to q as following

$$\mathbf{F}_{q \rightarrow p} = \lambda \frac{Q_q Q_p}{\|\mathbf{r}_{pq}\|^3} \mathbf{r}_{pq} \quad (4.1)$$

where λ is Coulomb’s constant with $\lambda = 1/(4\pi\epsilon_0)$ where ϵ_0 is the vacuum permittivity, Q_p is the electric charge of particle p and $\mathbf{r}_{pq} = \mathbf{x}_p - \mathbf{x}_q$ is the distance vector between particles p and q pointing to p as depicted in Fig. 4.1.

4.1.2 N-body problem

In a system of N_p charged particles, each particle interacts with all $N_p - 1$ particles in the computational domain, thus the total electrostatic force exerted on a particle \mathbf{F}_e is defined as

$$\mathbf{F}_e = \sum_{\substack{q=1 \\ q \neq p}}^{N_p} \mathbf{F}_{q \rightarrow p} . \quad (4.2)$$

¹But nature flies from the infinite; for the infinite is imperfect, and nature always seeks an end.

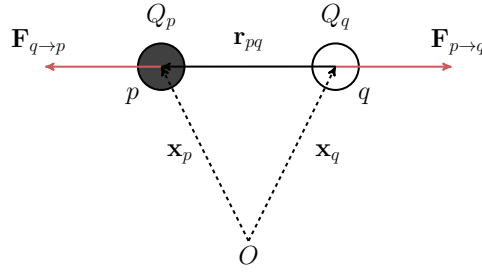


Figure 4.1: Notations in electrostatic interaction of a dipole of like-charged particles.

The problem of predicting the individual motions of all N_p particles interacting with each other electrostatically falls into the category of an N-body problem. This problem has interested astronomers, physicists and mathematicians for the last several hundred years. It has, in fact, motivated much of the theoretical work done during that time, from cosmology to solid state physics to differential equations and potential theory. Unfortunately, the equations of motion of systems $N_p > 2$ do not allow for an analytical solution.

Until the mid 80s, theoretical studies have been limited to determining the coarse qualitative behavior of the system. With the introduction of high-speed computers, however, the calculation of trajectories of many particles in detail became feasible (Greengard, 1990). The equations of motion of a system of N_p particles are described by a set of N_p ordinary differential equations, each of which is simply Newton's second law of motion applied to an individual particle (see Eq. (2.19) and Eq. (4.3)). Given initial positions and velocities, a numerical simulation follows all the trajectories by numerical integration as described in Subsect. 2.1.2.

Modification of particle motion equation

The task at every time-step is to move each particle according to its velocity, and then to update its velocity according to the force exerted by the other particles. If the particles are charged, then electrostatic force \mathbf{F}_e may be significant. Once the total electrostatic force \mathbf{F}_e exerted on a particle is calculated, it has to be taken into consideration in the equation of particle motion. Hence Eq. (2.20) becomes

$$m_p \frac{d\mathbf{u}_p}{dt} = \mathbf{F}_e . \quad (4.3)$$

It is clear that the amount of work required for moving all particles is proportional to N_p , but that the amount of work required for computing all forces is proportional to N_p^2 , since it involves determining all dipole interactions. This quadratic growth in cost has been a major limitation on the size of the systems which can be handled, even by the fastest supercomputers. Next section is dedicated to the numerical methods for computing electrostatic force \mathbf{F}_e .

4.2 Numerical calculation of particle-particle electrostatic forces

In the 80s, significant progress was made in reducing the cost of the numerical calculation of forces acting at a distance, such as electrostatic forces. The first breakthrough, allowing simulations with orders of magnitude more bodies, came with the advent of the Particle-Mesh (PM) approach introduced by Hockney & Eastwood (1988), which makes use of an underlying grid to speed up the evaluation of the long-range potential. An evolution of this method is

the PPPM or P³M method which consists in taking into account the short-range forces up to a certain inter-particle distance, while the long-range contributions are included by the particle-mesh procedure.

The P³M method requires modifying the long-range potential in Fourier space to avoid double counting the short-range and long-range contributions and scales with $\mathcal{O}(N \log N)$. This type of methods are extremely efficient when the particle distribution is more or less uniform and the required precision is relatively low. However, a severe degradation of performance is observed when the bodies are clustered and when the required precision is high.

Ewald (1921) developed the homonymous summation approach in order to handle long-range potentials accurately in periodic boxes. It consists in splitting the Coulomb potential into long-range and short-range contributions, each of which converges exponentially fast (Perram *et al.*, 1988). The fast converging short-range potential is evaluated using direct pairwise sums over the set of nearest neighbors within a cut-off radius and the slowly converging long-range contribution is solved in reciprocal space. However, this approach remains computationally demanding as the long-range contribution requires several Fourier transforms and the total scheme scales like $\mathcal{O}(N_p^{3/2})$ with an optimized cut-off radius (Deserno & Holm, 1998a,b).

In the 90s, a group of algorithms has been developed in the astrophysics community which have come to be known as "tree codes" or "hierarchical codes" (Appel, 1985, Barnes & Hut, 1986). They are designed to work well in a variety of settings, including ones where there is a high degree of clustering. The basic idea is to replace groups of distant particles by their centers of mass, and to compute the interactions between groups via this approximation. Although some accuracy is generally sacrificed, the computational cost of these methods grows as $\mathcal{O}(N_p \log N_p)$ rather than $\mathcal{O}(N_p^2)$.

Along with the development of these tree codes, while working in fluid dynamics, van Dommelen & Rundensteiner (1989) proposed a scheme for two-dimensional calculations which is also $\mathcal{O}(N_p \log N_p)$, but highly accurate. Although the physical intuition underlying their method is the same, the increased accuracy is obtained by the application of asymptotic analysis. A closely related scheme, the Fast Multipole Method (FMM) has been developed by Greengard & Rokhlin (1987). It is also highly accurate, as it involves a more elaborate asymptotic analysis and requires an amount of operations proportional to $\mathcal{O}(N_p)$.

More recently, Kolehmainen *et al.* (2016) presented a hybrid approach that calculates the electrostatic forces by calculating separately a long- and short range contribution. The former comes from an Eulerian electric field solved using the Poisson equation, while the latter using a truncated pairwise sum along with a correction to avoid double counting. Furthermore, Yao & Capecelatro (2018) deployed a Fourier-based Ewald summation P³M method, to accurately capture short- and long-range electrostatic forces that was compared to a classic PM method. It was found that the PM method was capable of quantitatively capturing particle segregation for like-charged particles. However, it was unable to capture particle chain and ring structures observed using the P³M method for systems with oppositely charged particles.

4.2.1 Electrostatic periodicity

This simplest and most accurate method for the calculation of inter-particle electrostatic forces consists in calculating the total electrostatic force on each particle by directly summing all the $N_p - 1$ terms that correspond to the electrostatic interactions of a particle with all particles but itself as seen by Eq. (4.2). However, one could use Newton's 3rd law for such a dipole that gives $\mathbf{F}_{p \rightarrow q} = -\mathbf{F}_{q \rightarrow p}$ in order to perform one operation per dipole thus divide the computational cost by two resulting in $N_p(N_p - 1)/2 \sim N_p^2$ operations, which is still forbiddingly expensive.

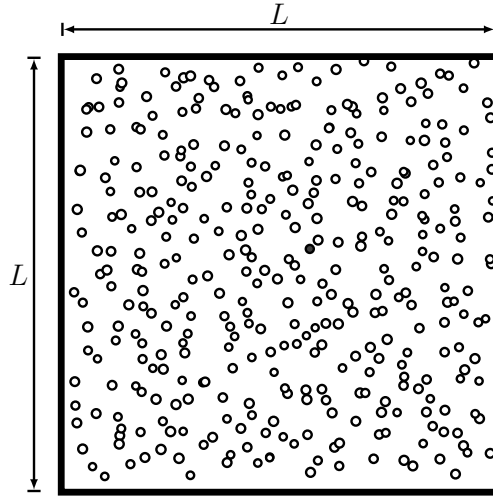


Figure 4.2: Computational domain of interest Ω of length L contains N_p particles. A particle (black dot) interacts electrostatically with all $N_p - 1$ other particles in the domain.

Periodic BCs for the particle phase correspond to an infinite domain. Therefore, to compute the electrostatic forces it is necessary to take into account the contributions of all particles, including those not really represented/computed in the computational domain.

Let a cubic computational domain Ω of length L as shown in Fig. 4.2. Consequently, consider a super-domain of (finite) length $(2N_{per} + 1)L$, where N_{per} is the number of domain images per direction i.e. the number of periodic layers around the domain (see Fig. 4.3). If d is the number of (periodic) physical dimensions, then the total number of periodic domain images including the original one is $(2N_{per} + 1)^d$. In theory, periodic BCs are exactly represented for $N_{per} \rightarrow \infty$, however in practice N_{per} will be considered finite based on a convergence criterion which entails a cut-off error (see Fig. 4.6), hence these BCs are considered as quasi-periodic.

Apparently, since the computational domain (and its periodic images) is cubic, the periodic super-domain is also cubic. This implies that for a finite number of periodic layers N_{per} , a particle that is close to the borders of the domain interacts roughly with N_{per} periodic domain images per direction towards that border, while with $N_{per} + 1$ images towards the opposite direction. Evidently, for $N_{per} \rightarrow \infty$ the ratio $(N_{per} + 1)/N_{per} \rightarrow 1$ but for N_{per} finite, this convergence is very slow as seen in Table 4.1.

Table 4.1: Slow convergence of periodic anisotropy

N_{per}	1	2	3	4	5	6	7	8	9	10
$\frac{N_{per}+1}{N_{per}}$	2.00	1.50	1.33	1.25	1.20	1.17	1.14	1.12	1.11	1.10

In fact, any particle with an offset from the domain center (essentially all particles) would always interact with more particles located to the direction of that offset than the opposite direction. Consequently, it would be subjected to a force that always points outwards of the domain (towards the closest border) that would be proportional to the offset in question, which implies an anisotropic distribution of long-range electrostatic forces. As a result, most particles would accelerate towards the domain borders and due to periodicity re-enter from the opposite side where they would re-accelerate outwards, which would eventually result in

volume. In practice, if the positions of N_p particles in the domain Ω are known, then for the calculation of \mathbf{F}_e only $N_p - 1$ distance vectors \mathbf{r}_{pq} are needed for the rest $(2N_{per} - 1)^3 (N_p - 1)$ particles in Ω and their images. For periodic BCs, the computational cost of the direct method, \mathcal{C} can be written, in terms of number of summations, as

$$\mathcal{C}(N_p, N_{per}) = \frac{(2N_{per} - 1)^3 N_p (N_p - 1)}{2} \sim 4N_{per}^3 N_p^2 .$$

Isotropy of the periodic (long-range) electrostatic forces

As explained earlier, it is very important for the correct representation of the simulated physics, that the quasi-periodic BCs are applied in such a way that the isotropy of the long-range electrostatic forces is ensured. To this end, one can calculate high order statistical moments on fluctuations \mathbf{F}'_e . Since \mathbf{F}_e is a vector field known at the particle positions, one can calculate Lagrangian tensor $\langle F'_{ei} \cdot F'_{ej} \rangle_p$, which is a measure of the corresponding electric field (see Subsect. 4.3.4) and contains 9 elements

$$\langle F'_{ei} \cdot F'_{ej} \rangle_p = \begin{bmatrix} \langle F'_{ex} \rangle_p & \langle F'_{ex} \cdot F'_{ey} \rangle_p & \langle F'_{ex} \cdot F'_{ez} \rangle_p \\ \langle F'_{ey} \cdot F'_{ex} \rangle_p & \langle F'_{ey} \rangle_p & \langle F'_{ey} \cdot F'_{ez} \rangle_p \\ \langle F'_{ez} \cdot F'_{ex} \rangle_p & \langle F'_{ez} \cdot F'_{ey} \rangle_p & \langle F'_{ez} \rangle_p \end{bmatrix} \quad (4.5)$$

whose intensity can be defined as

$$F^2 = \frac{\langle F'_{ex} \rangle_p + \langle F'_{ey} \rangle_p + \langle F'_{ez} \rangle_p}{3} .$$

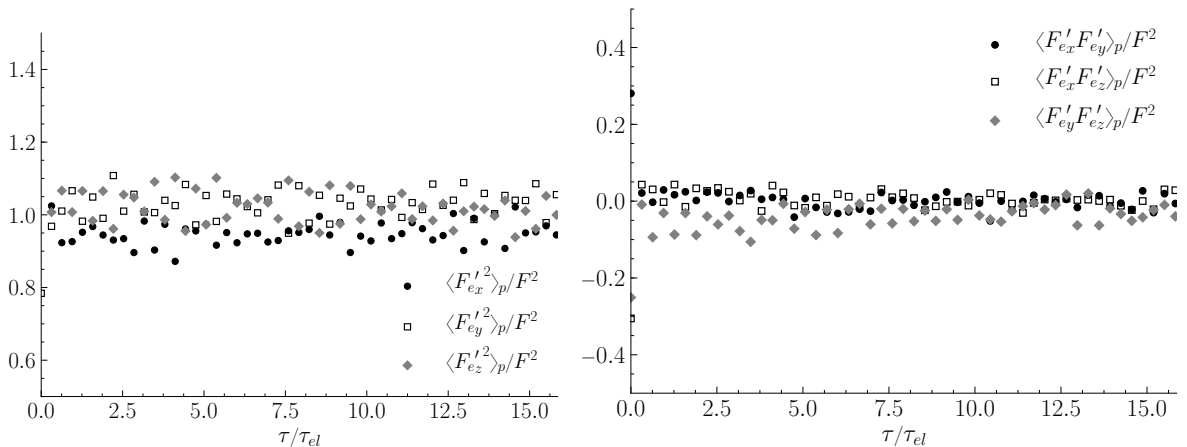
If the long-range electrostatic forces are isotropic, the following set of equations is to be satisfied

$$\langle F'_{ex} \rangle_p = \langle F'_{ey} \rangle_p = \langle F'_{ez} \rangle_p = F^2 \quad (4.6a)$$

$$\langle F'_{ei} \cdot F'_{ej} \rangle_p = 0, \quad \forall i, j = x, y, z, \quad i \neq j . \quad (4.6b)$$

To verify this, a case study has been considered with the following configuration

$$\rho_p = 2,750 \text{ kg/m}^3 \quad N_p = 10,000 \quad L = 2\pi \text{ m} \quad Q_p = 5 \times 10^{-9} \text{ C} \quad N_{per} = 1 .$$



(a) Diagonal elements Eq. (4.6a).

(b) Off-diagonal elements Eq. (4.6b).

Figure 4.4: Time evolution of Lagrangian tensor of electrostatic forces $\langle F'_{ei} \cdot F'_{ej} \rangle_p$.

The time evolution of the diagonal and off-diagonal components of the Lagrangian electrostatic forces tensor $\langle F_{e_i}^i \cdot F_{e_j}^j \rangle_p$ is presented in Fig. 4.4. It seems that Eqs. (4.6) are satisfied, which entails that the periodic electrostatic forces are isotropic.

Convergence of the periodic (long-range) electrostatic forces

Once the concept of periodic layers and volume is well established, the inevitable question rises: how many periodic layers N_{per} are needed to achieve convergence of the quasi-periodic electrostatic force calculation? Theoretically, from the point of view of a particle in the periodic volume, as more particle images are taken into account around it, there is a cut-off distance after which the long-range electrostatic forces that are exerted on it tend to cancel out as $N_{per} \rightarrow \infty$. As more periodic domain images are taken into consideration, a particle that lies in the computational domain interacts with more particles $\propto N_{per}^3$ that are placed in an increasingly greater distance $\|\mathbf{r}_{pq}^\dagger\| \propto N_{per}$. One can deduce that the electric potential energy stored in a particle, u_e can be calculated Lagrangianly as

$$u_e = \lambda Q_p \sum_{\substack{q=1 \\ q \neq p}}^{N_p} Q_q \sum_{\substack{l,m,n=-N_{per} \\ |r_{pq,i}^\dagger| \leq \alpha_c}}^{N_{per}} \frac{1}{\|\mathbf{r}_{pq}^\dagger\|} \propto N_{per}^2 \quad (4.7)$$

which implies that the particle electric potential energy diverges quadratically for tri-periodic BCs as shown by Fig. 4.5 (left). As far as the total electrostatic force on a particle is concerned, the same dynamics are in place due to periodicity, however it should be noted that $\mathbf{F}_e \propto 1/\|\mathbf{r}_{pq}\|^2 \propto 1/N_{per}^2$. In addition, although the number of electrostatic interactions scales with N_{per}^3 , the electrostatic force converges for $N_{per} \rightarrow \infty$ due to its vectorial nature and the symmetry of periodicity. From Eq. (4.2), one can deduce that

$$\mathbf{F}_e = \lambda Q_p \sum_{\substack{q=1 \\ q \neq p}}^{N_p} Q_q \sum_{\substack{l,m,n=-N_{per} \\ |r_{pq,i}^\dagger| \leq \alpha_c}}^{N_{per}} \frac{\hat{\mathbf{r}}_{pq}^\dagger}{\|\mathbf{r}_{pq}^\dagger\|^2} \propto \sum_{\substack{m=-N_{per} \\ |r_{pq,i}^\dagger| \leq \alpha_c}}^{N_{per}} \hat{\mathbf{f}}_e^{(m)} = \mathbf{f}_e. \quad (4.8)$$

In fact, Fig. 4.5 (right) shows that electrostatic forces converge very quickly for $N_{per} \geq 2$. This convergence is sufficient to correctly simulate periodic particle-particle electrostatic interactions, albeit the divergence of the electric potential energy, as \mathbf{F}_e drives particle motion (see Eq. (4.3)).

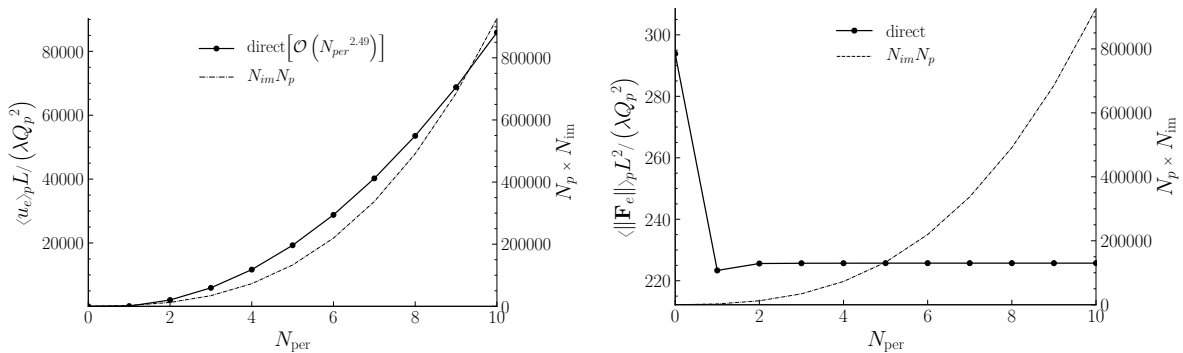


Figure 4.5: Average particle electric potential energy (left) and average norm of the electrostatic force (right) with regard to the number of periodic domain images for $N_p = 100$. Quadratic divergence is observed for the former, while convergence for the latter at $N_{per} \geq 2$.

Admittedly, the choice of a finite N_{per} entails a cut-off error. To estimate it, simulations have been performed with the same distribution of N_p particles for an increasing number of periodic layers N_{per} . Considering the simulation with the maximum number of periodic layers N_{per}^{max} as the simulation of highest fidelity, the relative error of the total electrostatic force for each particle p at $t = t_0$, $\epsilon_p^{N_{per}}(\mathbf{x}_p, t_0)$ has been calculated for each number of periodic layers N_{per} as

$$\epsilon_p^{N_{per}}(\mathbf{x}_p, t_0) = \frac{\left\| \mathbf{F}_e^{N_{per}}(\mathbf{x}_p, t_0) \Big|_{\text{direct}} - \mathbf{F}_e^{N_{per}^{max}}(\mathbf{x}_p, t_0) \Big|_{\text{direct}} \right\|}{\left\| \mathbf{F}_e^{N_{per}^{max}}(\mathbf{x}_p, t_0) \Big|_{\text{direct}} \right\|}.$$

Figure 4.6 shows that a fast convergence is achieved for $N_{per} \geq 2$, while for $N_{per} \geq 4$ absolute convergence is observed. However, the cut-off error for $N_{per} = 1$, albeit considerable, seems to be less than 20% for approximately 90% of the particles in the computational domain.

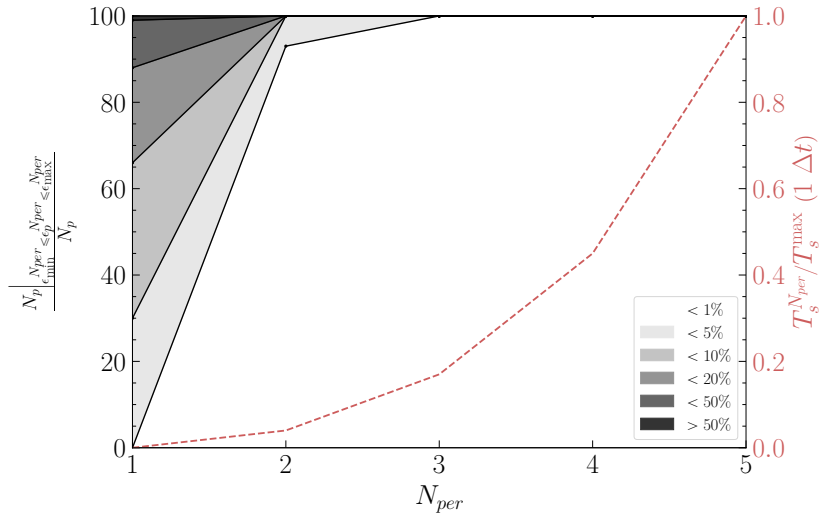


Figure 4.6: Relative cut-off error distribution of the electrostatic forces exerted on the particles for one time-step with regard to number of periodic layers N_{per} for direct algorithm with $N_p = 100$. Reference simulation is conducted with $N_{per} = 5$. A different shade of grey is attributed to the percentage of particles for which the cut-off error is between 0%, 1%, 5%, 10%, 20% and 50%. The red dashed line marks the cost of simulation. Sufficient convergence is observed for $N_{per} \geq 2$.

A way to understand the effect of the long-range field of electrostatic forces is to calculate the total electrostatic force that is exerted on a particle coming from particles that are found in an increasing distance.

$$\mathbf{F}_e(r) = \sum_{\substack{q=1, q \neq p \\ -\Delta r/2 \leq \|\mathbf{r}_{pq}\| - r \leq \Delta r/2}}^{N_p} \mathbf{F}_{q \rightarrow p}(\mathbf{r}_{pq})$$

Figure 4.7 shows that the contribution of the long-range part of electrostatic forces becomes negligible after a specific distance. The fact that this distance is smaller than half the size of the computational domain is what allows to correctly assume periodic boundary conditions in this system of charged particles, as well as justifies the choice of $N_{per} = 1$, albeit the local cut-off error.

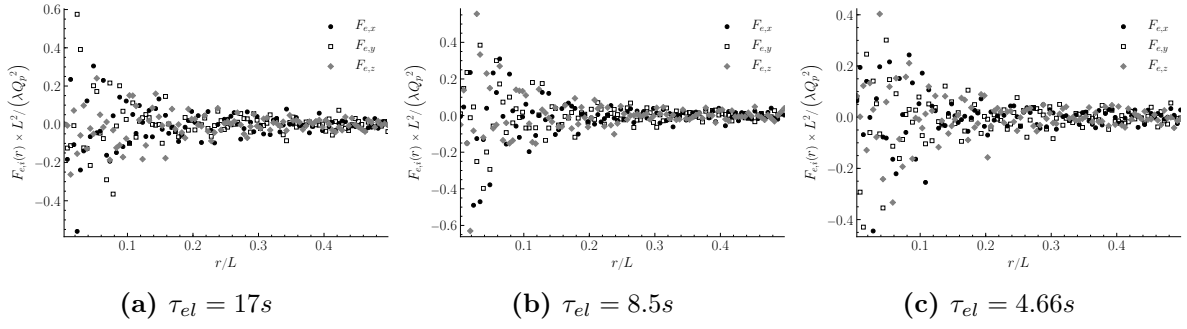


Figure 4.7: Total electrostatic force exerted on a particle due to interaction with particles that are found within an annular shell of between radius $r \pm \Delta r/2$ with $\Delta r = L/100$.

Furthermore, Fig. 4.8 shows the time evolution of several statistical moments in the transient and stationary regime. The observed attenuated oscillatory behavior is examined in Subsect. 4.3.4 where it occurs for considerably bigger time scales, as turbulence enhances the dampening of this response. It seems that the cut-off error for $N_{\text{per}} = 1$ affects mostly the transition to the statistically steady regime but not the statistical average after stationarity is reached.

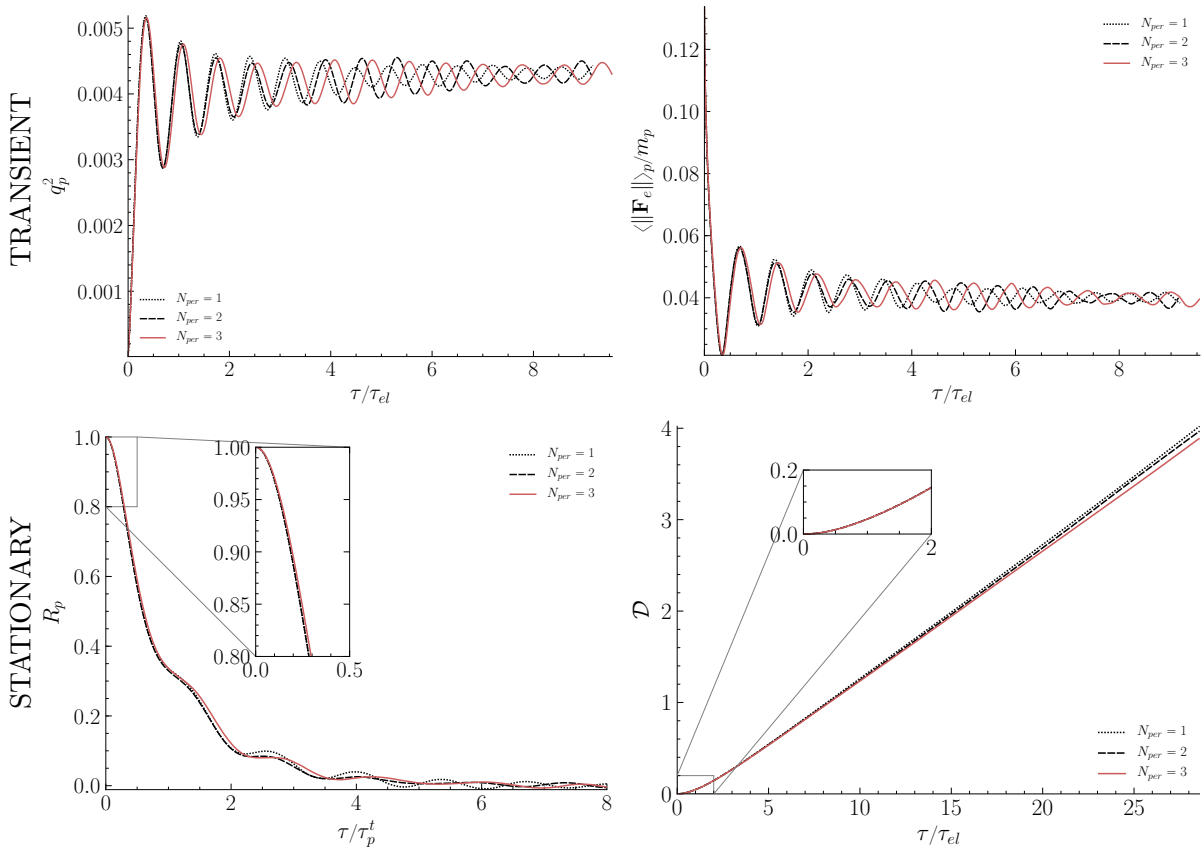


Figure 4.8: Evolution of particle agitation, Lagrangian particle velocity autocorrelation function, MSD and electrostatic acceleration for increasing number of periodic layers N_{per} . Convergence of statistics for the stationary regime is observed for $N_{\text{per}} \geq 1$.

Therefore, it can be considered negligible for a 1st order approximation, as it only affects higher-order dynamics of the granular flow, a conclusion that is in agreement with the conclusions of Bouchet & Hernquist (1988). In Table 4.2, statistical moments of the granular flow are presented for decreasing number of periodic layers N_{per} . Values for $N_{per} = 3$ are considered as the reference and relative errors are calculated for $N_{per} = 1, 2$. Despite the

Table 4.2: *Cut-off error of quasi-periodic BCs*

N_{per}	q_p^2	$\langle \ \mathbf{F}_e\ \rangle_p$	τ_p^t	D_p^t
	$10^{-3}[m^2s^{-2}]$	$10^{-2}[ms^{-2}]$	[s]	$10^{-2}[m^2s^{-1}]$
1	4.4628	3.8007	5.4487	1.6496
	0.45%	0.51%	4.14%	3.52%
2	4.4496	3.7747	5.4678	1.6320
	0.15%	-0.18%	4.50%	1.85%
3	4.4429	3.7816	5.2322	1.5935

significant cut-off errors observed in Fig. 4.6, the relative errors on the statistical moments are negligible ($< 5\%$). Thus, it seems reasonable for the simulations carried out in this work, to choose $N_{per} = 1$. This way, the domain is replicated only one time towards each direction, which means that each particle of the computational domain is centered in a cubic periodic volume of length L in which it interacts with $N_p - 1$ particles. This choice of N_{per} enables calculations of a big number of particles $10^4 \leq N_p \leq 10^6$ within reasonable computational time and acceptable statistical error.

4.2.2 Pseudo-particle method

Let the computational domain Ω be discretized in N_e cells per direction (see Fig. 4.9) of length $\Delta x_f = L/N_e$, so that each cell Ω_k contains $N_k = \sum_{n=1}^{N_p} \delta_k^{(n)} \sim N_p/N_e^3$ particles. Evidently, it is reasonable that $N_k \gg 1$ which leads to a maximum number of cells N_e^{\max} defined as

$$N_e^{\max} = N_p^{1/3}. \quad (4.9)$$

Each Ω_k forms a pseudo-particle, which is a cluster of particles "viewed" from distance as one particle of equivalent charge Q_k^{eq} and position \mathbf{x}_k^{eq} . The concept of pseudo-particles, inspired by Barnes & Hut (1986), is defined in Eq. (4.10)-(4.12) and is illustrated in Fig. 4.9.

$$Q_k^{eq} = \sum_{n=1}^{N_p} \delta_k^{(n)} Q_p \quad (4.10)$$

$$\mathbf{x}_k^{eq} = \frac{1}{Q_k^{eq}} \sum_{n=1}^{N_p} \delta_k^{(n)} Q_p \mathbf{x}_p \quad (4.11)$$

where $\delta_k^{(n)} = \delta(\mathbf{x}_p^{(n)} - \mathbf{x}_k^c)$ is the indicator function defined as

$$\delta(\mathbf{x}_p^{(n)} - \mathbf{x}_k^c) = \begin{cases} 1, & \text{if } n \in \Omega_k \\ 0, & \text{otherwise.} \end{cases} \quad (4.12)$$

and \mathbf{x}_k^c is the center of pseudo-particle cell Ω_k .

For each particle n , its neighborhood $V_p^{(n)}$ of size $\Delta x_v = (2N_v + 1) \Delta x_f$ is defined as the ensemble of $(2N_v + 1)^3$ cells around it. N_v is the number of cells for which the neighborhood

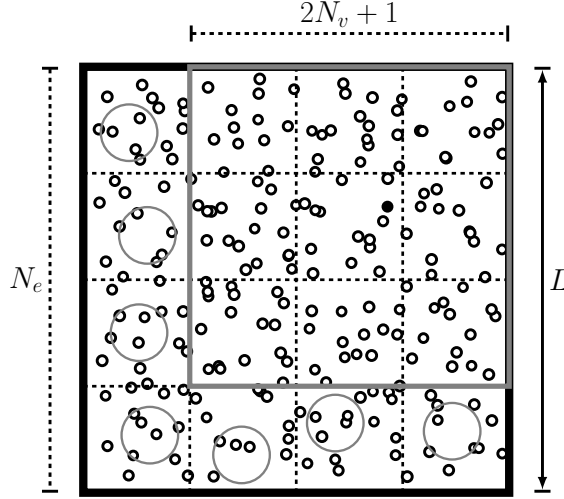


Figure 4.9: Computational domain Ω of length L is discretized in N_e cells per direction. For each particle p (black dot), its neighborhood V_p (bold gray) spans $2N_v + 1$ cells to each direction. Pseudo-particles (gray circles) are defined for every cell Ω_k outside of V_p .

spans towards every direction x, y, z (excluding the cell that contains the particle), i.e. the number of layers of direct computation around the cell of a particle. Therefore, each particle interacts directly with all particles in neighborhood V_p (short-range interaction), as well as with the pseudo-particles that are outside of V_p (long-range interaction). This allows to accurately calculate the short-range part of \mathbf{F}_e , which contains most of the information, while committing an acceptable approximation error for the long-range part. It should be noted that the total approximation error introduced from such a decoupling, depends both on the number of cells, N_e but also on the number of neighbour cells, N_v .

Observing Fig. 4.9, it is evident that for $N_v = 0$ the particle neighbourhood is limited to the very cell to which it belongs. This implies that if the particle in question is close to the borders of its cell, it would interact in proximity with the pseudo-particle of the adjacent cell which would be a violation of the very concept of pseudo-particles. For this reason, the pseudo-particle algorithm can provide reasonable results only for $N_v > 0$ (see Fig. 4.15).

The electrostatic force $\mathbf{F}_{k \rightarrow p}$ acting on particle p due to pseudo-particle Ω_k is calculated by treating Ω_k as another particle, meaning that Q_q is replaced by Q_k^{eq} and \mathbf{x}_q by \mathbf{x}_k^{eq} in Eq. (4.1). Hence, the total electrostatic force on particle p is calculated by performing direct and pseudo-particle summations inside and outside of V_p , respectively. Therefore, the total electrostatic force exerted on a particle is calculated as

$$\mathbf{F}_e = \underbrace{\sum_{\substack{k=1 \\ k \in V_p}}^{N_e^3} \sum_{\substack{q=1 \\ q \neq p}}^{N_e^3} \mathbf{F}_{q \rightarrow p}}_{\substack{\text{short-range} \\ (2N_v+1)^3 \frac{N_p}{N_e^3} - 1 \text{ terms}}} + \underbrace{\sum_{\substack{k=1 \\ k \notin V_p}}^{N_e^3} \mathbf{F}_{k \rightarrow p}}_{\substack{\text{long-range} \\ N_e^3 - (2N_v+1)^3 \text{ terms}}} . \quad (4.13)$$

Quasi-periodic boundary conditions

First of all, the following analysis is based on conclusions deduced in Subsect. 4.2.1 concerning the quasi-periodic BCs (isotropy and convergence of long-range interactions). Let

the computational domain Ω be discretized in N_e cells per direction. Evidently, the direct neighbourhood V_p that spans $2N_v + 1$ cells should fit inside the periodic cubic volume that spans $(2N_{per} - 1)N_e$ cells (as shown by Fig. 4.10), thus N_v and N_e must satisfy the inequality

$$2N_v + 1 \leq (2N_{per} - 1)N_e - 1. \quad (4.14)$$

As explained in Subsect. 4.2.1, the super-domain needed to impose periodic BCs for each particle is of length $2N_{per}L$, inside of which the periodic cubic volume of length $\alpha_c = (2N_{per} - 1)L$ is defined as shown in Fig. 4.10. The electrostatic force acting on a particle p due to a pseudo-particle Ω_k , $\mathbf{F}_{k \rightarrow p}$ is the sum of $(2N_{per} - 1)^3$ interactions due to Ω_k and its periodic images as

$$\mathbf{F}_{k \rightarrow p} = \lambda Q_k^{eq} Q_p \sum_{\substack{l,m,n=-N_{per} \\ |r_{kp,i}^\dagger| \leq \alpha_c}}^{N_{per}} \frac{\mathbf{r}_{kp}^\dagger}{\|\mathbf{r}_{kp}^\dagger\|^3} \quad (4.15)$$

where $\mathbf{r}_{kp} = \mathbf{x}_p - \mathbf{x}_k^{eq}$ is the distance vector between particle p and pseudo-particle Ω_k .

However, the notion of periodic cubic volume centered on each particle in combination with the pseudo-particles defined in each cell, introduces a subtle complexity regarding the treatment in the borders of the periodic cubic volume in question. In Fig. 4.10 one can observe that inevitably the borders of the periodic cubic volume will intersect specific cells (for each particle). Since each pseudo-particle Ω_k has an associated equivalent position \mathbf{x}_k^{eq} and charge

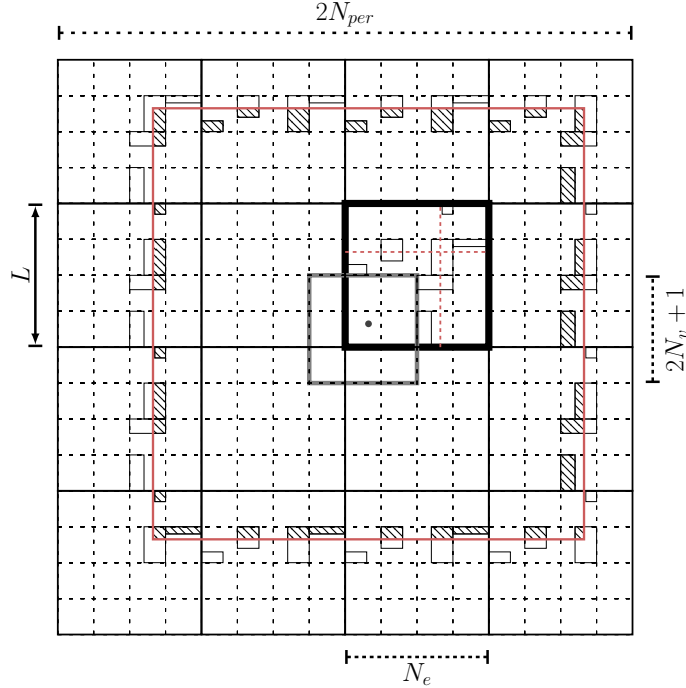


Figure 4.10: Domain of interest Ω (bold black) of length L , periodic domain images (thin black) with $N_{per} = 2$ and periodic cubic volume (thin gray) of edge $\alpha_c = 3L$. Neighborhood V_p (bold gray) with $N_v = 1$ could span over several images of Ω . Every pseudo-particle cell Ω_k can be represented by a rectangle of equivalent charge density $\rho_{q,k}^{eq}$ centered at \mathbf{x}_{eq}^k that extends up to the closest cell borders. Thus, a cell that is intersected by the periodic volume borders at position \mathbf{x}_c can be represented by a section of the corresponding rectangle (hatched).

Q_k^{eq} , a simple solution could be to include pseudo-particles that lie inside the periodic cubic volume based on their position \mathbf{x}_k^{eq} .

In fact, each pseudo-particle represents a large number of particles N_k , thus a significant contribution in \mathbf{F}_e . As a result, considering a uniform distribution of particles, every particle that has a significant offset from its cell center would be subjected to an electrostatic force that always points outwards of the domain (towards the closest border) that would be proportional to the offset in question, which implies an anisotropic long-range electrostatic force distribution. As a result, most particles would accelerate towards the cell borders and ultimately present a non physical behavior similar to that caused by an anisotropic application of the periodic BCs explained in Subsect. 4.2.1 this time on the level of the cells.

To ensure the isotropy of the long-range electrostatic interactions on the cell level, it is imperative that a smarter treatment should be put in place for the border cells of the periodic volume. Based on the work of Bouchet & Hernquist (1988), each pseudo-particle Ω_k can be represented as a rectangular charged cloud of particles X_k of total equivalent electric charge Q_k^{eq} that is centered at \mathbf{x}_k^{eq} and extends up to the closest cell borders. That means that this pseudo-particle rectangle, has an equivalent (constant) charge density $\rho_{q,k}^{eq}$ defined as

$$\rho_{q,k}^{eq} = \frac{Q_k^{eq}}{\Delta x_k \Delta y_k \Delta z_k}$$

where $\Delta \mathbf{x}_k$ are the dimensions of pseudo-particle rectangle X_k (see Sect. B.1). Evidently, for each particle the intersected cells can be easily found as the periodic volume intersects a periodic domain image at position \mathbf{x}_c , whose components can be calculated as

$$x_{c,i} = (x_{p,i} + \alpha_c) \bmod L .$$

Once the intersected pseudo-particle cells are identified, the correct section of the corresponding pseudo-particle rectangle has to be taken into account which depends on each translation to account for periodicity. Finally, using Eq. (4.15) for $\mathbf{F}_{k \rightarrow p}$ in Eq. (4.13), with the appropriate corrections for border cells, the total electrostatic force exerted on a particle can be calculated using the pseudo-particle method and quasi-periodic BCs.

Computational cost and performance

Therefore, for each particle in Ω we take into consideration $\sim (2N_v + 1)^3 N_p / N_e^3$ direct interactions and $(2N_{per} - 1)^3 N_e^3$ pseudo-particle interactions, considering the cost of pseudo-particle intersections negligible. As a result, the computational cost with periodic BCs becomes

$$\mathcal{C}(N_p, N_e, N_v, N_{per}) = N_p \left[\underbrace{(2N_v + 1)^3 N_p / N_e^3 - 1}_{\text{short-range}} + \underbrace{(2N_{per} - 1)^3 N_e^3 - (2N_v + 1)^3}_{\text{periodic long-range}} \right] \quad (4.16)$$

where it is evident that the computational cost of the (costly) short-range part is proportional to the number of particles N_p and the number of cells in the neighbourhood $\sim N_v^3$, while it is inversely proportional to the number of cells N_e^3 . However, the (smaller) long-range part is proportional N_e^3 . Therefore, the dependence of $\mathcal{C}(N_p, N_e, N_v, N_{per})$ on N_e is not evident. Figure 4.11 shows that if $N_v = \text{cst}$, as N_e increases it is evident that for $N_e \sim N_p^{1/3} \Rightarrow N_k \sim 1$ each cell Ω_k would contain at most one particle, hence the method would degrade to the direct method in terms of performance.

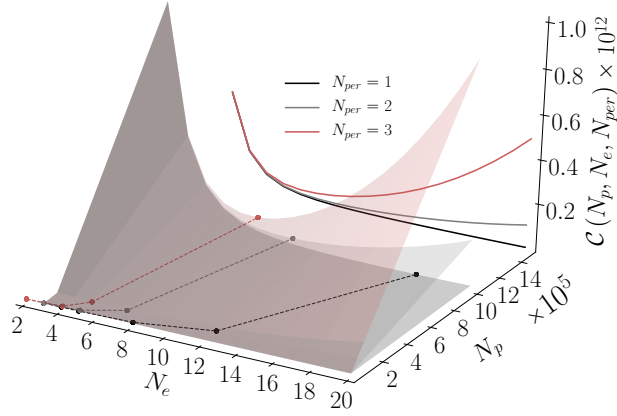


Figure 4.11: Theoretical computational cost of periodic pseudo-particle method for $N_v = 1$.

On the other hand, for smaller values of N_e , each cell would contain a large number of particles N_k , which means that a big portion of the electrostatic force calculations would be performed inside the neighbourhood as the size of each cell Δx_f would be relatively big, thus the neighbourhood size Δx_v would also be big. This means that for every number of particles N_p , there is an optimal number of cells $N_e^{opt} \in [(2N_v + 2) / (2N_{per} - 1), N_p^{1/3}]$ that minimizes the function of the computational cost of Eq. (4.16) (see Sect. B.2) which can be calculated as

$$N_e^{opt} = N_p^{\frac{1}{6}} \left(\frac{2N_v + 1}{2N_{per} - 1} \right)^{\frac{1}{2}}.$$

In this case the optimal computational cost would be

$$\mathcal{C}^{opt}(N_p, N_v, N_{per}) = N_p \left[2\sqrt{N_p (2N_{per} - 1)^3 (2N_v + 1)^3} - (2N_v + 1)^3 - 1 \right] \sim N_p^{\frac{3}{2}} N_v^{\frac{3}{2}} N_{per}^{\frac{3}{2}}.$$

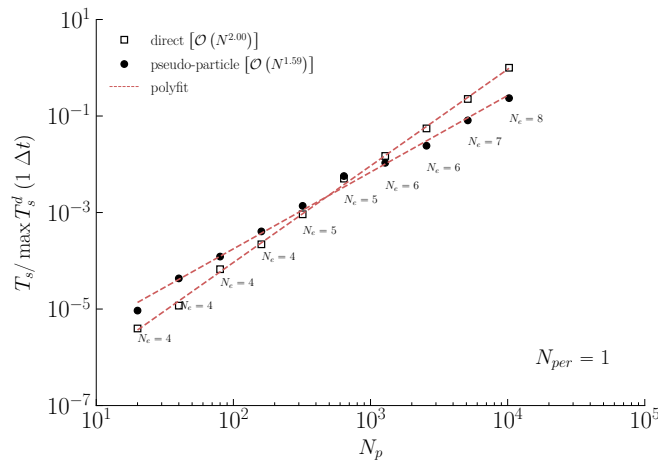


Figure 4.12: The simulation time ($1 \Delta t$) for direct and pseudo-particle algorithm ($N_v = 1$ and $N_{per} = 1$) normalized by its maximum value (for direct algorithm) is plotted against an increasing number of particles for optimal number of cells N_e^{opt} .

Figure 4.12 shows that the calculated order of complexity $\sim N_p^{1.5}$ is of similar order of magnitude than the expected theoretical one. The performance of the algorithm has been calculated for an optimal number of cells N_e^{opt} for every level of particle number N_p , as the algorithm has merit only for such a configuration. In addition, the observed slight overestimation of the anticipated theoretical value comes from the special treatment of the borders of the cubic volume in order to account for periodic BCs.

Approximation error analysis

The direct method is considered to be of high fidelity as it allows for an exact calculation of the electrostatic forces, except for the cut-off error due to quasi-periodic BCs. Hence the results obtained with this method constitute a reference for simulations using an approximative method such as the pseudo-particle method. Therefore, the relative error of total electrostatic force estimation for particle p at $t = t_0$, $\epsilon_p^{N_e}(\mathbf{x}_p, t_0)$ has been calculated for each number of cells per direction N_e as

$$\epsilon_p^{N_e}(\mathbf{x}_p, t_0) = \frac{\left\| \mathbf{F}_e^{N_e}(\mathbf{x}_p, t_0) \Big|_{\text{pseudo}} - \mathbf{F}_e^{N_{per}}(\mathbf{x}_p, t_0) \Big|_{\text{direct}} \right\|}{\left\| \mathbf{F}_e^{N_{per}}(\mathbf{x}_p, t_0) \Big|_{\text{direct}} \right\|}.$$

Figure 4.13 shows that the committed error is quasi-constant for $N_e < 10$ and then it decreases considerably for $N_e \geq 10$. For small values of N_e each pseudo-particle would contain a large number of particles N_p/N_e^3 , thus it would be a crude approximation of the cluster of particles that it represents. However, at the same time the size of each cell Δx_f would be relatively big, hence every such interaction would occur far away from the particle of interest at a distance $\geq \Delta x_v$. Therefore, the errors observed are rather moderate as only $\sim 10\%$ of particles have an

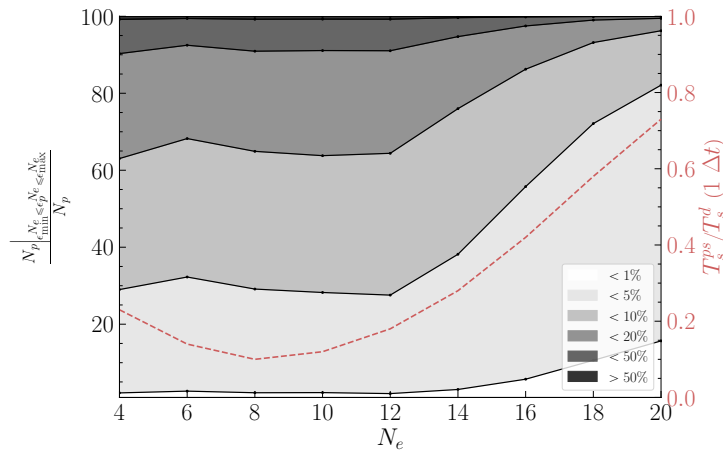


Figure 4.13: Relative approximation error distribution with regard to number of cells N_e of pseudo-particle algorithm for one time-step and $N_p = 10,000$. A different shade of gray is attributed to the percentage of particles for which the approximation error is between 0%, 1%, 5%, 10%, 20% and 50%. The red dashed line shows the simulation time of the pseudo-particle algorithm ($N_v = 1$, $N_{per} = 1$) normalized by that of the direct algorithm for the same case.

error $20\% < \epsilon_p^{N_e} < 50\%$. Increasing the number of cells N_e reduces the number of particles per cell $N_k = N_p/N_e^3$. However, at the limit of $N_k \sim 1$, where some cells contain at most one particle while some are empty, some of them will be cut by the periodic volume resulting in a

rather crude approximation of one particle via sections of the corresponding pseudo-particle rectangle which entails a remaining error that is hard to eliminate.

4.2.3 Verification of the numerical methods

To verify the direct method, one can use Newton's 3rd law that for a $p - q$ electric dipole states that the electrostatic force exerted on a particle p due to particle q is opposite of the force exerted on particle q due to particle p , or $\mathbf{F}_{p \rightarrow q} = -\mathbf{F}_{q \rightarrow p}$. For direct algorithm and quasi-periodic boundary conditions, every particle in the computational domain interacts with $(2N_{per} - 1)^3 N_p$ particles (real and images). Therefore, theoretically the average of electrostatic forces exerted on all N_p particles of the computational domain should be zero, or $\langle F_{e,i} \rangle_p = 0$, hence this can be used as a verification criterion. In order to examine that, the time evolution of the Lagrangian average of all three components of particle electrostatic forces $\langle F_{e,x} \rangle_p$, $\langle F_{e,y} \rangle_p$, $\langle F_{e,z} \rangle_p$ are plotted in Fig. 4.14.

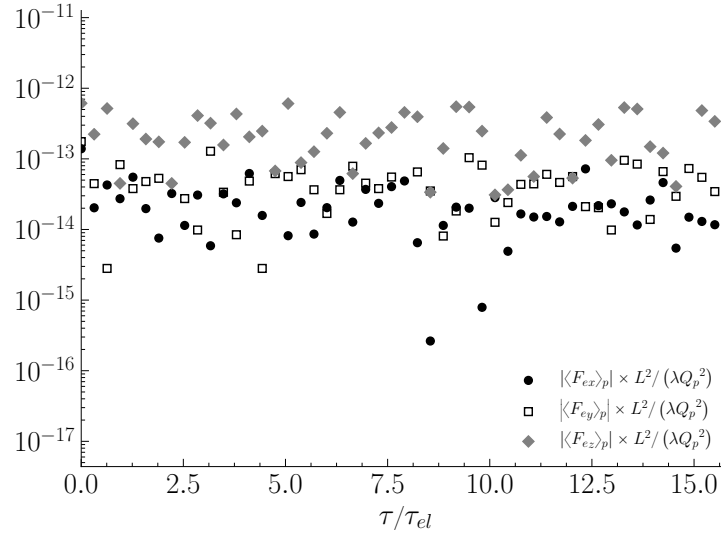


Figure 4.14: Verification of electrostatic forces calculation using Direct method.

As far as the pseudo-particle method is concerned, the equality is not perfectly satisfied, due to the approximation error from the pseudo-particle algorithm. The complexity of the pseudo-particle method with quasi-periodic BCs, stems not only from the decoupling of short- and long-range interactions (neighbourhood) but also from the notion of pseudo-particle rectangles and their sections that are specific to each periodic domain image under consideration (see Fig. 4.10). Therefore, in order to verify the electrostatic force calculation for each particle, one can calculate the sum of all charges with which it interacts, including charges of actual particles, pseudo-particles, and pseudo-particle rectangle sections. For each particle this sum should be exactly equal to $(2N_{per} - 1)^3 N_p \times Q_p$ in the case of an like-charged granular flow. This has been verified for the presented simulations, so the developed pseudo-particle algorithm and its extension for tri-periodic BCs is considered to be functioning according to its design.

4.2.4 Comparison of the numerical methods and configurations

Although the distribution of the approximation error $\epsilon_p^{N_e}(\mathbf{x}_p, t_0)$ seen in Fig. 4.13 provides a first comparison of pseudo-particle and direct method, in order to better understand how the impact

of the different numerical methods on the simulated physics, one has to examine characteristic statistical moments calculated via simulations with different numerical methods/configurations.

To this end, several simulations of an like-charged granular flow have been performed with $N_p = 10^4$ particles using Direct (DIR) and Pseudo-Particle (PS) algorithms with $N_{per} = 1$ quasi-periodic BCs. As stated in Subsect. 4.2.2, the number of cells N_e is dictated by the number of particles so as to have a desired average number of particles per cell N_k . For example, $N_k > 10$ would imply that $N_e < (N_p/10)^{1/3}$; for $N_p = 10^4$ this means that $N_e < 10$. Thus for simulations using the pseudo-particle algorithm, different numerical configurations are tested for $N_e = 4, 8$ and $N_v = 1, \dots, N_v^{\max}$. For a given number of cells N_e , the maximum number of short-range neighbourhood cells, N_v^{\max} is dictated by inequality (4.14). Table 4.3 contains N_v^{\max} for increasing number of periodic layers N_{per} and various numbers of cells N_e .

Table 4.3: Maximum number of short-range neighbourhood cells N_v^{\max}

$N_e \backslash N_{per}$	1	2	3
4	1	5	9
8	3	11	19

To begin with, Fig. 4.15 shows the need for $N_v > 0$ in pseudo-particle algorithm, as it was previously stated in Subsect. 4.2.2 which underlines the importance of a high-fidelity calculation of short-range electrostatic interactions. It is observed that the PDF of electrostatic forces obtained with pseudo-particle algorithm and $N_v = 0$ is substantially different from the one obtained using direct method which is considered the high-fidelity reference simulation. On the other hand, the shape of the PDF of electrostatic forces for pseudo-particle algorithm with $N_v > 0$ matches the one obtained via the direct method. Apparently as number of cells N_e

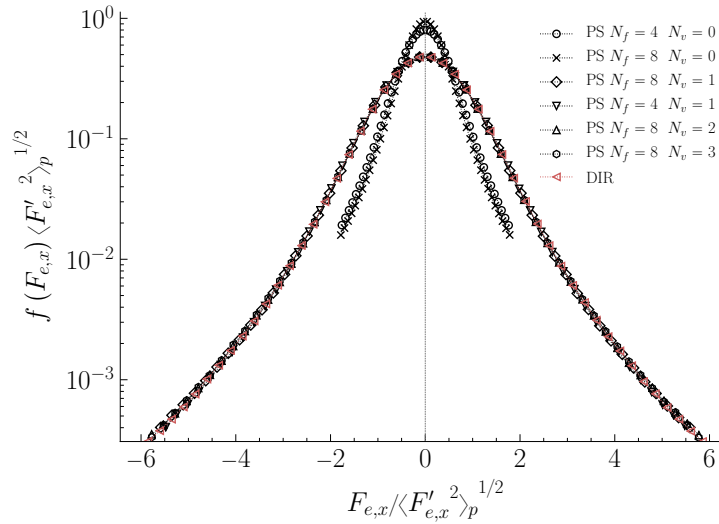


Figure 4.15: PDF of x -component of electrostatic forces for direct and pseudo-particle algorithm for various N_e with $N_v \geq 0$. Choice $N_v = 0$ should be avoided as it leads to a substantial error in the calculation of particle electrostatic forces.

increases, a greater number of cells N_v is needed into the short-range neighbourhood as the cell size decreases in order to maintain the same neighbourhood size Δx_v . In Table 4.4 statistical moments of the granular flow are presented for different numerical algorithms/configurations.

Their value using direct algorithm is considered as the value of reference and relative errors are calculated for each numerical configuration of the pseudo-particle algorithm. Despite the non-negligible approximation error observed in Fig. 4.13, it seems that it is reasonable to choose $N_e = 8$ and $N_v = 1$ for the simulations of $N_p = 10,000$ particles carried out in this work, considering the trade-off between the minimization of the approximation error and computational cost.

Table 4.4: *Approximation error for different numerical algorithms/configurations*

Algorithm		q_p^2	$\langle \ \mathbf{F}_e\ \rangle_p$	τ_p^t	D_p^t
		$10^{-3}[m^2s^{-2}]$	$10^{-2}[ms^{-2}]$	[s]	$10^{-2}[m^2s^{-1}]$
PS	$N_e = 8$	4.8537	3.9724	5.4897	1.7968
	$N_v = 1$	8.76%	4.52%	0.75%	8.92%
PS	$N_e = 4$	4.4839	4.0320	5.2013	1.7499
	$N_v = 1$	0.47%	6.09%	-4.54%	6.08%
PS	$N_e = 8$	4.6288	3.8561	5.3865	1.7002
	$N_v = 2$	3.72%	1.46%	-1.14%	3.07%
PS	$N_e = 8$	4.6026	3.8371	5.3710	1.7040
	$N_v = 3$	3.13%	0.96%	-1.43%	3.30%
DIR		4.4628	3.8007	5.4487	1.6496

4.3 Numerical simulation of dry like-charged granular flows

This section includes an analysis of numerical simulations of dry like-charged granular flows that aims to characterize the particle-particle electrostatic interactions without the influence of hydrodynamic drag or gravity forces.

4.3.1 Configuration of particle electrostatics

In this work, all particles are considered to bear equal positive charges. Practically, particles are charged via the phenomenon of triboelectrification (Grosshans & Papalexandris, 2017) which occurs when particles collide with walls and other particles. In the simulated periodic particulate flow, it is assumed that particles have had sufficient time to redistribute their charges among them via collisions. However, collisions and triboelectrification are neglected in this study because of the small solid volume fraction.

In fact, the particle phase in these numerical simulations has the characteristics described in Subsect. 2.2.4. Since particle diameter is smaller than the Kolmogorov scale, particles are numerically treated under the point-particle approximation. As such, the particle charge Q_p is considered to be concentrated in one point (particle's center of mass) defined as $Q_p = \pi d_p^2 \times \rho_Q$, where ρ_Q the particle surface charge density.

It should be noted here, that according to Hamamoto *et al.* (1992) there is a saturation limit of surface charge density for small spheres, which can be translated (via d_p) to a corresponding limit for point-particle charges. For the configuration presented in this work, this value can be estimated to be approximately $4 \times 10^{-9} C$. The various particle charges that have been considered in all numerical simulations, all given in terms of a reference charge $Q_0 = 1 \times 10^{-9} C$ are of the same order of magnitude as seen in Table 4.5.

Table 4.5: *Properties of particle electrostatics*

Parameters	Symbol	Value	Units
Reference particle density	ρ_0	100	kg/m^3
Reference electric charge	Q_0	1×10^{-9}	C
Pseudo-particle cells	N_e	8	-
Number of neighbourhood cells	N_v	1	-
Number of periodic layers	N_{per}	1	-
Time-step	Δt	5×10^{-3}	s

4.3.2 Coulomb collisions and electrostatic interactions

To analyze the effects of the charges, one should define a characteristic time scale of electrostatic interactions. This time scale is the duration of particle velocity decorrelation under the sole presence of electrostatic interactions. The mechanism of this velocity decorrelation is the Coulomb collision, which is an elastic collision between two charged particles interacting through their own electric field. In order to understand a Coulomb collision of two particles, we can imagine that they undergo an elastic collision with an effective Coulomb diameter d_{pq}^C as depicted by Fig. 4.16. These interactions are well resolved in the DNS carried out in this work and not modeled. The effective Coulomb diameter d_{pq}^C is a notion typically found in cold

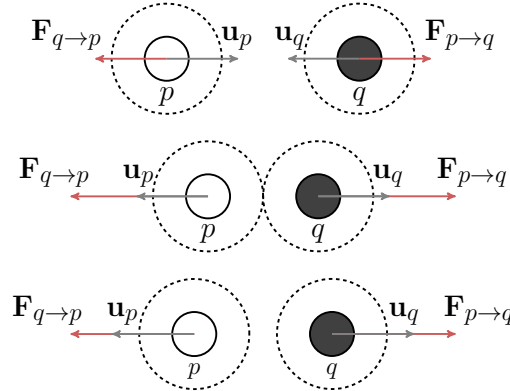


Figure 4.16: *Schematic of a Coulomb collision of two like-charged particles and notion of Coulomb diameter. Particle diameter d_p is depicted with a solid dark gray circle, while (fictitious) effective Coulomb diameter with a dashed black circle.*

plasma (Callen, 2003) and in this case it is defined as

$$d_{pq}^C = \lambda \frac{Q_p Q_q}{m_{pq} \langle \|\mathbf{w}_{pq}\| \rangle_p^2} \quad (4.17)$$

where the Lagrangian average of the norm of the relative particle velocity can be approximated by

$$\langle \|\mathbf{w}_{pq}\| \rangle_p = \sqrt{\frac{16}{\pi} \frac{2}{3} q_p^2}. \quad (4.18)$$

Additionally, $m_{pq} = m_p m_q / (m_p + m_q)$ is the reduced mass of a pair of particles p and q . If the kinetic energy of the particles is very large with regard to the electric potential energy, the deviation from the initial trajectories of the colliding particles is small. Therefore, $d_{pq}^C \leq d_p$ and particles would undergo a hard sphere collision, however the latter is not treated in our

simulations, as explained in Subsect. 2.2.4. This length scale is also used to determine the size of the neighborhood Δx_v as it should be 10 times bigger than the effective Coulomb diameter d_{pq}^C , $\Delta x_v \geq 10d_{pq}^C$. Thus, for a given number of cells N_e , one can deduce the minimum number of cells N_v^{\min} in the neighborhood of short-range interactions as

$$N_v^{\min} = \left\lceil \left(5 \frac{N_e d_{pq}^C}{L} - \frac{1}{2} \right) \right\rceil .$$

The Coulomb collision frequency, ν_{pq}^C is defined as

$$\nu_{pq}^C = \sqrt{2} n_p S_{pq}^C \langle \|\mathbf{w}_{pq}\| \rangle_p$$

where $S_{pq}^C = \pi d_{pq}^C{}^2/4$ is the effective section of the Coulomb collision. Therefore the characteristic time scale of Coulomb collisions is $\tau_{pq}^C = 1/\nu_{pq}^C$ which can be finally written as

$$\tau_{pq}^C = \frac{4}{\sqrt{2}\pi} \frac{m_{pq}^2}{\lambda^2 n_p Q_p^2 Q_q^2} \left(\frac{32}{3\pi} q_p^2 \right)^{\frac{3}{2}} .$$

Therefore in mono-disperse like-charged granular flows, $m_{pq} \sim m_p/2$ and $Q_p^2 Q_q^2 \sim Q_p^4$, so the characteristic time of Coulomb collisions can be simplified to

$$\tau_{pq}^C \simeq \frac{2}{\sqrt{2}} \frac{m_p^2}{\lambda^2 Q_p^4 n_p} \left(q_p^2 \right)^{\frac{3}{2}} . \quad (4.19)$$

An estimation of the characteristic time scale of electrostatic interactions, τ_{el} can be obtained via a simple dimensional analysis (as shown in Sect. C.1), using particle flow properties, that allows to write

$$\tau_{el} = \frac{1}{Q_p} \sqrt{\frac{2m_p}{\lambda n_p}} . \quad (4.20)$$

Dimensional analysis

To verify this, a numerical experiment is conducted, which consists of several DNS of like-charged granular flows. The particle characteristics are the ones described in Subsect. 2.2.4 and we consider as base parameters the following

$$Q_p = 5Q_0 \quad m_p = 1.80 \times 10^{-4} \text{ kg} \quad n_p = 40.314 \text{ m}^{-3} .$$

Only one of the parameters Q_p, m_p, n_p is modified at a time, while the others are kept constant. The values for m_p can be deduced from those for ρ_p of the 5 first particle classes found in Table 2.4 considering constant particle diameter d_p . Particle number density n_p depends both on the number of particles N_p and the domain size L . Therefore, keeping d_p and L constant, the values of parameters Q_p, ρ_p, N_p are chosen in the following intervals

$$Q_p \in \{1, 2, 3, 4, 5, 6\} \times Q_0 \quad \rho_p \in \{200, 100, 50, 27.5, 15\} \times \rho_0 \quad N_p \in \{10, 25, 50, 100, 150\} \times 10^3 .$$

For every simulation, the Lagrangian particle integral time scale τ_p^t can be calculated and since in such a flow particles move only due to inter-particle electrostatic interactions, it constitutes the characteristic time scale of electrostatic interactions. In this way, the effect of these parameters on τ_p^t can be isolated as shown by Fig. 4.17.

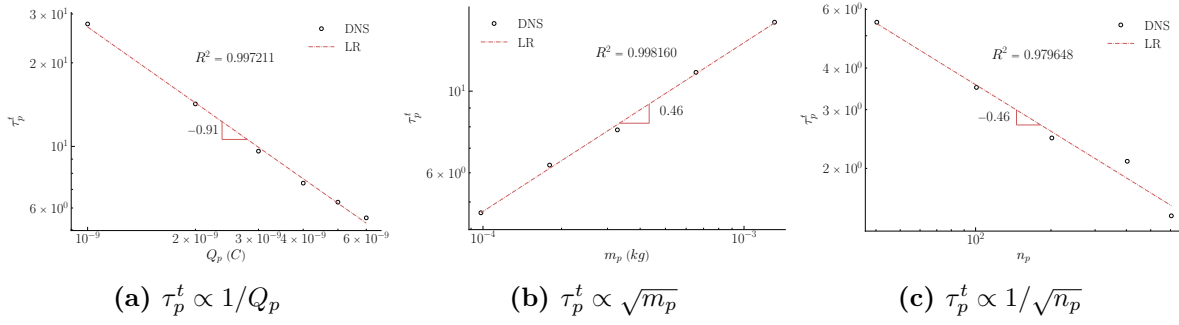


Figure 4.17: Lagrangian particle integral time scale τ_p^t for like-charged granular flow.

Considering Coulomb collisions a good physical interpretation of inter-particle electrostatic interactions, in order for τ_{el} to be a good candidate for the characteristic time scale of electrostatic interactions, it should be of the same order of magnitude as the characteristic time of Coulomb collisions, τ_{pq}^C . Thus, combining equations Eq. (4.19) and Eq. (4.20) one can deduce an estimation for particle agitation q_p^2 in like-charged granular flows as

$$q_p^2 \simeq \lambda \frac{Q_p^2 n_p^{1/3}}{m_p} \quad (4.21)$$

which in turn is confirmed by simulation results presented in Fig. 4.18.

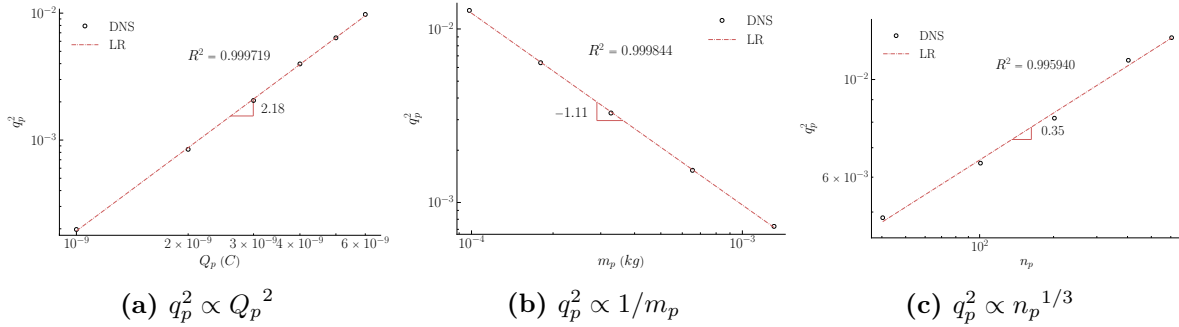


Figure 4.18: Particle agitation q_p^2 for like-charged granular flow.

Finally, Eq. (4.17) can now be simplified by replacing $\langle \|\mathbf{w}_{pq}\| \rangle_p$ with its definition from Eq. (4.18) and consequently q_p^2 from Eq. (4.21) that leads to

$$d_{pq}^C \simeq \frac{3\pi}{16} n_p^{-1/3} \approx 0.5891 n_p^{-1/3} \quad (4.22)$$

which implies that the effective Coulomb diameter in like-charged granular flows does not depend on the particle mass for like-charged granular flows. Although this is not straightforward, for such flows it can be explained by the fact that particle agitation q_p^2 depends solely on inter-particle electrostatic interactions. This means that particles are all agitated simultaneously in the same way via a self-similar repulsion mechanism that forces particles to the same homogeneous equidistant distribution. In fact, $n_p^{-1/3} = L/N_p^{1/3}$ denotes the distance between two particles if all N_p particles are put in an equidistant distribution in the cubic domain of length L , as $N_p^{1/3}$ would be the number of particles along length L . Particle mass only affects the level of this agitation (see Eq. (4.21)) and as a result, how fast this flow expands and contracts (see Eq. (4.19)) but not how far the electrostatic interactions extend.

Lastly, this analysis also allows to make an estimation of the magnitude of electrostatic forces exerted on the particles, or equivalently of the particle acceleration due to electrostatic forces, \mathbf{F}_e/m_p . Its magnitude can be estimated using characteristic time and length scales which ultimately yields

$$\frac{\langle \|\mathbf{F}_e\| \rangle_p}{m_p} \simeq 2 \frac{d_{pq}^C}{\tau_{el}^2} \approx \lambda \frac{2 Q_p^2 n_p^{2/3}}{3 m_p} = \frac{2}{3} q_p^2 n_p^{1/3} \quad (4.23)$$

which in turn is confirmed by simulation results presented in Fig. 4.19.

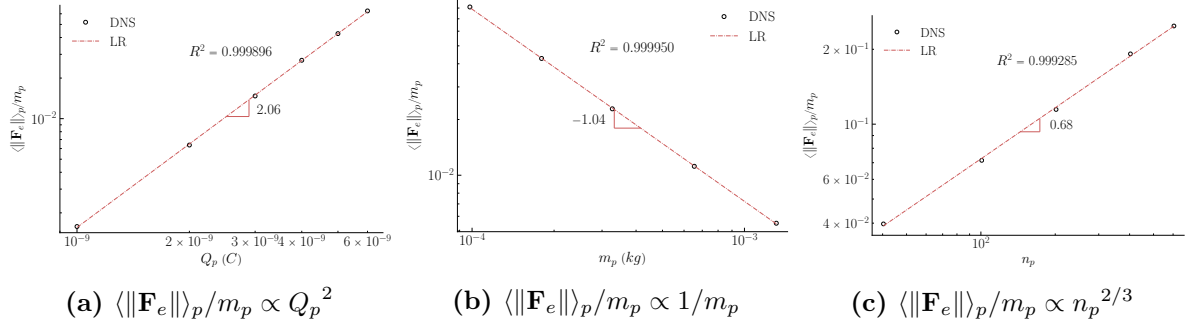


Figure 4.19: Electrostatic particle acceleration $\langle \|\mathbf{F}_e\| \rangle_p / m_p$ for like-charged granular flow.

These observations are confirmed in Table 4.6 that shows time and length scales for different particle classes and $Q_p = 5Q_0$.

Table 4.6: Characteristic scales of Coulomb interactions for $Q_p = 5Q_0$. Particles interact with each other having an effective Coulomb diameter $d_{pq}^C/d_p \simeq 34.36$.

class	τ_{el} [s]	ν_{pq}^C [s ⁻¹]	q_p^2 [10 ⁻² m ² s ⁻²]	$q_p^2 \times \frac{m_p}{\lambda Q_p^2 n_p^{2/3}}$	$\frac{\langle \ \mathbf{F}_e\ \rangle_p}{m_p} \times \frac{\tau_{el}^2}{2d_{pq}^C}$	τ_{el}/τ_p^t	$\delta l/d_{pq}^C$ [10 ⁻²]
1	17.00	0.0507	0.0652	1.107	1.162	1.190	3.299
2	12.02	0.0689	0.1339	1.137	1.146	1.124	2.240
3	8.50	0.0941	0.2740	1.164	1.147	1.134	1.530
4	6.30	0.1205	0.5157	1.205	1.147	1.147	1.078
5	4.66	0.1530	0.9866	1.257	1.166	1.039	0.747

4.3.3 Time-step sensitivity analysis

It is evident that in order to perform simulations with adequate resolution of Coulomb collisions, the simulation time-step should be appropriate in order to be able to capture correctly the modification of particle trajectories. Otherwise, approaching particles could fail to change trajectories so that they skip their (Coulomb) collision and thus re-accelerate towards the other opposite direction as seen in Fig. 4.20. Furthermore, we risk having superimposed particle dipoles that would result in a non-physical contribution $\mathbf{F}_{q \rightarrow p}$ to the short-range sum of Eq.(4.13). In any case, an inadequate time resolution seems to lead to a considerable overestimation of particle agitation. Even with an adequate time-step, it has been observed that for weak electrostatic forces, heavy particles can have a very small effective Coulomb diameter, sometimes even smaller than the physical one, $d_{pq}^C < d_p$ and as a result it is possible that particles undergo physical collisions. In this case, since physical collisions are not resolved

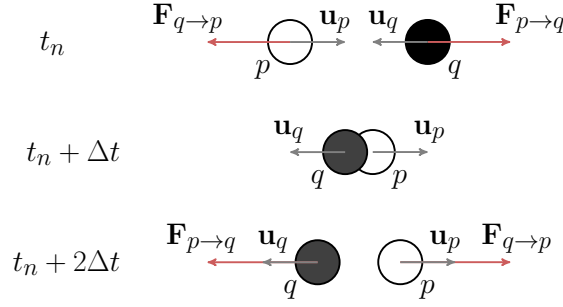


Figure 4.20: Under-resolved Coulomb collision. Contribution of superimposed particle dipole to the total electrostatic force exerted on the particles is neglected as it is non-physical.

in our simulations as explained in Subsect. 2.2.4, particles can overlap. For such a rare (in such dilute flows), but still probable event, we have taken the decision not to take into account the contribution of $\mathbf{F}_{q \rightarrow p}$ to the short-range sum of Eq.(4.13) as it would result in a non-physical particle acceleration.

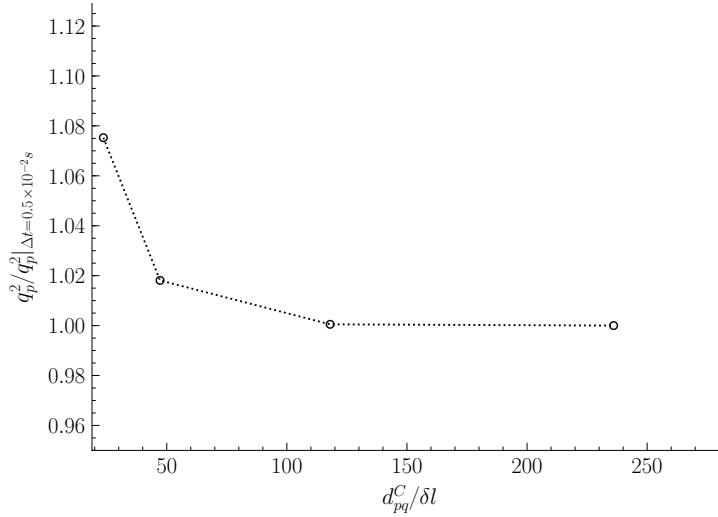


Figure 4.21: Time-step convergence.

In fact, the particle mean free path $\delta l = \langle \|\mathbf{w}_{pq}\| \rangle_p \Delta t$ should be several times smaller than the effective Coulomb diameter d_{pq}^C , hence the important parameter is $d_{pq}^C / \delta l$ which is found for every particle class in Table 4.6. This leads to the definition of a particle CFL-like condition as

$$\frac{\langle \|\mathbf{w}_{pq}\| \rangle_p \Delta t}{\max\{d_{pq}^C, d_p\}} \leq 0.01 \quad (4.24)$$

which allows to calculate a time-step threshold $\Delta t_{\max} \leq 0.01 \times \max\{d_{pq}^C, d_p\} / \langle \|\mathbf{w}_{pq}\| \rangle_p$, below which the resolution of electrostatic interactions is ensured. Figure 4.21 shows the convergence of q_p^2 for decreasing time-steps presented on Table 4.7, where it is clear that convergence for particle class #4 is achieved for $d_{pq}^C / \delta l \sim 100$ at $\Delta t \leq 1 \times 10^{-2} s$.

Table 4.7: *Time-step convergence*

Δt $10^{-2}[s]$	$d_{pq}^C/\delta l$	q_p^2 $10^{-3}[m^2s^{-2}]$	$\langle \ \mathbf{F}_e\ \rangle_p$ $10^{-2}[ms^{-2}]$	τ_p^t [s]	D_p^t $10^{-2}[m^2s^{-1}]$
5.0	23.60	5.2190 7.53%	4.0177 1.14%	9.2371 68.26%	2.7086 50.75%
2.5	47.21	4.9416 1.81%	3.9821 0.24%	5.3464 -2.61%	1.8587 3.45%
1.0	118.02	4.8562 0.05%	3.9717 -0.02%	5.4367 -0.97%	1.7934 -0.19%
0.5	236.03	4.8537	3.9724	5.4897	1.7968

4.3.4 Particle motion due to particle-induced electric field

In a charged granular flow, the only source of energy is the electric potential energy stored in the particles due to their electric charge and initial position. Figure 4.22 shows an instantaneous snapshot of the like-charged particle cloud where the velocities and electrostatic accelerations have been plotted for a qualitative appreciation of such a flow.

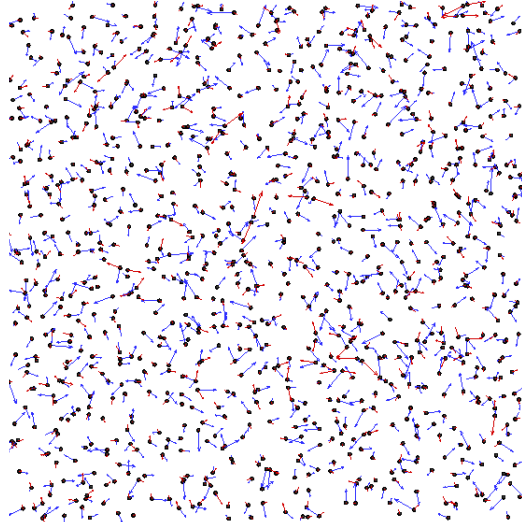


Figure 4.22: *Instantaneous snapshot of a dry like-charged particle cloud for $\tau_{el} = 8.5s$ and $\Delta x = L/10$. Particle velocities are depicted with blue color, while electrostatic forces with red.*

To get a better understanding of the physics of charged granular flows, one can begin by examining particle agitation. Figure 4.23 shows that for different levels of particle inertia, particle agitation follows an attenuated oscillation till it reaches a statistically steady value in the stationary regime. The observed oscillations are due to the expansion-contraction motion of the like-charged particle cloud due to the combination of repulsive electrostatic forces (same-sign charges) and periodic BCs.

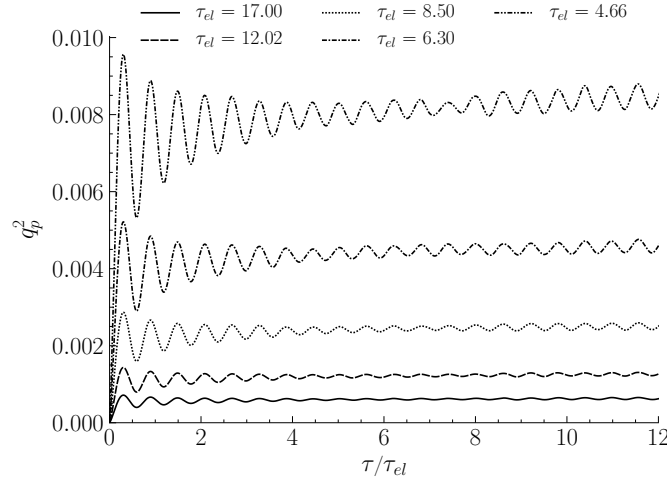


Figure 4.23: Time evolution of particle agitation for various levels of particle inertia.

Under the pdf framework for gas-particle flows presented by Simonin (2000) described in Chapter 3, the equation of the variation of particle agitation q_p^2 can be written as

$$\frac{\partial}{\partial t} q_p^2 = \frac{\langle \mathbf{F}'_e \mathbf{u}'_p \rangle_p}{m_p} \quad (4.25)$$

where the right-hand side $\langle \mathbf{F}'_e \mathbf{u}'_p \rangle_p$ is the particle-induced electrostatic power, which in the case of charged dry granular flows is equal to the time derivative of the work of electrostatic forces. By performing a simple dimensional analysis, the particle-induced electrostatic power $\mathbf{F}_e \mathbf{u}_p$ is proportional to the particle-induced electric potential ϕ .

$$\mathbf{F}_e \mathbf{u}_p \propto \frac{Q_p}{\tau_{el}} \times \phi(\mathbf{x}_p) .$$

The validity of the power balance in Eq. (4.25) is verified by Fig. 4.24 for various levels of particle inertia, where the same oscillation patterns are observed. In the stationary regime,

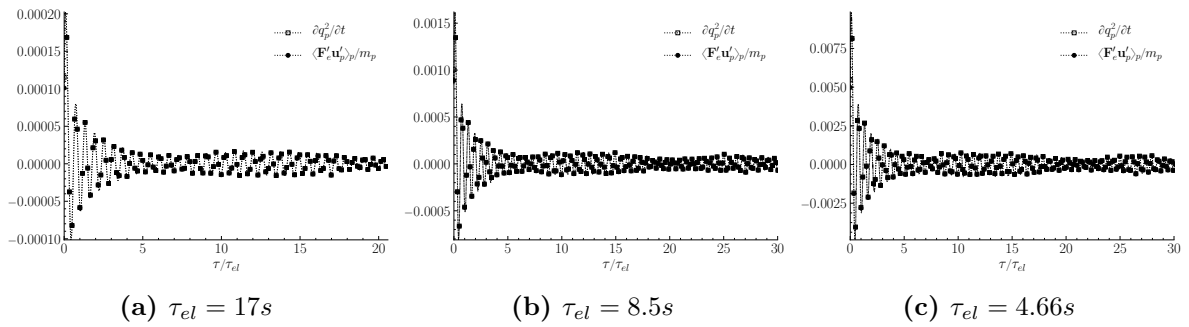


Figure 4.24: Terms of Eq. (4.25) in transient regime for increasing particle inertia.

$\partial q_p^2 / \partial t = \langle \mathbf{F}'_e \mathbf{u}'_p \rangle_p / m_p = 0$, which is in agreement with the minimum potential energy principle that is valid for conservative force fields, such as the electrostatic potential u_e . According to this principle, the system of charged particles is set to motion due to their initial electric potential energy (due to random initial position distribution), a part of which transforms to kinetic energy. Then, the system of particles tends to a (statistical) equilibrium of minimum

electric potential energy which implies that particles try to separate themselves as much as possible, hence the distance analytically predicted by Eq. (4.22). The effect of particle inertia

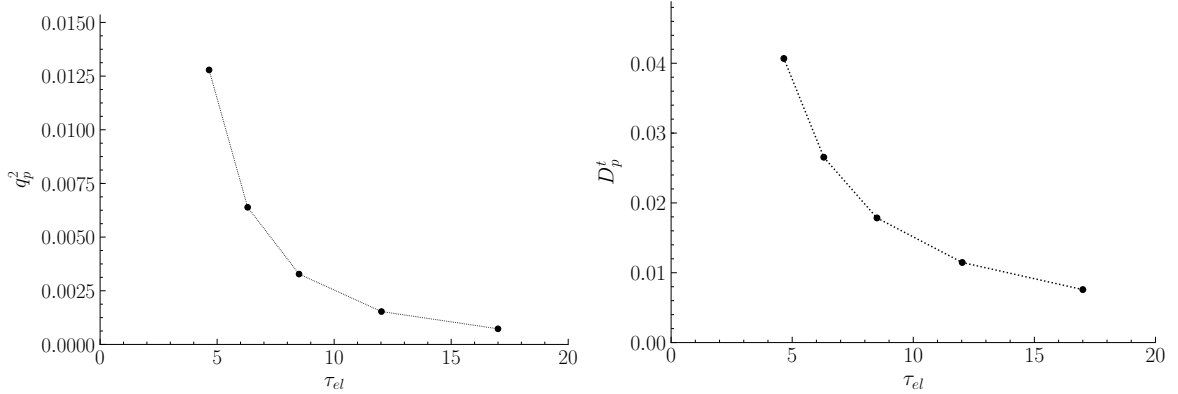


Figure 4.25: Average particle agitation and dispersion coefficient for various particle inertia.

on the average values of q_p^2 and D_p^t in the stationary regime is found in Fig. 4.25. Specifically, particle agitation and dispersion is found to decrease for increasing particle inertia. This is expected, as the initial electric potential energy stored in the particles does not depend on inertia, so it is the same for all particle classes leading to heavier particles experiencing lower levels of kinetic energy.

In Fig. 4.26 we compare the analytical models for q_p^2 of Eq. (4.21) and the theoretical Tchen-Hinze expression for D_p^t of Eq. (3.22). It seems that the latter is predicted accurately from the Tchen-Hinze theory, while the former is overestimated by the model based on macroscopic granular flow characteristics, but remains the same order of magnitude. This is probably due to accumulation of numerical error, as dry simulations have been run for long physical times in order to reach a stationary regime. So, since there is no dissipation of the particle motion any numerical error that comes from under-resolution of Coulomb collisions (can always happen even if the time-step is small) can accumulate over time and result in this overestimation (see low inertia q_p^2 in Fig. 4.23).

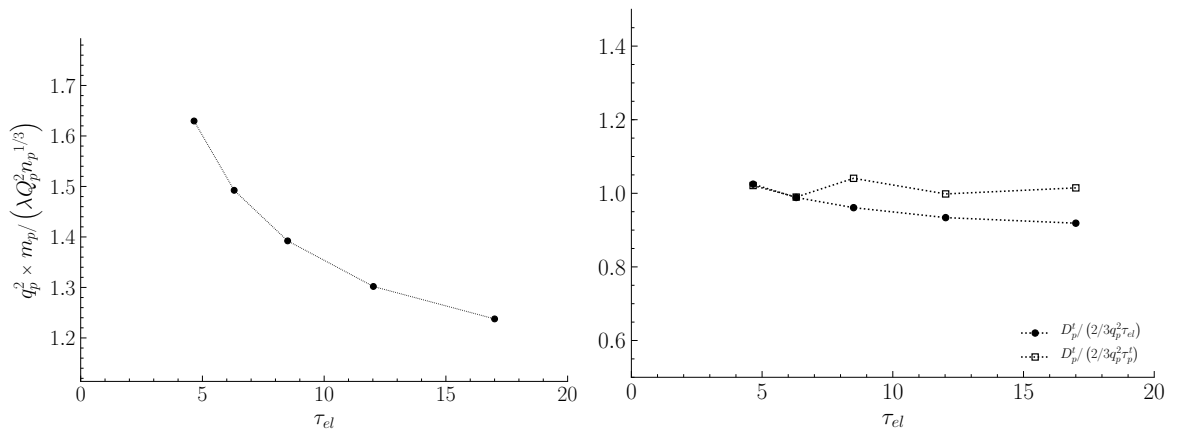


Figure 4.26: Average particle agitation and dispersion coefficient for various particle inertia.

Particle-induced electric field and potential

In a system of N_p (electrostatically) charged particles, at every time t , each particle found in position \mathbf{x}_p is immersed in a particle-induced electric field $\mathbf{E}(\mathbf{x}, t)$. Therefore, the electrostatic force \mathbf{F}_e exerted on it, is defined as

$$\mathbf{F}_e(\mathbf{x}_p) = Q_p \times \mathbf{E}(\mathbf{x}_p) \quad (4.26)$$

and the electric potential energy stored in a particle u_e as

$$u_e(\mathbf{x}_p) = Q_p \times \phi(\mathbf{x}_p) \quad (4.27)$$

where $\phi(\mathbf{x}, t)$ [V] is the particle-induced electric potential at position \mathbf{x} and time t . These two quantities are linked via Gauss's law for the electric field that describes the static electric field generated by a distribution of electric charges. It states that the electric flux through any closed surface is proportional to the total electric charge enclosed by this surface or

$$\begin{aligned} \nabla \mathbf{E} &= \frac{\rho q}{\epsilon_0} \\ \mathbf{E} &= -\nabla \phi \end{aligned}$$

where ρq is the volume charge density. Consequently, if the electrostatic forces and the electric potential energy are calculated Lagrangianly for all particles via Eq. (4.7) and (4.8), one could calculate \mathbf{E} using the definition of \mathbf{F}_e in Eq. (4.26) and ϕ using the definition of u_e in Eq. (4.27). In order to calculate \mathbf{E} and ϕ on an Eulerian N_e^3 grid, one has first to project \mathbf{F}_e/Q_p and

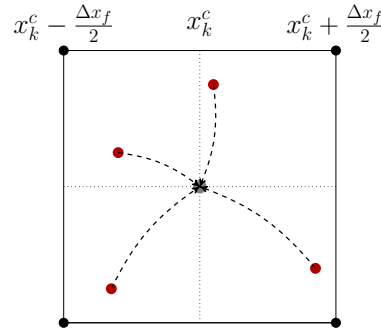


Figure 4.27: Projection of Lagrangian quantity to Eulerian cell center \mathbf{x}_k^c .

u_e/Q_p from the particles to the centers of the mesh. For each cell Ω_k with cell center \mathbf{x}_k^c , the simplest Lagrangian-Eulerian projection (see Fig. 4.27) is by calculating an average of the Lagrangian quantities of $N_k = \sum_{n=1}^{N_p} \delta_k^{(n)}$ particles inside Ω_k as

$$\begin{aligned} \mathbf{E}(\mathbf{x}_k^c) &= \frac{\sum_{n=1}^{N_p} \mathbf{F}_e(\mathbf{x}_p^{(n)}) \delta_k^{(n)}}{Q_p^{(n)} N_k} \\ \phi(\mathbf{x}_k^c) &= \frac{\sum_{n=1}^{N_p} u_e(\mathbf{x}_p^{(n)}) \delta_k^{(n)}}{Q_p^{(n)} N_k} \end{aligned}$$

where $\delta_k^{(n)} = \delta(\mathbf{x}_p^{(n)} - \mathbf{x}_k^c)$ is the indicator function defined in Eq. (4.12). After performing the before-mentioned projection, various statistics on the electric field and potential can be

calculated. The Eulerian average operator on the grid used for electrostatics is hereof denoted as $\langle \cdot \rangle_e$ in order to avoid confusions with Lagrangian averaging $\langle \cdot \rangle_p$ or Eulerian averaging on the grid used for the fluid phase $\langle \cdot \rangle_f$. Hence, the average values of the electric (vector) field and potential (scalar) field is

$$\begin{aligned}\langle \mathbf{E} \rangle_e &= \frac{1}{N_e^3} \sum_{k=1}^{N_e^3} \mathbf{E}(\mathbf{x}_k^c) \\ \langle \phi \rangle_e &= \frac{1}{N_e^3} \sum_{k=1}^{N_e^3} \phi(\mathbf{x}_k^c) .\end{aligned}$$

Therefore, one can also calculate higher order statistical moments on fluctuations \mathbf{E}' and ϕ' . Since \mathbf{E} is a vector field, one can calculate Eulerian tensor $\langle E'_i \cdot E'_j \rangle_e$ which contains 9 elements

$$\langle E'_i \cdot E'_j \rangle_e = \begin{bmatrix} \langle E'_x \cdot E'_x \rangle_e & \langle E'_x \cdot E'_y \rangle_e & \langle E'_x \cdot E'_z \rangle_e \\ \langle E'_y \cdot E'_x \rangle_e & \langle E'_y \cdot E'_y \rangle_e & \langle E'_y \cdot E'_z \rangle_e \\ \langle E'_z \cdot E'_x \rangle_e & \langle E'_z \cdot E'_y \rangle_e & \langle E'_z \cdot E'_z \rangle_e \end{bmatrix} . \quad (4.28)$$

The electric field intensity can be defined as

$$E^2 = \frac{\langle E'_x \cdot E'_x \rangle_e + \langle E'_y \cdot E'_y \rangle_e + \langle E'_z \cdot E'_z \rangle_e}{3}$$

however, another way of looking at the electric field is via the particles themselves as Eq. (4.26) Eq. (4.27) allow to know the electric field and potential at particle position. This means that instead of having the values of the electric field and potential in the center of N_e^3 cells, we can readily have them on the positions of $N_p \gg N_e^3$ particles that form a Lagrangian grid. This way the projection error is avoided and the statistics would be much more converged. In case

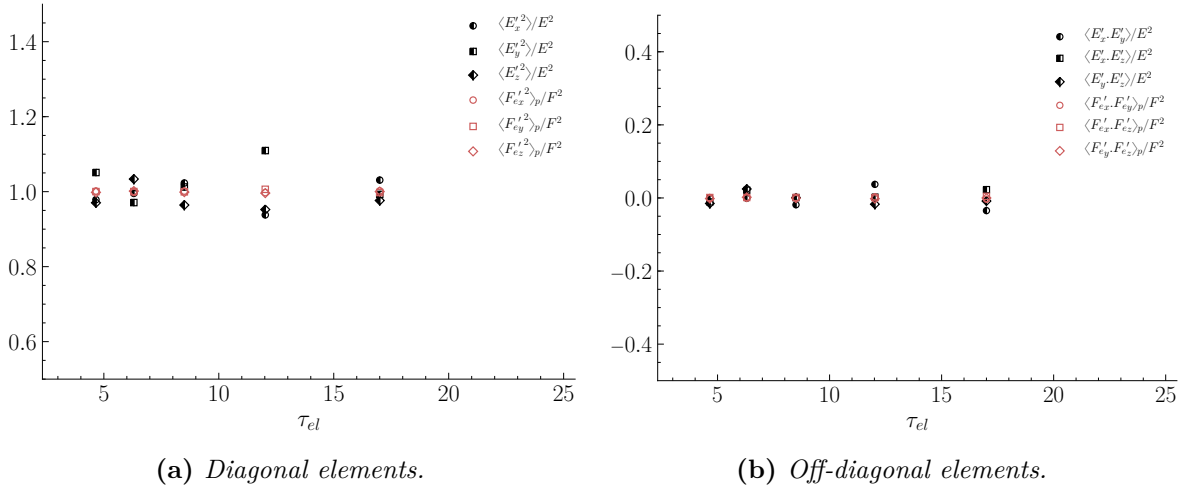


Figure 4.28: Time average of electric field tensor Eq. (4.28) with regard to τ_{el} for $Q_p = 5Q_0$.

of like-charged particles, each Eulerian covariance of the electric field $\langle E'_i \cdot E'_j \rangle_e$ of Eq. (4.28) should be of the same order of magnitude as the corresponding Lagrangian covariance of electrostatic forces $\langle F'_{ei} \cdot F'_{ej} \rangle_p$ of Eq. (4.5) normalized by the square of the particle charge as

$$\langle E'_i \cdot E'_j \rangle_e \sim \frac{\langle F'_{ei} \cdot F'_{ej} \rangle_p}{Q_p^2} .$$

Figure 4.28 shows that using the Lagrangian grid (the particles themselves) to calculate the electric field is significantly more accurate than projecting on the Eulerian grid's cell centers.

Based on Eq. (4.27), one could argue that for like-charged particles the Eulerian average of the electric potential is of the same order of magnitude as the Lagrangian average of the electrostatic potential normalized by the electric charge, or

$$\langle \phi \rangle_e \sim \frac{\langle u_e \rangle_p}{Q_p}.$$

The Eulerian average particle-induced electric potential $\langle \phi \rangle_e$ is seen in Fig. 4.29. However, it seems to fail to capture the oscillations of the Lagrangian average of the electrostatic potential.

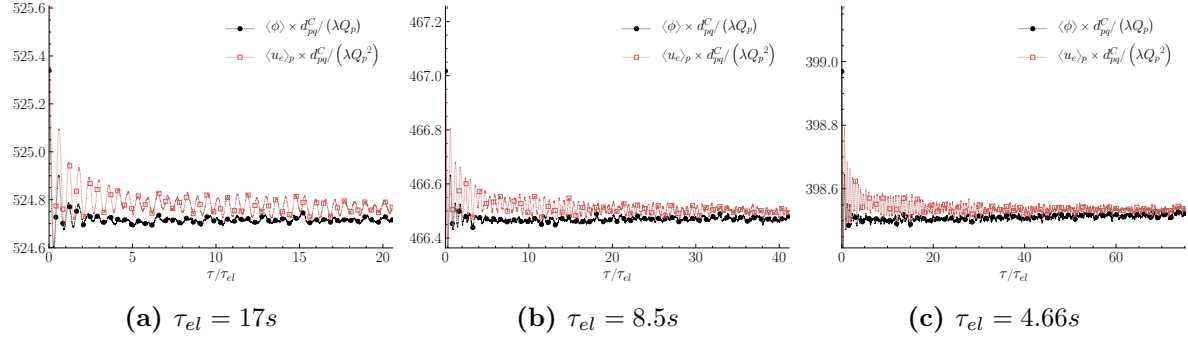


Figure 4.29: Time evolution of normalized average electric potential $\langle \phi \rangle_e \times d_{pq}^C / (\lambda Q_p)$ for various levels of particle inertia.

We observe that $\langle \phi \rangle_e$ reaches a statistical steady value in the stationary regime. The time evolution of the Eulerian variance of the electric potential $\langle \phi'^2 \rangle_e$ seen in Fig. 4.30 is more suitable as a criterion for the stationarity of the granular flow.

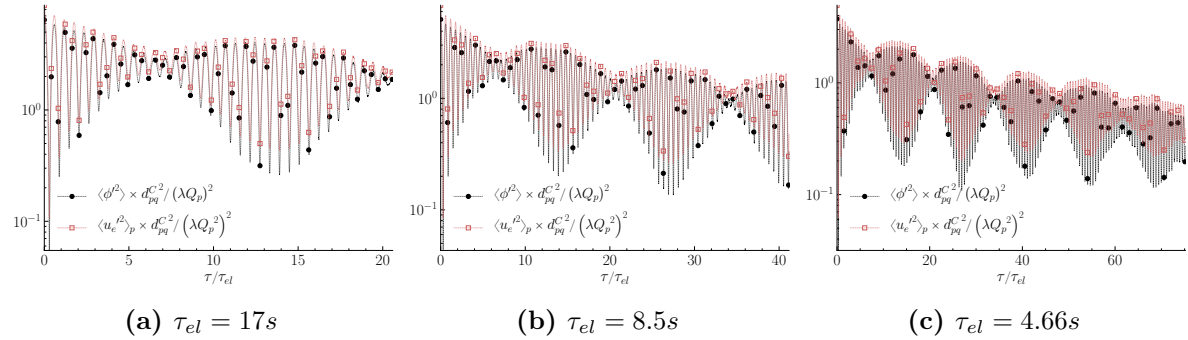


Figure 4.30: Time evolution of normalized variance of electric potential $\langle \phi'^2 \rangle_e \times d_{pq}^{C^2} / (\lambda Q_p)^2$ for various levels of particle inertia.

4.3.5 Distribution and time scale of electrostatic forces

In this Subsection, an analysis of the very nature of electrostatic forces is attempted via their distribution and their lifetime for a cloud of charged particles. Firstly, The Probability Density Function (PDF) of each component of the particle electrostatic force $f(F_{e,i})$ is calculated for each particle class. In order to do so, an interval has to be decided from the non-dimensional

analysis on the granular case study presented in Subsect. 4.3.2. Hence, an order of magnitude of the particle electrostatic force can be estimated based on Eq. (4.23) as $F_e^{\min} = -1/2 \times m_p L / \tau_{el}^2$ and $F_e^{\max} = 1/2 \times m_p L / \tau_{el}^2$.

In Fig. 4.31 one can observe the PDFs of the components of electrostatic forces, where it is evident they collapse on each other when normalized by the corresponding variance. This means that the distribution of electrostatic forces among the particles is independent of

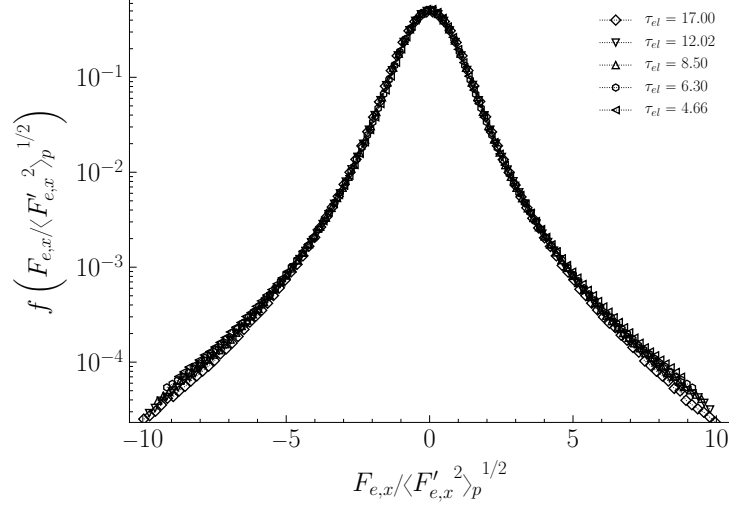


Figure 4.31: PDF of x -component of electrostatic forces for all particle classes ($Q_p = 5Q_0$).

particle inertia. Furthermore, in order to characterize the nature of inter-particle electrostatic interactions one can examine the Lagrangian autocorrelation function of electrostatic forces $R_{f_e}(\tau)$ exerted on the particles, which is defined as

$$R_{f_e}(\tau) = \frac{\langle F'_{e,i}(\mathbf{x}_p(t), t) F'_{e,i}(\mathbf{x}_p(t + \tau), t + \tau) \rangle_p}{\langle F_{e,i}^{\prime 2}(\mathbf{x}_p(t), t) \rangle_p}. \quad (4.29)$$

In Fig. 4.32 it is evident that electrostatic forces decorrelate rapidly, and follow an attenuated oscillation, which is due to the expansion-contraction motion of the like-charged particle cloud.

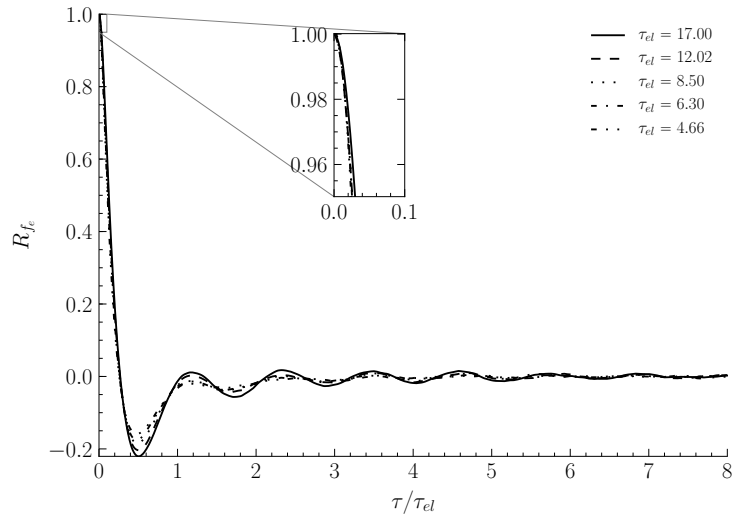


Figure 4.32: Autocorrelation function of electrostatic forces for various τ_{el} .

Finally, autocorrelation function R_{f_e} also has a negative part, which corresponds to an obtuse angle between the initial electrostatic force fluctuation $\mathbf{F}'_e(t)$ and the current fluctuation $\mathbf{F}'_e(t + \tau)$ as

$$\begin{aligned} \langle \mathbf{F}'_e(t) \mathbf{F}'_e(t + \tau) \rangle_p < 0 &\Leftrightarrow \\ \langle \cos [\angle (\mathbf{F}'_e(t), \mathbf{F}'_e(t + \tau))] \rangle_p < 0 &\Leftrightarrow \\ 3\pi/2 > \langle \angle (\mathbf{F}'_e(t), \mathbf{F}'_e(t + \tau)) \rangle_p > \pi/2 . \end{aligned}$$

This periodic change in orientation is characteristic of the periodic expansion-contraction motion of the charged particle cloud explained in Subsect. 4.3.4.

4.4 Conclusion

In order to isolate electrostatic interactions, like-charged dry particle clouds have been considered without the presence of any turbulent fluid flow. Trying to calculate such electrostatic forces, especially considering tri-periodic boundary conditions, a challenging problem arises: that of electrostatic periodicity. More specifically, the successful application of electrostatic periodicity requires the ensuring both of the convergence and of the isotropy of the long-range electrostatic field. In order to address that, and at the same time consider the computational cost as well as the accuracy of the calculations, a rather efficient algorithm has been created and its characteristics as well as the obtained results are extensively analyzed and documented. Following, an attempt to explain the nature of electrostatic interactions is made via an analogy with hard collisions. In fact, particle-particle (repulsive) electrostatic interactions can be viewed as (Coulomb) collisions happening with an effective Coulomb diameter that is proportional to the square of electric charge and inversely proportional to the square of the norm of relative particle velocity. By considering this analogy, one can deduce a Coulomb collision frequency and consequently a characteristic time scale of electrostatic interactions. A dimensional analysis supports this theory and it is verified via the corresponding measured quantities obtained by DNS of charged particle-laden flows. Finally, particle agitation is linked to the particle-induced electric field and the very nature of electrostatic forces is observed in detail.

Bibliography

- Appel, Andrew W. 1985. An Efficient Program for Many-Body Simulation. *Siam journal on scientific and statistical computing*.
- Barnes, Josh, & Hut, Piet. 1986. A hierarchical $O(N \log N)$ force-calculation algorithm. *Nature*, **324**, 446–449.
- Bouchet, F.R., & Hernquist, L. 1988. Cosmological Simulations Using The Hierarchical Tree Method. *The astrophysical journal supplement series*.
- Callen, J.D. 2003. *Fundamentals of plasma physics*. University of Wisconsin.
- Deserno, Markus, & Holm, Christian. 1998a. How to mesh up Ewald sums. I. A theoretical and numerical comparison of various particle mesh routines. *The journal of chemical physics*, **109**(18), 7678–7693. Publisher: American Institute of Physics.

- Deserno, Markus, & Holm, Christian. 1998b. How to mesh up Ewald sums. II. An accurate error estimate for the particle–particle–particle-mesh algorithm. *The journal of chemical physics*, **109**(18), 7694–7701. Publisher: American Institute of Physics.
- Ewald, P. P. 1921. Die Berechnung optischer und elektrostatischer Gitterpotentiale. *Annalen der physik*, **369**(3), 253–287.
- Greengard, L., & Rokhlin, V. 1987. A fast algorithm for particle simulations. *Journal of computational physics*, **73**(2), 325–348.
- Greengard, Leslie. 1990. The Numerical Solution of the N-Body Problem. *Computers in physics*, **4**(2), 142–152. Publisher: American Institute of Physics.
- Grosshans, H., & Papalexandris, M.V. 2017. Direct numerical simulation of triboelectric charging in particle-laden turbulent channel flows. *Journal of fluid mechanics*, **818**, 465–491.
- Hamamoto, N., Nakajima, Y., & Sato, T. 1992. Experimental discussion on maximum surface charge density of fine particles sustainable in normal atmosphere. *Journal of electrostatics*, **28**(2), 161–173.
- Hockney, R.W., & Eastwood, J.W. 1988. *Computer Simulation Using Particles*. CRC Press.
- Kolehmainen, J., Ozel, A., Boyce, C.M., & Sundaresan, S. 2016. A hybrid approach to computing electrostatic forces in fluidized beds of charged particles. *Aiche journal*, **62**(7), 2282–2295.
- Perram, John W., Petersen, Henrik G., & de Leeuw, Simon W. 1988. An algorithm for the simulation of condensed matter which grows as the $3/2$ power of the number of particles. *Molecular physics*, **65**, 875–893.
- Simonin, O. 2000. Statistical and continuum modelling of turbulent reactive particulate flows. part 1 : Theoretical derivation of dispersed eulerian modelling from probability density function kinetic equation. *Pages – of: Lecture series 2000-06, von karman institute for fluid dynamics, rhodes saint genèse (belgium)*. Von Karman Institute for Fluid Dynamics.
- van Dommelen, L., & Rundensteiner, E.A. 1989. Fast, adaptive summation of point forces in the two-dimensional Poisson equation. *Journal of computational physics*, **83**(1), 126–147.
- Yao, Yuan, & Capecelatro, Jesse. 2018. Competition between drag and Coulomb interactions in turbulent particle-laden flows using a coupled-fluid–Ewald-summation based approach. *Physical review fluids*, **3**(3), 034301.

5

Electrically charged particle-laden turbulent gas flows

“ἐν μόνον ἀγαθὸν εἶναι, τὴν ἐπιστήμην,
καὶ ἐν μόνον κακόν, τὴν ἀμαθίαν¹”

- Socrates, c. 470 – c. 399 BC

Abstract

In this chapter, the complete physics that are in the epicenter of this PhD are simulated: a like-charged inertial particle cloud transported by a stationary homogeneous isotropic turbulent gas flow. At first, the configuration for the simulations is presented where an electrostatic Stokes number is defined. Then, we examine the effect of electric charge on particle dispersion where the obtained results are verified via the transport equations of particle agitation and fluid-particle velocity covariance. The observed trends are interpreted physically using classical notions of particle-laden flows as well as the concept of Coulomb collisions presented in Chapter 4. To deepen our understanding of this effect, various statistics have been deployed such as autocorrelation functions of fluid and particle velocity, mean square particle displacement, probability density functions of particle velocities and electrostatic forces, etc. Following, we focus on the effect of charges on spatial particle distribution and relative motion via PDFs of particle concentration, RDFs of inter-particle distance and relative velocity as well as nearest-neighbor distance characteristics. Lastly, we are interested in the effect of particle number density.

5.1 Configuration of like-charged case studies

In Chapter 4 we analyzed particle-particle electrostatic interactions in dry charged granular flows. However, in the case of charged particles transported by a turbulent gas flow, although the fundamental elements of that analysis stay the same, the physics change considerably. Namely in such a flow, particles are set in motion both due to the electrostatic force \mathbf{F}_e and the drag force \mathbf{F}_d , hence Eq. (2.20) becomes

$$m_p \frac{d\mathbf{u}_p}{dt} = \mathbf{F}_d + \mathbf{F}_e . \quad (5.1)$$

To characterize the competition between the hydrodynamic drag and electrostatic forces, one could define an electrostatic Stokes number in analogy with the particles Stokes number. Having defined a characteristic time scale of electrostatic interactions τ_{el} in Subsect. 4.3.2, the electrostatic Stokes number is defined as τ_{fp}^F/τ_{el} , which is directly proportional to the electric charge. It should be noted that such a definition of the electrostatic Stokes number is substantially different from those found in literature. Indeed, on one hand Alipchenkov *et al.* (2004) use the Coulomb number defined as the ratio of the potential energy of Coulomb inter-particle interaction to the kinetic energy at small scales of the turbulence. On the other hand, Karnik & Shrimpton (2012) defined an electric settling velocity representing the terminal velocity of a particle under the influence of a given electric field. Furthermore, one could

¹There is only one good, knowledge, and one evil, ignorance.

attempt to link particle and electrostatic Stokes numbers and describe their dependence on fluid-particle-electrostatics properties. An elementary dimensional analysis allows to rewrite the electrostatic Stokes number τ_p^{St}/τ_{el} in terms of the particle Stokes number τ_p^{St}/τ_f^t as

$$\frac{\tau_p^{St}}{\tau_{el}} = Q_p \sqrt{\frac{\lambda n_p \tau_f^t}{\pi d_p \mu_f}} \times \left(\frac{\tau_p^{St}}{\tau_f^t} \right)^{1/2}. \quad (5.2)$$

Simulations of like-charged particle-laden turbulent gas flows are performed using the pseudo-particle method described in Subsect. 4.2.2 for particles of various inertia levels (see Table 5.1). Configuration for particle electrostatics can be found in Table 4.5. Since electrostatic interactions are directly linked with particle electric charge Q_p , in order to investigate how electrostatic interactions affect particle dynamics, in the following analysis statistical quantities are presented either for $Q_p = 5Q_0$ (when focusing on the transient regime). The same statistics are also presented for various levels of electric charges in comparison with the charge-free case (when focusing on the stationary regime). Therefore, the important parameters are

$$Q_p \in \{1, 2, 3, 4, 5, 6, 8, 10\} \times Q_0 \quad \rho_p \in \{200, 100, 50, 27.5, 15, 7.5, 4, 2\} \times \rho_0.$$

Figure 5.1 shows that the relation between the two Stokes numbers is quadratic and that Eq. (5.2) fits well DNS data. Although expressions of d_{pq}^C , $\langle \|\mathbf{w}_{pq}\| \rangle_p$ and τ_{el} given by Eqs. (4.17)–

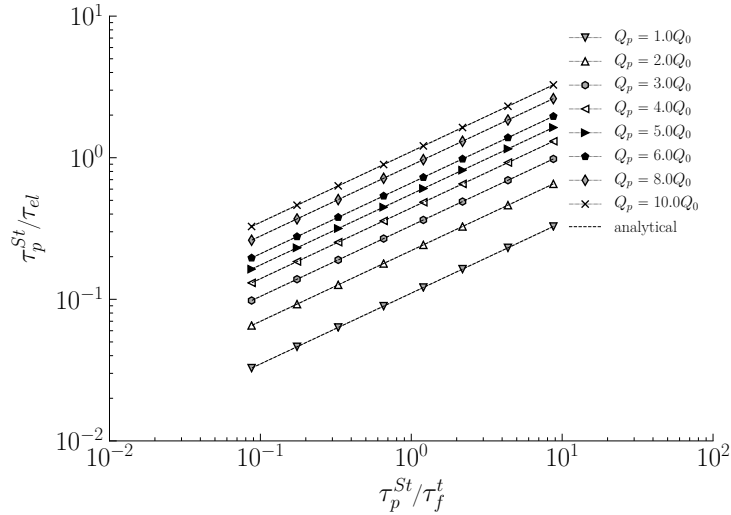


Figure 5.1: *Electrostatic Stokes with regard to the particle Stokes number for various levels of electric charge. Symbols correspond to the numerical simulation and the dashed lines to the analytical Eq. (5.2).*

(4.20) are still valid by definition, theoretical estimations for q_p^2 , d_{pq}^C and $\langle \|\mathbf{F}_e\| \rangle_p/m_p$ of Eqs. (4.21)–(4.23) do not remain the same since they were deduced in the absence of fluid in the flow. Based on a measurement of particle agitation, one can calculate the characteristic quantities of electrostatic interactions that are aggregated in Table 5.1 along with the aforementioned electrostatic Stokes number τ_p^{St}/τ_{el} for the eight particle classes of Table 2.4.

The last column of Table 5.1 provides the criterion of time-step convergence for each particle class. Surprisingly, for the same time-step, the motion of heavier particles seems to be less resolved. This is due to the fact that heavier particles undergo more binary Coulomb collisions than those of light particles in the sense of smaller effective Coulomb diameters

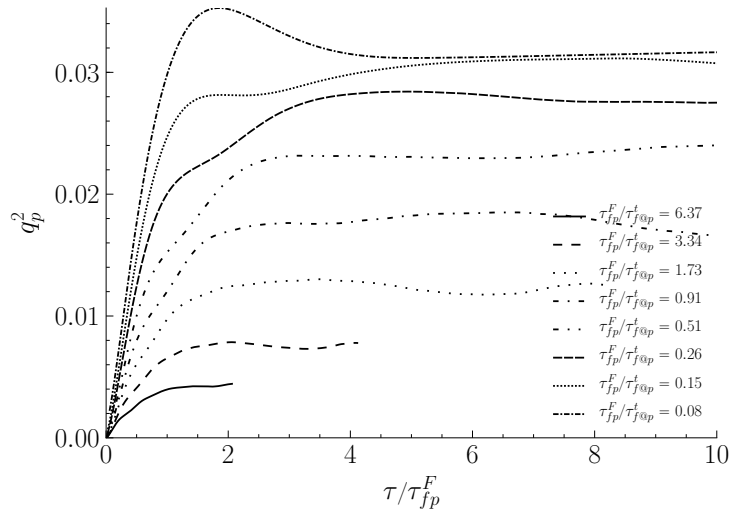
Table 5.1: Stokes numbers and characteristic scales of Coulomb interactions of like-charged particles in turbulent gas flow for $Q_p = 5Q_0$.

class	τ_p^{St}/τ_K	τ_{fp}^F/τ_f^t	$\tau_{fp}^F/\tau_{f@p}^t$	τ_{fp}^F/τ_{el}	d_{pq}^C/d_p	ν_{pq}^C	q_p^2	$d_{pq}^C/\delta l$
						$[10^{-2}s^{-1}]$	$[10^{-2}m^2s^{-2}]$	
1	53.8	7.57	6.37	1.41	4.54	0.840	0.445	36.9
2	26.9	3.81	3.34	1.01	5.27	0.502	0.768	32.6
3	13.4	1.92	1.732	0.72	6.49	0.969	1.25	31.5
4	7.39	1.07	0.910	0.54	8.30	1.89	1.78	33.9
5	4.03	0.596	0.510	0.41	11.6	4.23	2.33	41.2
6	2.02	0.304	0.263	0.29	19.2	12.7	2.81	62.1
7	1.08	0.164	0.147	0.22	33.3	39.9	3.03	104
8	0.538	0.0825	0.0774	0.15	66.5	155	3.09	202

and lower collision frequency (resembling physical collisions in a dilute regime). This implies that for the former, although a Coulomb collision is more unlikely to occur, when it does, a smaller time step is needed to resolve them accurately. In addition, for weak electric charges, the effective Coulomb diameter can also be smaller than the physical diameter of the (heavy) particles, which means that they would undergo hard collisions as well. However, since this is a rather rare event in dilute flows, it can be neglected with a negligible loss of accuracy in the representation of the physics.

5.2 Effect of same-sign electric charges on particle dispersion

This section demonstrates and analyzes the effects of inter-particle (repulsive) electrostatic forces on particle dispersion. Figure 5.2 illustrates the evolution of particle agitation with regard to time normalized by the particle relaxation time τ_{fp}^F (see Eq. (2.42)).

**Figure 5.2:** Evolution of particle agitation for various Stokes numbers in the transient regime for $Q_p = 5Q_0$. Stationarity is reached after several multiples of τ_{fp}^F .

It is evident that the agitation of like-charged inertial particles, transported by a turbulent

gas flow, achieves a stationary regime after several multiples of the particle relaxation time. Lighter particles achieve this stationary regime later in terms of τ_{fp}^F . To ensure the stationarity of the granular flow, one needs to check the time evolution of the Eulerian variance of the electric potential $\langle \phi'^2 \rangle_e$ seen in Fig. 5.3. It seems that despite the particles being electrically charged, $\langle \phi'^2 \rangle_e$ becomes quickly statistically steady, which signifies the stationary regime of the turbulent charged particle-laden gas flow. For the stationary regime, $\partial q_p^2 / \partial t = 0$, in addition

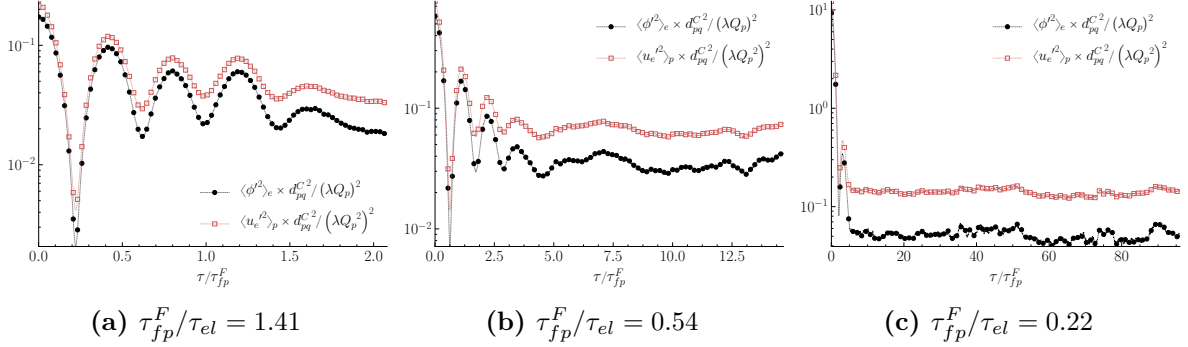


Figure 5.3: Time evolution of normalized variance of electric potential $\langle \phi'^2 \rangle_e \times d_{pq}^{C2} / (\lambda Q_p)^2$ for various levels of particle inertia for $Q_p = 5Q_0$.

to spatial averaging (allowed by homogeneity) one can perform time averaging (allowed by stationarity), due to the ergodicity property. Therefore, the ensemble average $\langle \cdot \rangle_p$ operator takes the form of Eq.(2.46). Lastly, Fig. 5.4 depicts the time average of the diagonal and off-diagonal elements of the electric field tensor, which both confirm the isotropy of the electric field, hence of the field of electrostatic forces. Finally, statistical moments have been calculated

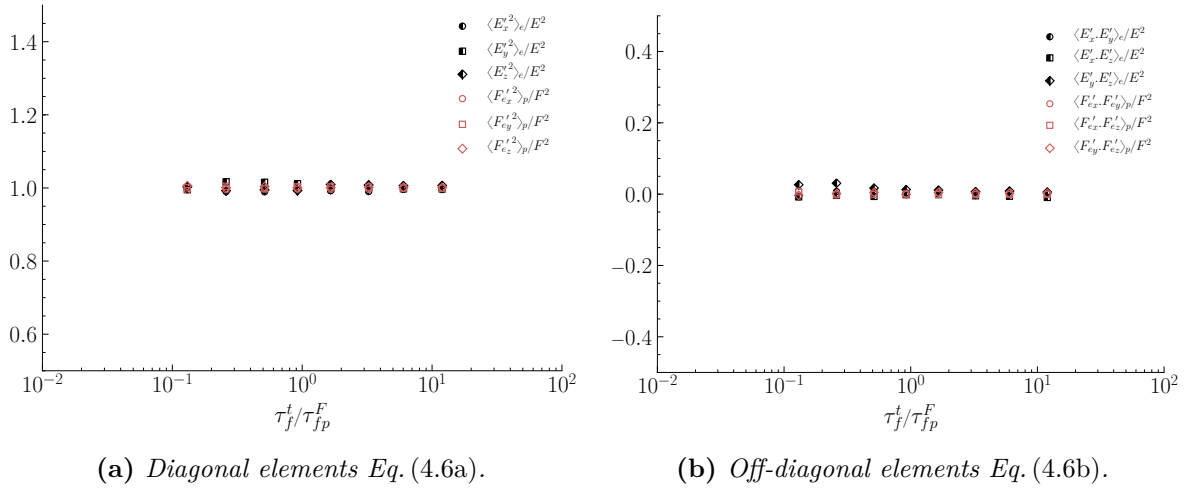


Figure 5.4: Time average of electric field tensor Eq. (4.28) with regard to particle inertia for $Q_p = 5Q_0$.

over a sufficiently long duration $T_{stat} \simeq 5 \times \max\{\tau_{f@p}^t, \tau_{fp}^F, \tau_{el}\}$ in order to achieve statistical convergence. Also all time-lag statistics presented here (autocorrelation functions, MSD, etc...) have been calculated as the average of 10 realizations that have been launched consecutively after a sufficient offset ΔT_{off} .

5.2.1 Energy transfer from turbulence to charged particles

In turbulent (electrically) charged particle-laden gas flows, particles move due to the hydrodynamic drag forces that are exerted on them from the fluid turbulent velocity field and the electrostatic forces that are exerted on them due to the particle-induced electric field. More specifically, there are three mechanisms that dictate the particle motion: a particle accelerates due to the hydrodynamic drag force and the total electrostatic force exerted on it while at the same time its kinetic energy is dissipated due to viscosity via the former.

Effect of electrostatic interactions on particle agitation

To examine the effect of particle-particle electrostatic interactions on particle agitation, we shall reproduce the extension of the Tchen-Hinze law Eq. (3.9) for various electric charges. As seen by Fig. 5.5, the effect of electrostatic interactions on particle agitation is not straightforward. Particles with large inertia $\tau_{fp}^F \rightarrow \infty$, are not particularly affected by electrostatic interactions, those with moderate inertia $\tau_{fp}^F \sim \tau_f^t$ exhibit an increase in agitation, while on the contrary lighter particles $\tau_{fp}^F \rightarrow 0$ undergo a significant decrease in their levels of agitation. To

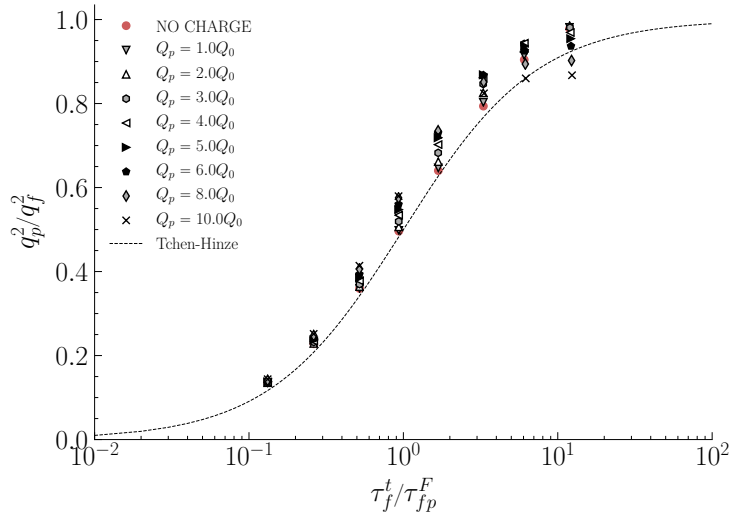


Figure 5.5: Effect of electrostatic interactions on particle agitation with regard to particle inertia for various levels of electric charge. The black dashed line corresponds to the Tchen-Hinze theory given by Eq. (3.10) and the red markers to the charge-free case.

understand this behavior, one should consider the transport equation of particle agitation which can be derived in the pdf framework for gas-particle flows presented by Simonin (2000). For $\mathbf{F}_g = 0$ the total force exerted on a particle is

$$\mathbf{F}_p = -m_p \frac{\mathbf{u}'_p - \mathbf{u}'_{f@p}}{\tau_p} + \mathbf{F}_e . \quad (5.3)$$

Under a linear approximation for the drag force, which implies $\tau_p = \text{const.}$, Eq. (3.26) considering Eq. (5.3) becomes

$$\frac{\partial}{\partial t} q_p^2 = \frac{q_{fp}}{\tau_{fp}^F} - \frac{2q_p^2}{\tau_{fp}^F} + \frac{\langle \mathbf{F}'_e \mathbf{u}'_p \rangle_p}{m_p} . \quad (5.4)$$

The four terms of Eq. (5.4) are shown by Fig. 5.6 and the balance of the equation is verified in the transient regime for $Q_p = 5Q_0$ for particle class corresponding to an electrostatic Stokes number of $\tau_{fp}^F/\tau_{el} = 0.72$.

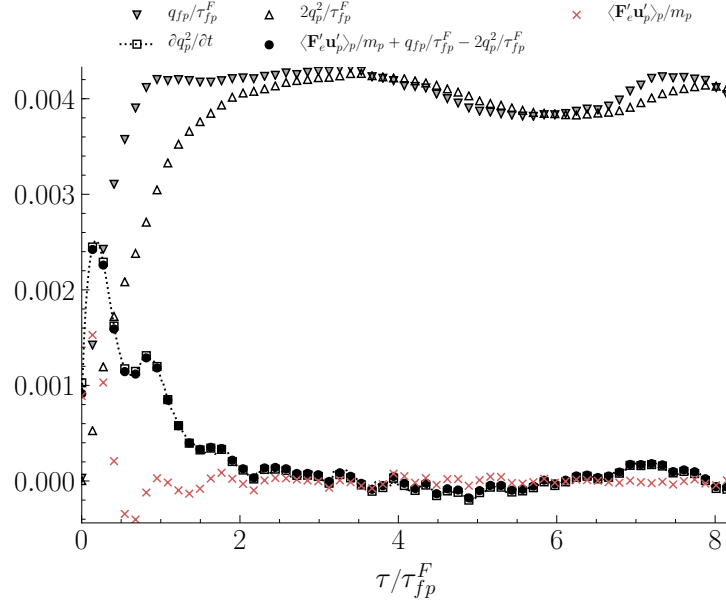


Figure 5.6: Time evolution of terms of Eq. (5.4) in transient regime for $\tau_{fp}^F/\tau_{el} = 0.72$.

In case of stationary flow $\partial q_p^2/\partial t = 0$, so Eq. (5.4) becomes

$$q_p^2 = \frac{1}{2}q_{fp} + \frac{1}{2}\tau_{fp}^F \frac{\langle \mathbf{F}'_e \mathbf{u}'_p \rangle_p}{m_p}. \quad (5.5)$$

which is the modification of Tchen-Hinze law Eq.(3.29) to account for electrostatic interactions. The additional term $\tau_{fp}^F \langle \mathbf{F}'_e \mathbf{u}'_p \rangle_p / m_p$ represents the particle-induced electric potential energy per unit mass which is equal to the work of electrostatic forces (see Subsect. C.2). This means that particle agitation depends on fluid-particle velocity covariance (i.e. the particle-turbulence interaction) and particle-induced electric potential energy. Term $\tau_{fp}^F \langle \mathbf{F}'_e \mathbf{u}'_p \rangle_p / m_p$ is strongly affected by τ_{fp}^F which includes the effect of particle inertia, so in order to obtain a better understanding we examine the term $\langle \mathbf{F}'_e \mathbf{u}'_p \rangle_p / (\langle \mathbf{F}'_e \mathbf{u}'_p \rangle_p^2 \langle \mathbf{u}'_p \mathbf{u}'_p \rangle_p)^{1/2}$ to isolate the effect of the particle-induced electric potential energy. In fact, As shown by Fig. 5.7, term $\langle \mathbf{F}'_e \mathbf{u}'_p \rangle_p$ can be considered negligible. The physical meaning of this term could be better understood by considering Coulomb collisions which are considered elastic collisions at a distance as electrostatic forces are conservative. Therefore, they should not have an effect on particle agitation and so does this term.

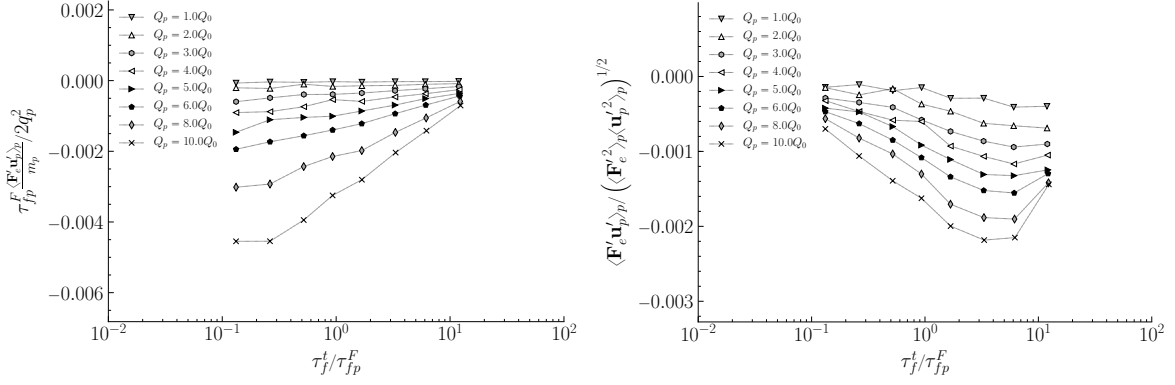


Figure 5.7: Effect of electrostatic interactions on term $\langle \mathbf{F}'_e \mathbf{u}'_p \rangle_p / m_p$ with regard to particle inertia for various levels of electric charge.

Figure 5.8 shows that q_{fp} is the most important term of Eq. (5.5), in that it accounts for most of the variation of particle agitation. Indeed, the observed variation of q_p^2/q_{fp} is of the order of magnitude $\sim 0.5\%$ of that of $\langle \mathbf{F}'_e \mathbf{u}'_p \rangle_p / q_p^2$ seen by Fig. 5.7.

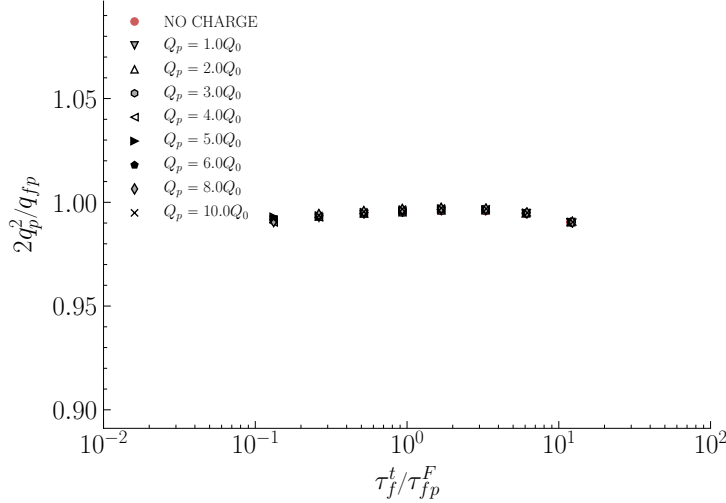


Figure 5.8: Effect of electrostatic interactions on the ratio between the particle kinetic energy and the fluid-particle velocity covariance with regard to particle inertia for various levels of electric charge.

Effect of electrostatic interactions on fluid-particle velocity covariance

It is shown in Subsect. 3.2.1 that the key to understanding the behavior of particle agitation in such a flow, is to understand fluid-particle velocity covariance q_{fp} , which is a measure of fluid-particle correlation. Figure 5.5 shows that particles with large inertia, are not particularly affected by electrostatic interactions, those with moderate inertia exhibit an increase both in $q_{fp} \simeq 2q_p^2$ and in $\tau_{f@p}^t$, while on the contrary the lightest particles undergo a significant decrease in their levels of fluid-particle velocity covariance.

To understand this behavior, one should consider the transport equation of the fluid-particle velocity covariance, which can be derived in the pdf framework for gas-particle flows presented by Simonin (2000). For $\mathbf{F}_g = 0$ the total particle force is given in Eq. (5.3). Under

a linear approximation for the drag force, which implies $\tau_p = \text{const.}$, Eq. (3.30) considering Eq. (5.3) becomes

$$\frac{\partial}{\partial t} q_{fp} = \langle \mathbf{a}'_{f@p} \mathbf{u}'_p \rangle_p - \frac{q_{fp}}{\tau_{fp}^F} + \frac{2q_{f@p}^2}{\tau_{fp}^F} + \frac{\langle \mathbf{F}'_e \mathbf{u}'_{f@p} \rangle_p}{m_p}. \quad (5.6)$$

In Subsect. 3.2.2 it is shown that the fluid-particle destruction term $\langle \mathbf{a}'_{f@p} \mathbf{u}'_p \rangle_p$ is usually modeled in literature (Zaichik *et al.*, 2003) as $-q_{fp}/\tau_{fp}^t$, which is even less accurate under the influence of electrostatic forces as shown by Fig. 5.9. However, the introduced model of Eq. (3.40) seems to be closer to the DNS measurements although the effect of electrostatic interactions seems not to be taken into account, especially using Eq. (3.39a) instead of Eq. (3.42) for $\tau_{a@p}\tau_\epsilon$. Figure 5.10 depicts all five terms of Eq. (5.6) and the power equilibrium is verified

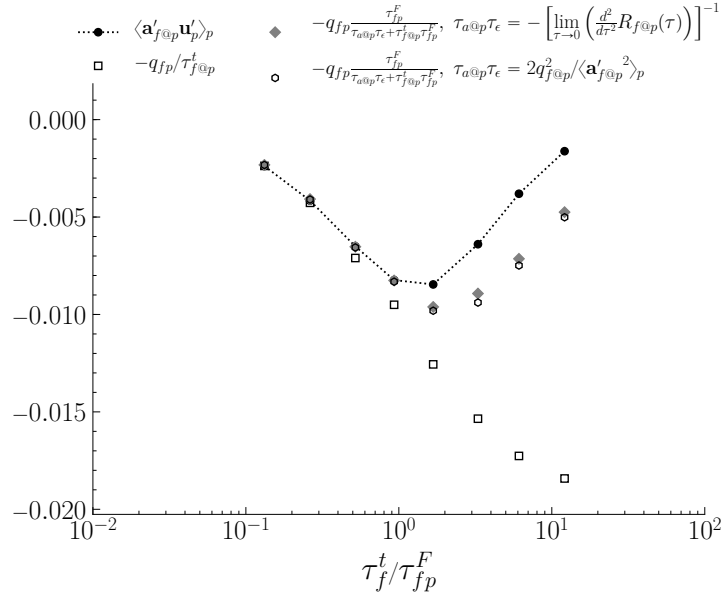


Figure 5.9: Comparison between DNS results (●) and the predictions of the Langevin model (□) and the introduced stochastic model (◆, ○) of the fluid acceleration - particle velocity covariance $\langle \mathbf{a}'_{f@p} \mathbf{u}'_p \rangle_p$ with regard to particle Stokes number for $Q_p = 5Q_0$.

in the transient regime for $\tau_{fp}^F/\tau_{el} = 0.72$. Furthermore, for stationary flows $\partial q_{fp}/\partial t = 0$, so Eq. (5.6) becomes

$$q_{fp} = \tau_{fp}^F \langle \mathbf{a}'_{f@p} \mathbf{u}'_p \rangle_p + 2q_{f@p}^2 + \tau_{fp}^F \frac{\langle \mathbf{F}'_e \mathbf{u}'_{f@p} \rangle_p}{m_p} \quad (5.7)$$

which is the modification of Tchen-Hinze law Eq.(3.32) to account for electrostatic interactions. Term $\tau_{fp}^F \langle \mathbf{F}'_e \mathbf{u}'_{f@p} \rangle_p / m_p$ represents the turbulence-induced electric potential energy.

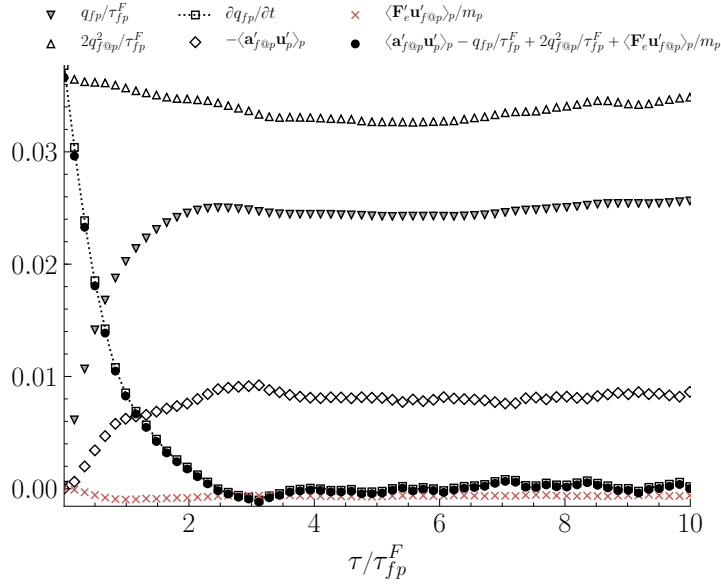


Figure 5.10: Time evolution of terms of Eq. (5.6) in transient regime for $\tau_{fp}^F/\tau_{el} = 0.41$.

To explain the behavior of q_p^2 observed in Fig. 5.5 via q_{fp} , one needs to examine the three terms of the right hand side of Eq. (5.7). Term $\tau_{fp}^F \langle \mathbf{F}'_e \mathbf{u}'_{f@p} \rangle_p / m_p$ is strongly affected by τ_{fp}^F which includes the effect of particle inertia, so in order to obtain a better understanding we examine the term $\langle \mathbf{F}'_e \mathbf{u}'_{f@p} \rangle_p / (\langle \mathbf{F}'_e{}^2 \rangle_p \langle \mathbf{u}'_{f@p}{}^2 \rangle_p)^{1/2}$ so that we isolate the effect of the turbulence-induced electric potential energy. Increasing particle charge, term $\langle \mathbf{F}'_e \mathbf{u}'_{f@p} \rangle_p / m_p$ becomes very important, especially for light particles as shown by Fig. 5.11. Therefore, in

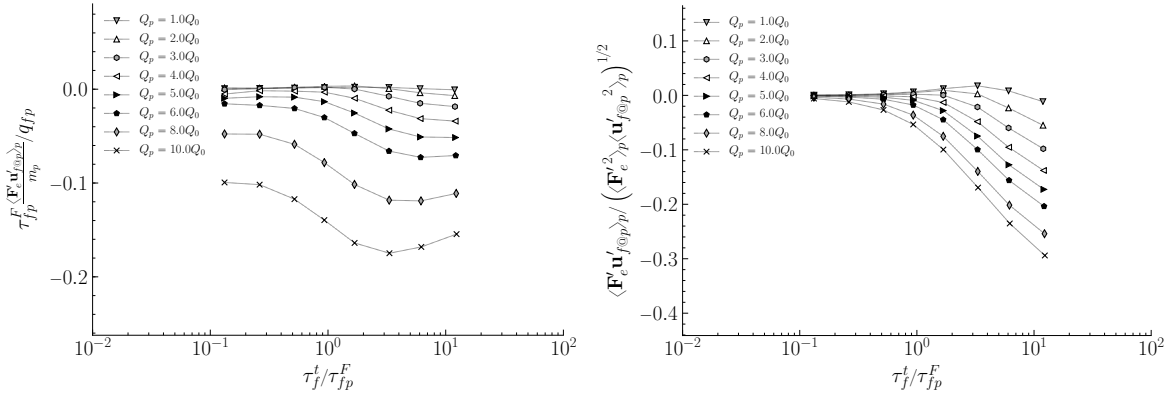


Figure 5.11: Effect of electrostatic interactions on term $\langle \mathbf{F}'_e \mathbf{u}'_{f@p} \rangle_p / m_p$ with regard to particle inertia for various levels of electric charge.

presence of electric charges the hydrodynamic forces compete with the repulsive electrostatic forces as the latter tend to constantly decorrelate the particle velocities from the fluid turbulent velocity field. This leads to a decorrelation of fluid-particle velocity, hence the negative sign of this term that serves as a destruction term of fluid-particle velocity covariance. However, it does not account for the increase of fluid-particle velocity covariance in the case of moderate inertia particles, $\tau_{fp}^F/\tau_f^t \sim 1$ as shown by Fig. 5.5. This increase is due to the first term of Eq. (5.7), thus due to a modification of $\tau_{fp}^F \langle \mathbf{a}'_{f@p} \mathbf{u}'_p \rangle_p$. Indeed, Fig. 5.12 shows that term

$\tau_{fp}^F \langle \mathbf{a}'_{f@p} \mathbf{u}'_p \rangle_p$ is modified by electrostatic forces. This term is strongly affected by τ_{fp}^F which

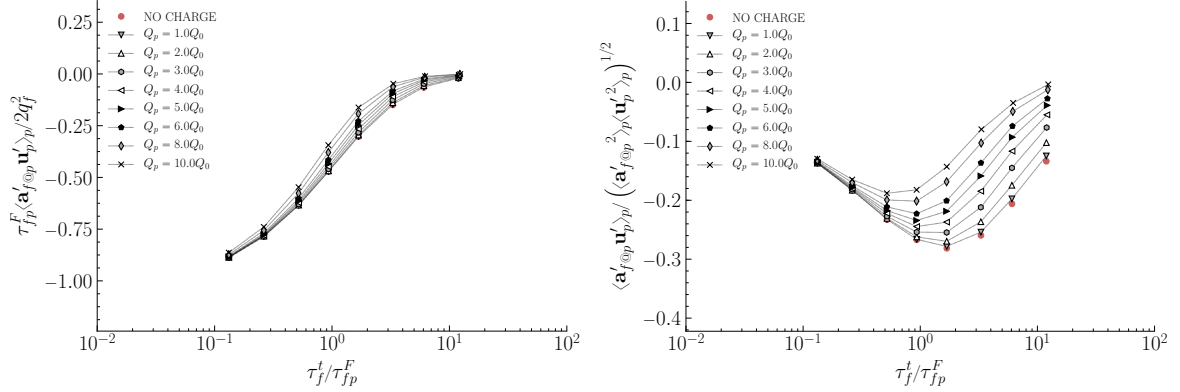


Figure 5.12: Effect of electrostatic interactions on acceleration term $\langle \mathbf{a}'_{f@p} \mathbf{u}'_p \rangle_p$ with regard to particle inertia for various levels of electric charge.

includes the effect of particle inertia, so in order to obtain a better understanding we examine the term $\langle \mathbf{u}'_p \mathbf{a}'_{f@p} \rangle_p / (\langle \mathbf{u}'_p \mathbf{u}'_p \rangle_p \langle \mathbf{a}'_{f@p} \mathbf{a}'_{f@p} \rangle_p)^{1/2}$ so that we isolate the effect of fluid acceleration and particle velocity. In particular, this term decreases in absolute value for an increasing electric charge and since it's a destruction term, this leads to an increase of fluid-particle velocity covariance especially for particles of moderate inertia, $\tau_{fp}^F / \tau_f^t \sim 1$.

In Fig. 5.13, it is evident that the dissipation rate of fluid-particle correlation τ_{fp}^a increases for increasing electric charges, which essentially means that q_{fp} dissipates in lower rates, resulting to its increase. At this point, it would be interesting to examine the effect of

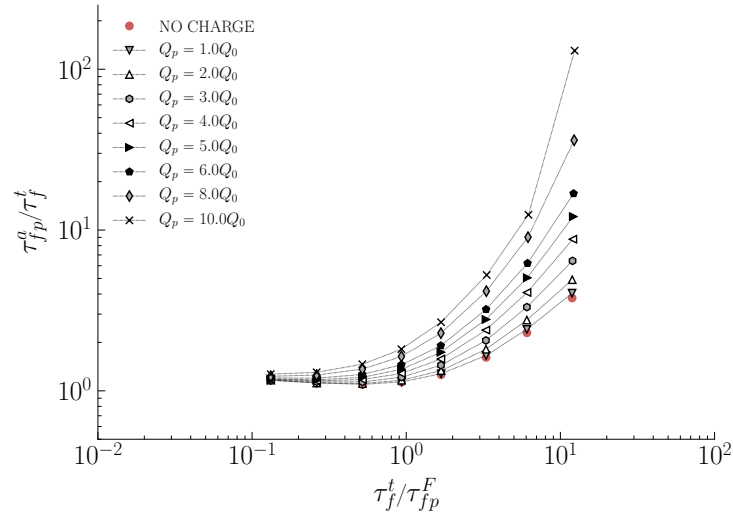


Figure 5.13: Effect of electrostatic interactions on time scale τ_{fp}^a with regard to particle inertia for various levels of electric charge.

electrostatic interactions on fluid acceleration seen at the position of particles $\langle \mathbf{a}'_{f@p} \mathbf{u}'_p \rangle_p$. In Fig. 5.14, it is apparent that for increasing electric charges there is a small decrease of $\langle \mathbf{a}'_{f@p} \mathbf{u}'_p \rangle_p$ for particles of moderate inertia and a considerable increase for light particles. However, for both cases the variance of fluid acceleration measured at the particles' position tends to the value of the fluid acceleration variance measured along fluid elements. This implies that particles

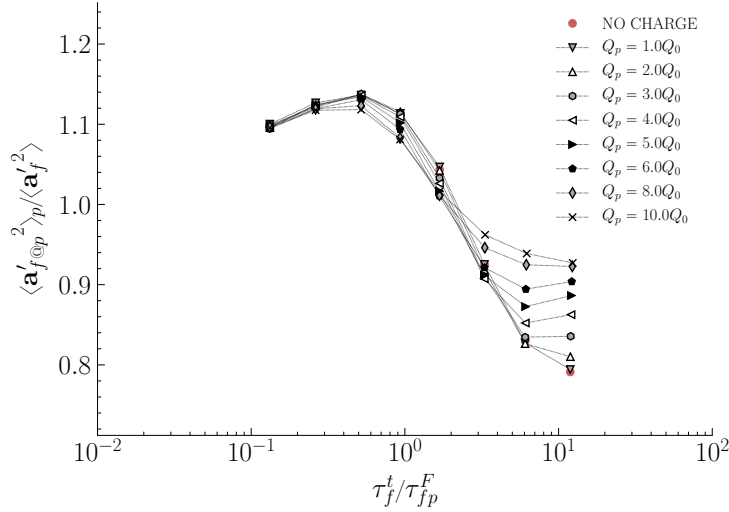


Figure 5.14: Effect of electrostatic interactions on fluid acceleration at the particles position $\langle \mathbf{a}'_{f@p}{}^2 \rangle_p$ with regard to particle inertia for various levels of electric charge.

tend to be distributed more homogeneously.

Lastly, it would be also interesting to examine the behavior of $q_{f@p}^2$. As far as the second term of Eq. (5.7) is concerned, in Fig. 5.15, it is shown that an increase in electric charge implies an increase in the fluid agitation from the point of view of the particles. More specifically, $q_{f@p}^2$ has the tendency to flatten to the value of q_f^2 for heavy particles, $\tau_{fp}^F \rightarrow \infty$ and to increase even further for moderate and light particles. To explain this behavior, we first have to examine

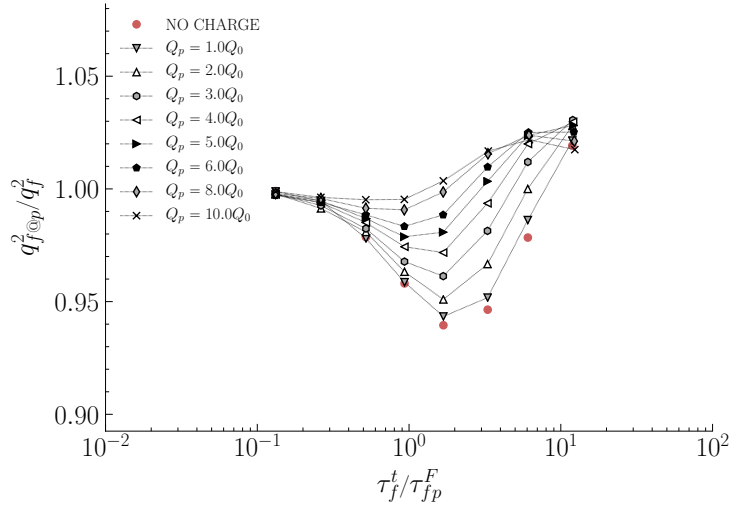


Figure 5.15: Effect of electrostatic interactions on fluid agitation "seen" by the particles with regard to particle inertia for various levels of electric charge.

the levels of $q_{f@p}^2$ in the case of no electric charge. Indeed, inertial and light particles "see" the same fluid agitation, as the former are rather transported by large turbulent structures and the latter behave close to fluid elements. However, particles of moderate inertia get trapped in regions of low vorticity and therefore "see" slightly lower levels of fluid agitation. Under the influence of electric charges, inertial particles are not as affected, while moderate particles are

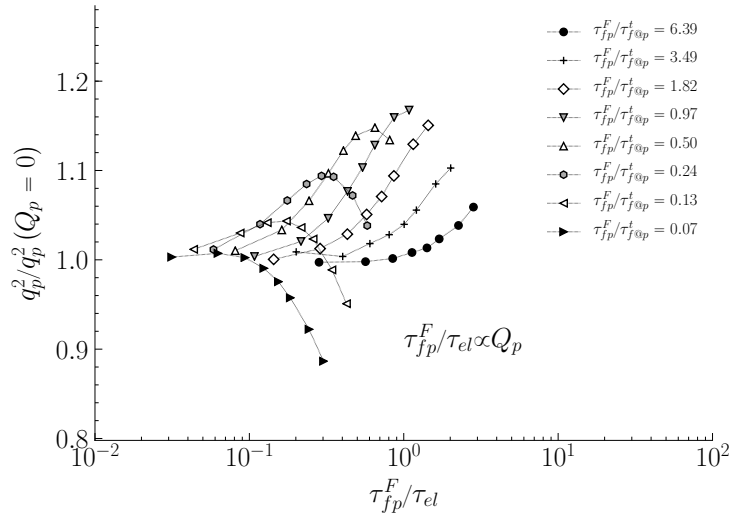


Figure 5.16: Particle agitation normalized by the value without charge with regard to electrostatic Stokes number. Stokes numbers τ_{fp}^F/τ_{fp}^t correspond to the value without charge.

less prone to preferential concentration, thus they "see" a fluid agitation close to q_f^2 . However, less inertial particles exhibit an increase in $q_{f@p}^2$ which needs to be further investigated.

Finally, it seems that combining Eqs. (5.5) and (5.7), one can write particle agitation in terms of the different examined statistical moments.

$$q_p^2 = q_{f@p}^2 + \frac{1}{2}\tau_{fp}^F \left(\langle \mathbf{a}'_{f@p} \mathbf{u}'_p \rangle_p + \frac{\langle \mathbf{F}'_e \mathbf{u}'_{f@p} \rangle_p}{m_p} + \frac{\langle \mathbf{F}'_e \mathbf{u}'_p \rangle_p}{m_p} \right). \quad (5.8)$$

Figure 5.16 provides an overview of what has been discussed. It shows that for a given level of particle inertia, increasing particle charge leads to an increase of particle agitation due to an increase of $q_{f@p}^2$ (see Fig. 5.15) and $\tau_{fp}^F \langle \mathbf{a}'_{f@p} \mathbf{u}'_p \rangle_p$ (see Fig. 5.12), which are the first two terms of Eq. (5.8). This occurs up to a saturation limit where q_p^2 starts to decrease as the third (destruction) term of Eq. (5.8), $\tau_{fp}^F \langle \mathbf{F}'_e \mathbf{u}'_{f@p} \rangle_p / m_p$ becomes more important (see Fig. 5.11). Increasing particle inertia, actually moves that saturation limit to lower electrostatic time scales $\tau_{el} \rightarrow 0$, thus higher electric charges.

Effect of electrostatic interactions on relative fluid-particle velocity covariance

The relative fluid-particle agitation q_r^2 is defined as

$$q_r^2 = \langle u'_{r,i} u'_{r,i} \rangle_p \quad (5.9)$$

where $\mathbf{u}_r = \mathbf{u}_p - \mathbf{u}_{f@p}$ is the relative fluid-particle velocity. From the definition of Eq. (5.9), one can deduce that

$$q_r^2 = 2q_p^2 + 2q_{f@p}^2 - 2q_{fp}. \quad (5.10)$$

Thus, by replacing q_p^2 from Eq. (5.5) into Eq. (5.10) the following expression for q_r^2 can be deduced

$$q_r^2 = \tau_{fp}^F \frac{\langle \mathbf{F}'_e \mathbf{u}'_p \rangle_p}{m_p} + 2q_{f@p}^2 - q_{fp}. \quad (5.11)$$

Continuing, the difference $2q_{f@p}^2 - q_{fp}^2$ can be rewritten using Eq. (5.7) as

$$2q_{f@p}^2 - q_{fp}^2 = -\tau_{fp}^F \langle \mathbf{a}'_{f@p} \mathbf{u}'_p \rangle_p - \tau_{fp}^F \frac{\langle \mathbf{F}'_e \mathbf{u}'_p \rangle_p}{m_p}$$

and replace it into Eq.(5.11) that finally gives

$$q_r^2 = \tau_{fp}^F \left(\frac{\langle \mathbf{F}'_e \mathbf{u}'_p \rangle_p}{m_p} - \langle \mathbf{a}'_{f@p} \mathbf{u}'_p \rangle_p \right) \quad (5.12)$$

where $\langle \mathbf{F}'_e \mathbf{u}'_p \rangle_p = \langle \mathbf{F}'_e \mathbf{u}'_p \rangle_p - \langle \mathbf{F}'_e \mathbf{u}'_{f@p} \rangle_p$ is a measure of the relative fluid-particle electric potential energy. In order to understand the effect of electrostatic forces on q_r^2 , one should compare the behavior of term $\tau_{fp}^F \langle \mathbf{F}'_e \mathbf{u}'_p \rangle_p / m_p$ for different levels of particle electric charge and particle inertia. However, it is strongly affected by τ_{fp}^F which includes the effect of particle inertia, so in order to obtain a better understanding we examine the term $\langle \mathbf{F}'_e \mathbf{u}'_p \rangle_p / (\langle \mathbf{F}'_e{}^2 \rangle_p \langle \mathbf{u}'_p{}^2 \rangle_p)^{1/2}$ so that we isolate $\langle \mathbf{F}'_e \mathbf{u}'_p \rangle_p$. Figure 5.17 shows that this term increases for decreasing particle inertia and high levels of electric charge.

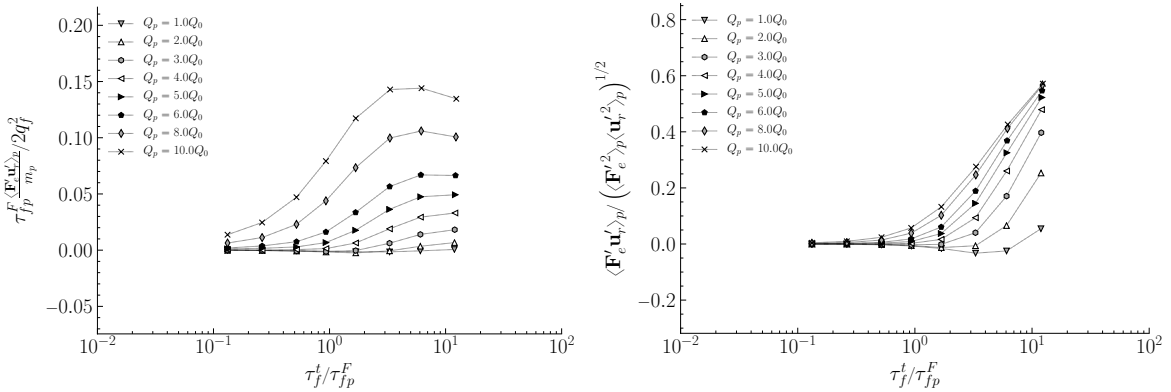


Figure 5.17: Effect of electrostatic interactions on term $\langle \mathbf{F}'_e \mathbf{u}'_p \rangle_p / m_p$ with regard to particle inertia for various levels of electric charge.

To investigate this, one could compare the value of q_r^2 measured under the effect of electrostatic interactions to the one measured in the charge-free case. Figure 5.18 shows that q_r^2 remains rather unaffected by electrostatic interactions except for light particles. Since terms $-\langle \mathbf{a}'_{f@p} \mathbf{u}'_p \rangle_p$ and $\langle \mathbf{F}'_e \mathbf{u}'_p \rangle_p / m_p$ are in competition in Eq. (5.12) it seems that the effect of electrostatic interactions on the two terms is of the same order of magnitude except for light particles. For them, q_r^2 increases for increasing particle electric charge. This happens because in the charge-free case, light particles seem to follow closely the fluid velocity ($q_r^2 \simeq 0$), while electrostatic forces create a substantial differential of the relative fluid-particle velocity ($q_r^2 \gg 0$). This is the reason why, $\tau_{fp}^F \propto \|\mathbf{u}_r\|^{-0.687}$ exhibits the inverse trend, however its modification due to electrostatic forces is found to be quite smaller.

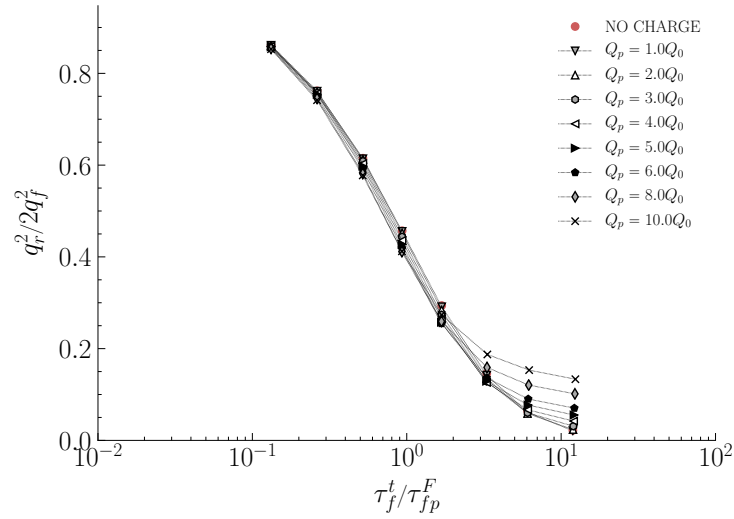


Figure 5.18: Effect of electrostatic interactions on relative fluid-particle agitation number with regard to particle inertia for various levels of electric charge.

The same behavior is observed when examining the effect of electrostatic interactions on the particle Reynolds number (see Fig. 5.19), which is defined in Eq.(2.23). This is because it is a function of the relative fluid-particle velocity \mathbf{u}_r , since it can be written as $Re_p = d_p \|\mathbf{u}_r\| / \nu_f$.

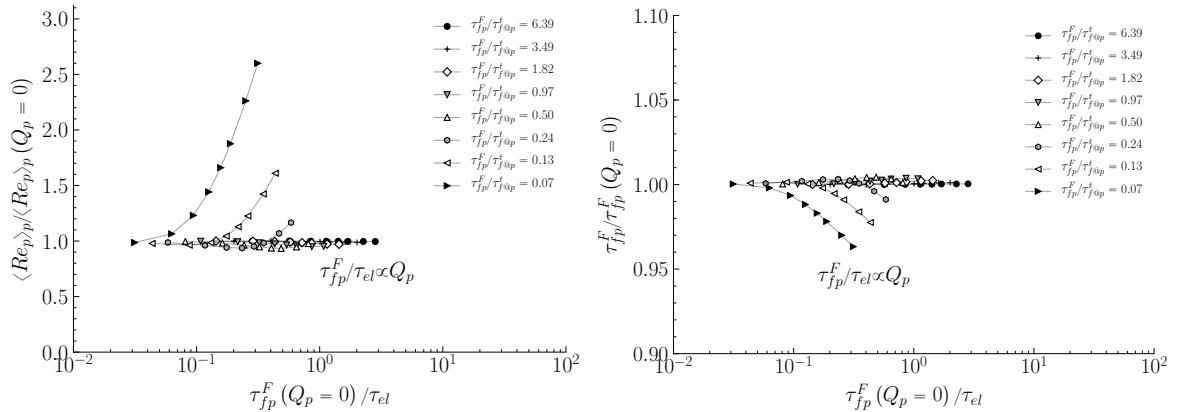


Figure 5.19: Comparison of $\langle Re_p \rangle_p$ and τ_{fp}^F to the charge-free case with regard to electrostatic Stokes number.

5.2.2 Autocorrelation functions of fluid and particle velocity

Figure 5.20 presents the autocorrelation functions of "seen" fluid and particle velocities for various Stokes numbers for $Q_p = 5Q_0$. The time has been normalized with the integral of the autocorrelation functions. Evidently, heavier particles exhibit a steeper decorrelation of their velocity and the fluid velocity "seen" at their position in comparison with particles of lower inertia. Under the Coulomb collisions theory, this observation can be justified due to the lower frequency abrupt motion of heavier particles and the higher frequency smooth movement of lighter particles. However, in order to examine the effect of electric charge on autocorrelation

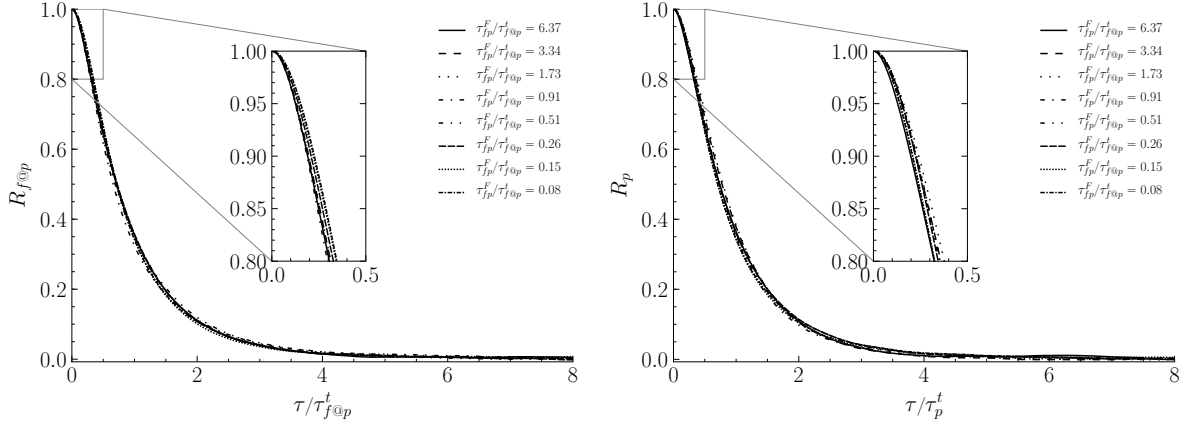


Figure 5.20: Autocorrelation function $R_{f@p}$ of fluid velocity "seen" at the particle positions (left) and R_p of particle velocity (right) with regard to time normalized by corresponding integral time scale for various Stokes numbers in the case of $Q_p = 5Q_0$.

functions, we have to examine how the autocorrelation functions are modified for increasing particle electric charge for each Stokes number.

Autocorrelation function $R_{f@p}$

In Fig. 5.21 one can observe that inter-particle electrostatic interactions do not have a strong effect on the shape of autocorrelation functions of fluid velocity "seen" by the particles even for high values of particle electric charge Q_p . Evidently, there is no significant modification in the shape of the functions which essentially means that electric charge does not affect the way with which $\mathbf{u}_{f@p}$ decorrelates, but only the time scale that it takes for the decorrelation of the "seen" fluid turbulent velocity.

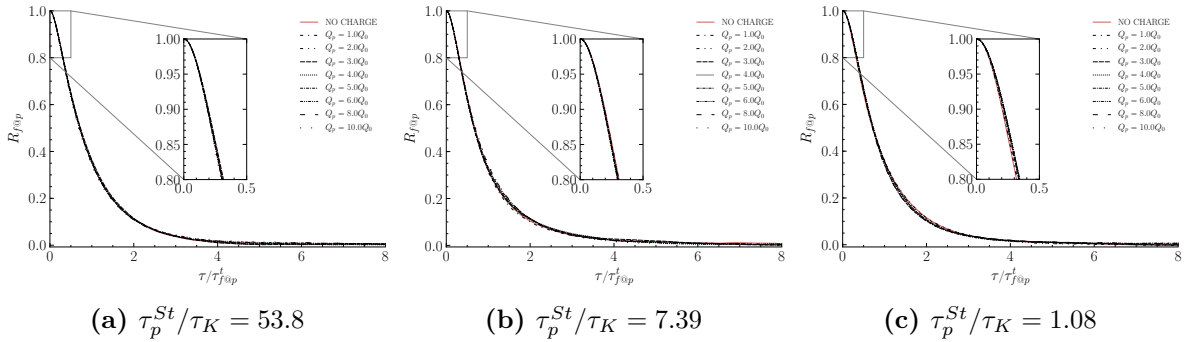


Figure 5.21: Effect of electrostatic interactions on autocorrelation functions of fluid velocity "seen" by the particles, $R_{f@p}$ for various levels of electric charge and three levels of inertia.

Indeed, the effect of electrostatic forces on the Lagrangian integral time scale of the fluid "seen" at the particle position, $\tau_{f@p}^t$ is small but not negligible. In Fig. 5.22 it becomes evident that the comprehension of this effect is not as straight forward. Figure 5.22 draws a comparison between $\tau_{f@p}^t$ for the charge-free reference case and $\tau_{f@p}^t$ at increasing levels of particle electric charge that correspond to increasing electrostatic Stokes numbers τ_{fp}^F/τ_{el} . Each curve corresponds to a different particle Stokes number $\tau_{fp}^F/\tau_{f@p}^t$. It seems that for

light particles this characteristic time scale becomes smaller under the stronger electrostatic interactions as their ability to follow fluid trajectories is enhanced. For moderate inertia particles this time scale undergoes a slight decrease with it being considerable only for high electric charges. These particles exhibit preferential concentration that implies slower decorrelation, thus higher $\tau_{f@p}^t$, a phenomenon that is still present for weak electric charges and is mitigated for strong ones, hence a decrease in $\tau_{f@p}^t$. Lastly, heavy particles exhibit an increase of $\tau_{f@p}^t$ for strong electric charges, which implies that electrostatic forces enhance their ability to act as observers.

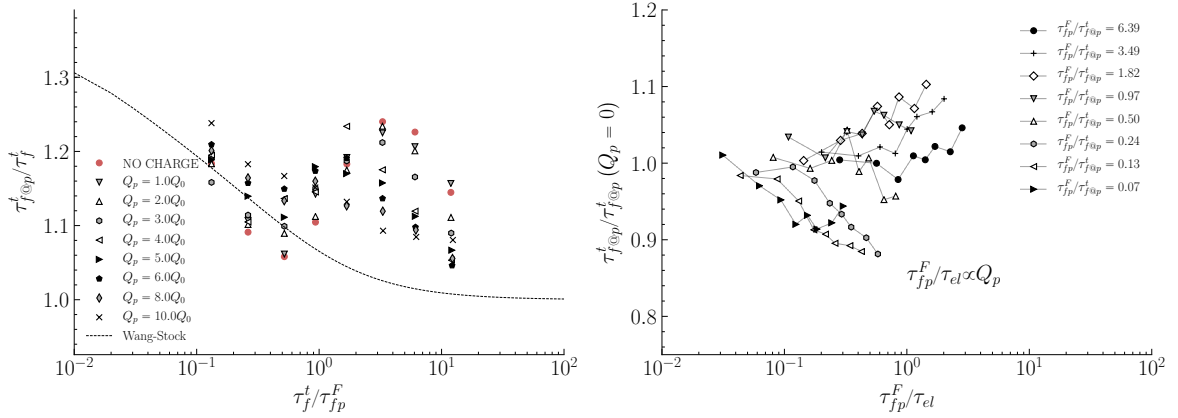


Figure 5.22: Effect of electrostatic interactions on $\tau_{f@p}^t$ with regard to particle inertia for various levels of electric charge.

More specifically, one can distinguish three different regimes based on particle inertia (Stokes number) as following

- i. heavy particles: in the absence of electric field, these particles present minimum preferential concentration so they tend to "see" act almost as immobile observers in the sense that their Lagrangian integral time scale of the measured fluid velocity field is close to τ_E . In the presence of (repulsive) electrostatic forces their trajectories become even more decorrelated from the turbulent velocity field and as a result their ability to act as randomly distributed observers is enhanced, thus the higher values of $\tau_{f@p}^t < \tau_E$. Of course at the limit of $\tau_{fp}^F \rightarrow \infty$ the electrostatic interactions should not have any effect on $\tau_{f@p}^t \rightarrow \tau_E$.
- ii. particles of moderate inertia: in the absence of electric field, these particles demonstrate high levels of preferential concentration which imply a low "seen" fluid velocity decorrelation rate as they tend to concentrate in regions of the flow of high strain rate and low vorticity, thus relatively high values of $\tau_{f@p}^t$. In the presence of (repulsive) electrostatic forces, this preferential concentration tends to mitigate, thus the spectrum of turbulence that they "see" is less preferential, thus $\tau_{f@p}^t$ decreases.
- iii. light particles: in the absence of electric field, these particles follow a motion that approaches that of fluid elements with some effect of inertia (weak preferential concentration). In the presence of (repulsive) electrostatic forces, these particles move along the fluid element trajectories but at the same time try to be equidistant from each other which in fact enhances their fluid-like behavior as they continue their motion with minimum-to-zero levels of preferential concentration, thus the lower values of $\tau_{f@p}^t > \tau_f^t$. Of course at the limit of $\tau_{fp}^F \rightarrow 0$ the electrostatic interactions should not have any effect on $\tau_{f@p}^t \rightarrow \tau_f^t$.

Autocorrelation function R_p

In Fig. 5.23 one can observe that inter-particle electrostatic interactions have a strong effect on the shape of autocorrelation functions of particle velocity, especially for high values of particle electric charge Q_p . Evidently, the shape of the functions becomes steeper for increasing electric charge which essentially means electrostatic interactions expedite the decorrelation process, as well as the time scale that it takes for the full decorrelation of the particle velocity. In addition,

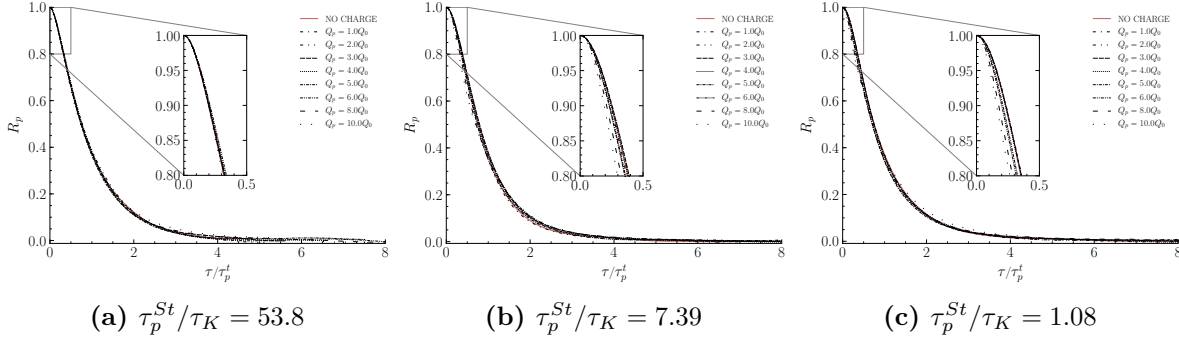


Figure 5.23: Effect of electrostatic interactions on autocorrelation functions of particle velocity, R_p with regard to τ/τ_p^t for various levels of electric and three levels of particle inertia.

Fig. 5.24, indicates a significant decrease in τ_p^t due to electrostatic interactions, which implies an increase in the rate of particle velocity decorrelation. This effect is pronounced for inertial particles, $\tau_{fp}^F \rightarrow \infty$, as electrostatic forces abruptly alter particle trajectories and as a result force their velocities to decorrelate faster than they would in charge-free case. For lighter particles, this is almost negligible as those already decorrelate in faster rates, close to fluid elements as $\tau_p^t \rightarrow \tau_f^t$, hence electrostatic forces are unable to further "enhance" their particle velocity decorrelation.

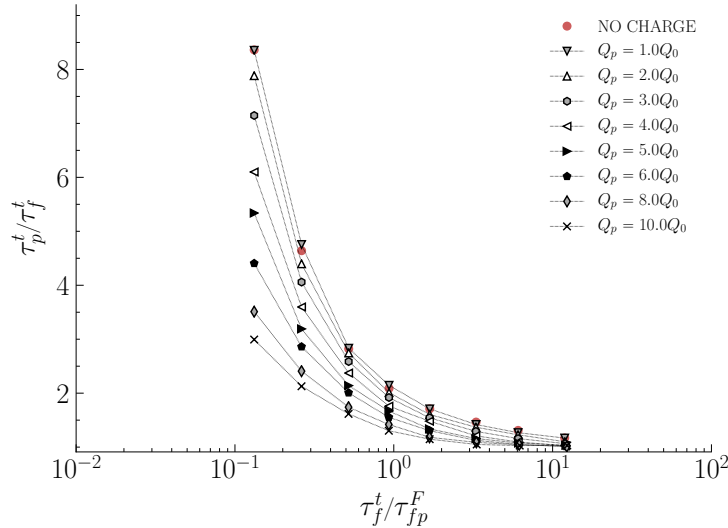


Figure 5.24: Effect of electrostatic interactions on τ_p^t with regard to particle inertia for various levels of electric charge.

Figure 5.25 draws a comparison between τ_p^t for the reference charge-free case and τ_p^t at increasing levels of particle electric charge that correspond to increasing electrostatic Stokes

numbers τ_{fp}^F/τ_{el} . Each curve corresponds to a different particle Stokes number $\tau_{fp}^F/\tau_{f@p}^t$. It seems that for all levels of particle inertia, time scale τ_p^t decreases for increasing particle charge, however the effect becomes significantly more important for heavier particles. This is in agreement with the aforementioned binary regime of Coulomb collisions (low frequency, small effective diameter), under which these particles follow high deflection trajectories.

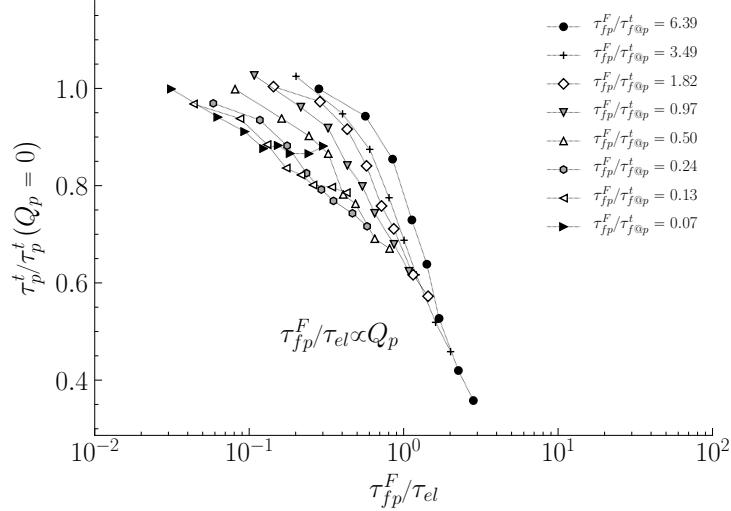


Figure 5.25: Comparison of τ_p^t with its charge-free values with regard to electrostatic Stokes number for various particle Stokes numbers.

5.2.3 Particle dispersion coefficient

Figure 5.26 shows how MSD and particle dispersion is modified by increasing particle electric charge for various particle Stokes numbers. It is evident that for the same period of normalized time, the achieved level of MSD is significantly reduced for most particle Stokes numbers as electric charge increases. This means that the slope of the $\mathcal{D} - \tau$ line decreases for increasing electric particle charge which results to a decrease of particle dispersion as implied by Eq. (3.43). This behavior is due to the repulsive nature of electrostatic forces for like-charged particle clouds, as the consequent constant repulsion forces the particles to flow in an equidistant distribution which corresponds to a minimum electric potential energy. Under high electric charges, particles are not free to wander off since they constantly collide with each other via the mechanism of Coulomb collisions.

This kind of particle "confinement" has also been observed in terms of particle agitation (see Fig. 5.5) and leads to a decrease of particle displacement and particle dispersion. It should be noted here, that for moderate Stokes numbers and low levels of electric charge, a slight increase of MSD is observed that most likely has to do with the slight increase of particle agitation due to the observed decrease of the turbulent dissipation rate of fluid-particle correlation. However, further increase of particle electric charge leads to strong (repulsive) electrostatic forces that result to a decrease of particle displacement.

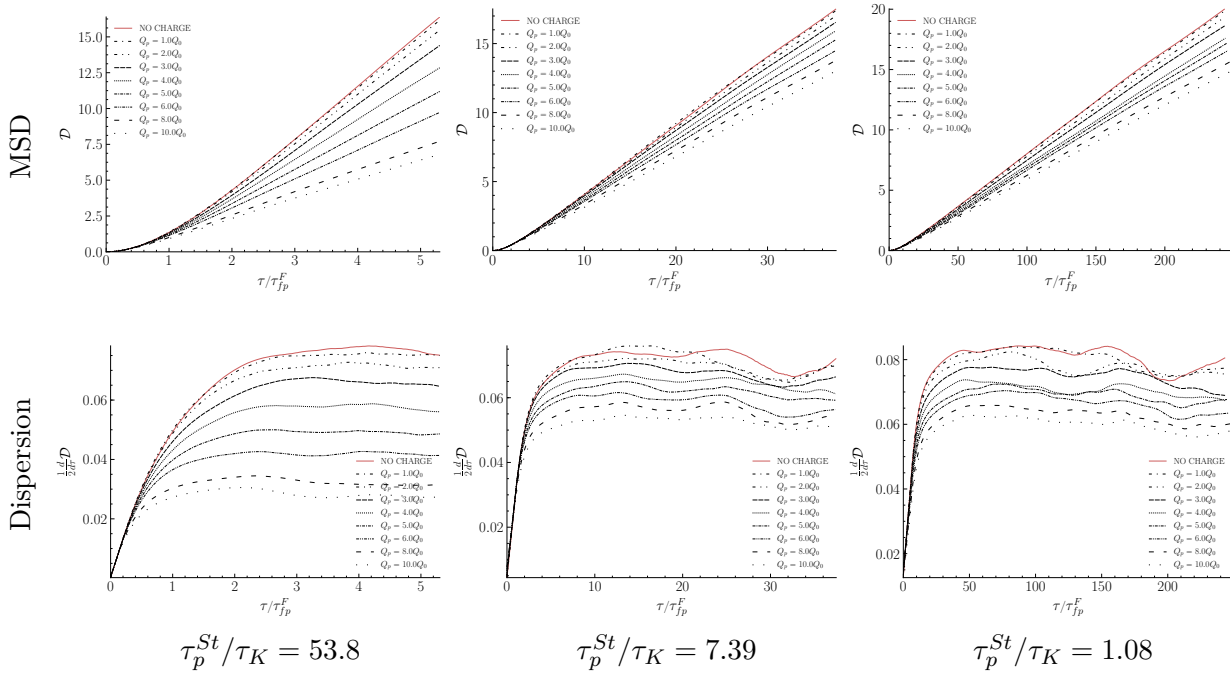


Figure 5.26: Effect of electrostatic interactions on MSD and its time derivative with regard to τ/τ_{fp}^F for various levels of electric charge and three levels of particle inertia.

Figure 5.27 demonstrates the effects of electrostatic interactions on particle dispersion coefficient D_p^t for increasing particle electric charges. Particle dispersion coefficient is found to decrease under the influence of electrostatic forces, which is more pronounced for heavier particles. This confirms the phenomenon of particle "confinement" that derives from the combination of repulsive electrostatic forces in like-charged particle clouds and periodic BCs.

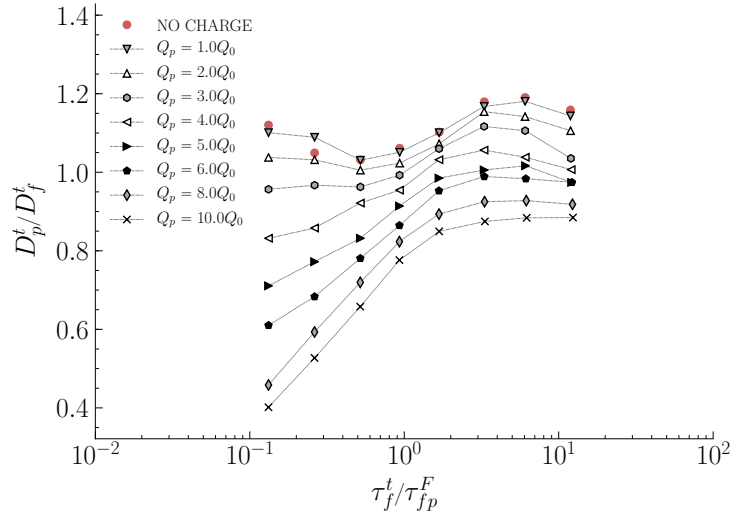


Figure 5.27: Effect of electrostatic interactions on particle dispersion coefficient with regard to particle inertia for various levels of electric charge.

Furthermore, in Fig. 5.28 we attempt to verify the validity of two Tchen-Hinze theoretical expressions of Eq. (3.44) for particle dispersion under the influence of electrostatic interactions.

It becomes evident that as (repulsive) electrostatic forces become more important, $2/3 \times q_p^2 \tau_p^t$ seems to correctly estimate the particle dispersion coefficient with a maximum deviation of $\sim 5\%$ for heavy particles and high electric charges. On the contrary, this is not true for $2/3 \times q_{f@p}^2 \tau_{f@p}^t$ as it seems that it overestimates particle dispersion, especially for heavy particles. The reason for this overestimation is quite complex as it has to do with the modification of both $q_{f@p}^2$ and $\tau_{f@p}^t$ seen in Figs. 5.15 and 5.22, respectively. By observing these two Figures, it seems that $2/3 \times q_{f@p}^2 \tau_{f@p}^t$ increases mostly due to the pronounced increase of $q_{f@p}^2$ which is the opposite trend of measured D_p^t presented in Fig. 5.27. To get a better

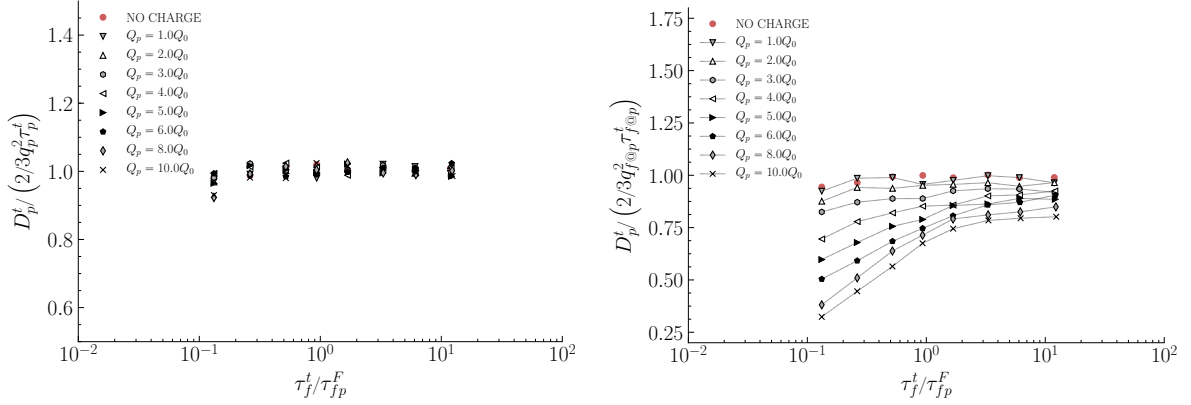


Figure 5.28: Particle dispersion coefficient models' validity for various levels of electric charges and particle Stokes numbers. To the left, $2/3 \times q_p^2 \tau_p^t$ seems to give a good estimate and to the right $2/3 \times q_{f@p}^2 \tau_{f@p}^t$ seems to overestimate of D_p^t for like-charged particles.

appreciation of the effect of particle electric charge on particle dispersion coefficient, its values for the charge-free reference case are compared to the corresponding values obtained under the presence of electrostatic forces, for a wide range of particle inertia. It seems that particle

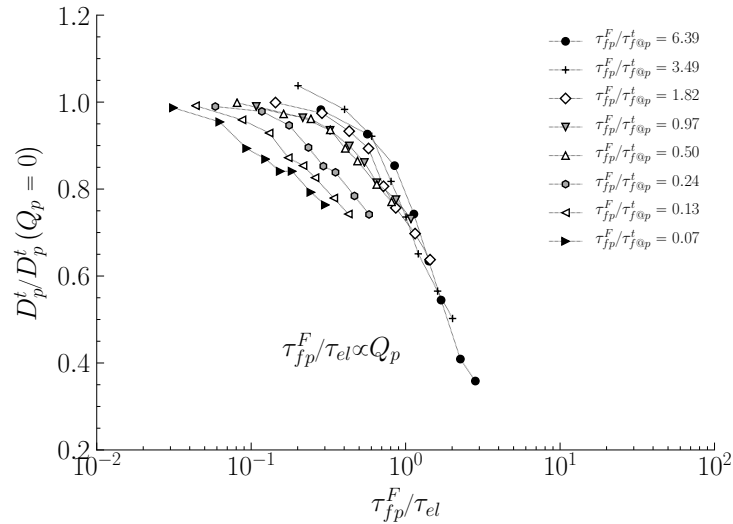


Figure 5.29: Comparison of particle dispersion coefficient under the effect of electrostatic forces in the charge-free case.

dispersion coefficient decreases under repulsive electrostatic interactions and this decrease

becomes prominent $\sim 60\%$ for heavier particles. In order to understand this, we refer to the fundamental result of Tchen-Hinze theory (see Eq. (3.22)). According to it, particle dispersion coefficient is nothing more than the product of particle agitation and Lagrangian integral time scale, which represent the kinetic energy level and the "memory" of the particles, respectively. In the charge-free case, heavy particles have low kinetic energy but high "memory" and light particles the opposite. Under the influence of electrostatic forces, particle kinetic state does not change dramatically (see Fig. 5.16), but their velocities tend to decorrelate faster and as a result reduce their "memory" (see Fig. 5.25) which in turn reduces their dispersion coefficient.

5.2.4 Inter-particle electrostatic interactions in turbulent flows

Since the effects of electrostatic interactions on particle motion have been detailed in previous subsections, at this point it would be interesting to examine the very nature of repulsive electrostatic forces that develop in a like-charged particle cloud that is transported by stationary homogeneous isotropic turbulence.

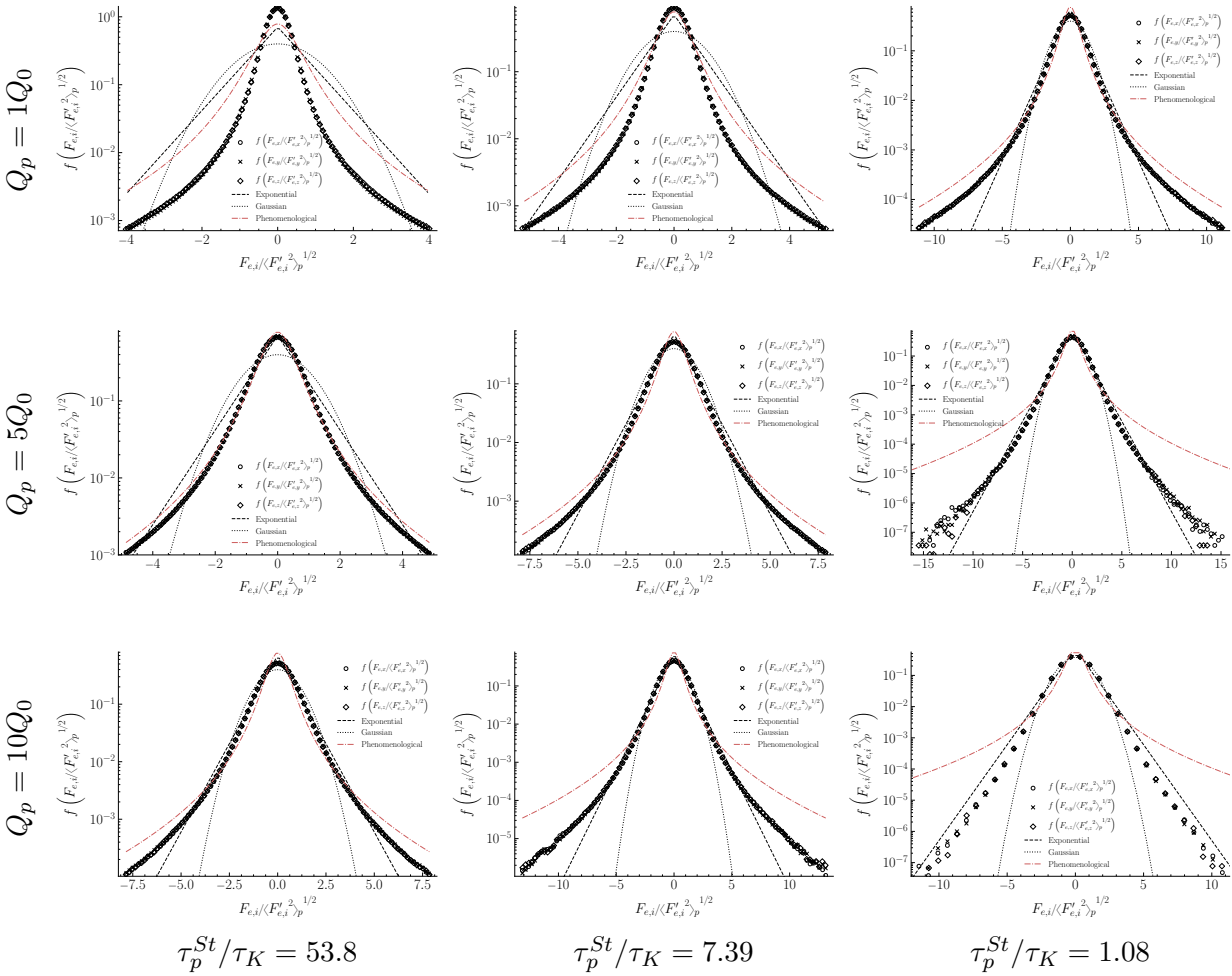


Figure 5.30: PDF of the three components of electrostatic forces for various levels of particle inertia and electric charge. The distributions are compared with the corresponding exponential and Gaussian distributions from Eq. (3.55) and the phenomenological ones from Eq. (5.13).

PDF of electrostatic forces

As seen in Subsect. 4.3.5, to extract useful information on the distribution of electrostatic forces, we need to examine the PDFs of their components for various levels of inertia. From Fig. 5.30, it can be deduced that, since the PDFs overlap, the distribution of electrostatic forces exerted on the particles is indeed isotropic as orientation does not modify the shape of the PDFs. This is in agreement with the expected isotropy of the particle-induced electric field shown by Fig. 5.4. In order to obtain a more precise idea of the form of the PDFs of $F_{e,i}$, they have been plotted in Fig. 5.30 with exponential and Gaussian functions that are obtained by the relation (3.55). One can make two observations based on Fig. 5.30. Their shape is rather peculiar, as it is far from Gaussian, has characteristics of an exponential distribution but it is neither a perfect exponential distribution. In addition, we observe that for a given level of inertia, increasing electric charge widens the PDF of electrostatic forces.

We note that the Gaussian PDF model predicts $\langle \|\mathbf{F}_e\| \rangle_p / \langle \mathbf{F}_e'^2 \rangle_p^{1/2} = \sqrt{8/(3\pi)} = 0.9213$ (Fede, 2004, Wang *et al.*, 1998). The DNS measured values of $\langle \|\mathbf{F}_e\| \rangle_p / \langle \mathbf{F}_e'^2 \rangle_p^{1/2}$ are visualized in Fig. 5.31. It seems that for the same level of particle electric charge, the PDFs of electrostatic forces are far from the Gaussian distribution, $\langle \|\mathbf{F}_e\| \rangle_p / \langle \mathbf{F}_e'^2 \rangle_p^{1/2} \leq 0.9213$. As particle inertia decreases, there are several cases for high levels of electric charges for which the ratio tends to the this value, however the distributions partially resemble to either Gaussian or exponential distributions, so it is likely that the latter exhibits a ratio of average-to-standard deviation that is close to that number. In fact, The examined PDFs seem to approach the exponential distribution in the case of either light particles and strong electrostatic forces or heavy particles and moderate-to-strong electrostatic forces for $|F_{e,i}| < 5 \langle F_{e,i}'^2 \rangle_p^{1/2}$.

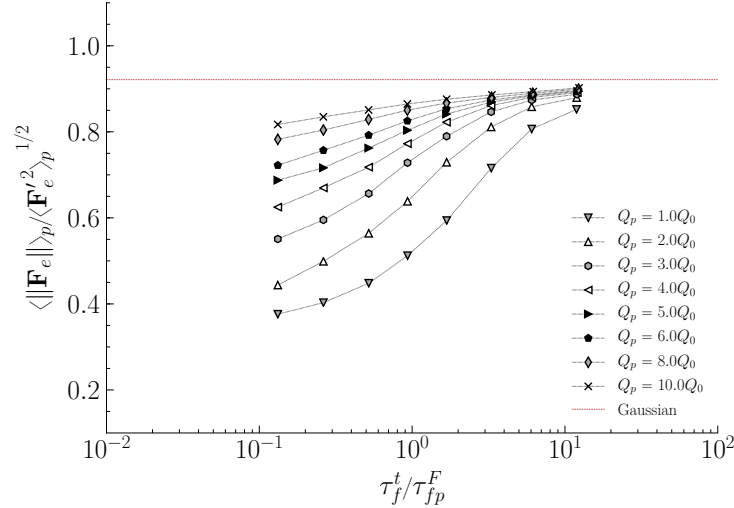


Figure 5.31: Effect of electrostatic interactions on the shape of the PDFs of electrostatic forces via ratio $\langle \|\mathbf{F}_e\| \rangle_p / \langle \mathbf{F}_e'^2 \rangle_p^{1/2}$. The horizontal line corresponds to its theoretical value for Gaussian distribution (Fede, 2004, Wang *et al.*, 1998).

This rather peculiar shape has been seen before in the work of Voth *et al.* (2002) as the shape of PDFs of particle accelerations. This is interesting because, in fact, electrostatic forces are nothing else than electrostatic particle acceleration multiplied by particle mass. Voth *et al.* (2002) actually propose a phenomenological function that gives the shape of particle acceleration PDF for inertial particles in stationary HIT that can be written as a function of a

variable x (whose variance is equal to unity) as

$$A(x) = C \exp\left\{\frac{-x^2}{(1 + |\beta x/\sigma|^\gamma) \sigma^2}\right\}. \quad (5.13)$$

where parameters $C = 0.786$, $\beta = 0.539$, $\gamma = 1.588$ are calibrated in their work using DNS data at $Re_\lambda = 970$. Although this model needs parameter calibration to match the profile of the less intense simulated turbulence of $Re_\lambda = 42.86$, it seems that this shape corresponds qualitatively to the measured shape of electrostatic particle accelerations.

Figure 5.32 shows the effect of inertia on the PDF of the x -component of the particle electrostatic forces. Increasing particle inertia narrows the range of electrostatic forces exerted on the particles. This is in agreement with the Coulomb collision regime for light particles that collide virtually with high frequency and large effective Coulomb diameters, while heavier particles interact with each other in a rather binary way. This essentially means that for higher values of electric charge, particle-particle electrostatic interactions approach more the Coulomb regime that describes cold plasma flows, and inertia effect becomes less important.

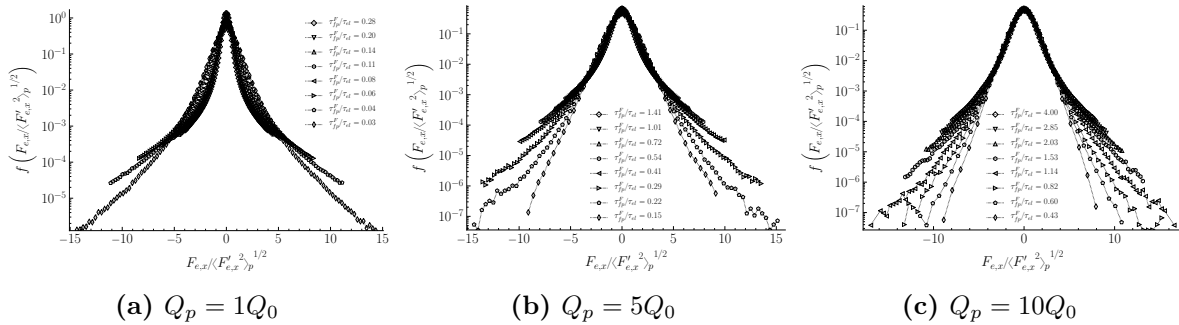


Figure 5.32: Effect of particle inertia on the PDF of the x -axis component of electrostatic forces for $Q_p = [1, 5, 10] Q_0$. Increasing particle inertia narrows the range of electrostatic forces, while increasing electric charge widens it.

Figure 5.33 illustrates the effect of particle electric charge on the average and variance of the norm of electrostatic acceleration. It seems that for increasing electric charge, the average norm of electrostatic acceleration increases, as it scales with the square of the latter. In addition, for the same level of particle electric charge, lighter particles exhibit higher levels of electrostatic acceleration. This is in agreement with the high frequency and long-distance Coulomb collision regime that characterizes their motion. Frequent Coulomb collisions that occur in longer distances imply constant particle motion with larger accelerations due to electrostatic forces. As far as its variance is concerned, it becomes evident that it is significant only for high electric charges and light particles, while it drops to zero for weak electric charges and heavy particles, as it has also been observed in Fig. 5.32.

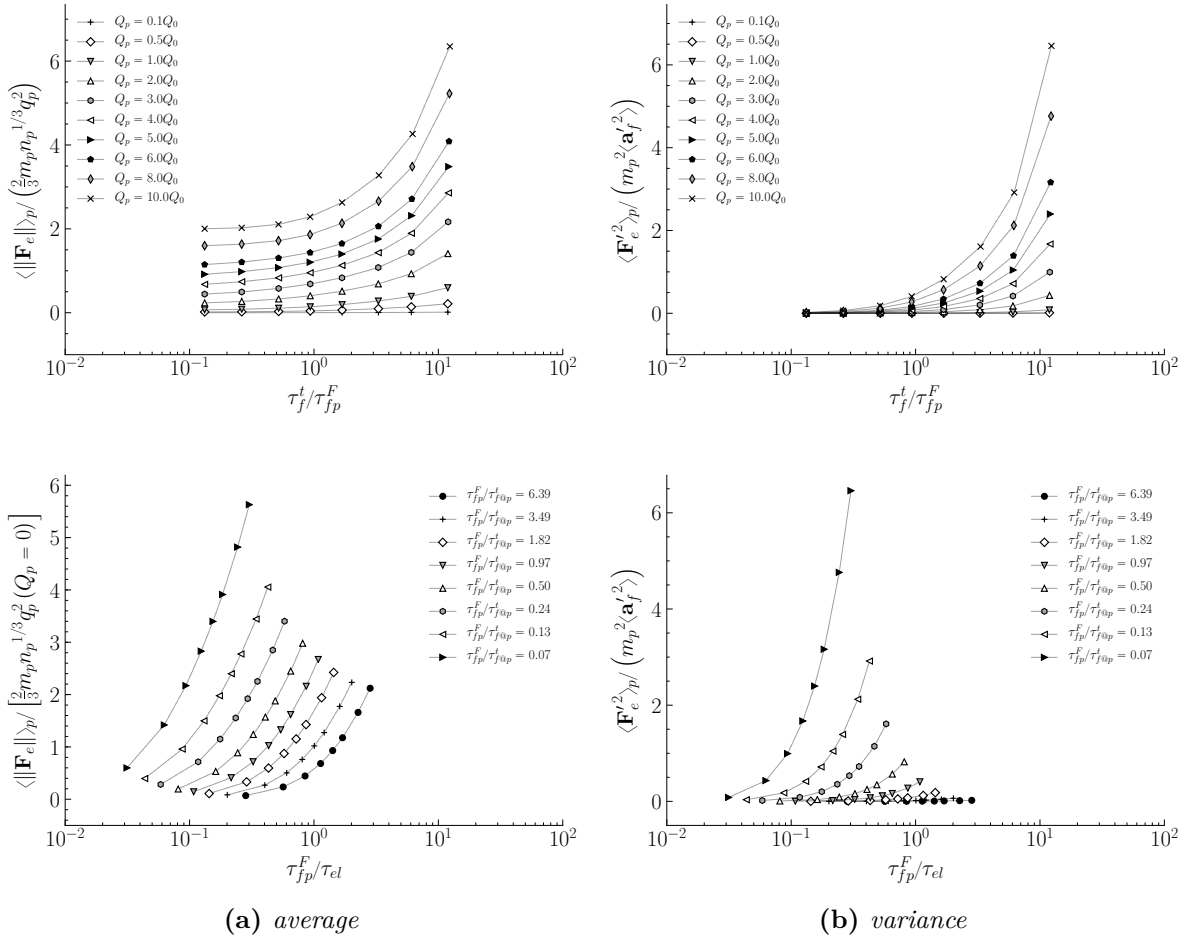


Figure 5.33: Effect of electrostatic interactions on the average of the norm (left), and variance (right) of electrostatic force with regard to particle inertia.

Autocorrelation function of electrostatic forces

In Fig. 5.34 one can observe the autocorrelation function of electrostatic forces for various levels of particle inertia. Time has been normalized by the Lagrangian electrostatic integral time scale, τ_{fe}^t , which is defined as the integral of the autocorrelation function of electrostatic forces as

$$\tau_{fe}^t = \int_0^\infty R_{fe}(\tau) d\tau. \quad (5.14)$$

Similar shapes of autocorrelation functions have been shown by Pope (1994) and later again by Pope (2002) which in these cases correspond to autocorrelation functions of particle accelerations. In fact, electrostatic forces can be also viewed as electrostatic particle accelerations, as it was also observed in Fig. 5.30 and due to the properties of homogeneity and isotropy of the electrostatic field, they constitute a homogeneous isotropic vectorial field of accelerations/forces that alters the kinetic situation of the particles. It is evident that electrostatic forces decorrelate rapidly, especially for heavier particles. More specifically, heavier particles undergo more abrupt modifications in their acceleration, hence the steep descent of the autocorrelation function R_{fe} . To better understand this, one should refer to the Coulomb collision frequency that decreases for increasing inertia (see Table 5.1). As a result, Coulomb collisions, hence electrostatic interactions of heavier particles are rather binary for inertial particles which implies a faster

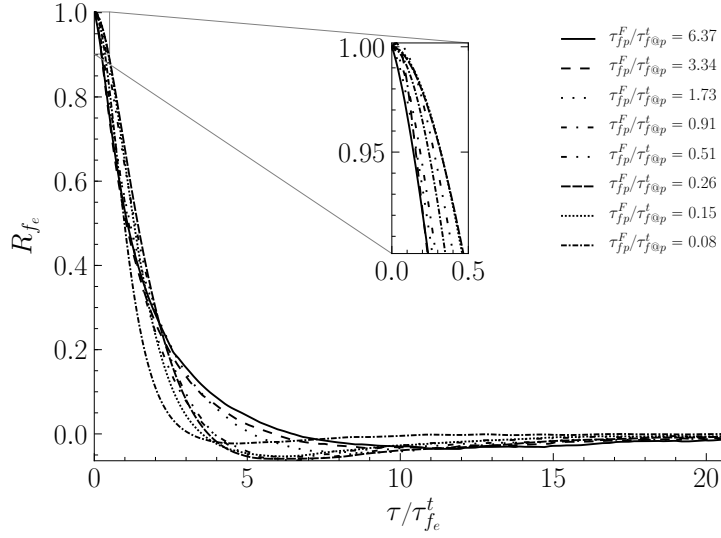


Figure 5.34: Autocorrelation functions of electrostatic forces, R_{f_e} with regard to time normalized by the corresponding integral time scale for various Stokes numbers in the case of $Q_p = 5Q_0$.

decorrelation of electrostatic acceleration. On the other hand, lighter particles exhibit a high Coulomb frequency which means that their acceleration is modified in a more smooth and continuous way. Furthermore, one can observe a negative part of autocorrelation function

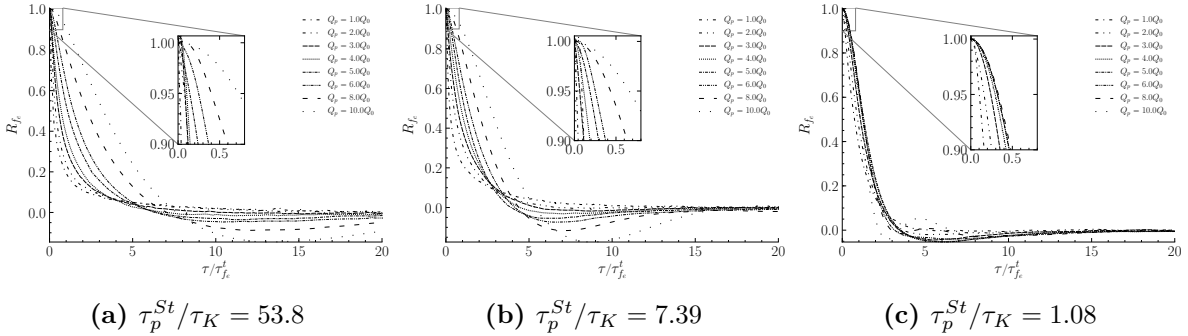


Figure 5.35: Effect of electrostatic interactions on autocorrelation functions of electrostatic forces, R_{f_e} with regard to $\tau/\tau_{f_e}^t$ for various levels of electric charge and three levels of inertia.

which corresponds to an obtuse angle between the initial electrostatic force fluctuation $\mathbf{F}'_e(t_0)$ and the current fluctuation $\mathbf{F}'_e(t_0 + \tau)$ as explained in Subsect. 4.3.5. This significant change in orientation is characteristic of the light particles' Coulomb regime and shows that the exerted electrostatic force/acceleration on such particles changes drastically (but gradually) both in magnitude and orientation along their trajectory. Figure 5.35 shows how autocorrelation functions of electrostatic forces or equivalently electrostatic accelerations are modified by increasing particle electric charge for a given particle Stokes numbers. It becomes evident that the shape of the autocorrelation function of electrostatic forces is modified by increasing particle electric charge, which denotes a change in the very nature of their decorrelation. More specifically, it seems that for increasing particle electric charge the electrostatic force remains autocorrelated for a shorter period of time.

Figure 5.36 shows how the Lagrangian electrostatic integral time scale, $\tau_{f_e}^t$ is modified for increasing levels of particle electric charge. In fact, $\tau_{f_e}^t$ becomes smaller as particle electric charge increases due to faster decorrelation of electrostatic forces for higher levels of electric charge. This is in agreement with previous observations as for high levels of particle electric charge, particles are undergoing high frequency Coulomb collisions that lead to a rapid change in the orientation and magnitude of the total electrostatic force that is exerted on them.

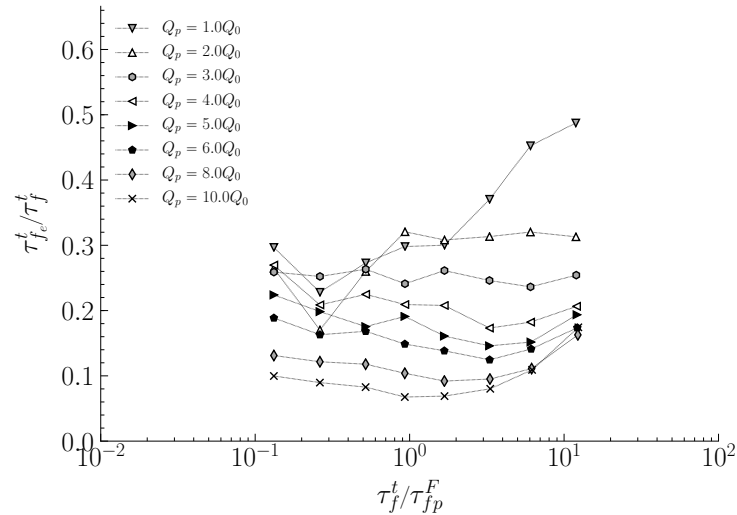


Figure 5.36: Effect of electrostatic interactions on electrostatic integral time scale $\tau_{f_e}^t$ with regard to particle inertia.

5.3 Effect of repulsive electrostatic forces on spatial particle distribution

This section deals with the effect of inter-particle electrostatic interactions on the spatial distribution of particles transported by a homogeneous isotropic turbulence. As explained in Chapter 3, in the absence of electric charge, solid particles transported by a turbulent flow field tend to accumulate in low-vorticity regions of the flow (Fessler *et al.*, 1994, Squires & Eaton, 1991), a phenomenon that is called preferential concentration.

In general, external forces may modify preferential concentration, as for example, Fede & Simonin (2010) showed that inter-particle collisions enhance preferential concentration. In addition, Dejoan & Monchaux (2013) investigated experimentally the effect of gravity on preferential concentration. There are several literature studies, which focus on the modification of preferential concentration in the case of charged particles transported by HIT such as (Di Renzo & Urzay, 2018, Karnik & Shrimpton, 2012, Lu & Shaw, 2015, Lu *et al.*, 2010, Yao & Capecehatro, 2018) or by turbulent channel flow (Rambaud *et al.*, 2002).

In order to obtain a better understanding of the effect of inter-particle electrostatic interactions on the spatial distribution of particles, several statistics have been calculated that offer an insight on the distribution of particles in the turbulent charged particle-laden gas flow.

5.3.1 Preferential particle concentration

In case of like-charged particles, one could reflect on the nature of electrostatic interactions by observing instantaneous snapshots of the particle flow in the stationary regime. In Fig. 5.37 it

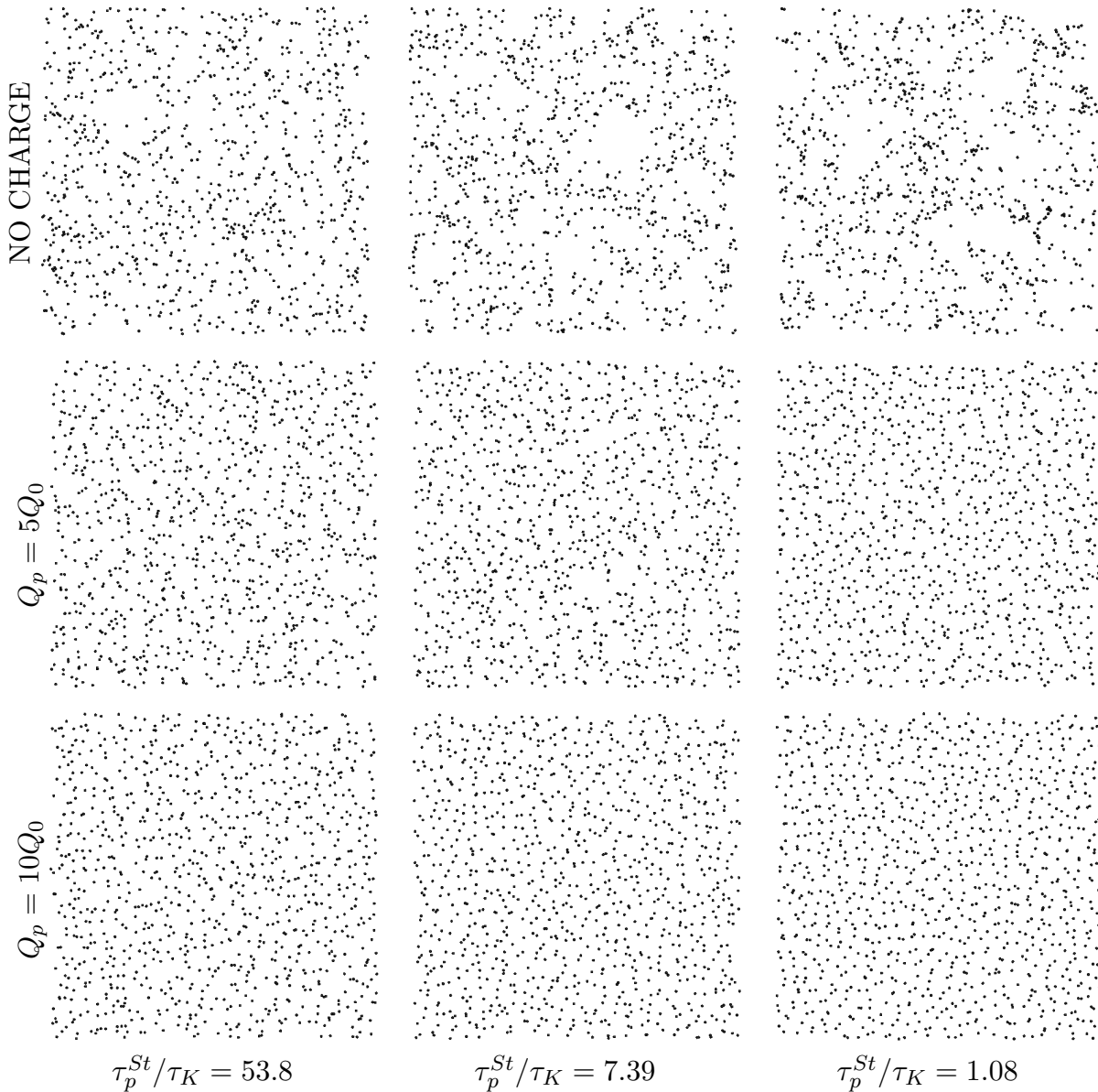


Figure 5.37: Instantaneous snapshots of like-charged particle-laden turbulent gas flows for various levels of inertia and electric charges for $\Delta x = L_f$.

is observed that such electrostatic interactions tend to homogenize the particle distribution due to the repulsive nature of the electrostatic forces. This leads to a mitigation and eventually an elimination of preferential concentration especially for light particles.

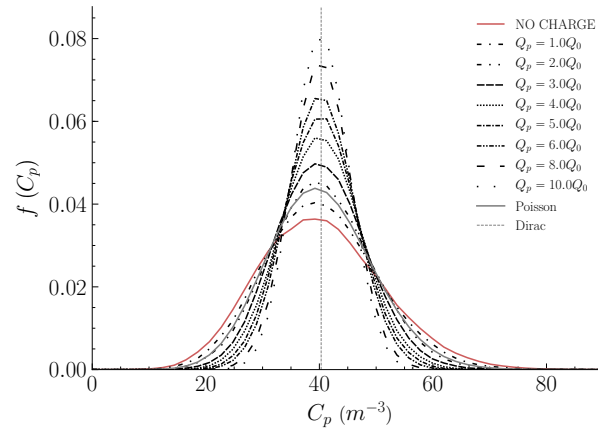
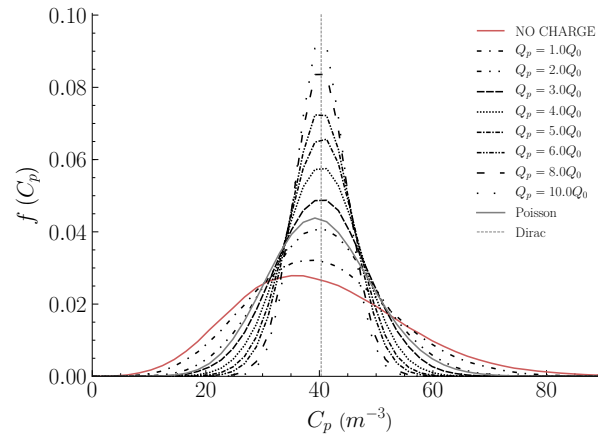
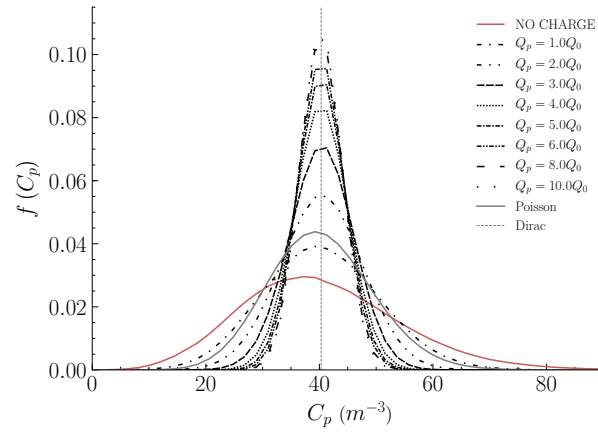
(a) $\tau_p^{St}/\tau_K = 53.8$ (b) $\tau_p^{St}/\tau_K = 7.39$ (c) $\tau_p^{St}/\tau_K = 1.08$

Figure 5.38: Effect of electrostatic interactions on particle concentration distributions for various levels of electric charge and three levels of particle inertia.

Electrostatic forces are conservative forces, thus a system of charged particles under their influence will start evolving with an initial electric potential energy, part of which will gradually transform to kinetic energy. However, in the presence of a fluid turbulent flow, the physics of the charged particle-laden turbulent gas flow are slightly more complex, so in order to gain

some more insight we should consider three main mechanisms that govern it.

Firstly, according to the minimum potential energy principle, which is valid for conservative forces such as the electrostatic, the system of particles tends to an equilibrium of minimum electric potential energy which implies that the particles will try to separate themselves as much as possible. On the other hand, it has been mentioned in Sect. 3.2.4, that in turbulent particle-laden gas flows there are certain regions in the flow (high strain rate, low vorticity) that favor particle concentration resulting in a local increase of electric potential energy and thus in further production of kinetic energy.

Lastly, the additional production by electrostatic effects tends to increase the average stationary level of q_p^2 . This kinetic energy production is compensated, in stationary flow, by an additional dissipation due to the drag force of the fluid which dissipates it in heat by viscous effect. Figure 5.38 depicts the effect of electrostatic interactions on particle concentration distribution. Specifically, for increasing particle electric charge it seems that $f(C_p)$ tends to a Dirac distribution at the particle density n_p (see Eq. (3.47)).

This occurs for like-charged particles because inter-particle repulsive electrostatic forces tend to homogenize the particle distribution across the computational domain. In fact, this behavior is characteristic of the conservative field of electrostatic forces that tends to force the particles in such a distribution that the total electrostatic potential stored in the charged particle cloud is minimized. This means that electrostatic interactions mitigate or even eliminate the phenomenon of preferential concentration as previously shown by work by Karnik & Shrimpton (2012), Lu & Shaw (2015), Lu *et al.* (2010), Yao & Capecelatro (2018).

These observations are also confirmed by Fig. 5.39 which depicts the effect of electrostatic interactions on global particle accumulation. Increasing electric charge, leads to stronger inter-particle repulsive electrostatic forces which tend to diverge the global particle accumulation close to that predicted by a Dirac distribution, for which $\sigma_{C_p} = 0$ so that Eq. (3.48) gives $\Sigma_p = -\sigma_P/n$, where $n = N_p/N_c$. In order to deepen our analysis on the structure of the

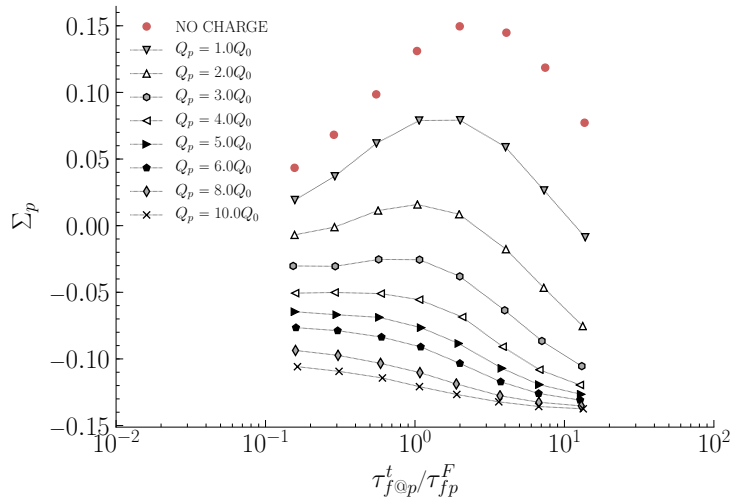


Figure 5.39: Effect of electrostatic interactions on global particle accumulation levels with regard to particle inertia for various levels of electric charge.

particle distribution under the effect of electrostatic forces, we investigate in Fig. 5.40 their effect on the PDF of the nearest-neighbor particle distance. Specifically, for increasing particle electric charge it seems there is no probability that a particle be close to another particle.

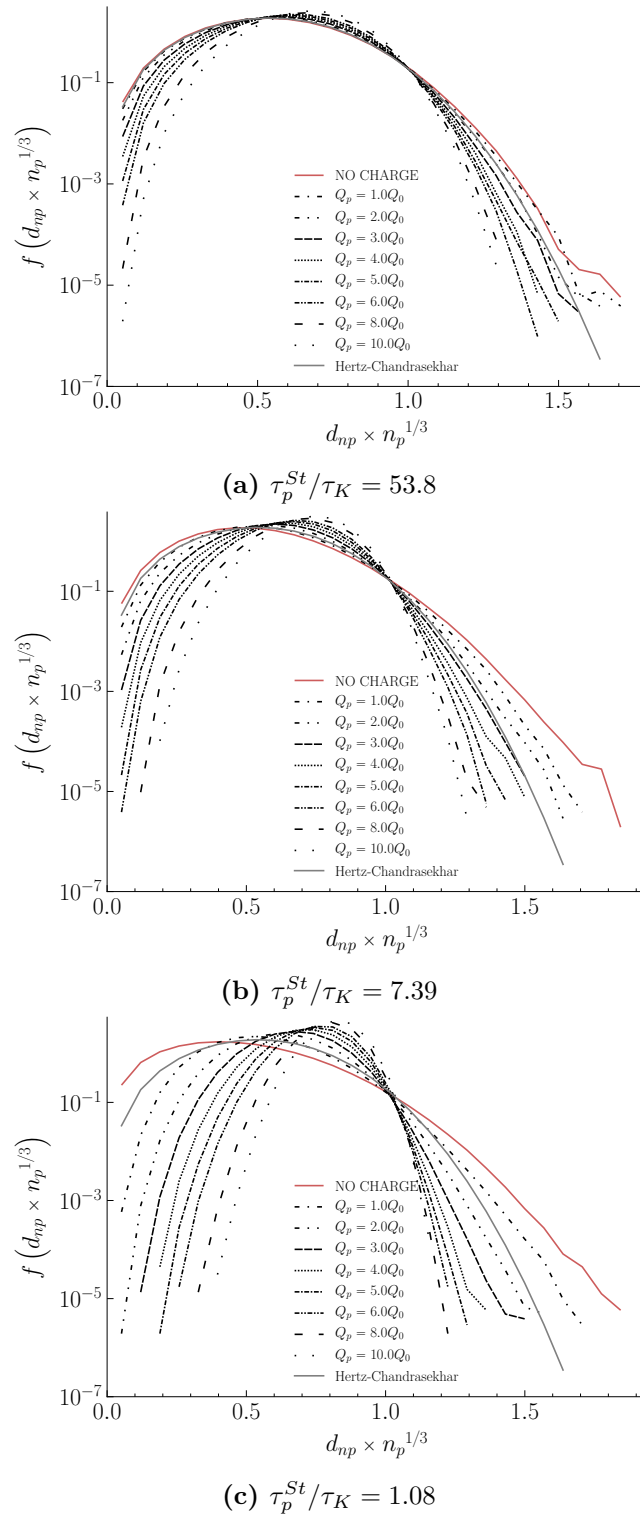


Figure 5.40: Effect of electrostatic interactions on PDF of nearest-neighbor particle distance for various levels of electric charge and three levels of particle inertia.

This constitutes first evidence of the existence of an exclusion sphere around each particle where no other particle can enter as the repulsive electrostatic force generated at such small distances is too big to be overcome by hydrodynamic forces. Interestingly, this is in agreement

with the implications of the Coulomb collision mechanism used as an explanation of the inter-particle electrostatic interactions. According to that mechanism, particles act as if they perform collisions at a distance, or collisions with a fictitious effective Coulomb diameter d_{pq}^C which is substantially large for lighter particles, an observation made in Fig. 5.40c.

Figure 5.41 illustrates the effect of electrostatic interactions on the average and variance of the nearest-neighbor particle distance. It seems that increasing the electric charge, the average minimum inter-particle distance increases, as repulsive electrostatic forces become stronger and particle distribution becomes homogeneous. In addition, for the same level of particle electric charge, lighter particles exhibit bigger inter-particle distances in average approaching an average distance of an equidistant distribution $n_p^{-1/3}$, which once again confirms the high-frequency Coulomb collision regime hypothesis for light particles. As far as the variance of d_{np} is concerned, it becomes evident that it diminishes as particle inertia and electric charge increase, as has also been observed in Fig. 5.40.

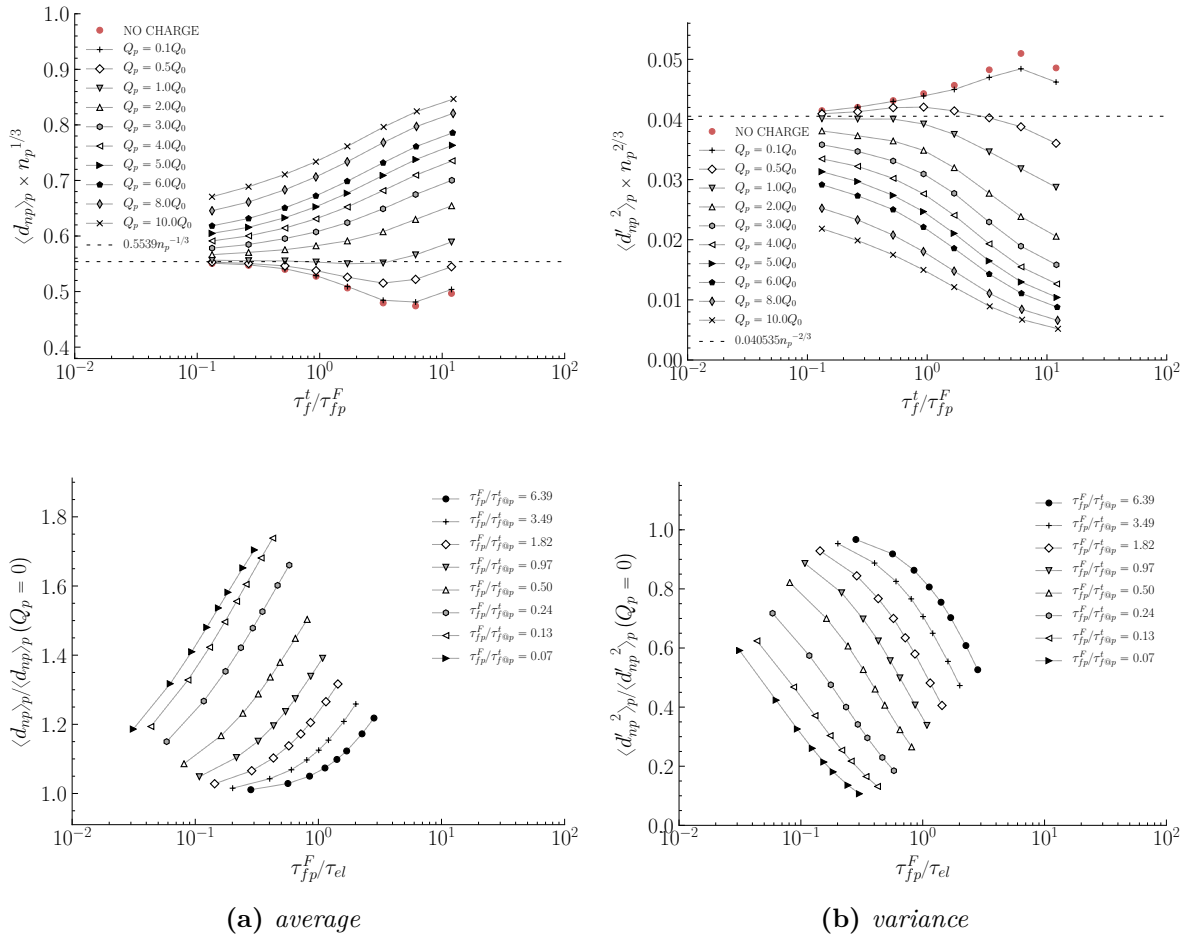


Figure 5.41: Effect of electrostatic interactions on average (left), and variance (right) of the nearest-neighbor particle distance.

Figure 5.42 depicts how the radial distribution function is affected by electrostatic interactions. Specifically, for increasing particle electric charge it seems that $g(r)$ tends to start from increasingly lower values. This is more pronounced for light particles and it indicates that preferential concentration is strongly mitigated for weak electrostatic forces and even eliminated for strong ones. This is an expected phenomenon that has been first documented

by Alipchenkov *et al.* (2004), Karnik & Shrimpton (2012), Yao & Capecelatro (2018).

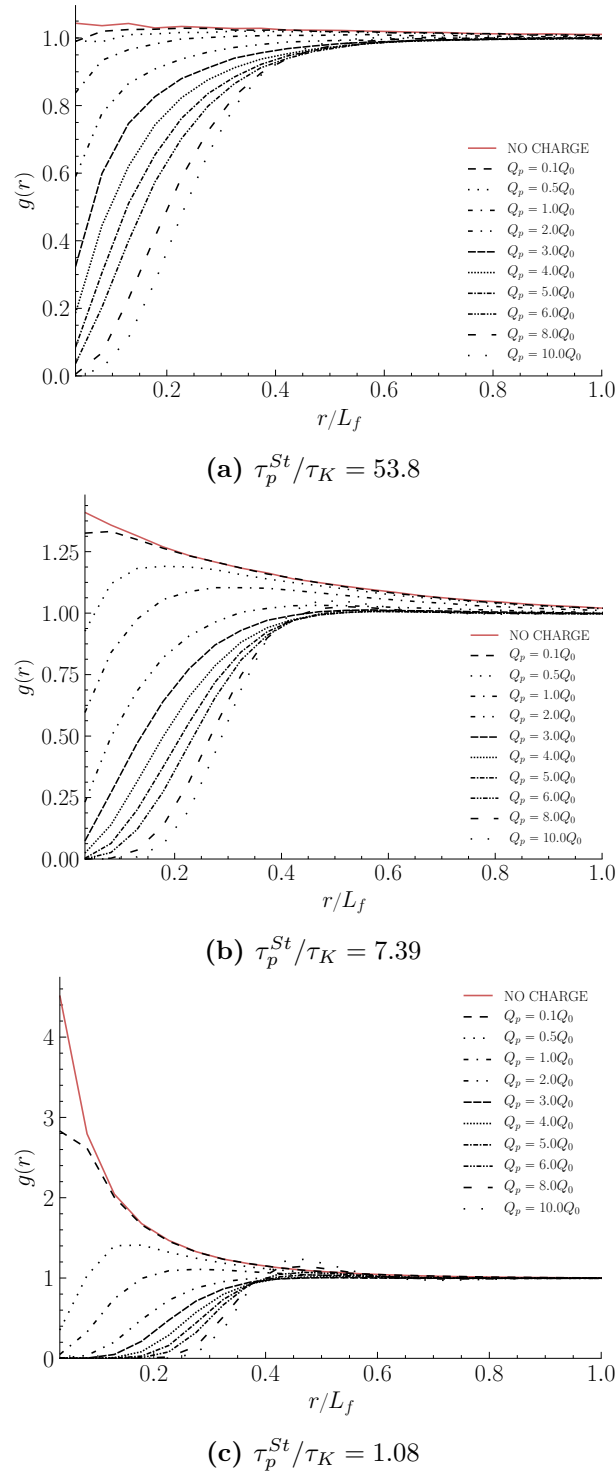


Figure 5.42: Effect of electrostatic interactions on particle concentration distributions for various levels of electric charge and three levels of particle inertia.

Finally, these observations are confirmed by Fig. 5.43 which depicts the effect of electrostatic interactions on RDF at separation distance $r = d_p$. Increasing particle electric charge,

leads to stronger inter-particle repulsive electrostatic forces which tend to flatten the $g(r = d_p)$ curve to zero, as all particles develop exclusion zones around them. In fact, for a given level of electric charge, this exclusion zone is more pronounced for lighter particles. Characteristically, for weak electric charge, the (low) agglomeration of heavy particles is not considerably affected, while for light particles it decreases significantly.

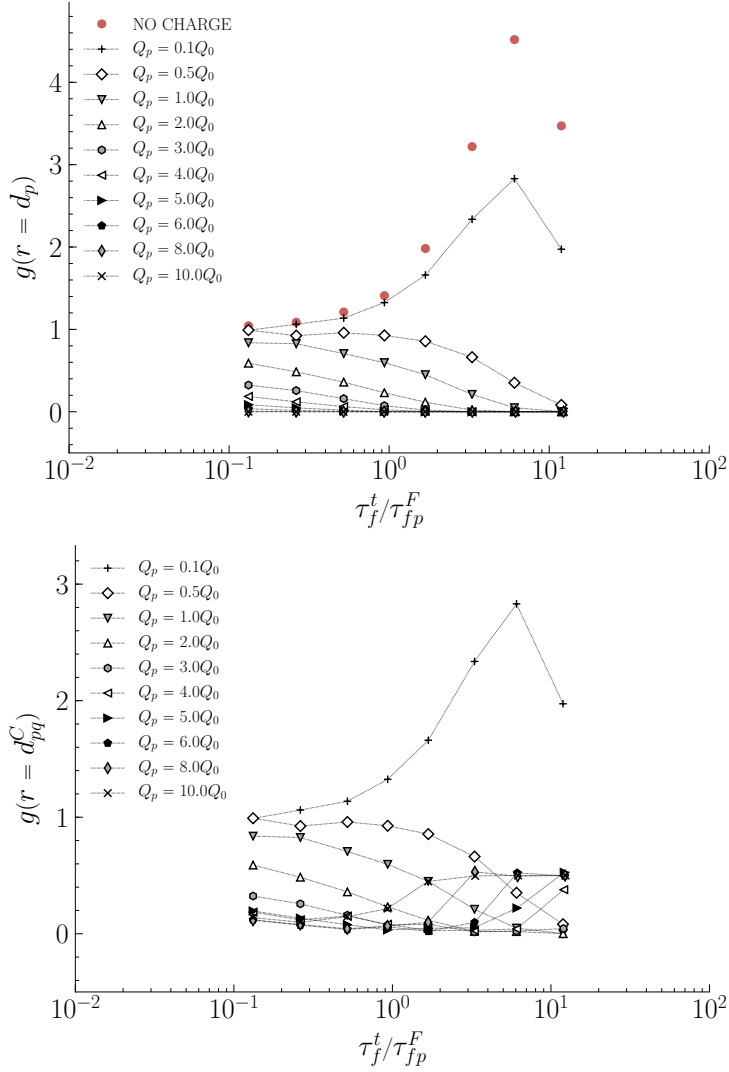


Figure 5.43: *RDF at separation distance $r = d_p$ and $r = d_p^C$ with regard to particle inertia for various levels of electric charge. The red markers correspond to the charge-free case.*

It should be noted here that these observations seem to match (qualitatively) the ones made in the published work of Alipchenkov *et al.* (2004), Lu *et al.* (2010) and Lu & Shaw (2015). Specifically in the latter, Lu & Shaw (2015) deals with particles of low Stokes numbers τ_{fp}^F/τ_K and weak electric charges. Under these assumptions, and for the dissipative turbulent length range $r < \eta_K$, they decompose the radial relative particle velocity into turbulence and Coulomb terms w_s and w_e , respectively

$$w_r = w_s + w_e \quad (5.15)$$

where w_e is the terminal Coulomb velocity

$$w_e = \frac{2\lambda Q_p^2}{m_p r^2} \tau_{fp}^F \quad (5.16)$$

and they provide a model for the calculation of the RDF of like-charged particles as

$$g(r) = c_0 \left(\frac{\eta_K}{r} \right)^{c_1} \left[1 - \operatorname{erf} \left(w_e \tau_K \frac{1}{r} \sqrt{\frac{15}{2}} \right) \right] . \quad (5.17)$$

where c_0 and c_1 are the coefficients that have been calculated by curve fitting of the power law of Eq. (3.52) (Chun *et al.*, 2005) to the DNS data for RDFs of charge-free inertial particles. Figure 5.44 shows the RDFs for a turbulent length range bigger than the dissipative, $\eta_K < r < 25\eta_K$ and for particles with the lowest Stokes number examined in this work for several levels of weak electric charges. It seems that the theoretical model of Lu & Shaw (2015) tends to match the trend of the DNS data at the limit of low Stokes numbers and of weak electric charges (two main hypotheses of the model). It should be noted here, that the aforementioned model was validated for lower Stokes numbers $\tau_{fp}^F/\tau_K \in [0.06, 0.18]$, but the apparent discrepancies are more likely to be related to its adaptation for a bigger turbulent length range, that is one of the main hypotheses of the Chun *et al.* (2005) model for the radial distribution function in the charge-free case (see Subsect. 3.2.4) upon which this model is based to include the effect of electric charges.

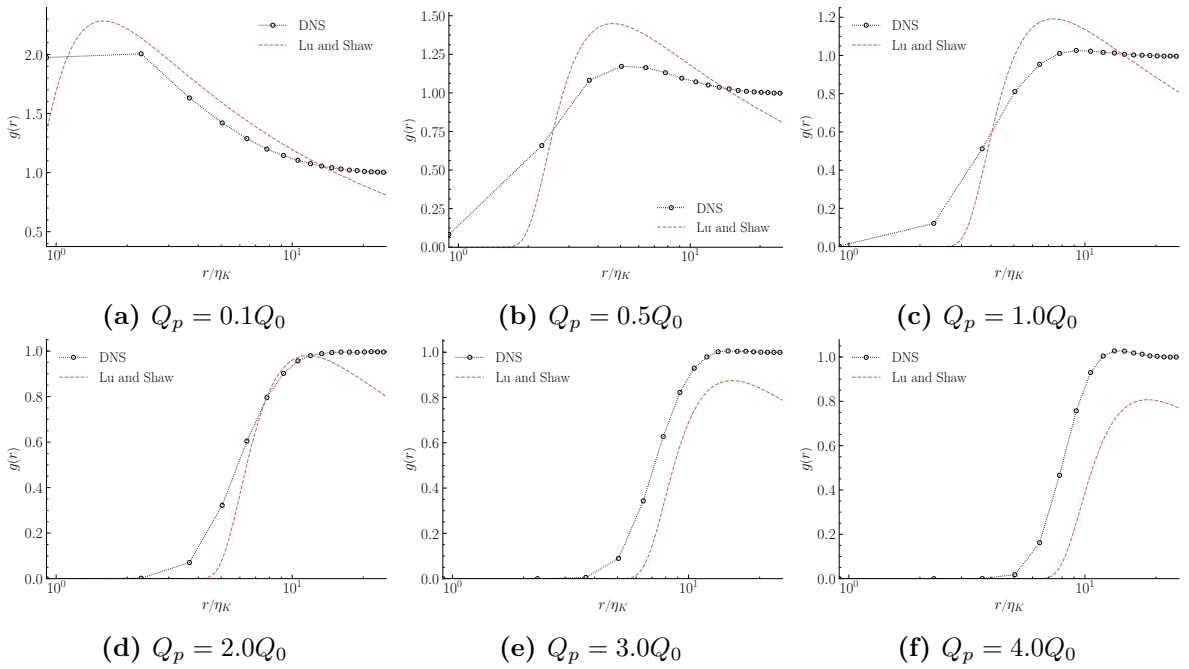
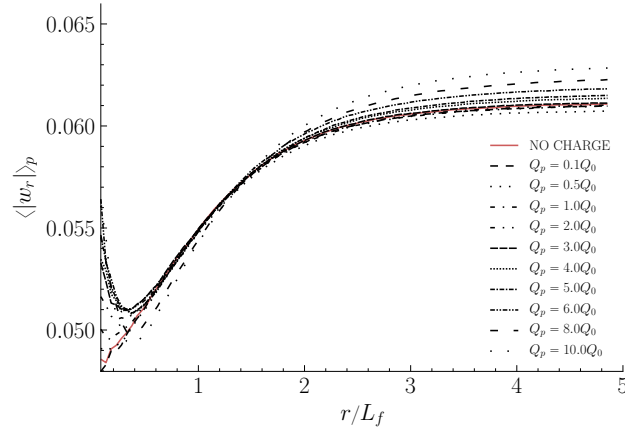


Figure 5.44: *RDFs of the lighter particles compared with Lu & Shaw (2015) model of Eq. (5.17) for various levels of electric charges. We observe an agreement on the trend of the evolution of RDFs for weak electric charges, one of the hypotheses of the cited model.*

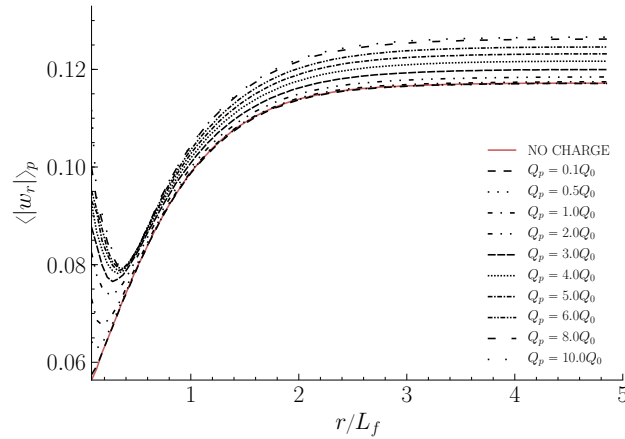
5.3.2 Relative inter-particle motion

Figure 5.45 shows the effect of electric charge on RDFs of radial relative particle velocity for three levels of particle inertia. An increase of its value for short particle separation distance is

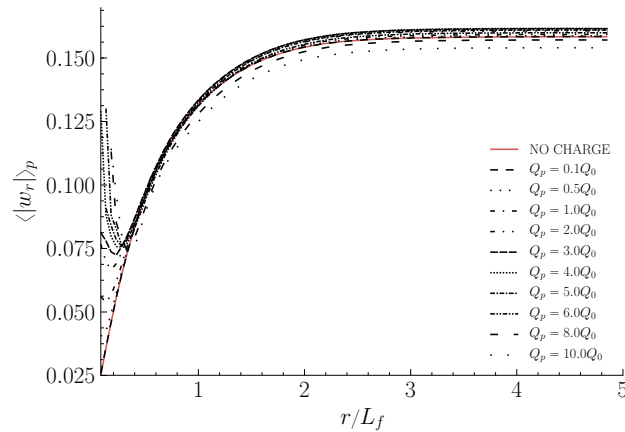
observed which can be due to the strong repulsive electrostatic forces at such distances. As the separation distance increases, $\langle |w_r| \rangle_p$ follows the trend of the charge-free case as electrostatic forces become weaker.



(a) $\tau_p^{St}/\tau_K = 53.8$



(b) $\tau_p^{St}/\tau_K = 7.39$



(c) $\tau_p^{St}/\tau_K = 1.08$

Figure 5.45: Effect of electrostatic interactions on RDFs of radial relative particle velocity for various levels of electric charge and three levels of particle inertia. Most affected are the particles of moderate inertia that exhibit preferential concentration in the charge-free case.

For large separation distances $r \sim 5L_f$, $\langle |w_r| \rangle_p$ seems to slightly increase for heavy particles and slightly decrease for light particles as the former are more while the latter are less agitated due to electrostatic forces. However, for moderate particle inertia, the average radial relative velocity, $\langle |w_r| \rangle_p$ seems to increase for increasing electric charge. This can be explained by the strong competition of the hydrodynamic and electrostatic forces for moderate particle inertia. For these particles, the former are strictly responsible for particle approaching motion (preferential concentration), while the latter partially responsible (drag is also responsible for this) for particle departing motion (electrostatic repulsion).

In Fig. 5.46 the average value $\langle |w_r| \rangle_p$ and variance $\langle w_r'^2 \rangle_p$ of the radial relative particle velocity is presented for various levels of electric charges and particle inertia. It seems that for intermediate Stokes numbers, both average and variance slightly increase due to electrostatic interactions as they experience an increase in agitation. On the contrary, for low Stokes numbers, the same statistics decrease as they experience a decrease in agitation.

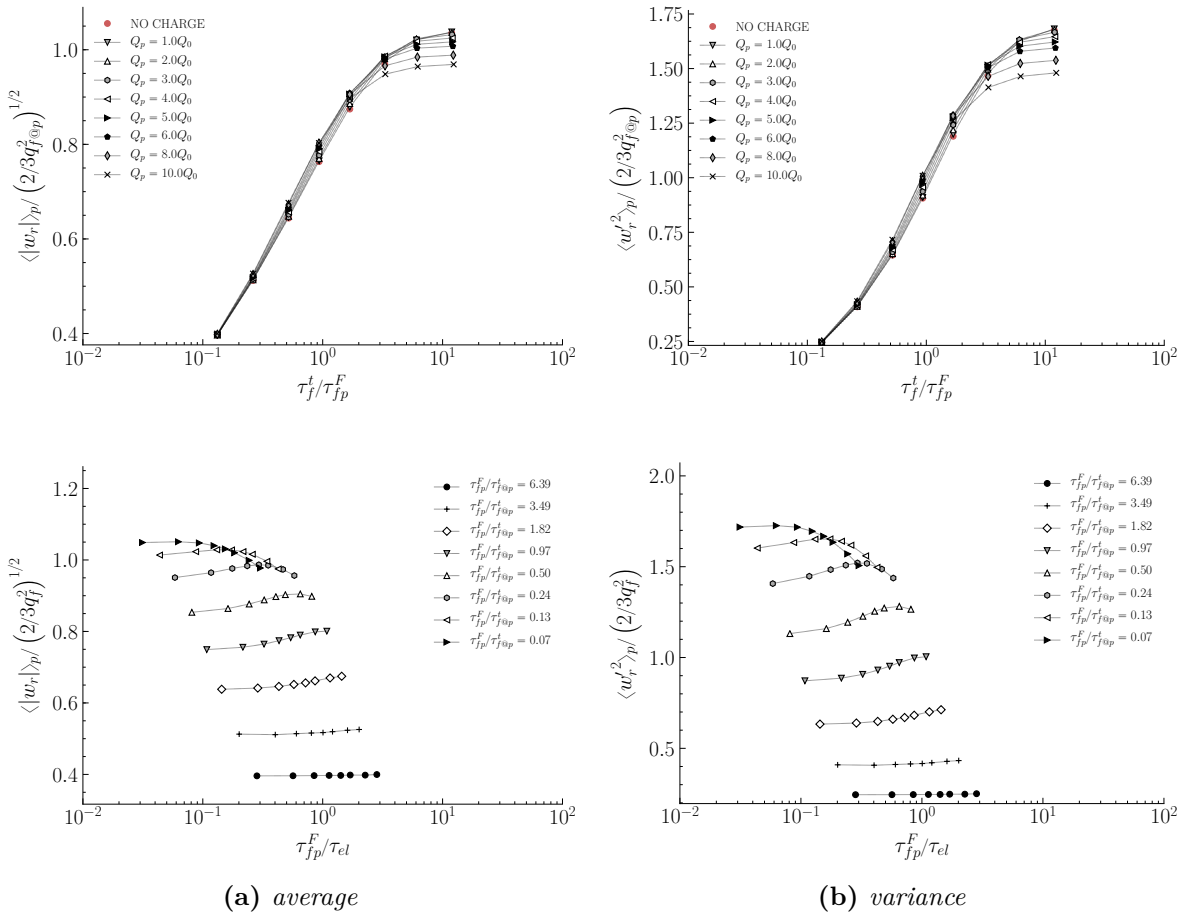


Figure 5.46: Effect of electrostatic interactions on average (left), and variance (right) of the radial relative particle velocity normalized by $2/3q_f^2$.

It should be noted here, that these observations seem to match (qualitatively) the ones made in the published work of Alipchenkov *et al.* (2004), Lu *et al.* (2010) and Lu & Shaw (2015). Specifically in the latter, Lu & Shaw (2015) provide a model for the calculation of the radial relative particle velocity of like-charged particles, for particles of low Stokes numbers

τ_{fp}^F/τ_K and weak electric charges, written as

$$\langle |w_r| \rangle_p = \sqrt{\frac{2}{\pi}} \sigma \frac{\exp\left(-\frac{w_e^2}{2\sigma^2}\right)}{1 - \operatorname{erf}\left(\frac{w_e}{\sqrt{2}\sigma}\right)} - w_e \quad (5.18)$$

where σ , defined in Eq. (3.53) is the standard deviation of the Gaussian distribution of the turbulent part of the radial relative particle velocity, w_s (see Eq. (5.15)) for the dissipative turbulent length range $r < \eta_K$, and w_e is the terminal Coulomb velocity (see Eq. (5.16)). In Fig. 5.47 we observe that the DNS data do not match the model's predictions. The reason for this is twofold, as it is suitable for particles of very low Stokes numbers, but also it was based on Saffman & Turner (1956) model for the radial relative velocity, which is valid for the dissipative turbulent length range $r < \eta_K$ and here it is used outside of this length range.

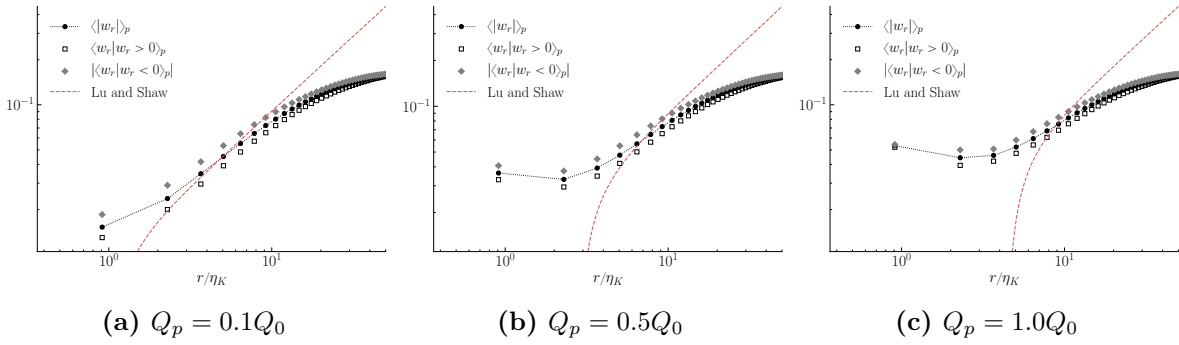


Figure 5.47: *RDFs of the average radial relative velocity for low particle Stokes numbers compared with Lu & Shaw (2015) model of Eq. (5.18) for three levels of (weak) electric charges.*

PDF of particle velocities

Figure 5.48 shows the PDF of the three components of particle velocities for various levels of inertia. It can be deduced that, since the PDFs overlap, the distribution of particle velocities is isotropic as orientation does not affect the shape of the PDFs. This is in agreement with the known isotropy properties of the electric field (as shown by Fig. 5.4) and of the simulated turbulence. In order to obtain a more precise idea of the form of the PDF of $u_{p,i}$, they have been plotted in Fig. 5.48 with exponential and Gaussian functions that are obtained via relation (3.55). One can make two observations based on Fig. 5.48. First, it seems that the

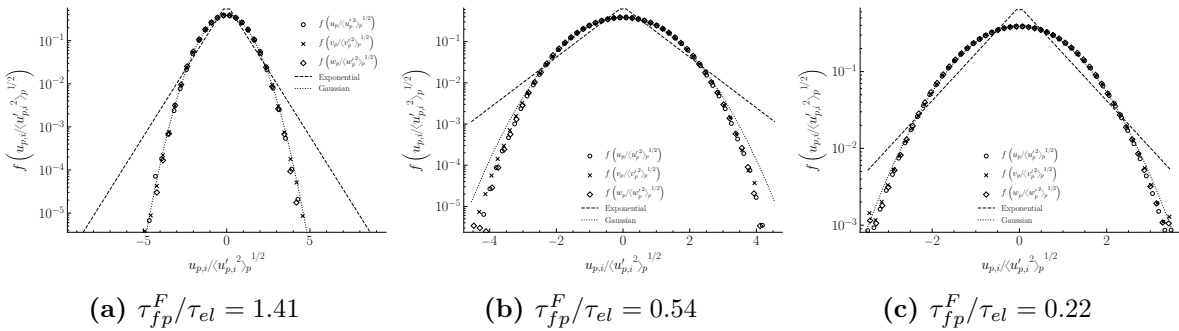


Figure 5.48: *PDF of the three components of particle velocities for various levels of particle inertia and $Q_p = 5Q_0$. The distributions are perfectly Gaussian (see Eq. (3.55)).*

PDFs of particle velocities are almost perfect Gaussian distributions, while for the same level of particle electric charge, as particle inertia increases their range increases. Furthermore, Fig. 5.49 shows the effect of electrostatic interactions on the PDF of the x -axis component of the particle velocity for different levels of particle inertia. It seems that particle-particle electrostatic interactions have no effect on the distribution of particle velocities. This implies that they affect mostly the spatial structure of the gas-particle flow and modify the fluid-particle correlation instead of directly altering the kinetic state of the particles.

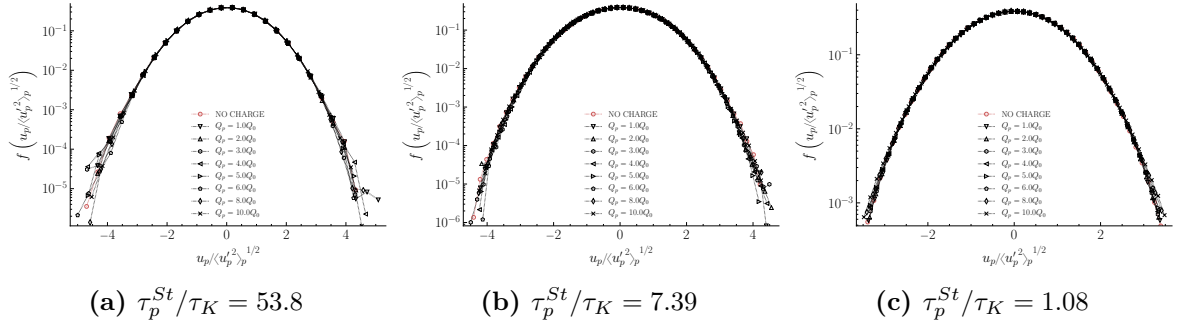


Figure 5.49: Effect of electrostatic interactions on the PDF of the x -axis component of the particle velocity for various levels of electric charge and three levels of particle inertia. Increasing particle electric charge does not seem to affect the distribution of particle velocities.

5.4 Effect of particle number density

At this point, we examine the effect of particle number density on the dynamics of a like-charged particle-laden turbulent gas flow. To do this, inertial particles of Stokes number $\tau_p^{St}/\tau_K = 4.03$ (class 5 in Table 2.4) are considered in a computational domain of constant size $L/\pi = 2$.

A three-fold approach is followed: at first particle flow dynamics are examined for increasing particle numbers $N_p = [1, 5, 10, 20] \times 10^4$ in the charge-free case. Then the particle electric charge is kept constant at $Q_p = 5Q_0$ and flow dynamics are examined for increasing particle numbers $N_p = [1, 5, 10, 20] \times 10^4$. Finally, for each level of particle number density n_p , particle flow dynamics are examined for calculated levels of particle electric charge for which τ_{el} is kept constant, based on the premise that τ_{el} dictates the electrostatics of particle dynamics. For the latter, following Eq.(4.20) for a given particle mass m_p and domain size L , it is possible to calculate an equivalent particle electric charge Q'_p that corresponds to a charged particle cloud of N'_p that has the same τ_{el} with that of (N_p, Q_p) . Thus, one can write

$$(N'_p, Q'_p) \equiv (N_p, Q_p) \Leftrightarrow \tau_{el}(N'_p, Q'_p) = \tau_{el}(N_p, Q_p) \Leftrightarrow Q'_p = Q_p \sqrt{\frac{N_p}{N'_p}}$$

For this level of particle inertia and domain size, charged particle cloud $(10^4, 5Q_0)$ has electrostatic time scale $\tau_{el} = 2.5s$. To to keep the same particle dynamics via a constant τ_{el} , an equivalent electric charge is calculated for an increasing particle number N_p in Table 5.2.

Table 5.2: Equivalent particle electric charge for increasing N_p and given τ_{el}

$N_p/10^4$	1	5	10	20
2.5	$5Q_0$	$5/\sqrt{5}Q_0$	$5/\sqrt{10}Q_0$	$5/\sqrt{20}Q_0$

Figure 5.50 shows flow snapshots for the twelve (in fact eleven) (N_p, Q_p) configurations.

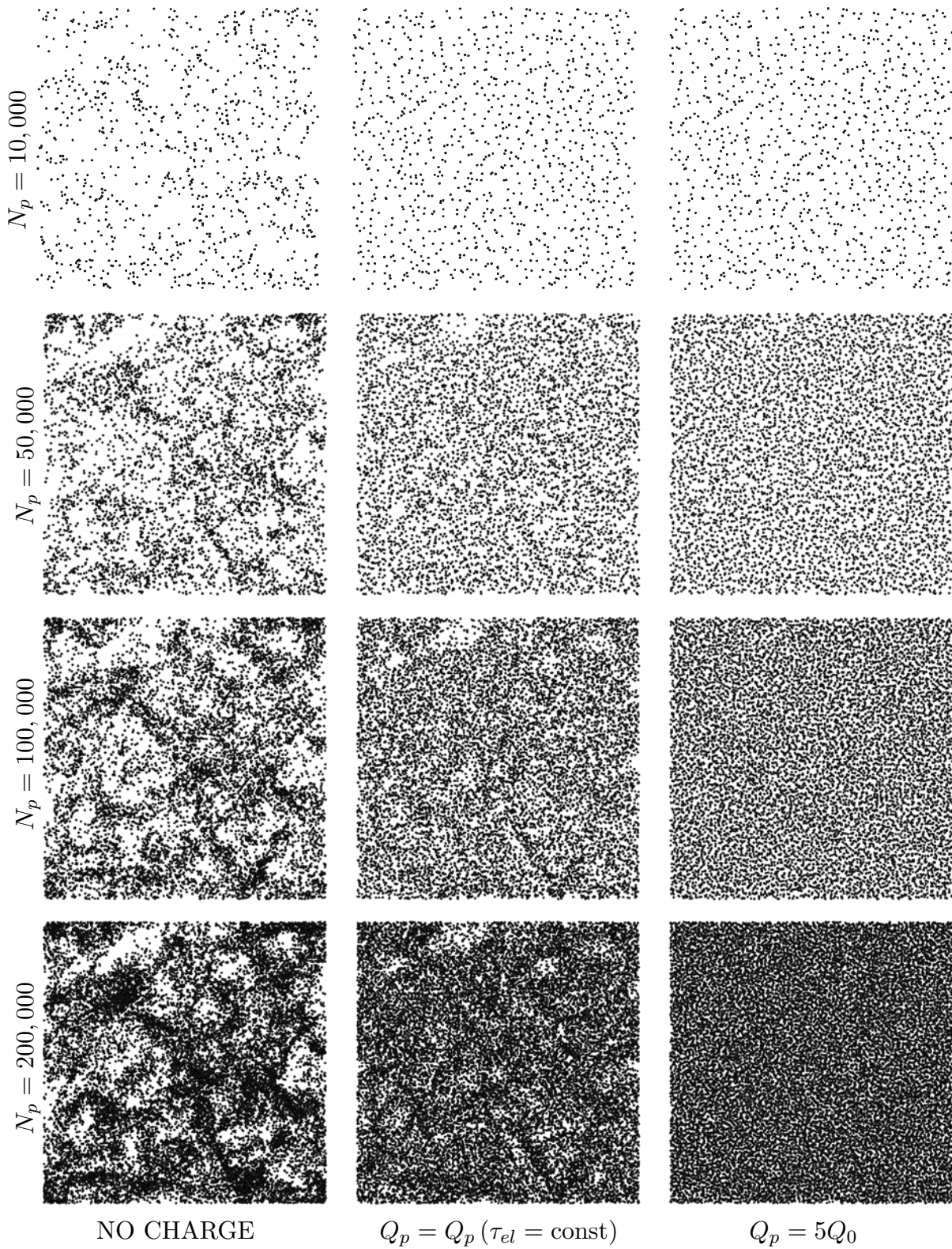


Figure 5.50: Instantaneous snapshots of like-charged particle-laden turbulent gas flows for various levels of particle number and electric charges for $\Delta x = L_f$.

Figure 5.51 visualizes the case studies that have been examined in terms of particle electric charge Q_p . For each level of particle number density, apart from the charge-free case, there are two particle electric charges examined: $5Q_0$ and $Q_p = Q_p(\tau_{el} = \text{const})$. As expected, while keeping particle electric charge constant, increasing particle volume/number density entails a smaller electrostatic time scale, since electrostatic interactions become stronger and the Coulomb collision frequency increases. To examine the latter, one can calculate the Lagrangian

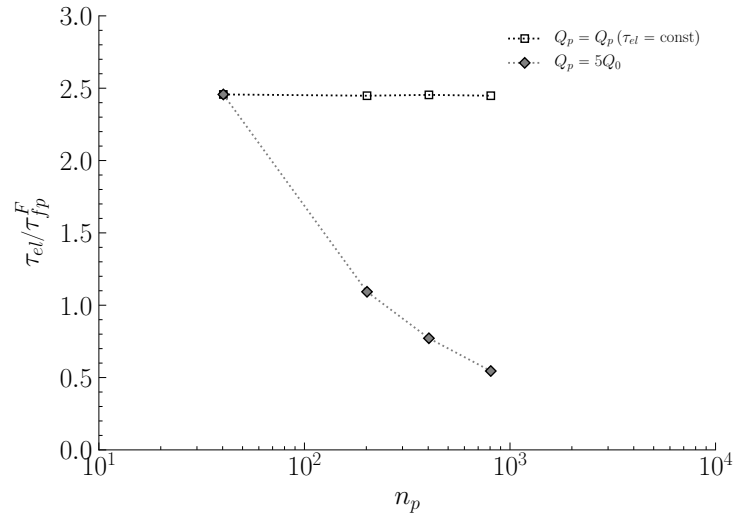


Figure 5.51: *Electrostatic time scale for increasing particle number density.*

particle integral time scale as shown in Fig. 5.52. This Figure shows that particle-particle (repulsive) electrostatic interactions enhance particle velocity decorrelation, as indicated by the decrease of τ_p^t . In fact, it seems that constant τ_{el} entails (somewhat) constant τ_p^t , as for strong electrostatic interactions the latter is strongly tied to the former. However, for constant levels of particle charge Q_p , increasing particle number density further enhances the particle velocity decorrelation as particle charge density increases. This concept of "stronger" electrostatic interactions can be viewed by Fig. 5.53. Indeed, τ_{el} seems a very good candidate

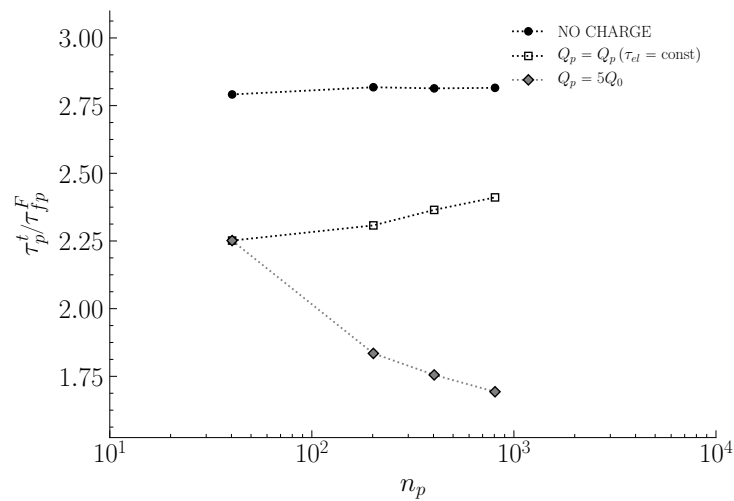


Figure 5.52: *Lagrangian particle integral time scale for increasing particle number density.*

for characterizing the kinetic energy levels of the like-charged particle cloud as both $\langle \|F_e\| \rangle_p$ and q_p^2 remain slightly unaffected by n_p for constant τ_{el} . However, for constant particle electric charge, an increase of n_p implies a dramatic increase of the average norm of the electrostatic forces applied on the particles. One cannot say the same for particle agitation which seems to reach a saturation level at $q_p^2 \simeq 0.8 \times q_{f@p}^2$ as kinetic energy is dissipated by turbulent viscosity.

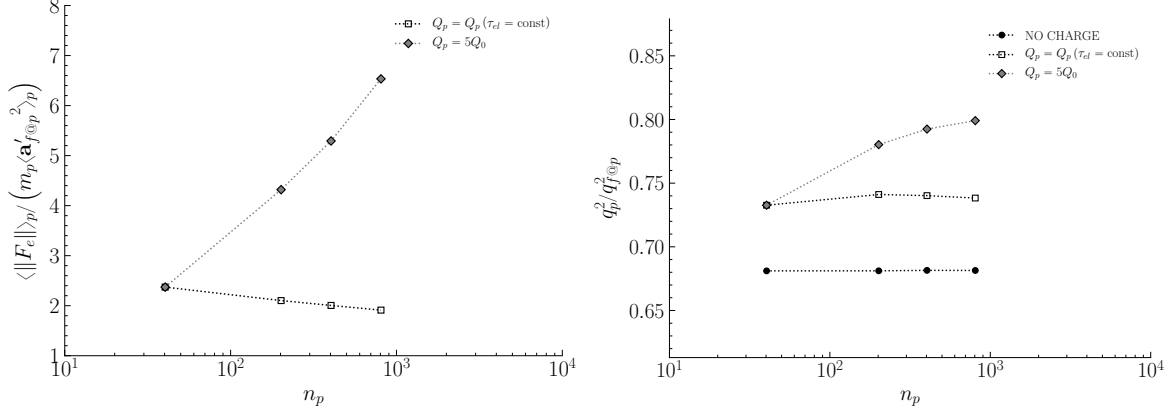


Figure 5.53: Effect of particle number density on Lagrangian average of the norm of electrostatic forces (left) and particle agitation (right) for different levels of particle charge.

Finally, there are several interesting observations to be made considering Fig. 5.54. Indeed, the effect of particle number density on particle distribution is more intricate for the different examined levels of particle electric charge. For example, in the charge-free case the nearest-neighbor particle distance remains unaffected as $\langle d_{np} \rangle_p \simeq 1/2n_p^{-1/3}$ for increasing particle number density n_p . For $Q_p = 5Q_0$, since the increase of particle number density implies stronger electrostatic interactions, $\langle d_{np} \rangle_p$ approaches the equidistant-distribution distance $n_p^{-1/3}$ for increasing n_p . However, for $Q_p = Q_p (\tau_{el} = \text{const})$, d_{np} decreases slightly with

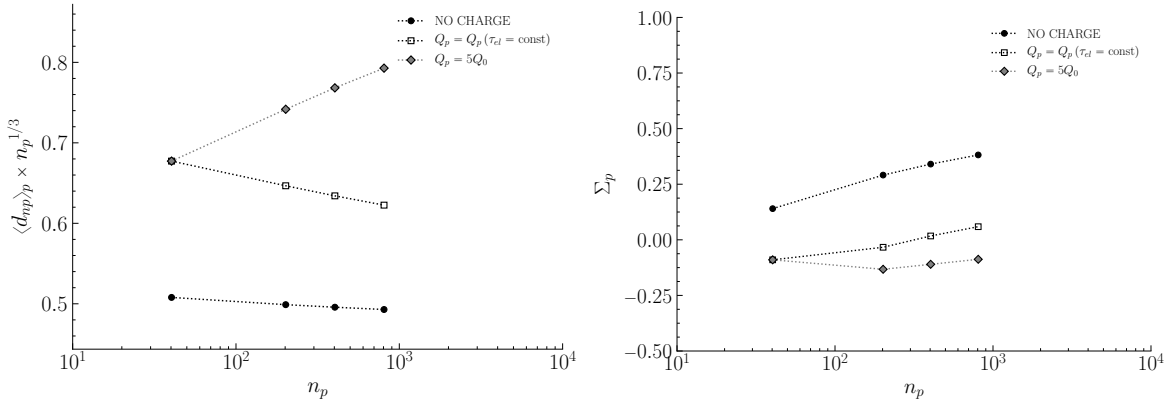


Figure 5.54: Effect of particle number density on particle distribution for different levels of particle charge. Nearest-neighbor particle distance (left), global particle accumulation (right).

regards to $n_p^{-1/3}$ which means that when keeping the same level of electrostatic interactions the distribution tends to be more uniform and less equidistant due to the largest number of particles per volume. This observation is also backed by the effect of n_p on the evolution of the global particle accumulation Σ_p which seems to increase in the iso- τ_{el} case.

Last but not least, Fig. 5.55 examines the behavior of the exclusion zone phenomenon under the influence of growing particle number density. On one hand, at a distance close to the physical collision, The particle accumulation levels remain the same for the charge-free case, as the fundamental mechanisms of preferential concentration remain the same. On the other hand, keeping particle electric charge constant and increasing particle number density leads to a high content of particle electric charge density, which leads to a strong exclusion zone around each particle. On the contrary, keeping the same electrostatic time scale and increasing the particle number density, inevitably leads to slightly higher levels of accumulation since it is not otherwise possible to maintain the same levels of particle charge density while increasing particle number density. Coulomb collision mechanism is found to present some-kind of self-similarity as, although Coulomb effective diameter d_{pq}^C does not directly depend on particle number density (only for dry granular flows), the radial distribution functions at $r = d_{pq}^C$ collapse for different levels of electrostatic interactions.

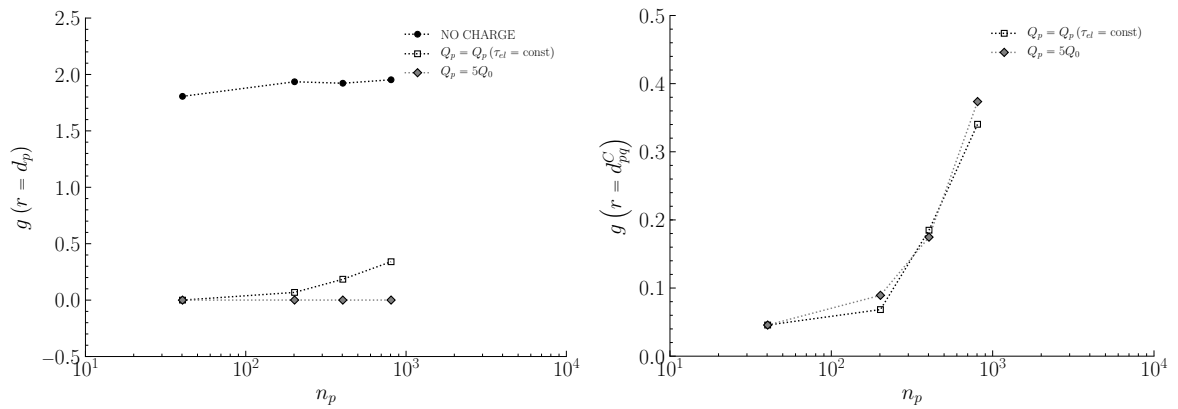


Figure 5.55: Effect of particle number density on particle distribution for different levels of particle charge. RDF at particle collision (left) and RDF at Coulomb collision (right).

5.5 Conclusion

This chapter presents the results obtained from DNS of electrically charged particles transported by homogeneous isotropic turbulence and their statistical analysis. In such a configuration, the two main mechanisms that drive particle behavior are the hydrodynamic drag and the electrostatic forces. To characterize the competition between the two, an electrostatic Stokes number is devised and linked theoretically to the particle Stokes number.

Then, the effect of electrostatic interactions on particle dispersion is examined via a modification of the classic theoretical Tchen-Hinze framework (Hinze, 1972). The basic observation is that for increasing particle electric charge, particle agitation increases for particles of moderate inertia and decreases for light particles, while heavy particles remain unaffected. This modification of particle agitation is not direct, but rather comes from a corresponding modification of fluid-particle covariance, which is a measure of fluid-particle correlation. In fact, a closer look at the flow dynamics shows that electrostatic forces slow down the turbulent dissipation rate of fluid-particle correlation, thus increasing fluid-particle correlation. However, at the same time turbulence-induced electrostatic energy destroys this correlation. This essentially means that for a given level of particle inertia, stronger electrostatic interactions lead to fluid-particle correlation increase up to a saturation electric

charge, above which it starts to decrease. Same goes for particle agitation.

Moreover, as far as the characteristic time scales are concerned, the Lagrangian integral time scale of the particle velocity, τ_p^t is considerably reduced by electrostatic interactions as particle velocities decorrelate faster under the influence of electrostatic forces, while their effect on the corresponding time scale of the turbulent velocity "seen" at the particles position, $\tau_{f@p}^t$ is not so straight forward. In fact, electrostatic interaction enhance the ability of light particles to follow fluid trajectories, while for heavy particles the opposite trend is observed, hence they tend to become even more decorrelated from the turbulent flow. The former time scale seems to be the reason for a significant reduction of the particle dispersion coefficient, which entails an equivalent reduction of particle dispersion. Particles that are constantly repelled from each other, are less prone to wander off their initial positions as they have to "navigate" through paths of minimum resistance, hence this observed behavior.

Furthermore, follows an extensive analysis of electrostatic forces themselves, which brings to light their rather peculiar distribution whose form seems to be greatly different from Exponential and Gaussian distributions. In addition, a characteristic time scale of electrostatic interactions is defined and it could be used to determine the lifetime of the application of such a force distribution in a stochastic model. The spatial distribution of the like-charged particle cloud is examined and two main interesting observations are drawn. Firstly, preferential concentration is mitigated for weak particle electric charges and completely eliminated for strong ones. Secondly, there appears to be an exclusion zone around each particle, that stems from the fact that inside this zone, the repulsive electrostatic forces are substantially strong so that no particle can ever stay in this zone, leading to an equidistant particle distribution.

Finally, we examine the effect of particle number density on particle flow characteristics. There is a clear distinction between the "kinetic state" of the gas-particle flow and the spatial structure of the charged particle cloud. In fact, τ_{el} seems to be a very good candidate at describing the kinetic energy content of such a flow, however the spatial distribution of particles seems to be considerably affected by the particle number density. Simply, more particles per volume normally entail more particle accumulation. However, more particles per volume of the same level of electric charge, entail a higher particle charge density which leads to a rather homogeneous (equidistant distribution) but inevitably that of a smaller inter-particle distance.

Bibliography

- Alipchenkov, V.M., Zaichik, L.I., & Petrov, O.F. 2004. Clustering of charged particles in isotropic turbulence. *High temperature*, **42**(6), 919–927.
- Chun, Jaehun, Koch, Donald L., Rani, Sarma L., Ahluwalia, Aruj, & Collins, Lance R. 2005. Clustering of aerosol particles in isotropic turbulence. *Journal of fluid mechanics*, **536**(Aug.), 219–251. Publisher: Cambridge University Press.
- Dejoan, A., & Monchaux, R. 2013. Preferential concentration and settling of heavy particles in homogeneous turbulence. *Physics of fluids*, **25**(1).
- Di Renzo, M., & Urzay, J. 2018. Aerodynamic generation of electric fields in turbulence laden with charged inertial particles. *Nature communications*, **9**(1), 1676.
- Fede, P. 2004. *Modélisation et simulation numérique de l'influence de la turbulence sur les collisions dans les écoulements mono- et bi-solides*. Ph.D. thesis, Institut National Polytechnique de Toulouse.

- Fede, P., & Simonin, O. 2010. Effect of particle-particle collisions on the spatial distribution of inertial particles suspended in homogeneous isotropic turbulent flows. *Pages 119–125 of: Turbulence and interactions*. Notes on Numerical Fluid Mechanics and Multidisciplinary Design, vol. 110. Springer Berlin Heidelberg.
- Fessler, J.R., Kulick, J.D., & Eaton, J.K. 1994. Preferential concentration of heavy particles in a turbulent channel flow. *Physics of fluids*, **6**, 3742–3749.
- Hinze, J.O. 1972. Turbulent fluid and particle interaction. *Prog. heat and mass transfer*, **6**, 433–452.
- Karnik, A.U., & Shrimpton, J.S. 2012. Mitigation of preferential concentration of small inertial particles in stationary isotropic turbulence using electrical and gravitational body forces. *Physics of fluids*, **24**(7), 073301.
- Lu, J., & Shaw, R.A. 2015. Charged particle dynamics in turbulence: Theory and direct numerical simulations. *Physics of fluids*, **27**(6), 065111.
- Lu, J., Nordsiek, H., Saw, E.W., & Shaw, R.A. 2010. Clustering of charged inertial particles in turbulence. *Physical review letters*, **104**(May), 184505.
- Pope, S B. 1994. Lagrangian PDF Methods for Turbulent Flows. *Annual review of fluid mechanics*, **26**(1), 23–63.
- Pope, S.B. 2002. A stochastic Lagrangian model for acceleration in turbulent flows. *Physics of fluids*, **14**(7), 2360–2375.
- Rambaud, P., Tanière, A., Oesterlé, B., & Buchlin, J.M. 2002. On the behavior of charged particles in the near wall region of a channel flow. *Powder technology*, **125**, 199–205.
- Saffman, P. G., & Turner, J. S. 1956. On the collision of drops in turbulent clouds. *Journal of fluid mechanics*, **1**(1), 16–30. Publisher: Cambridge University Press.
- Simonin, O. 2000. Statistical and continuum modelling of turbulent reactive particulate flows. part 1 : Theoretical derivation of dispersed eulerian modelling from probability density function kinetic equation. *Pages – of: Lecture series 2000-06, von karman institute for fluid dynamics, rhodes saint genève (belgium)*. Von Karman Institute for Fluid Dynamics.
- Squires, K.D., & Eaton, J.K. 1991. Preferential concentration of particles by turbulence. *Physics of fluids a: Fluid dynamics*, **3**(5), 1169–1178.
- Voth, Greg A., Porta, A. La, Crawford, Alice M., Alexander, Jim, & Bodenschatz, Eberhard. 2002. Measurement of particle accelerations in fully developed turbulence. *Journal of fluid mechanics*, **469**(Oct.), 121–160. Publisher: Cambridge University Press.
- Wang, Lian-Ping, Wexler, Anthony S., & Zhou, Yong. 1998. Statistical mechanical descriptions of turbulent coagulation. *Physics of fluids*, **10**(10), 2647–2651. Publisher: American Institute of Physics.
- Yao, Yuan, & Capecelatro, Jesse. 2018. Competition between drag and Coulomb interactions in turbulent particle-laden flows using a coupled-fluid–Ewald-summation based approach. *Physical review fluids*, **3**(3), 034301.

-
- Zaichik, L.I., Simonin, O., & Alipchenkov, V.M. 2003. Two statistical models for predicting collision rates of inertial particles in homogeneous isotropic turbulence. *Physics of fluids*, **15**, 2995–3005.

6

Conclusion and prospects

*“ὅλον δέ ἐστιν τὸ ἔχον ἀρχὴν
καὶ μέσον καὶ τελευτήν¹”*

- Aristotle, c. 384 – c. 322 BC

6.1 Conclusions

The work presented in this PhD thesis has basically covered three topics: turbulent gas-particle flows, inter-particle electrostatic interactions and turbulent charged particle-laden gas flows.

To begin with, in order to simulate stationary homogeneous isotropic turbulence, one needs to add a kinetic energy production term that should balance the turbulent dissipation. Furthermore, when particles are transported by a fluid turbulent flow, one needs to carefully consider the involved length scales. If the inertial particles are smaller than the Kolmogorov length scale, they interact with rather large turbulent structures and the point-particle approximation can be used. This along with the fact that the particles are considered considerably more dense than the fluid, allows for a simplification of the forces exerted on them: the hydrodynamic drag, the gravity force and the electrostatic forces. Finally, several statistics have been deployed that allow for the calculation of characteristic scales that are of paramount importance in the understanding of the dynamics of such gas-particle flows.

A first step in understanding the dynamics of electrically charged particle-laden turbulent flows, is to acquire a concrete appreciation of the corresponding charge-free case. Such flows have been studied for many decades now, and there is a number of theoretical frameworks that facilitate their study, such as the Tchen-Hinze theory. A simulation of particle-laden turbulent gas flow without electric charges has been carried out. This requires the setup of a case of resolved stationary HIT and the calibration of the particle phase according to a desired range of Stokes numbers, which yields several particle classes based on different densities. This calibration occurs by performing a statistical analysis of the flow, by using velocity autocorrelation functions that allow to estimate characteristic time scales of the fluid and particle flow. This statistical analysis enables to recreate Tchen-Hinze theory concerning particle agitation which serves as verification of a successful particle-laden turbulent gas flow simulation. The key property that characterizes particle dynamics in turbulent gas-particle flows is particle inertia.

In a first order approximation, particle agitation, hence particle dispersion is more pronounced for lighter particles as for decreasing inertia - to the limit of fluid elements - particles tend to be more susceptible to local fluid fluctuations. However, it is shown that particle agitation depends on fluid-particle covariance which is a measure of fluid-particle correlation. An attempt to describe the turbulent dissipation of the latter via the fluid acceleration - particle velocity covariance has been made. For the latter it is shown that a

¹A whole is that which has beginning, middle and end.

model based on a stochastic equation for fluid acceleration measured at particle positions, predicts it with better accuracy if the supposed form of the fluid autocorrelation function is a double exponential. Furthermore, while the latter dissipation mechanism is not greatly affected by the decrease of particle inertia, its effect via the hydrodynamic force becomes predominant and leads to fluid-particle decorrelation. An even deeper analysis of such flows involves the structure of the spatial particle distribution in the turbulent flow. By observing the appropriate statistics (PDF of particle concentration and nearest-neighbor particle distance, radial distribution functions) a well studied behavior emerges: preferential concentration. According to this phenomenon, particles of moderate inertia tend to gather in low-vorticity regions of the flow and as a result, particle accumulation is observed.

Moreover, in order to isolate electrostatic interactions, like-charged dry particle clouds have been considered without the presence of any turbulent fluid flow. The combination of tri-periodic boundary conditions, and particle-particle electrostatic interactions has been found to pose a challenging and complicated problem, that of electrostatic periodicity. More specifically, the successful application of electrostatic periodicity requires the ensuring both of the convergence and of the isotropy of the long-range electrostatic field. In order to address that, and at the same time consider the computational cost as well as the accuracy of the calculations, a rather efficient algorithm has been created and its characteristics as well as the obtained results are extensively analyzed and documented.

The computational cost of the N_p -body problem is prohibitively high $\mathcal{O}(N_p^2)$. However, separating the interactions in short- and long-range can be a viable solution. Such a method, is the pseudo-particle method that is more efficient $\mathcal{O}(N_p^{1.5})$ and with an acceptable error. Furthermore, in case of tri-periodic BCs, since electrostatic forces depend on the distance of particle images, electrostatic periodicity entails an additional cost which scales with the cube of the number of periodic images per direction. However, it is shown that in order to represent accurately enough the periodic BCs, one periodic layer is enough so as to respect the isotropy and convergence of the long-range force field. In order to ensure such periodic isotropy, every particle has to interact with particles within a cubic periodic volume centered at its position.

In addition, an attempt to explain the nature of electrostatic interactions is made via an analogy with hard collisions. In fact, particle-particle (repulsive) electrostatic interactions can be viewed as (Coulomb) collisions happening at a distance with an effective Coulomb diameter that is proportional to the square of electric charge and inversely proportional to the square of the norm of particle relative velocity. By considering this analogy, one can deduce a Coulomb collision frequency and consequently a characteristic time scale of electrostatic interactions. A dimensional analysis supports this theory and it is verified via the corresponding measured quantities obtained by DNS of like-charged particle-laden flows. Effectively, particle agitation is linked to the particle-induced electric field and the very nature of electrostatic forces is observed in detail. Hence, a time scale of electrostatic interactions is proposed, whose order of magnitude has been compared to the characteristic time of Coulomb collisions.

To examine the competition between hydrodynamic drag and electrostatic forces, several like-charged particle-laden turbulent gas flows have been simulated with different particle charges in order to investigate the effects of electrostatic interactions on particle agitation. A statistical analysis of these flows has been carried out so as to acquire an insight of their behavioral dynamics. This statistical analysis, along with a theoretical one enables to rewrite the transient equations of important statistical moments and effectively derive the modified Tchen-Hinze theory for the stationary regime in the presence of electrostatic forces. In such a configuration, the two main mechanisms that drive particle behavior are the hydrodynamic drag and the electrostatic forces. To characterize the competition between the two, an electrostatic

Stokes number is devised and linked theoretically to the particle Stokes number.

Then, the effect of electrostatic interactions on particle dispersion is examined via a modification of the classic theoretical Tchen-Hinze framework. The basic observation is that for increasing particle electric charge, particle agitation increases for particles of moderate inertia and decreases for light particles, while heavy particles remain unaffected. This modification of particle agitation is not direct, but rather comes from a corresponding modification of fluid-particle covariance, which is a measure of fluid-particle correlation. In fact, a closer look at the flow dynamics shows that (repulsive) electrostatic forces slow down the turbulent dissipation rate of fluid-particle correlation, thus increasing fluid-particle correlation, while at the same time turbulence-induced electrostatic energy destroys this correlation. This essentially means that for a given level of particle inertia, stronger electrostatic interactions lead to a greater fluid-particle correlation up to a saturation level of electric charge, above which it starts to decrease. Same goes for particle agitation.

As far as the characteristic time scales are concerned, the Lagrangian integral time scale of the particle velocity, τ_p^t is considerably reduced by electrostatic interactions as particle velocities decorrelate faster under the influence of electrostatic forces, while their effect on the corresponding time scale of the turbulent velocity "seen" at the particles position, $\tau_{f@p}^t$ is not so straight forward. In fact, electrostatic interaction enhance the ability of light particles to follow fluid trajectories, while for heavy particles the opposite trend is observed, hence they tend to become even more decorrelated from the turbulent flow. The former time scale seems to be the reason for a significant reduction of the particle dispersion coefficient, which entails an equivalent reduction of particle dispersion. Particles that are constantly repelled from each other, are less prone to wander off their initial positions as they have to "navigate" through paths of minimum resistance, hence this observed behavior.

An extensive analysis of electrostatic forces themselves, has been also carried out which brings to light their rather peculiar distribution whose form seems to be greatly different from Exponential and Gaussian distributions. In addition, a characteristic time scale of electrostatic interactions is defined and it could be used to determine the lifetime of the application of such a force distribution in a stochastic model. The spatial distribution of the like-charged particle cloud is examined and two main interesting observations are drawn. Firstly, the preferential concentration is mitigated for weak particle electric charges and completely eliminated for strong ones. Secondly, there appears to be an exclusion zone around each particle, that stems from the fact that inside this zone, the repulsive electrostatic forces are substantially strong so that no particle can ever stay in this zone, leading to an equidistant particle distribution.

Finally, the effect of particle number density on particle flow characteristics has been examined. It becomes evident that there is a clear distinction between the "kinetic state" of the gas-particle flow and the spatial structure of the charged particle cloud. In fact τ_{el} seems to be a very good candidate at describing the kinetic energy content of such a flow, however the spatial particle distribution seems to be considerably affected by the particle number density. Simply, more particles per volume normally entail more particle accumulation, however more particles per volume of the same level of electric charge, entail a higher particle charge density which leads to a rather homogeneous (equidistant distribution) but inevitably that of a smaller inter-particle distance.

6.2 Future work

Although most of the fundamental goals set at the beginning of this PhD have been achieved, there are several topics that have not been well investigated and more work needs to be done

towards this direction, in order to make more progress in this subject.

To begin with, as far as the gas-particle part is concerned, there are a lot of points that could be reconsidered. First, one could consider more dense particulate flows which would require to take into account particle-particle (physical) collisions and/or the introduction of two-way coupling. In this case, this would allow for a more accurate representation of the simulated physics. There is practically no end in how complex physics, one could try to simulate, so in the same spirit, one could imagine non-spherical particles that would require the addition of supplementary forces (e.g. buoyancy/lubrication force, rotation) and/or orientation, etc. Lastly, it would be certainly interesting to be able to add walls in any direction of preference and simulate turbulent channel flows which is representative of more real-life applications. Continuing with the charge-free physics, in the future, more work needs to be carried out towards the modeling of the fluid acceleration - particle velocity covariance, especially for light particles, and the work presented in this PhD offers a rather comprehensive approach to do so.

As far as the computational methods for the calculation of electrostatic forces are concerned, there is certainly room for improvement and expansion in this front. Although the presented algorithm is very robust and efficient for the requirements of this work, one could implement a very competitive FMM algorithm with tri-periodic BCs. That would allow for a very fast, robust and accurate calculation of the inter-particle electrostatic interactions for considerably more particles ($\sim N_p \in [10^7, 10^8]$). Such an algorithm would also allow for a more generic application of boundary conditions, where one can imagine charged walls (Dirichlet), insulated walls (Neumann), that could potentially bare interest for more industry-oriented applications.

In the same spirit of more accurate representation of particle electrostatics, one could also envisage to simulate distributions of particle charges. In addition, charges of different polarity would certainly require the resolution of physical particle collisions. The epitome of such a capability would be a time-variable particle electric charge distribution that is potentially modified at every time-step via wall- and particle-particle hard/soft physical collisions along with a triboelectricity model. However, in order to perform simulations of oppositely charged particles, one would need to be very careful with the time resolution of their collisions, as electrostatic forces would present strongly non-linear behavior as they scale quadratically with the inverse of the inter-particle distance.

As far as the observed physics are concerned, more clarification is needed towards the investigation of the effect of electrostatic interactions on the autocorrelation functions of fluid velocity "seen" by inertial particles. More specifically, the modification of the turbulent spectrum "seen" by the charged inertial particles due to electrostatic interactions has not been thoroughly understood in the presented work. Increasing the number of particles from $N_p = 10^4$ to 10^5 would be the first step towards that, as the calculation of the autocorrelation function would be significantly more accurate, thus allowing for a more confident analysis. Such a study could allow us to further investigate particle dispersion, preferential concentration as well as modeling the electrostatic-related terms in the modified Tchen-Hinze equation.

Moreover, it would be equally interesting to examine the effect of gravity in such a system, thus to study the dispersion of charged inertial particles settling in stationary homogeneous isotropic turbulence. This would be of great interest for applications that focus on particle deposition and would be closer to real-life applications. Of course, the inclusion of the gravity force, would increase considerably the complexity of the system as particles move preferentially towards the direction of the gravity and special treatment is needed for the statistical description of such a flow.

Another interesting direction that could be taken as continuation of this work is the creation of a stochastic model for predicting inter-particle electrostatic interactions of inertial

charged particles in stationary HIT. In fact, the electrostatic interactions have been well documented in this work, and all the elements needed for such a work are available. Such are the average value and variance of the electrostatic forces for various levels of particle inertia and electric charges, the characteristic lifetime of electrostatic interactions, the PDF of electrostatic forces, etc. However, more work needs to be done towards the modeling of these elements so that the knowledge obtained via the physical analysis of high fidelity DNS data is transferred to lower fidelity stochastic models. The latter are of great interest for engineering applications that look into at larger-scale simulations.

Appendices

APPENDIX **A**

Numerical schemes

A.1 2nd order Adams-Bashforth numerical schemes

Assuming a constant time step, the 2nd order Adams-Bashforth numerical scheme takes the following form:

$$\frac{df_i}{dt} = g_i \Rightarrow \frac{f_i^{n+1} - f_i^n}{\Delta t} = \frac{3}{2}g_i^n - \frac{1}{2}g_i^{n-1} . \quad (\text{A.1})$$

A.1.1 Discretization of N-S momentum equation

N-S equation of momentum with turbulent forcing (2.14) is re-written as

$$\frac{d\hat{u}_{f,i}}{dt} + \nu_f \kappa^2 \hat{u}_{f,i} + \hat{R}_i = 0 \quad (\text{A.2})$$

where \hat{R}_i contains the advection and non-linear terms of the (spectral) N-S equations as well as the turbulence forcing term and is defined as

$$\hat{R}_i = \left[\delta_{ij} - \frac{\kappa_i \kappa_j}{\kappa^2} \right] \hat{N}_j - \hat{a}_i .$$

Equation (A.2) is strictly equivalent to

$$\frac{d}{dt} \left(\hat{u}_{f,i} e^{\nu_f \kappa^2 t} \right) + \hat{R}_i e^{\nu_f \kappa^2 t} = 0 . \quad (\text{A.3})$$

Discretizing (A.3) using 2nd order Adams-Bashforth numerical scheme of Eq. (A.1) (as shown in Sect. A.1.1) yields an equation for advancing fluid velocity in the frequency domain that gives

$$\hat{u}_{f,i}^{n+1} = \hat{u}_{f,i}^n e^{-\nu_f \kappa^2 \Delta t} - \frac{\Delta t}{2} \left[3\hat{R}_i^n e^{-\nu_f \kappa^2 \Delta t} - \hat{R}_i^{n-1} e^{\nu_f \kappa^2 t} e^{-2\nu_f \kappa^2 \Delta t} \right] .$$

Applying this scheme to discretize equation of momentum (A.3) yields

$$\begin{aligned} \frac{\hat{u}_i e^{\nu_f \kappa^2 t} \Big|^{n+1} - \hat{u}_i e^{\nu_f \kappa^2 t} \Big|^n}{\Delta t} &= -\frac{3}{2} \hat{R}_i e^{\nu_f \kappa^2 t} \Big|^n + \frac{1}{2} \hat{R}_i e^{\nu_f \kappa^2 t} \Big|^{n-1} \\ \frac{\hat{u}_i^{n+1} e^{\nu_f \kappa^2 (t+\Delta t)} - \hat{u}_i^n e^{\nu_f \kappa^2 t}}{\Delta t} &= -\frac{3}{2} \hat{R}_i^n e^{\nu_f \kappa^2 t} + \frac{1}{2} \hat{R}_i^{n-1} e^{\nu_f \kappa^2 (t-\Delta t)} \\ \hat{u}_i^{n+1} e^{\nu_f \kappa^2 (t+\Delta t)} - \hat{u}_i^n e^{\nu_f \kappa^2 t} &= -\frac{\Delta t}{2} \left[3\hat{R}_i^n e^{\nu_f \kappa^2 t} - \hat{R}_i^{n-1} e^{\nu_f \kappa^2 (t-\Delta t)} \right] . \end{aligned}$$

Expanding the exponential terms and simplifying gives

$$\begin{aligned} \hat{u}_i^{n+1} e^{\nu_f \kappa^2 t} e^{\nu_f \kappa^2 \Delta t} - \hat{u}_i^n e^{\nu_f \kappa^2 t} &= -\frac{\Delta t}{2} \left[3\hat{R}_i^n e^{\nu_f \kappa^2 t} - \hat{R}_i^{n-1} e^{\nu_f \kappa^2 t} e^{-\nu_f \kappa^2 \Delta t} \right] \\ \hat{u}_i^{n+1} e^{\nu_f \kappa^2 \Delta t} - \hat{u}_i^n &= -\frac{\Delta t}{2} \left[3\hat{R}_i^n - \hat{R}_i^{n-1} e^{-\nu_f \kappa^2 \Delta t} \right] . \end{aligned}$$

Finally, fluid velocity is advanced in the frequency domain via the following equation

$$\hat{u}_i^{n+1} = \hat{u}_i^n e^{-\nu_f \kappa^2 \Delta t} - \frac{\Delta t}{2} \left[3\hat{R}_i^n e^{-\nu_f \kappa^2 \Delta t} - \hat{R}_i^{n-1} e^{\nu_f \kappa^2 t} e^{-2\nu_f \kappa^2 \Delta t} \right] .$$

A.1.2 Discretization of particle motion equation

The particle trajectory equation Eq. (2.20) can be written as

$$\frac{du_{p,i}}{dt} = -\alpha u_{p,i} + \beta \quad (\text{A.4})$$

with

$$\alpha = \frac{1}{\tau_p} \quad \text{and} \quad \beta = \frac{uf@p,i}{\tau_p} + \frac{F_{e,i}}{m_p} - g \cdot \delta_{i3}$$

Equation (A.4) is strictly equivalent to

$$\frac{d(u_{p,i}e^{\alpha t})}{dt} = \beta e^{\alpha t}. \quad (\text{A.5})$$

Discretizing (A.5) using 2nd order Adams-Bashforth numerical scheme of Eq. (A.1) (as shown in Sect. A.1.2) yields an equation for advancing particle velocity time that gives

$$u_{p,i}^{n+1} = u_{p,i}^n e^{-\Delta t/\tau_p} + \frac{\Delta t}{2} \left[3\beta^n e^{-\Delta t/\tau_p} - \beta^{n-1} e^{-2\Delta t/\tau_p} \right].$$

Applying this scheme to discretize the equation of particle motion (A.5) yields

$$\begin{aligned} \frac{u_{p,i}e^{\alpha t}|^{n+1} - u_{p,i}e^{\alpha t}|^n}{\Delta t} &= \frac{3}{2}\beta e^{\alpha t}|^n - \frac{1}{2}\beta e^{\alpha t}|^{n-1} \\ \frac{u_{p,i}^{n+1}e^{\alpha^{n+1}(t+\Delta t)} - u_{p,i}^n e^{\alpha^n(t)}}{\Delta t} &= \frac{3}{2}\beta^n e^{\alpha^n t} - \frac{1}{2}\beta^{n-1} e^{\alpha^{n-1}(t-\Delta t)}. \end{aligned}$$

Since $\alpha = \alpha(t)$, the above equation cannot be further simplified. However, it is reasonable to assume that the particle response has small fluctuations between two time steps. Under such an assumption $\alpha^{n-1} = \alpha^n = \alpha^{n+1} = \alpha$, therefore

$$\begin{aligned} u_{p,i}^{n+1} e^{\alpha(t+\Delta t)} - u_{p,i}^n e^{\alpha t} &= \frac{\Delta t}{2} \left[3\beta^n e^{\alpha t} - \beta^{n-1} e^{\alpha(t-\Delta t)} \right] \\ u_{p,i}^{n+1} e^{\alpha \Delta t} - u_{p,i}^n &= \frac{\Delta t}{2} \left[3\beta^n - \beta^{n-1} e^{-\alpha \Delta t} \right] \\ u_{p,i}^{n+1} &= u_{p,i}^n e^{-\alpha \Delta t} + \frac{\Delta t}{2} \left[3\beta^n e^{-\alpha \Delta t} - \beta^{n-1} e^{-2\alpha \Delta t} \right]. \end{aligned}$$

Finally, the time-integration of particle momentum equation is performed by the following equation

$$u_{p,i}^{n+1} = u_{p,i}^n e^{-\Delta t/\tau_p} + \frac{\Delta t}{2} \left[3\beta^n e^{-\Delta t/\tau_p} - \beta^{n-1} e^{-2\Delta t/\tau_p} \right].$$

A.2 Lagrange polynomial interpolation schemes

Below, the Lagrange polynomials defined by Eq. (2.24) are calculated for 1st, 2nd, 3rd and 4th order.

1st order

For $n = 1$, at least $N = 2$ points are needed in order to perform the interpolation as

$$P(x) = f(x_1)p_1 + f(x_2)p_2$$

with $n + 1 = 2$ base polynomials

$$p_1 = \frac{x - x_2}{x_1 - x_2} = 1 - \alpha$$

$$p_2 = \frac{x - x_1}{x_2 - x_1} = \alpha .$$

2nd order

For $n = 2$, at least $N = 3$ points are needed in order to perform the interpolation as

$$P(x) = f(x_1)p_1 + f(x_2)p_2 + f(x_3)p_3$$

with $n + 1 = 3$ base polynomials

$$p_1 = \frac{x - x_2}{x_1 - x_2} \times \frac{x - x_3}{x_1 - x_3} = \frac{1}{2}(\alpha - 1)(\alpha - 2)$$

$$p_2 = \frac{x - x_1}{x_2 - x_1} \times \frac{x - x_3}{x_2 - x_3} = -\alpha(\alpha - 2)$$

$$p_3 = \frac{x - x_1}{x_3 - x_1} \times \frac{x - x_2}{x_3 - x_2} = \frac{1}{2}\alpha(\alpha - 1) .$$

3rd order

For $n = 3$, at least $N = 4$ points are needed in order to perform the interpolation as

$$P(x) = f(x_1)p_1 + f(x_2)p_2 + f(x_3)p_3 + f(x_4)p_4$$

with $n + 1 = 4$ base polynomials

$$p_1 = \frac{x - x_2}{x_1 - x_2} \times \frac{x - x_3}{x_1 - x_3} \times \frac{x - x_4}{x_1 - x_4} = -\frac{1}{6}(\alpha - 1)(\alpha - 2)(\alpha - 3)$$

$$p_2 = \frac{x - x_1}{x_2 - x_1} \times \frac{x - x_3}{x_2 - x_3} \times \frac{x - x_4}{x_1 - x_4} = \frac{1}{2}\alpha(\alpha - 2)(\alpha - 3)$$

$$p_3 = \frac{x - x_1}{x_3 - x_1} \times \frac{x - x_2}{x_3 - x_2} \times \frac{x - x_4}{x_1 - x_4} = -\frac{1}{2}\alpha(\alpha - 1)(\alpha - 3)$$

$$p_4 = \frac{x - x_1}{x_3 - x_1} \times \frac{x - x_2}{x_3 - x_2} \times \frac{x - x_4}{x_1 - x_4} = \frac{1}{6}\alpha(\alpha - 1)(\alpha - 2) .$$

4th order

For $n = 4$, at least $N = 5$ points are needed in order to perform the interpolation as

$$P(x) = f(x_1)p_1 + f(x_2)p_2 + f(x_3)p_3 + f(x_4)p_4 + f(x_5)p_5$$

with $n + 1 = 5$ base polynomials

$$\begin{aligned}
 p_1 &= \frac{x - x_2}{x_1 - x_2} \times \frac{x - x_3}{x_1 - x_3} \times \frac{x - x_4}{x_1 - x_4} \times \frac{x - x_5}{x_1 - x_5} = \frac{1}{24} (\alpha - 1) (\alpha - 2) (\alpha - 3) (\alpha - 4) \\
 p_2 &= \frac{x - x_1}{x_2 - x_1} \times \frac{x - x_3}{x_2 - x_3} \times \frac{x - x_4}{x_1 - x_4} \times \frac{x - x_5}{x_1 - x_5} = -\frac{1}{6} \alpha (\alpha - 2) (\alpha - 3) (\alpha - 4) \\
 p_3 &= \frac{x - x_1}{x_3 - x_1} \times \frac{x - x_2}{x_3 - x_2} \times \frac{x - x_4}{x_1 - x_4} \times \frac{x - x_5}{x_1 - x_5} = \frac{1}{4} \alpha (\alpha - 1) (\alpha - 3) (\alpha - 4) \\
 p_4 &= \frac{x - x_1}{x_3 - x_1} \times \frac{x - x_2}{x_3 - x_2} \times \frac{x - x_4}{x_1 - x_4} \times \frac{x - x_5}{x_1 - x_5} = -\frac{1}{6} \alpha (\alpha - 1) (\alpha - 2) (\alpha - 4) \\
 p_5 &= \frac{x - x_1}{x_3 - x_1} \times \frac{x - x_2}{x_3 - x_2} \times \frac{x - x_4}{x_1 - x_4} \times \frac{x - x_5}{x_1 - x_5} = \frac{1}{24} \alpha (\alpha - 1) (\alpha - 2) (\alpha - 3) .
 \end{aligned}$$

APPENDIX B

Pseudo-particle algorithm

B.1 Pseudo-particle rectangles

A pseudo-particle rectangle X_k centered in position \mathbf{x}_k^{eq} of equivalent pseudo-particle Ω_k , is defined in a cell whose center is denoted as \mathbf{x}_k^c . Its dimensions are $\Delta \mathbf{x}_k^{eq} = \mathbf{x}_{k \min}^{eq} - \mathbf{x}_{k \max}^{eq}$ where $\mathbf{x}_{k \min}^{eq}$ and $\mathbf{x}_{k \max}^{eq}$ are its borders.

$$x_{k,i \min}^{eq} = \begin{cases} x_{k,i}^c - \frac{\Delta x_f}{2}, & \text{if } x_{k,i}^{eq} < x_{k,i}^c \\ 2x_{k,i}^{eq} - x_{k,i}^c - \frac{\Delta x_f}{2}, & \text{otherwise} \end{cases} \quad (\text{B.1})$$

and

$$x_{k,i \max}^{eq} = \begin{cases} 2x_{k,i}^{eq} - x_{k,i}^c + \frac{\Delta x_f}{2}, & \text{if } x_{k,i}^{eq} < x_{k,i}^c \\ x_{k,i}^c + \frac{\Delta x_f}{2}, & \text{otherwise} \end{cases}. \quad (\text{B.2})$$

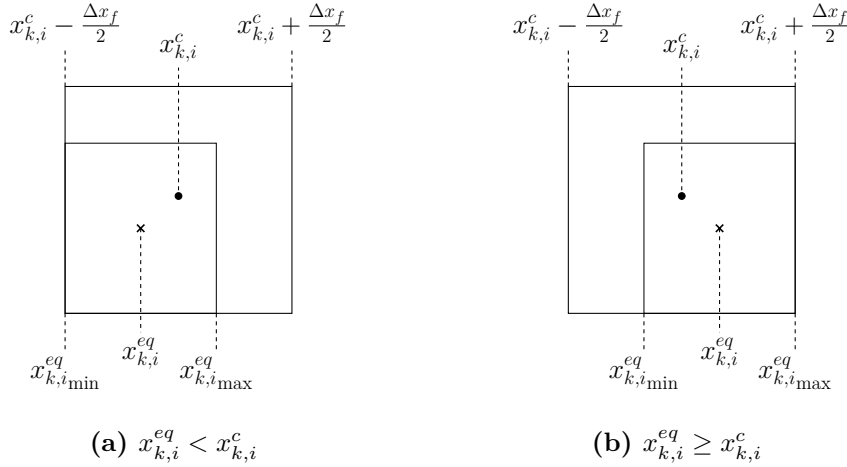


Figure B.1: Two different possible pseudo-particle positions \mathbf{x}_k^{eq} relative to cell center \mathbf{x}_k^c .

B.2 Optimal computational cost

The computational cost of the pseudo-particle algorithm with periodic boundary conditions depends on the number of particles N_p , the number of cells N_e , the number of neighborhood cells N_v and the number of periodic domain images N_{per} . Its function has been estimated theoretically in Eq. (4.16) and can be rewritten as

$$\mathcal{C}(N_p, N_e, N_v, N_{per}) = N_p \left[(2N_v + 1)^3 \frac{N_p}{N_e^3} + (2N_{per} - 1)^3 N_e^3 - (2N_v + 1)^3 - 1 \right]. \quad (\text{B.3})$$

For given N_p , N_v and N_{per} there is an optimal number of cells $N_e^{opt} \in [(2N_v + 2) / (2N_{per} - 1), N_p^{1/3}]$ that minimizes the function of the computational cost. In order to calculate N_e^{opt} , one can write the partial derivative

$$\frac{\partial C}{\partial N_e} = -3N_p^2 (2N_v + 1)^3 N_e^{-4} + 3(2N_{per} - 1)^3 N_e^2 N_p .$$

Hence, N_e^{opt} is the solution of Eq. (B.2) with regards to N_e

$$\begin{aligned} \frac{\partial C}{\partial N_e} &= 0 \\ N_p (2N_v + 1)^3 N_e^{-4} &= (2N_{per} - 1)^3 N_e^2 \\ N_e^6 &= N_p \left(\frac{2N_v + 1}{2N_{per} - 1} \right)^3 \\ N_e^{opt} &= N_p^{1/6} \left(\frac{2N_v + 1}{2N_{per} - 1} \right)^{1/2} . \end{aligned}$$

If $N_n = 2N_v + 1$ and $N_{im} = 2N_{per} - 1$, then $N_e^{opt} = N_p^{1/6} (N_n/N_{im})^{1/2}$ and the optimal (minimum) computational cost would be

$$\begin{aligned} C^{opt}(N_p, N_v, N_{per}) &= C^{opt}(N_p, N_e^{opt}, N_v, N_{per}) \\ &= N_p \left[N_n^3 \frac{N_p}{N_p^{1/2}} \left(\frac{N_{im}}{N_n} \right)^{3/2} + N_{im}^3 N_p^{1/2} \left(\frac{N_n}{N_{im}} \right)^{3/2} - N_n^3 - 1 \right] \\ &= N_p \left[N_n^{3/2} N_p^{1/2} N_{im}^{3/2} + N_n^{3/2} N_p^{1/2} N_{im}^{3/2} - N_n^3 - 1 \right] \\ &= N_p \left[2N_n^{3/2} N_p^{1/2} N_{im}^{3/2} - N_n^3 - 1 \right] \\ &\sim N_p^{3/2} N_v^{3/2} N_{per}^{3/2} \end{aligned}$$

and the corresponding optimal number of particles per cell is

$$N_k^{opt} = N_p^{1/2} \left(\frac{2N_{per} - 1}{2N_v + 1} \right)^{3/2} .$$

Turbulent charged particle-laden gas flows

C.1 Nondimensionalization of the particle motion equation

In case of turbulent charged particle-laden gas flows with periodic boundary conditions, the equation of particle motion 2.20 can be written as

$$m_p \frac{d\mathbf{u}_p}{dt} = \sum_{\substack{q=1 \\ q \neq p}}^{N_p} \sum_{\substack{l, m, n = -N_{per} \\ |r_{pq, i}^\dagger| \leq \alpha_c}}^{N_{per}} \lambda \frac{Q_q Q_p}{\|\mathbf{r}_{pq}^\dagger\|^3} \mathbf{r}_{pq}^\dagger - m_p \frac{\mathbf{u}_p - \mathbf{u}_{f@p}}{\tau_p} - m_p g \hat{\mathbf{k}}. \quad (\text{C.1})$$

To nondimensionalize this equation, one should write every physical quantity q as $q = Q \cdot \tilde{q}$, where Q is a reference quantity and \tilde{q} the non-dimensional instance of quantity q . Table C.1, presents the quantities for the particle motion problem in charged granular flows. To begin

Table C.1: Reference quantities for the particle motion problem

Parameters	Symbol	Units
Length	L	m
Time	τ_{el}	s
Charge	Q_0	C
Mass	m_0	kg
Velocity	L/τ_{el}	m/s
Acceleration	L/τ_{el}^2	m/s^2

with, normalizing Eq. (C.1) with particle mass m_p gives

$$\frac{d\mathbf{u}_p}{dt} = \frac{1}{m_p} \sum_{\substack{q=1 \\ q \neq p}}^{N_p} \sum_{\substack{l, m, n = -N_{per} \\ |r_{pq, i}^\dagger| \leq \alpha_c}}^{N_{per}} \lambda \frac{Q_q Q_p}{\|\mathbf{r}_{pq}^\dagger\|^3} \mathbf{r}_{pq}^\dagger - \frac{\mathbf{u}_p - \mathbf{u}_{f@p}}{\tau_p} - g \hat{\mathbf{k}}.$$

Finally by inserting the non-dimensional quantities in the equations one can get

$$\begin{aligned} \frac{L}{\tau_{el}^2} \frac{d\tilde{\mathbf{u}}_p}{d\tilde{t}} &= \frac{1}{m_0} \cdot \frac{1}{\tilde{m}_p} \sum_{\substack{q=1 \\ q \neq p}}^{N_p} \sum_{\substack{l, m, n = -N_{per} \\ |r_{pq, i}^\dagger| \leq \alpha_c}}^{N_{per}} \frac{\lambda Q_0^2}{L^2} \frac{\tilde{Q}_q \tilde{Q}_p}{\|\tilde{\mathbf{r}}_{pq}^\dagger\|^3} \tilde{\mathbf{r}}_{pq}^\dagger - \frac{L}{\tau_{el}^2} \frac{\tilde{\mathbf{u}}_p - \tilde{\mathbf{u}}_{f@p}}{\tilde{\tau}_p} - \frac{L}{\tau_{el}^2} \tilde{g} \hat{\mathbf{k}} \\ \frac{d\tilde{\mathbf{u}}_p}{d\tilde{t}} &= \frac{\lambda Q_0^2}{m_0 L^2} \frac{\tau_{el}^2}{L} \cdot \frac{1}{\tilde{m}_p} \sum_{\substack{q=1 \\ q \neq p}}^{N_p} \sum_{\substack{l, m, n = -N_{per} \\ |r_{pq, i}^\dagger| \leq \alpha_c}}^{N_{per}} \frac{\tilde{Q}_q \tilde{Q}_p}{\|\tilde{\mathbf{r}}_{pq}^\dagger\|^3} \tilde{\mathbf{r}}_{pq}^\dagger - \frac{\tilde{\mathbf{u}}_p - \tilde{\mathbf{u}}_{f@p}}{\tilde{\tau}_p} - \tilde{g} \hat{\mathbf{k}} \\ \frac{d\tilde{\mathbf{u}}_p}{d\tilde{t}} &= \frac{\lambda Q_0^2 \tau_{el}^2}{m_0 L^3} \cdot N_p \frac{\tilde{\mathbf{F}}_e}{\tilde{m}_p} + \frac{\tilde{\mathbf{F}}_d}{\tilde{m}_p} + \frac{\tilde{\mathbf{F}}_g}{\tilde{m}_p}. \end{aligned}$$

This last equation is dimensionless and the ratio $\lambda N_p Q_0^2 \tau_{el}^2 / (m_0 L^3)$ is also a dimensionless number. For a 1st order approximation, one could assume $\lambda N_p Q_0^2 \tau_{el}^2 / (m_0 L^3) \sim 1$, which yields

$$\begin{aligned}\tau_{el} &\propto \sqrt{\frac{m_0 L^3}{N_p Q_0^2 \lambda}} \\ \tau_{el} &\propto \frac{1}{Q_0} \sqrt{\frac{m_0 L^3}{N_p \lambda}} \\ \tau_{el} &\propto \frac{1}{Q_0} \sqrt{\frac{m_0}{\lambda n_p}}.\end{aligned}$$

C.2 Particle electric potential energy

For the following analysis, we introduce the kinetic energy e_{k_p} and the total electric potential energy u_e of the system defined as following

$$e_{k_p} = \frac{1}{2} m_p \|\mathbf{u}_p\|^2 \quad (\text{C.2})$$

$$u_e = \sum_{\substack{q=1 \\ q \neq p}}^{N_p} \lambda \frac{Q_q Q_p}{\|\mathbf{r}_{pq}\|}. \quad (\text{C.3})$$

According to the kinetic energy theorem, the kinetic energy variation of a particle system between two time instants is equal to the sum of the work of all the forces applied to each particle of the system along the trajectory of each of these points in the same time interval. Considering the dry granular case, the work of the electrostatic forces exerted on the particles is a measure of kinetic energy variation between two positions, say (1) and (2): $W_{1 \rightarrow 2} / m_p = \Delta q_p^2 \Big|_{1 \rightarrow 2}$ and $W_{1 \rightarrow 2} = \sum_{i=1}^{N_p} \int_1^2 \mathbf{F}_e^{(i)} \cdot \mathbf{u}_p^{(i)} \delta t$. In order to get an equation for the kinetic energy, one can multiply Eq. (2.20) by \mathbf{u}_p using the identity $q\dot{q} = \frac{1}{2} \frac{d}{dt} q^2$ for $q = q(\mathbf{x}_p, t)$:

$$\begin{aligned}\frac{1}{2} \frac{d}{dt} \mathbf{u}_p^2 &= \frac{1}{m_p} \mathbf{F}_e \cdot \mathbf{u}_p + \frac{1}{m_p} \mathbf{F}_d \cdot \mathbf{u}_p \\ \underbrace{\frac{1}{2} \frac{d}{dt} \mathbf{u}_p^2}_{\text{kinetic energy}} &= \underbrace{\frac{1}{m_p} \frac{W_e}{\delta t}}_{\text{electrostatic force work}} + \underbrace{\frac{1}{m_p} \frac{W_d}{\delta t}}_{\text{drag force work}}.\end{aligned} \quad (\text{C.4})$$

Essentially, this last power balance is basically the 2nd thermodynamic law. The first term of the right hand side represents the specific electrostatic power

$$\frac{P_e}{m_p} = \frac{1}{m_p} \frac{W_e}{\delta t} = \frac{1}{m_p} \frac{d}{dt} U_e = \frac{1}{m_p} \frac{d}{dt} \mathbf{F}_e \cdot \mathbf{x}_p = \frac{\mathbf{F}_e}{m_p} \cdot \mathbf{u}_p. \quad (\text{C.5})$$